DIELECTROPHORESIS BASED METHODS FOR SEPARATING PARTICLES ON LAB-ON-CHIP PLATFORMS

by

Samuel J. Dickerson

B.S. in Computer Engineering, University of Pittsburgh, 2003

M.S. in Electrical Engineering, University of Pittsburgh, 2007

Submitted to the Graduate Faculty of

Swanson School of Engineering in partial fulfillment

of the requirements for the degree of

Doctor of Philosophy

University of Pittsburgh

2012

UNIVERSITY OF PITTSBURGH

SWANSON SCHOOL OF ENGINEERING

This dissertation was presented

by

Samuel J. Dickerson

It was defended on

November 20, 2012

and approved by

Zhi-Hong Mao, PhD, Assistant Professor, Department of Electrical and Computer Engineering

Minhee Yun, PhD, Associate Professor, Department of Electrical and Computer Engineering

Fred L. Homa, PhD, Associate Professor, Department of Microbiology and Molecular Genetics

Mingui Sun, PhD, Professor, Departments of Bioengineering and Electrical Engineering

Co-Director: Donald M. Chiarulli, PhD, Professor, Department of Computer Science

Co-Director: Steven P. Levitan, PhD, Professor, Department of Electrical and Computer Engineering

DIELECTROPHORESIS BASED METHODS FOR SEPARATING PARTICLES ON LAB-ON-CHIP PLATFORMS

Samuel J. Dickerson, PhD

University of Pittsburgh, 2012

Lab-on-chip devices are an emerging microsystem technology in which laboratory functions are miniaturized into compact, chip-scale packages. Such devices enable analyses to be performed at lower cost and higher speed than with traditional methods. One major application area for these devices is their use in sorting and separating biological particles.

In this dissertation, we present a new technique for separating biological particles on lab-on-chip platforms. The foundation of our method is dielectrophoresis, a technique where AC electric fields are used to manipulate particles in a fluid, based on their inherent electrical properties. These electrical properties reflect differences not just in size, but also capture subtle variations in the internal composition of the particle. Using a novel time-multiplexed combination of dielectrophoresis methods over very dense electrode arrays, we can create strong electric fields with a high degree of spatial resolution. When placed in the presence of these fields, particles with variations in composition can be made to experience different amounts of force, forces in opposite directions, or no force at all simply by applying fields of specific frequency and phase in particular regions of the electrode array. By time-multiplexing, or rapidly alternating the field configuration over time, we can exert differential forces on particles of varying types. Time-multiplexing dielectrophoresis enables separations between particle types to take place under conditions that would otherwise make them inseparable. The application of the method significantly loosens the requirements competing methods have on

maintaining a buffer with specific electric properties and has the ability to increase the differential rate at which particles migrate apart. As a result of our method, the use of dielectrophoresis to separate particles becomes a viable alternative in real-world situations.

To demonstrate our claims we have created a small library of five particle types, including yeast cells and polystyrene microspheres of varying types. We have selected appropriate electrical models for each of these particles and use the models to analytically validate our methodology. For this dissertation, we have also developed a novel lab-on-chip hardware platform to experimentally validate our models and demonstrate the effectiveness of our technique. The presented methodology and its implementation have the potential to serve as the basis for a new class of point-of-care, portable diagnostic devices by allowing researchers to sort and assay particles of interest based on their structure and composition without the use of expensive and destructive biochemical labeling techniques.

TABLE OF CONTENTS

1.0 INTRODUCTION 1

1.1 PROBLEM STATEMENT AND HYPOTHESIS 4

1.2 STATEMENT OF WORK 5

1.3 RESEARCH CONTRIBUTIONS 6

1.4 DISSERTATION ROADMAP 7

2.0 BACKGROUND AND MOTIVATION 9

2.1 MOTIVATION FOR DIELECTROPHORESIS-BASED LAB-ON-CHIP TECHNOLOGY 9

2.2 THEORY OF DIELECTROPHORESIS 15

2.3 TRAVELING-WAVE DIELECTROPHORESIS 19

2.4 DIELECTROPHORESIS BASED METHODS FOR SEPARATING PARTICLES 23

2.5 SOURCES OF NOISE IN DIELECTROPHORESIS MICROSYSTEMS .. 26

2.5.1 AC Electroosmosis 27

2.5.2 Electro-thermal forces 31

2.5.3 Random Brownian force 31

2.5.4 Buoyancy forces 32

3.0 DIELECTROPHORETIC CHARACTERIZATION OF PARTICLES 34

3.1 COMPLEX PERMITTIVITY PARTICLE MODELS 35

3.1.1 Polystyrene Microspheres (10um) 35

3.1.2 Polystyrene-COOH Microspheres (10um) 39

3.1.3 Polystyrene-COOH Microspheres (6um) 43

3.1.4 Live Yeast Cells 45

3.1.5 Dead Yeast Cells 52

3.2 COMPARISON OF DIELECTROPHORESIS FORCES TO NOISE SOURCES 57

4.0 PROPOSED METHODOLOGY: SEPARATION OF PARTICLES BY TIME-MULTIPLEXED DIELECTROPHORESIS 59

4.1 GENERATING DIFFERENTIAL PARTICLE MOTION VIA TIME-MULTIPLEXING DIELECTROPHORESIS FIELDS 60

4.2 SEPARATING PARTICLES VIA TIME-MULTIPLEXED DIELECTROPHORESIS 65

4.3 CREATING SEPARABLE CONDITIONS USING TIME-MULTIPLEXED DIELECTROPHORESIS 76

4.4 ADDITIONAL ADVANTAGES OF TIME-MULTIPLEXING DIELECTROPHORESIS 85

5.0 EXPERIMENTAL DESIGN: LAB-ON-CHIP HARDWARE PLATFORM 91

5.1 DIELECTROPHORESIS ELECTRODES 92

5.1.1 Quadrupole Characterization Electrodes Design 93

5.1.1.1 Finite-Element Analysis Simulations of Quadrupole Characterization Electrodes 96

5.1.2 Linear Separation Electrode Array Design 104

5.1.2.1 Finite-Element Analysis Simulations of Separation Electrode Array 104

5.1.3 Electrode Fabrication and Packaging 107

5.1.3.1 Packaging of Quadrupole Electrodes 111

5.1.3.2 Packaging of Separation Electrode Array 112

5.2 MICROFLUIDIC INTERFACES 114

5.2.1 Quadrupole Characterization Chip Microfluidic Interface 117

5.2.2 Separation Chip Microfluidic Interface 119

5.3 ELECTRONIC DESIGN 123

5.3.1 Electronic Design for Quadrupole Characterization Electrodes 123

5.3.2 Electronic Design for Separation Electrodes 126

5.3.3 Software User Interface 128

6.0 EXPERIMENTAL CHARACTERIZATION OF PARTICLE LIBRARY 131

6.1 CHARACTERIZATION RESULTS 135

6.1.1 Polystyrene Microspheres (10um) 135

6.1.2 Polystyrene-COOH Microspheres (10um) 139

6.1.3 Polystyrene-COOH Microspheres (6um) 143

6.1.4 Live Yeast Cells 147

6.1.5 Dead Yeast Cells 152

6.2 DISCUSSION OF RESULTS 156

7.0 SEPARABILITY OF PARTICLES USING TIME-MULTIPLEXED DIELECTROPHORESIS 158

7.1 ANALYTICAL SEPARABILITY RESULTS 160

7.1.1 Live Yeast and Dead Yeast 160

7.1.2 Polystyrene-COOH (10um) and Live Yeast 163

7.1.3 Polystyrene-COOH (10um) and Dead Yeast 166

7.1.4 Polystyrene-COOH (10um) and Polystyrene (10um) 169

7.1.5 Polystyrene (10um) and Live Yeast 172

7.1.6 Polystyrene (10um) and Dead Yeast 175

7.1.7 Polystyrene-COOH (6um) and Live Yeast 178

7.1.8 Polystyrene-COOH (6um) and Dead Yeast 181

7.1.9 Polystyrene-COOH (6um) and Polystyrene-COOH (10um) 184

7.1.10 Polystyrene-COOH (6um) and Polystyrene (10um) 187

7.2 DISCUSSION OF RESULTS 190

8.0 TIME-MULTIPLEXED DIELECTROPHORESIS EXPERIMENTAL TRIALS 195

8.1 EXPERIMENTAL RESULTS 195

8.1.1 Time-Multiplexed Dielectrophoresis of Live and Dead Yeast Cells 196

8.1.2 Time-Multiplexed Dielectrophoresis of Live Yeast Cells and 10μm PS-COOH 214

8.2 DISCUSSION OF RESULTS 218

9.0 SUMMARY AND CONCLUSIONS 219

9.1 SUMMARY 219

9.2 CONCLUSIONS 221

10.0 FUTURE WORK 226

APPENDIX A. ALTERNATIVE HARDWARE IMPLEMENTATIONS 229

BIBLIOGRAPHY 236

LIST OF TABLES

Table 6.1 10μm Polystyrene microspheres model parameters extracted from measurements ... 138

Table 6.2 10μm Polystyrene-COOH microspheres model parameters extracted from measurements ... 142

Table 6.3 6μm Polystyrene-COOH microspheres model parameters extracted from measurements ... 146

Table 6.4 Live yeast cell model parameters extracted from measurements ... 151

Table 6.5 Dead yeast cell model parameters extracted from measurements ... 155

Table 6.6 Summary of Experimental Characterization Results ... 157

Table 7.1 Summary of calculated multiplexing parameters for separating particles and separation velocities ... 194

LIST OF FIGURES

Figure 1.1 Lab-on-Chip Technology: Miniaturization of biological and biochemical laboratory processes [1]..... 1

Figure 2.1 Depiction of primary components in a typical fluorescence activated cell sorter [22] 12

Figure 2.2 FACSCalibur Fluorescent Activated Cell Sorter manufactured by BD Biosciences [23]..... 14

Figure 2.3 Electrically neutral particles become polarized in the presence of a spatially non-uniform electric-field and the induced dipole moment results in a translational force that is exerted on the particle. 16

Figure 2.4 Example dielectrophoretic spectrum when $\sigma_p < \sigma_m$ and $\varepsilon_p > \varepsilon_m$ 18

Figure 2.5 Electrode configuration used for traveling wave dielectrophoresis 20

Figure 2.6 Typical spectrum for the real part of the Clausius-Mossotti factor for a homogenous particle..... 22

Figure 2.7 Typical spectrum for the imaginary part of the Clausius-Mossotti factor for a homogenous particle 22

Figure 2.8 Particle separation by differential dielectrophoresis affinity. Type A particles are repelled from the local E-field maxima by negative dielectrophoresis forces while type B particles simultaneously undergo positive dielectrophoresis and are attracted to it. 25

Figure 2.9 Particle separation by field-flow fractionation. Because of the differences in electrical characteristics, type A particles travel significantly faster than type B and separate from them. 26

Figure 2.10 Electrical double layer created above an electrode that resides in a buffer solution. 28

Figure 2.11 Mobile ions in double layer move under the influence of an electric field, dragging the fluid along with them and induce electroosmotic flow 28

Figure 2.12 Traveling-wave electroosmotic pumping ions 30

Figure 3.1 Homogenous dielectric sphere model for 10μm polystyrene microspheres and resulting Clausius-Mossotti factor when in a KCL medium of $\varepsilon m = 78\varepsilon 0$ and $\sigma m = 5 \times 10 - 3\ S/m$ 36

Figure 3.2 Real part of Clausius-Mossotti Factor for 10μm Polystyrene Microspheres 37

Figure 3.3 Imaginary part of Clausius-Mossotti Factor for 10μm Polystyrene Microspheres 37

Figure 3.4 Ohmic-dielectric sphere model for 10μm polystyrene-COOH microspheres and resulting Clausius-Mossotti factor when in a KCL medium of $\varepsilon m = 78\varepsilon 0$ and $\sigma m = 5 \times 10 - 3\ S/m$ 40

Figure 3.5 Real part of Clausius-Mossotti factor for 10μm Polystyrene-COOH Microspheres .. 42

Figure 3.6 Imaginary part of Clausius-Mossotti factor for 10μm Polystyrene-COOH Microspheres 42

Figure 3.7 Ohmic-dielectric sphere model for 6μm polystyrene-COOH microspheres and resulting Clausius-Mossotti factor when in a medium of $\varepsilon m = 78\varepsilon 0$ and $\sigma m = 5 \times 10 - 3\ S/m$ 43

Figure 3.8 Real part of Clausius-Mossotti Factor for 6μm Polystyrene-COOH Microspheres.... 44

Figure 3.9 Imaginary part of Clausius-Mossotti factor for 6μm Polystyrene-COOH Microspheres 44

Figure 3.10 Microphotograph of a yeast cell and diagram of its internal structure [48] 46

Figure 3.11 Approximating the effective complex permittivity of a two concentric spheres via use of the smearing method to determine the equivalent homogenous sphere complex permittivity. 47

Figure 3.12 5-layer multi-shell models used for calculating the effective permittivity of viable yeast cells 48

Figure 3.13 Clausius-Mossotti factor spectrum for 5-layer mutli-shell model of viable yeast cells in reference medium of $\varepsilon m = 78\varepsilon 0$ and $\sigma m = 5 \times 10 - 3\ S/m$ 49

Figure 3.14 Real part of Clausius-Mossotti Factor for viable yeast cells 50

Figure 3.15 Imaginary part of the Clausius-Mossotti Factor for viable yeast cells 50

Figure 3.16 Mixture of living yeast cells and dead cells that have been stained with dye 53

Figure 3.17 3-layer multi-shell models used for calculating the effective permittivity of non-viable yeast cells 54

Figure 3.18 Clausius-Mossotti factor spectrum for 3-layer mutli-shell model of non-viable yeast cells in the reference medium of $\varepsilon m = 78\varepsilon 0$ and $\sigma m = 5 \times 10 - 3\, S/m$..... 54

Figure 3.19 Real part of Clausius-Mossotti Factor for non-viable yeast cells..... 55

Figure 3.20 Imaginary part of Clausius-Mossotti Factor for non-viable yeast cells 55

Figure 3.21 TWDEP force spectrum for 6μm PS-COOH microspheres plotted against the spectra for AC electroosmosis, Brownian motion and electrothermal noise..... 58

Figure 4.1 DEP and TWDEP velocity profiles for all the particles of chapter 3, showing the differences in velocity that occurs as a result of their relative differences in electrical properties..... 60

Figure 4.2 DEP and TWDEP velocity profiles for two theoretical particle types mixed above the electrode array..... 66

Figure 4.3 First field configuration where type A and type B cells are made to float above the electrode array and travel laterally in the direction opposite the phase gradient. A frequency is selected such that type A cells move faster than type B cells. 68

Figure 4.4 Second field configuration is applied where type A cells are made to move slower than the previous step, but in the opposite direction. Type B cells move faster than type A cells during the application of this configuration. Type B cells also move faster than they did in the previous step..... 71

Figure 4.5 The net effect of repeatedly applying the two field configurations in sequence is that cells are made to have average net velocities in opposing directions causing them to separate from another..... 72

Figure 4.6 Traps for particle types are created by spatially reversing phase gradient in the trapping region with respect to the phase gradient across the electrodes used for separating. These traps are positioned at the ends of the array, so that only particles with a net velocity in the direction of a given trap collect in that region. 73

Figure 4.7 Comparison of TWDEP and DEP velocities for models of live and dead yeast cells in a 5mS/m KCL buffer solution. Models parameters for cells extracted from best-fit analysis of experimental data..... 77

Figure 4.8 Close-up view of DEP and TWDEP spectrums for live and dead yeast cells. The plot is centered around the frequency chosen for configuration #1, *f = 100 kHz*, and shows the velocities evaluated at this frequency 80

Figure 4.9 Close-up view of DEP and TWDEP spectrums for live and dead yeast cells. The plot is centered around the frequency chosen for configuration #2, *f = 25 MHz*, and shows the velocities evaluated at this frequency 80

Figure 4.10 Average y-velocity after multiplexing as a function of duty-cycle. The average velocity due to DEP for live yeast is negative when the duty cycle ranges for 75% < D < 100%. 82

Figure 4.11 Average net x-component of velocity after multiplexing, plotted as a function of duty-cycle. The net TWDEP velocity of live yeast cells and dead yeast cells are made to be opposite in sign when the duty cycle ranges for 58% < D < 85%. The overlap of this range and the duty cycle range of figure 4.10 yield values of D for which the particles can be separated, 58% < D < 78%. 83

Figure 4.12 Time-multiplexing dielectrophoresis use to fractionate sample containing more than just two distinguishable particle types, a case that is impossible using affinity methods. 87

Figure 4.13 Experimental work plan used to evaluate the time-multiplexing dielectrophoresis methodology 89

Figure 5.1 Conceptual depiction of lab-on-chip hardware platform. Lab-on-chip device is used to characterize and separate particle samples delivered via a microfluidic interface. Signal generation electronics are used to create time-multiplexing dielectrophoresis fields and results of separations are captured by a digital imager. 91

Figure 5.2 Quadrupole electrodes with voltages configured to make a DEP characterization field. Particles undergoing nDEP will be pushed towards the center, while particles undergoing pDEP will be pulled towards the gaps. The DEP force exerted on a particle can be measured indirectly by observing its velocity. 94

Figure 5.3 Quadrupole electrodes with voltages configured to make a TWDEP characterization field. Particles become circularly polarized and rotate. Measurement of the particles orbital velocity allows TWDEP forces to be indirectly observed..... 95

Figure 5.4 Quadrupole electrodes with voltages configured to make a DEP characterization field. Particles undergoing nDEP will be pushed towards the center, while particles undergoing pDEP will be pulled towards the gaps. The DEP force exerted on a particle can be measured indirectly by observing its velocity. 96

Figure 5.5 Simulations of quadrupole electrodes electric field magnitude with 30μm gap and varying filet distances when configured to characterize DEP velocities of particles . 97

Figure 5.6 Simulations of quadrupole electrodes electric field magnitude with 30μm gap and 150μm filet distances when configured to characterize TWDEP velocities of particles 99

Figure 5.7 3D simulation model of quadrupole electrodes. Slice-plot shows electric field magnitude when device is configured in DEP characterization mode. 100

Figure 5.8 Initial distribution of 6μm PS-COOH microsphere models at time t = 0..... 101

Figure 5.9 Distribution 6μm PS-COOH microspheres after 60 seconds of application of DEP characterization field. The voltages used were 2Vpp at a frequency of 1MHz. At this frequency, the particles undergo negative dielectrophoresis. Particles near the center are pulled in to the null region in the center, while particles are repelled from the high intensity field regions near the gaps..... 103

Figure 5.10 Simulation results of electric field magnitude profile generated in fluid containment region when traveling-wave voltages are applied. The electrode gaps and spacing are 30μm and the voltages are 2Vpp, 1MHz signals. The phase of each electrode is shifted 90^0 with respect to its neighbor (going left to right), resulting in a positive phase gradient. 105

Figure 5.11 Top shows 2D particle motion simulation model and initial random distribution of particles. Bottom shows particles reaching a steady-state levitation height of 60μm due to DEP forces balancing out with gravity and traveling in the negative x-direction due to the TWDEP field created by the electrodes. 106

Figure 5.12 Gold and aluminum processed wafers with multiple copies of both electrode structure types 108

Figure 5.13 Close-up view of one of the gold quadrupole characterization chips after processing 110

Figure 5.14 Close-up view of one of the gold separation electrode arrays after processing 110

Figure 5.15 Quadrupole electrode chip after being diced, bonded to the surface of a PCB, and soldered 111

Figure 5.16 Separation electrode electrode array. A chip with 32, 30μm electrodes is shown. 112

Figure 5.17 Separation electrode chip after dicing, attachment to a dual-inline package and wire-bonding 113

Figure 5.18 Hole drilled in back of package so that separation electrode array could be illuminated from its underside 113

Figure 5.19 Setup for creating microfluidic prototypes using a digital craft cutter. The top left shows the CAD software and cutting device. The top right hand side shows a transparency coverslip layer shortly after being patterned. The bottom shows a patterned double-sided adhesive layer (white) and its corresponding coverslip 115

Figure 5.20 Cross section view of microfluidic devices after application of transparency and adhesive layers to the substrate. The height of the fluid channels formed is determined by the thickness of the adhesive layer..... 116

Figure 5.21 Microfluidic containment designed to interface to quadrupole electrodes 118

Figure 5.22 Microfluidic interface applied to a set of quadrupole electrodes 118

Figure 5.23 Evolution of microfluidic interface for separation electrode array 120

Figure 5.24 Microfluidic channels and containment designed to interface to separation electrode array 120

Figure 5.25 Top shows separation electrode chip with microfluidic channels and access ports affixed on top. Bottom shows syringe and tubing setup used to deliver samples to the region near the electrodes 122

Figure 5.26 Top shows schematic for quadrupole electrodes. Bottom shows completely assembled quadrupole characterization device. 124

Figure 5.27 Top shows microspheres being manipulated by quadrupole at t = 0s and t = 120s. Bottom shows shows simulations at same times. 125

Figure 5.28 Top shows schematic for connectivity of electrodes in the separation array. Bottom shows corresponding printed circuit board. 127

Figure 5.29 Top shows the custom software interface developed to control multiplexing voltage waveforms being operated via a touchscreen tablet computer. Bottom shows signals of 100 kHz with a positive phase gradient and 1 MHz with a negative phase gradient being time-multiplexed. 129

Figure 5.30 Completed lab-on-chip hardware platform, including packaged dielectrophoresis chip, microfluidic interface, electronic control and software interface. 130

Figure 6.1 Example DEP velocity measurement for 6μm polystyrene microspheres. Measurement was taken by applying an nDEP field and observing the time it takes for a particle to traverse a set of concentric circles as it moves towards the center. pDEP measurements were taken by recording time it takes to travel from center outward. 132

Figure 6.2 Example TWDEP velocity measurement for live yeast cells. Measurement was taken by applying a TWDEP field configuration and observing the time it takes for the cell to travel around its axis of rotation and the distance traveled..... 134

Figure 6.3 10μm Polystyrene microspheres characterized by quadrupole characterization chip 137

Figure 6.4 Measured DEP and TWDEP velocities for 10μm Polystyrene microspheres and best-fit curves..... 137

Figure 6.5 Measurements for 10μm Polystyrene microspheres and models with averaged best-fit parameters..... 138

Figure 6.6 10μm Polystyrene-COOH microspheres characterized by quadrupole characterization chip..... 141

Figure 6.7 Measured DEP and TWDEP velocities for 10μm Polystyrene-COOH microspheres and best-fit curves..... 141

Figure 6.8 Measurements for 10μm Polystyrene-COOH microspheres and models with averaged best-fit parameters..... 142

Figure 6.9 6μm Polystyrene-COOH microspheres characterized by quadrupole characterization chip..... 145

Figure 6.10 Measured DEP and TWDEP velocities for 6μm Polystyrene-COOH microspheres and best-fit curves..... 145

Figure 6.11 Measurements for 6μm Polystyrene-COOH microspheres and models with averaged best-fit parameters..... 146

Figure 6.12 Live yeast cells characterized by quadrupole characterization chip 150

Figure 6.13 Measured DEP and TWDEP velocities for live yeast cells and best-fit curves 150

Figure 6.14 Measurements for live yeast cells and models with averaged best-fit parameters.. 151

Figure 6.15 Dead yeast cells characterized by quadrupole characterization chip 154

Figure 6.16 Measured DEP and TWDEP velocities for live yeast cells and best-fit curves 154

Figure 6.17 Measurements for dead yeast cells and models with averaged best-fit parameters 155

Figure 7.1 DEP and TWDEP velocity spectra for live and dead yeast cells 161

Figure 7.2 Separation velocity for live and dead yeast cells when field configurations are frequency multiplexed. $maxvdiff = 6.55\mu m/s$ when $\omega 1 = 100\ kHz$, $\omega 2 = 25\ MHz$, and $D = 0.81$ 162

Figure 7.3 Separation velocity for extracted live and dead yeast cell models when field configurations are frequency multiplexed. $maxvdiff = 13.33\mu m/s$ when $\omega 1 = 250\ kHz$, $\omega 2 = 50\ MHz$, and $D = 0.85$ 162

Figure 7.4 DEP and TWDEP velocity spectra for 10μm PS-COOH microspheres and live yeast cells 164

Figure 7.5 Separation velocity for 10μm PS-COOH and live yeast cells when field configurations are frequency multiplexed. $maxvdiff = 11.16\mu m/s$ when $\omega 1 = 100\ kHz$, $\omega 2 = 500\ kHz$, and $D = 0.70$ 165

Figure 7.6 Separation velocity for extracted 10μm PS-COOH and live yeast cell models when field configurations are frequency multiplexed. $maxvdiff = 12.50\mu m/s$ when $\omega 1 = 100\ kHz$, $\omega 2 = 500\ kHz$, and $D = 0.72$ 165

Figure 7.7 DEP and TWDEP velocity spectra for 10μm PS-COOH microspheres and dead yeast cells 167

Figure 7.8 Separation velocity of 10μm PS-COOH and dead yeast cells when field configurations are phase and frequency multiplexed. $maxvdiff = 4.12\mu m/s$ when $\omega 1 = 25\ MHz$, $\omega 2 = 250\ MHz$, and $D = 0.66$ 168

Figure 7.9 Separation velocity of extracted 10μm PS-COOH and dead yeast models when field configurations are phase and frequency multiplexed. $maxvdiff = 6.06\mu m/s$ when $\omega 1 = 2.5\ MHz$, $\omega 2 = 50\ MHz$, and $D = 0.53$ 168

Figure 7.10 DEP and TWDEP velocity spectra for 10μm PS-COOH and 10μm PS microspheres 170

Figure 7.11 Separation velocity between 10μm PS-COOH and 10μm PS microspheres when field configurations are frequency multiplexed. $maxvdiff = 1.83\mu m/s$ when $\omega 1 = 2.5\ MHz$, $\omega 2 = 2.5\ MHz$, and $D = 0.50$ 171

Figure 7.12 Separation velocity between extracted 10μm PS-COOH and 10μm PS models when field configurations are frequency multiplexed. $maxvdiff = 1.31\mu m/s$ when $\omega 1 = 1\ MHz$, $\omega 2 = 1\ MHz$, and $D = 0.50$ 171

Figure 7.13 DEP and TWDEP velocity spectra for 10μm PS microspheres and live yeast cells 173

Figure 7.14 Separation velocity of live yeast cells and10μm PS microspheres when field configurations are phase and frequency multiplexed. $maxvdiff = 7.91\mu m/s$ when $\omega 1 = 100\ kHz$, $\omega 2 = 2.5\ MHz$, and $D = 0.86$ 174

Figure 7.15 Separation velocity of extracted live yeast and10μm PS models when field configurations are phase and frequency multiplexed. $maxvdiff = 11.85\mu m/s$ when $\omega 1 = 500\ kHz$, $\omega 2 = 250\ MHz$, and $D = 0.01$ 174

Figure 7.16 DEP and TWDEP velocity spectra for 10μm PS microspheres and dead yeast cells 176

Figure 7.17 Separation velocity of 10μm PS and dead yeast cells when field configurations are frequency multiplexed. $maxvdiff = 1.32\mu m/s$ when $\omega 1 = 2.5\ MHz$, $\omega 2 = 100\ MHz$, and $D = 0.23$ 177

Figure 7.18 Separation velocity of extracted 10μm PS and dead yeast cells models when field configurations are frequency multiplexed. $maxvdiff = 3.24\mu m/s$ when $\omega 1 = 10\ MHz$, $\omega 2 = 100\ MHz$, and $D = 0.54$ 177

Figure 7.19 DEP and TWDEP velocity spectra for 6μm PS-COOH microspheres and live yeast cells 179

Figure 7.20 Separation velocity between 6μm PS-COOH and live yeast cells when field configurations are frequency multiplexed. $maxvdiff = 11.6\ \mu m/s$ when $\omega 1 = 100\ kHz$, $\omega 2 = 250\ kHz$, and $D = 0.64$..... 180

Figure 7.21 Separation velocity of extracted 6μm PS-COOH and live yeast cell models when field configurations are frequency multiplexed. $maxvdiff = 18.46\mu m/s$ when $\omega 1 = 250\ kHz$, $\omega 2 = 500\ kHz$, and $D = 0.88$ 180

Figure 7.22 DEP and TWDEP velocity spectra for 6μm PS-COOH microspheres and dead yeast cells 182

Figure 7.23 Separation velocity of 6μm PS-COOH and dead yeast when field configurations are phase and frequency multiplexed. $maxvdiff = 4.04\ \mu m/s$ when $\omega 1 = 25\ MHz$, $\omega 2 = 250\ MHz$, and $D = 0.64$ 183

Figure 7.24 Separation velocity of extracted 6μm PS-COOH and dead yeast models when field configurations are phase and frequency multiplexed. $maxvdiff = 5.94\mu m/s$ when $\omega 1 = 2.5\ MHz$, $\omega 2 = 50\ MHz$, and $D = 0.54$ 183

Figure 7.25 DEP and TWDEP velocity spectra for 6μm PS-COOH and 10μm PS-COOH microspheres 185

Figure 7.26 Separation velocity of 6μm PS-COOH and 10μm PS microspheres when field configurations are phase and frequency multiplexed. $maxvdiff = 0.12\ \mu m/s$ when $\omega 1 = 750\ kHz$, $\omega 2 = 2.5\ MHz$, and $D = 0.56$ 186

Figure 7.27 Separation velocity of extracted 6μm PS-COOH and 10μm PS models when field configurations are phase and frequency multiplexed. $maxvdiff = 0.03 \mu m/s$ when $\omega 1 = 500\ kHz$, $\omega 2 = 2.5\ MHz$, and $D = 0.56$ 186

Figure 7.28 DEP and TWDEP velocity spectra for 6μm PS-COOH and 10μm PS microspheres 188

Figure 7.29 Separation velocity between 6μm PS-COOH and 10μm PS microspheres when field configurations are frequency multiplexed. $maxvdiff = 1.57\ \mu m/s$ when $\omega 1 = 2.5\ MHz$, $\omega 2 = 2.5\ MHz$, and $D = 0.5$ 189

Figure 7.30 Separation velocity between extracted 6μm PS-COOH and 10μm PS models when field configurations are frequency multiplexed. $maxvdiff = 1.00 \mu m/s$ when $\omega 1 = 1\ MHz$, $\omega 2 = 1\ MHz$, and $D = 0.5$ 189

Figure 8.1 Top of figure shows initial position of a sample containing only dead yeast cells. Bottom of figure shows position of cells after a 2Vpp, 25MHz TWDEP field with a negative phase gradient is applied for 30s, resulting in an average lateral velocity of 1.5 μm/s. 197

Figure 8.2 Top of figure shows initial position of a sample containing only dead yeast cells. Bottom of figure shows position of cells after a 2Vpp, 25MHz TWDEP field with a positive phase gradient is applied for 35s, nDEP forces levitate the cells while TWDEP forces result in an average lateral velocity of -1.8 μm/s. 198

Figure 8.3 Top of figure shows dead yeast cell sample before application of fields. Bottom of figure shows distribution of dead yeast cells after the application of a $2V_{pp}$, 100 kHz TWDEP field for 30 seconds. The cells levitate due to nDEP forces and there is little to no lateral displacement due to TWDEP forces 200

Figure 8.4 Top of figure shows initial position of a sample containing only live yeast cells. Bottom of figure shows position of cells after a 2Vpp, 100 kHz TWDEP field with a positive phase gradient is applied for 15s, resulting in an average lateral velocity of 6 μm/s. 202

Figure 8.5 Top of figure shows initial position of a sample containing only live yeast cells. Bottom of figure shows position of cells after a 2Vpp, 100 kHz TWDEP field with a negative phase gradient is applied for 18s, resulting in an average lateral velocity of -6.7 μm/s. 203

Figure 8.6 Top of figure shows initial position of a sample containing only live yeast cells. Bottom of figure shows position of cells after a 2Vpp, 25 MHz TWDEP field is applied. The cells immediately are rendered immobile by pDEP forces and cannot move..... 205

Figure 8.7 Simulation of electric field magnitude generated in region above electrode array. The field magnitude gradient is largest at the electrode corners, causing cells that undergo pDEP to be attracted to there. 206

Figure 8.8 Top of figure shows frame from TWDEP electrodes before application of multiplexing fields. Bottom of figure shows distribution of cells after 10 minutes of multiplexing between 100 kHz and 25 MHz with a 67% duty cycle. Dead cells are stained in blue and gathered on the left, while live cells have collected in the TWDEP trap on the right. 208

Figure 8.9 a) Initial position of live yeast cell b) TWDEP forces propel a live cell from left to right. c) As soon as 25 MHz field is applied, the cell moves down and backwards due to pDEP forces. d) Final position of cell, showing how pDEP forces disrupted the advancement made by TWDEP forces during the first phase of the multiplexing cycle 209

Figure 8.10 Top of figure shows initial distribution of cells in mixture containing live and dead yeast cells. Bottom of figure shows particles after 40 seconds of multiplexing between 100 kHz and 25 MHz. In this trial, the duration of each muxing cycle was shortened to 50us, short enough to average out the effects of the pDEP phase of the cycle 211

Figure 8.11 Time multiplexing dielectrophoresis trial on a 2 week old cell culture containing cells at various stages in their life cycle. The multiplexing configuration is between frequencies of 100 kHz and 25 MHz at a duty cycle of 80%. The cells bifurcate into the trapping regions after 40 seconds of multiplexing. 213

Figure 8.12 Top of figure shows initial distribution of sample containing 10um PS-COOH and live yeast cells. Bottom of figure shows sample after application of a 1.25 MHz TWDEP field. Negative DEP forces cause the microspheres to levitate and TWDEP forces propel the microspheres from right to left, while positive DEP forces render the cells immobile. 215

Figure 8.13 Time multiplexing of 10um PS-COOH and live yeast cells with frequencies of 100 kHz and 500 kHz at a duty cycle of 70%. Top of figure shows particle distribution shortly after application of fields, the middle shows their positions after 20 seconds and the bottom shows that the particles have migrated apart after 40 seconds. 217

Figure 10.1 Possible implementation for lab-on-chip assay/diagnostic by using laser optics and photodetectors to sense the presence of separated particle fractions 228

Figure A.1 Top shows custom PCB implementation of lab-on-chip. Bottom shows close-up view of electrodes formed from PCB traces and containment trench created by etching away the solder mask layer. 231

Figure A.2 Left side shows PCB implementation being used to manipulate 43μm polystyrene microspheres and right side shows device being used to manipulate 6μm polystyrene-COOH microspheres. 232

Figure A.3 Organization of nanoscale 3D integrated circuit implementation. The device contained three integrated circuit tiers: digital control circuitry, analogy waveform generation circuits and nanoscale electrodes. 233

Figure A.4 Top shows 3D integrated circuit implementation after fabrication. Bottom shows close up of nanoscale polysilicon electrodes. 235

PREFACE

There are many people I would like to thank in connection with the many years of work that has gone into this dissertation. Firstly, I would like to thank my wonderful wife Naomi who has been so patient while I've spent the past many years at 'work'. I truly do feel I have the world's greatest wife, 我爱你.

I would also like to thank my two advisors Professors Steven Levitan and Donald Chiarulli. Most graduate students are fortunate to have one good advisor; I've had two great ones who have contributed to my development as a researcher in their own way.

I am also very appreciative of the many wild and wacky research group members I have had the pleasure of working with throughout the years. A special thanks to Jason Boles, Bryan Brady, Joe Jezak, and Arnaldo Noyola for really going out of their way to help me when needed.

Finally, I would like to thank the staff in the department of electrical and computer engineering, who have had an immense role in making this work possible. Special thanks to Joni Carlin, Sandy Weisberg, Bill Mcgahey, Jim Lyle and the many other faculty and staff members who have been nothing but helpful to me over the years that I've been here.

1.0 INTRODUCTION

Lab-on-a-chip devices are an emerging microsystem technology in which multiple laboratory functions are integrated on to a compact chip-scale package (figure 1.1). They typically employ the use of microfluidics and research in this area is highly interdisciplinary, bridging the fields of engineering and the life sciences. There is growing excitement about lab-on-chip technology due to the numerous advantages these devices provide including faster and more precise analyses, a reduction in sample size requirements, portability, and reduction in cost.

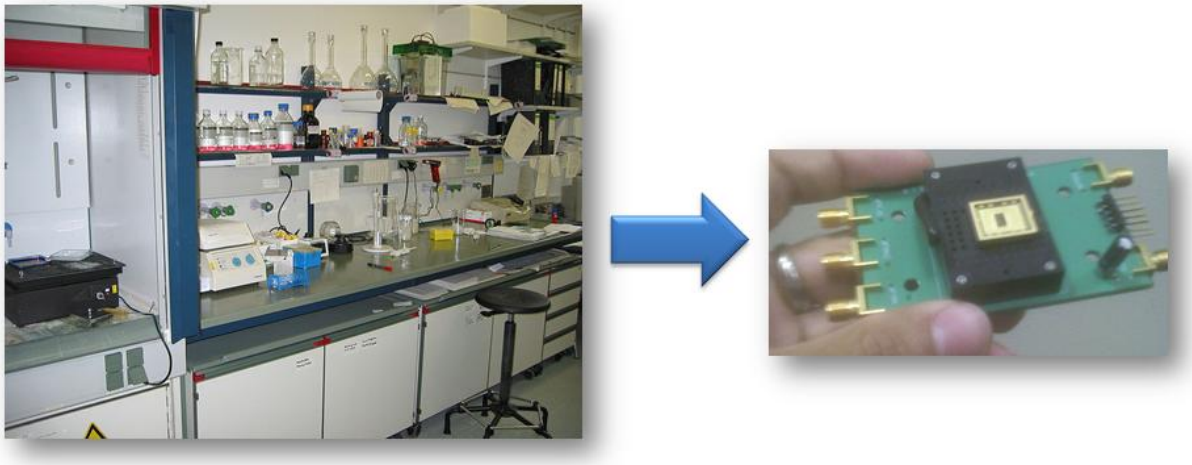

Figure 1.1 Lab-on-Chip Technology: Miniaturization of biological and biochemical laboratory processes [1].

The general focus area of this dissertation research is the application of lab-on-chip devices, and the development of techniques for them, to sort biological particles. Cytometry is the process of sorting and analyzing particles. Within the life sciences, this procedure is commonly performed on samples containing cells or viruses. In addition to being vital to medical diagnostics, cytometry has a wide spectrum of applications ranging from drug discovery, to agriculture and bio-defense. Even though cytometry is a vital laboratory technique, it remains a process that is very expensive, time consuming and difficult. As a result, there is growing interest to be able to carry out cytometry using lab-on-chip technology.

One of the promising prospects to implementing cytometry in a chip-scale package is using dielectrophoresis. Dielectrophoresis is the use of AC electric fields to transport particles [2]. When a particle is placed in a non-uniform AC electric field, an electrokinetic force will act on the particle and cause it to move. These AC fields are typically generated by electrodes driven by voltage sources. High intensity electric fields are required in order to generate enough force to cause displacement of a particle. The intensity of an electric-field can be increased by either raising the magnitude of the voltage or scaling down the dimensions of the electrodes. Advancements in micro-fabrication technology have made very small microelectrodes more accessible than ever before. As a result, it is now possible to create dielectrophoresis lab-on-chip devices with the capability to generate strong fields using easily realizable, low voltages.

The motivation for using dielectrophoresis to carry out the task of separating particles is that the direction and magnitude of the exerted on a particle can be controlled externally by certain electric field parameters and the forces can be targeted towards a particle of a particular type. This high level of contactless yet specific control is possible because the inherent electrical

characteristics of particles vary based on their makeup. The electrical properties of particles not only reflect differences in their size and structure, but also capture subtle variations in their internal composition. Particles of different types have dissimilar electrical conductivities and permittivities that result in unique frequency/phase dependencies. These dependencies translate into distinct responses when introduced into an AC electric field. For our research, we exploit this property and use dielectrophoresis methods to both characterize particles and then carry out fractionations on mixtures of them.

Our unique approach is to use a time-multiplexed combination of dielectrophoresis fields over a dense microelectrode array, creating strong electric fields with a high degree of spatial resolution. By time multiplexing, or switching very rapidly, between sequences of dielectrophoresis field configurations over this array, particles with small variations in composition will be made to experience different amounts of force, forces in opposite directions, or no force at all. Multiplexed field configurations can vary in frequency, phase, amplitude and duty cycle and each is optimized to apply maximal force to a specific particle type. By applying a time multiplexed sequence of these customized field configurations, an aggregate effect is generated in which the net force on each particle type is different and thus separation can be achieved. As will be presented in this dissertation, there are several advantages the time-multiplexing of dielectrophoresis fields have over similar approaches. Our methodology enables particles of varying types to be separated under conditions that would be impossible for other dielectrophoresis-based methods, alleviating the need for tight control of the buffer that the particles reside in. In addition, time-multiplexing dielectrophoresis has the ability to increase the rate at which particle types migrate apart, making it possible to distinguish particles previously considered too similar by other methods and with a reduction in the number of electrodes

required to do so. These innovations lead to more efficient and more realizable lab-on-chip implementations for separating particles.

The broader impact of this work will enable a reduction in both the time and the cost for the fractionation of mixtures containing biological particles and enable fundamental changes to the laboratory methods used in microbiology and virology. Additionally, our technology will have a large impact by enabling a new class of point-of-care, portable diagnostic devices. One potential example is in the diagnosis of AIDS. Medical clinics diagnose AIDS by sorting and measuring the density of CD4 and CD8 lymphocytes in a blood sample. The use of cytometers is the gold standard for such diagnostics [3]. However, it is prohibitively expensive (requiring $50,000+ machines) and difficult (requiring large laboratories and trained technicians) for the developing countries who need it most. The application of our methodology could potentially carry out this diagnostic assay at a fraction of the cost, in a portable package and with a much faster turnaround time.

In following sections, we provide a statement of the research problems we are attempting to solve, our hypothesis and a statement of work to test our hypothesis. This will provide the reader with an overview of the central components of the proposed research, as all of these ideas are elaborated in the subsequent chapters. Also included are the expected contributions and a roadmap for the remainder of the document.

1.1 PROBLEM STATEMENT AND HYPOTHESIS

The central issue this dissertation addresses is that given the limitations of current methods for sorting particles via dielectrophoresis, how can we improve the ability to differentiate particles

on a given lab-on-chip platform? Can a platform and accompanying methodology be designed that will enable the separation between particle types that previously would have been considered too similar to be differentiated from each other? And can a method be devised that will allows particles to be separated while under conditions that make them otherwise inseparable using other dielectrophoresis methods?

Since particles of different types and composition have different electrical characteristics, they will have unique responses to changes in the electric field in which they reside. Therefore, we hypothesize that we can achieve fine-grain particle fractionations by employing the use of microelectrode arrays to apply specific combinations electric field phase and frequency repeatedly over time. These configurations can be selected such that particles contained in a fluid that are of dissimilar type can be made to travel in opposite directions and eventually separate from one another. The application of this technique will enable lab-on-chip platforms that can carry out these separations in conditions that would otherwise make separations impossible, while requiring fewer electrodes than comparable dielectrophoresis-based implementations.

1.2 STATEMENT OF WORK

We tested our hypothesis by first identifying and creating a small library of particles of varying type. We then determined how best these particles and their characteristics should be modeled electrically. Using these models, we analyzed the effectiveness of the use of time-multiplexing dielectrophoresis fields to separate particles and compared it to the differentiation capabilities of similar methods. In order to further validate our claims, we designed and used a novel hardware platform to experimentally characterize the particles included our library and refine our models.

With the use of these refined models, we analyzed the limits of the differentiation capabilities of our method. The hardware platform was also used to experimentally demonstrate the ability of our method to exert differential forces on particles of varying type and separate them.

1.3 RESEARCH CONTRIBUTIONS

As a result of the work plan, we have made the following primary research contributions:

- ***New technique for separation of particles based on dielectrophoresis:*** The presented method for separating particles enables more efficient lab-on-chip devices with greatly improved separation capabilities. The application of our technique results in three tangible benefits in comparison to similar dielectrophoresis-based separation methods:
    - Time-multiplexing dielectrophoresis allows for separations between particle types to take place under conditions that would otherwise make them inseparable. The application of the method significantly loosens the requirements competing methods have on maintaining a buffer with specific electric properties. As a result of our method, the use of dielectrophoresis to separate particles becomes a viable alternative in real-world situations.
    - The method increases the differential velocity at which particle types migrate apart, enhancing the efficiency with which particles are separated from one another.
    - The implementation of the method leads to lab-on-chip devices that require fewer electrodes to carry out particle separations.

- ***Novel lab-on-chip hardware designs:*** We present a novel hardware platform that incorporates the use dielectrophoresis electrodes, microfluidics and sophisticated electronic control. The design presented here serves as a basis for future lab-on-chip based cytometers.

- ***Dielectric classification methodology for Particles*:** Resulting from our work is new a methodology for accurately extracting an electrical model for a specific particle type from measured data. This contribution lays the groundwork for being able to classify particles into electrical subtypes and for creating a library of electrical models for known particles.

1.4 DISSERTATION ROADMAP

The remainder of this dissertation proposal is organized as follows: In chapter 2 we provide the reader with further background information, discussing the motivation behind designing lab-on-chip platforms for sorting particles. We also explain the fundamentals of the theory of dielectrophoresis. In chapter 3, we introduce the selection of particles we used to test our hypothesis and the models that electrically describe them. In Chapter 4, we provide a detailed description of our proposed approach, time-multiplexing dielectrophoresis. Chapter 5 provides the implementation details of the design of our hardware lab-on-chip platform, including the designs of the dielectrophoresis electrodes, their microfluidic interfaces and supporting electronic control. In chapter 6 we present the results of experimentally characterizing our particle library and then correlate that data back to our models. In chapter 7, we use our refined models to analyze the limits on the capacity of the technique to separate particles. In chapter 8, we present our experimental separation results. Chapter 9 contains a summary and a discussion

of our conclusions. Chapter 10 is a description of the future research that could come from the work carried out in this dissertation.

2.0 BACKGROUND AND MOTIVATION

Our research is at the intersection of the fields of lab-on-chip technology and cytometry. In this chapter we give the motivation for our work. We also provide background information on dielectrophoresis, a technique commonly utilized in lab-on-chip instrumentation to sort mixtures of particles.

2.1 MOTIVATION FOR DIELECTROPHORESIS-BASED LAB-ON-CHIP TECHNOLOGY

Dielectrophoresis is the use of spatially non-uniform electric fields to control the motion of particles in a fluid. The recent rapid growth in the amount of dielectrophoresis research taking place is primarily driven by its large potential to be used in real-world, practical applications. Dielectrophoresis applications currently being researched range from drug discovery, genetic analysis, and single cell analysis to bio-sensors and drug screening [4]. As some examples of its practical applications, Gascoyne et. al. have shown dielectrophoresis can be used to characterize human leukemia cells [5]. Hu et. al have demonstrated systems based on dielectrophoresis that are able to perform high-throughput filtering of rare cells in heterogeneous mixtures [6]. Chin et al. have shown how dielectrophoresis can be used to greatly reduce the time required to study clonal stem cells [7]. It has even been successfully demonstrated by Morgan et. al., that

dielectrophoresis can be selective enough to separate particles according to changes in just surface chemistry [8].

Dielectrophoresis has also been successfully applied to particles much smaller than cells. For example, dielectrophoresis can provide reliable and fast ways for manipulating viruses [9]. Hughes [10] and Morgan [11] showed that dielectrophoresis can be used to fractionate heterogeneous mixtures of submicron particles, separating mixtures containing tobacco mosaic virus, HSV-1, and plastic spheres. Hughes in particular [12, 13, and 14], has characterized the electrical properties of HSV-1 and its response to dielectrophoretic forces. Dielectrophoresis is even being investigated in applications below the virus scale as researchers such as Washizu et. al have successfully used dielectrophoresis, to separate, manipulate and stretch DNA particles [15]. Applications of dielectrophoresis are even now starting to be realized outside the biomedical life sciences domain. For example, one of the most published non-biological applications of dielectrophoresis has been the use of it to sort and assemble carbon nanotubes, e.g., [16, 17 and 18].

The large appeal of dielectrophoresis and its use in so many practical applications is that dielectrophoresis methods can be implemented in small scale lab-on-chip packages. One of the primary drivers behind lab-on-chip technology is that it can greatly reduce the time needed to perform an assay. In a conventional laboratory setting, it often takes hours to prepare a test, and waiting for it to complete takes even more time. This process is very inefficient and even expensive since it occupies a clinician's time. Commercial lab-on-chip devices have already demonstrated their ability to speed up this process. One of the few commercially available lab-on-chip platforms is the 2100 Bioanalyzer by Agilent Technologies [19]. The 2100 Bioanalyzer consists of microfluidic channels and electrodes that can be configured for a variety analyses.

One of the functions it performs is on-chip flow cytometry. This chip cytometer supports the sorting of up to two particle types based on fluorescent labeling. The device is targeted for cells and can perform an assay of 20,000 cells in less than 30 minutes, a process that would take hours using a typical cell-sorter.

The potential of lab-on-chip devices is further boosted by their ability to conduct an experiment with nano or pico liter scale volumes, drastically reducing sample size requirements in comparison to conventional diagnostic equipment. Since experimentation at the macro scale is limited by the high costs of reagents, the small volumes required to conduct a lab-on-a-chip experiments are expected to greatly increase the adoption rate of these devices, particularly in the pharmaceutical industry where scarcity of samples is a major issue [20,21].

In addition to the costs savings that come from being able to perform faster analyses with smaller biological samples and lower expenses for labor, lab-on-a-chip devices have much lower fabrication costs when compared to traditional equipment. This is because the primary components are integrated onto a single, inexpensive substrate. The chips are typically manufactured using methods borrowed from mature industries, such as consumer electronics, and can easily be mass produced. Due to advances in fabrication technology, it is now possible to create microelectrode arrays rather inexpensively.

Because of the advantages they have to offer, lab-on-chip devices stand to make a large impact on particle sorting applications. In the next section we discuss the motivation for applying lab-on-chip technology to this market.

There are a number of instruments that can be used to perform particle sorting tasks, however in today's market, the most widely used are cytometers based on fluorescence-activated cell sorting (FACS). The market for these devices is rapidly growing and Frost and Sullivan

forecasts that by the year 2014, it will generate nearly $2 billion dollars in the United States alone [20].

Figure 2.1 is a depiction of a typical FACS device [22]. With these devices, complex mixtures of biological particles are sent, single-file, in a stream past a light detection system that is composed of lasers and photodetectors. As fluorescently labeled particles cross the detection area one by one, the color that has been assigned to the particle (using fluorescent antibodies) is sensed. That optical signal is converted to an electrical signal and analyzed by software. The controlling computer then determines which particle type was detected. That information is used as feedback to determine which container the particle should be sorted into. After detection, the particle is forced through a nozzle and encapsulated into a droplet. The droplet is assigned a charge and routed to the appropriate bin by way of an electrostatic deflection system.

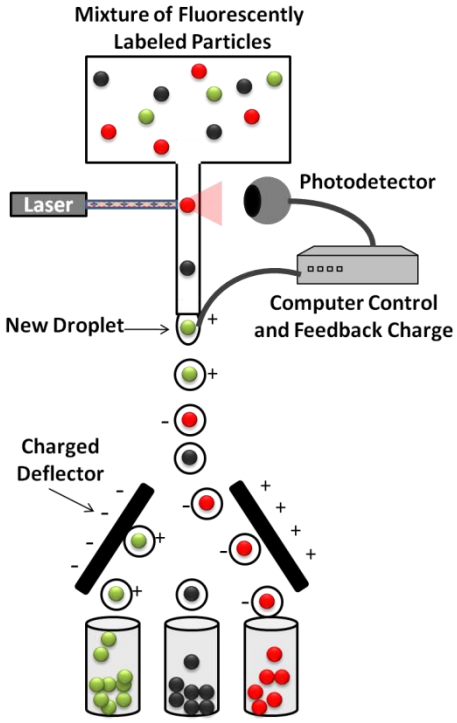

Figure 2.1 Depiction of primary components in a typical fluorescence activated cell sorter [22]

Modern flow cytometers are able perform this process at a rate of several thousand particles every second; however they are not without drawbacks. Fluorescence-activated cell sorters are bulky pieces of equipment and are not suitable for point-of-care diagnostics. They are also very expensive, costing anywhere from tens of thousands of dollars, for low-end or used machines, to hundreds of thousands of dollars for high-end pieces of equipment [20,21].

There are also many functional disadvantages to FACS systems. They require a great deal of sample preparation, as the particles have to be tagged with fluorescent antibodies. Since these particles have to labeled, the scientist or technician must have detailed knowledge about the mixture composition prior to carrying out the cytometric analysis. These systems are also severely limited in the number of different particle types they can sort because a different color is required for each type. Today's high-end systems can support approximately 10-16 different tagged species [21].

With FACS, there is also a limitation on the size of the particle that can be reliably counted and sorted. In the life sciences, FACS systems are primarily targeted to applications that require counting and sorting of cells, which are on the order in size of a few microns. This is primarily because the particles in these systems have to be individually encapsulated inside of a droplet, the size of which is determined by the diameter of the droplet forming nozzle. For the case of nanoscale biological particles, such as viruses, one cannot reliably ensure the number of particles inside of the droplet if the droplet is too large.

The application of lab-on-chip devices and methods to the field of cytometry has the potential to have broad, far-reaching impacts. Take for example the potential gains when comparing current FACS instrumentation to a possible lab-on-chip implementation. An example

of a typical cytometer marketed to life science researchers is the FACSCalibur (figure 2.4), manufactured by BD Biosciences [23]. It weighs over 200 pounds, consumes more than 2,000 watts of power, costs over $100,000 USD and requires trained technicians to operate. By comparison, the technique we are proposing requires relatively low voltages and can be implemented as a portable device, using inexpensive electronic fabrication methods. The FACSCalibur can only sort particles based on 15 parameters: 13 fluorescent colors and the detection of 2 light scattering parameters. In contrast, instead of using of a small, discrete set of predetermined colors, as we explain in chapters 3 and 4, our proposed implementations differentiate particles based on their inherent electrical characteristics that span a continuous spectrum. The minimum size particle that can be used in the FACSCalibur is 500 nm in diameter, limiting it to the sorting of cells. Since our method sorts based a particle's electrical characteristics, our implementations will have the capability to perform cytometry experiments on much smaller organisms such as viruses. Beyond the separation of virus mixtures, our proposed methods have the potential to enable new fields of research such as classification of pathogenic and non-pathogenic forms of the same virus.

Figure 2.2 FACSCalibur Fluorescent Activated Cell Sorter manufactured by BD Biosciences [23]

One technique that is well-suited for future a lab-on-chip cytometer implementations is dielectrophoresis. Dielectrophoresis is the foundation for our research and in the next section, we explain its theoretical background and survey current research associated with its use.

2.2 THEORY OF DIELECTROPHORESIS

Electrokinetic phenomena have been used for decades to manipulate particles. One of the early, and still widely used, techniques is electrophoresis. Electrophoresis is the movement of electrically charged particles under the influence of a spatially uniform DC electric field [24]. Electrophoresis can be used to separate charged particles, such as DNA and other macromolecules based on their net charge and size. These properties determine the speed at which particles will travel through a viscous medium and can be used to fractionate populations of particles according to their species. The disadvantage of electrophoresis is that is that it only can be used with particles that have a net charge, which excludes it for use on a large class of biological particles such as whole cells and viruses.

Dielectrophoresis (DEP) is the use of AC electric fields to control the movement of particles [2]. In contrast to electrophoresis, dielectrophoresis can be used on particles that have no net charge. Dielectrophoresis is the central mechanism we use in our research to manipulate particles. In this section, we provide an overview of dielectrophoresis, explain a variation of it called traveling wave dielectrophoresis and provide an overview of current research involving these techniques.

When an electrically neutral particle is placed in the presence of a spatially non-uniform electric field, the particle becomes polarized. As a result of this polarization (figure 2.3), the

particle's inherent negative charges are separated by a small distance from the positive charges. Since the particles are neutral, the two charges on the body are opposite but equal in magnitude and can be modeled as a dipole [25].

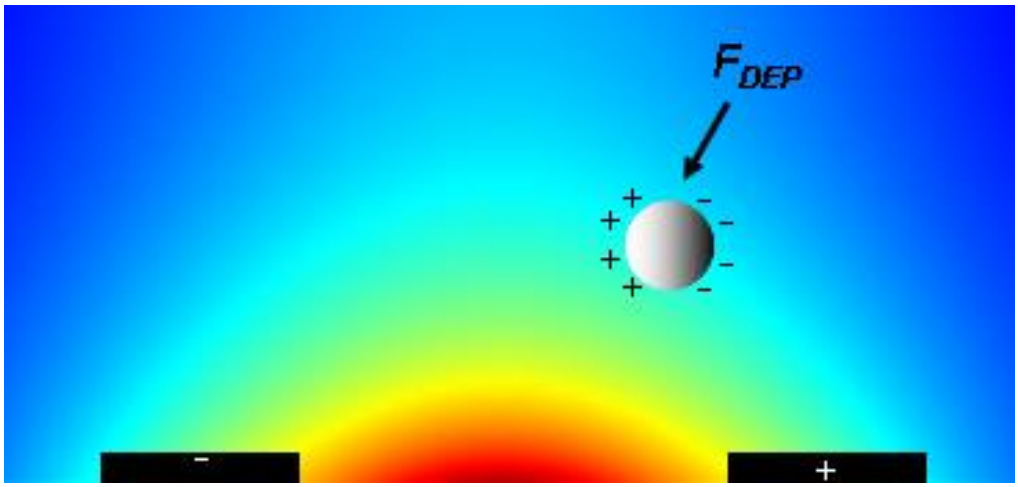

Figure 2.3 Electrically neutral particles become polarized in the presence of a spatially non-uniform electric-field and the induced dipole moment results in a translational force that is exerted on the particle.

The force on an infinitesimal dipole within an electric field $\vec{E}$ is described by the expression:

$$\vec{F}_{dipole} = \vec{p}_{\,eff} \cdot \nabla \vec{E} \tag{2.1}$$

where p_{eff} is the effective dipole moment. From equation (2.1), we see that the force is proportional to the gradient of the electric field; therefore there is no net force on a dipole unless the externally imposed electric field is non-uniform. For the case of a sphere suspended in a dielectric medium (for dielectrophoresis, the medium is typically an aqueous solution), the effective dipole moment is

$$\vec{p}_{\,eff} = 4\pi r_p^3 \varepsilon_m \left(\frac{\varepsilon_p^* - \varepsilon_m^*}{\varepsilon_p^* + 2\varepsilon_{pm}^*} \right) \vec{E} \tag{2.2}$$

where r_p is the radius of the particle, ε_m is the permittivity of the medium and ε_p^* denotes the complex permittivity of the particle. Complex permittivity is a function of the conductivity, σ, of an object and is given by:

$$\boldsymbol{\varepsilon^* = \varepsilon - j\frac{\sigma}{\omega}} \tag{2.3}$$

at an angular frequency of ω of the field. From equations (2.1) and (2.2) the expression for the time averaged force exerted on the particle in an spatially non-uniform AC field is:

$$\boldsymbol{\langle \vec{F}_{DEP} \rangle = 2\pi\varepsilon_m r_p^3 Re[K_{CM}]\nabla E_{RMS}^2} \tag{2.4}$$

where

$$\boldsymbol{K_{CM} = \frac{\varepsilon_p^* - \varepsilon_m^*}{\varepsilon_p^* + 2\varepsilon_m^*}} \tag{2.5}$$

The term K_{CM} is known as the Clausius-Mossotti factor [25] and is a measure of relative permittivities between the particle and the surrounding medium. It can be seen from equations (2.4) and (2.5) that this factor determines the direction of the dielectrophoretic force. When the sign of $Re[K_{cm}]$ is positive, the particle is more polarizable than its surrounding medium and it undergoes what is known as positive dielectrophoresis (pDEP). While undergoing positive dielectrophoresis, the force vector is directed along the gradient of electric field intensity ∇E_{RMS}^2. Under these conditions, the particles are attracted to the locations of electric field intensity maxima and repelled from the minima. The opposite occurs when $Re[K_{cm}]$ is negative. This is called negative dielectrophoresis (nDEP).

By substituting equation (2.3) into (2.5), the high and low frequency limits for $Re[K_{cm}]$ are found to be

$$\lim_{\omega \to 0} Re[K_{CM}] = \frac{\sigma_p - \sigma_m}{\sigma_p + 2\sigma_m} \tag{2.6}$$

$$\lim_{\omega \to \infty} Re[K_{CM}] = \frac{\varepsilon_p - \varepsilon_m}{\varepsilon_p + 2\varepsilon_m} \tag{2.7}$$

Equations (2.6) and (2.7) show that the relative difference in conductivity dominates the low frequency behavior of $\vec{F}_{DEP}$, while dielectric polarization effects, characterized by permittivity, are more significant at high frequencies. These equations also show that $Re[K_{cm}]$ is bounded ($-\frac{1}{2} < Re[K_{cm}] < 1$) regardless of frequency. Figure 2.6 shows an example dielectrophoretic spectrum with $\sigma_p < \sigma_m$ and $\varepsilon_p > \varepsilon_m$. For this case, the particles would move under the influence of nDEP forces at low frequencies and pDEP forces at all frequencies above the zero-crossing frequency of $Re[K_{cm}]$.

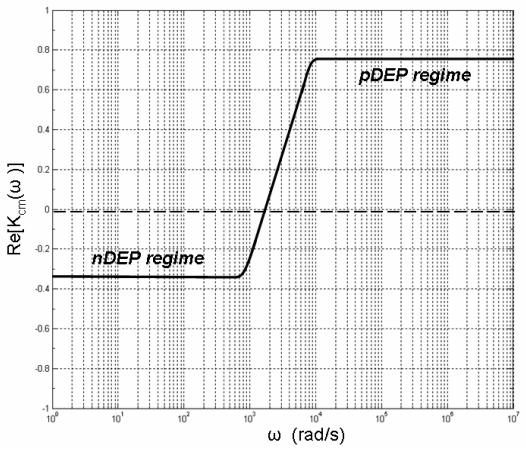

Figure 2.4 Example dielectrophoretic spectrum when $\sigma_p < \sigma_m$ and $\varepsilon_p > \varepsilon_m$

Dielectrophoresis can be implemented in a number of different ways, one of which is traveling-wave dielectrophoresis. The technique we propose in this work uses this variation of dielectrophoresis and in the next section we explain its operating principles

2.3 TRAVELING-WAVE DIELECTROPHORESIS

Traveling-wave dielectrophoresis is a form of dielectrophoresis in which the AC electric field is spatially non-uniform in both amplitude and phase [25]. If both the in-phase and out-of-phase components of the dipole moment of the particle are taken into consideration, the complete expression for the time averaged force on a particle due to dielectrophoresis is [26]

$$\langle \vec{F}_{DEP} \rangle = 2\pi\varepsilon_m r^3 \left[Re(K_{CM}) \nabla \left(E_x^2 + E_y^2 + E_z^2 \right) + Im(K_{CM}) \left(E_x^2 \nabla \phi_x + E_y^2 \nabla \phi_y + E_z^2 \nabla \phi_z \right) \right] \quad (2.8)$$

where ϕ is the phase of the AC electric-field.

Typically, traveling-wave configurations employ a linear electrode array as shown in figure 2.5. In this case, the electrodes are driven by AC voltage signals, with each electrode having a constant shift in phase with respect to its neighbor. This causes the magnitude of the electric field to be uniform along the x-axis. In addition, because of symmetry, the magnitude of the electric field along the z-axis is also constant, therefore

$$\nabla E_x^2 = \nabla E_z^2 = 0 \quad (2.9)$$

Similarly, the phase of the field is constant about the y and z axes, thus

$$\nabla \phi_y^2 = \nabla \phi_z^2 = 0 \quad (2.10)$$

Therefore, the traveling-wave dielectrophoresis time- averaged force equation reduces to

$$\boldsymbol{\langle \vec{F}_{DEP} \rangle = 2\pi\varepsilon_m r^3 \left[Re(K_{CM}) \nabla E_y^2 + Im(K_{CM}) E_x^2 \nabla \phi_x \right]} \quad (2.11)$$

From this expression, we see that the traveling-wave dielectrophoresis forces consist of y-component that levitates the particle vertically with strength proportional the field magnitude gradient, ∇E_y^2 , and a horizontal force that moves the particle along the x-axis with strength proportional to the product of the electric field intensity and phase gradient $E_x^2 \nabla \phi_x$. For the case shown in figure 2.5, the phase gradient equals 2π/4d radians per meter, where d is the pitch

between electrodes. In more general terms, equation 2.11 can also be expressed simply in terms of its two primary force components

$$\langle \vec{F}_{DEP} \rangle = \vec{F}_{DEP_Y} + \vec{F}_{TWDEP_X} \tag{2.12}$$

where $\vec{F}_{DEP_Y}$ is generally referred to as the dielectrophoresis (**DEP**) component of force [26] and $\vec{F}_{DEP_X} = \vec{F}_{TWDEP_X}$ and is known as the traveling-wave dielectrophoresis (**TWDEP**) force component.

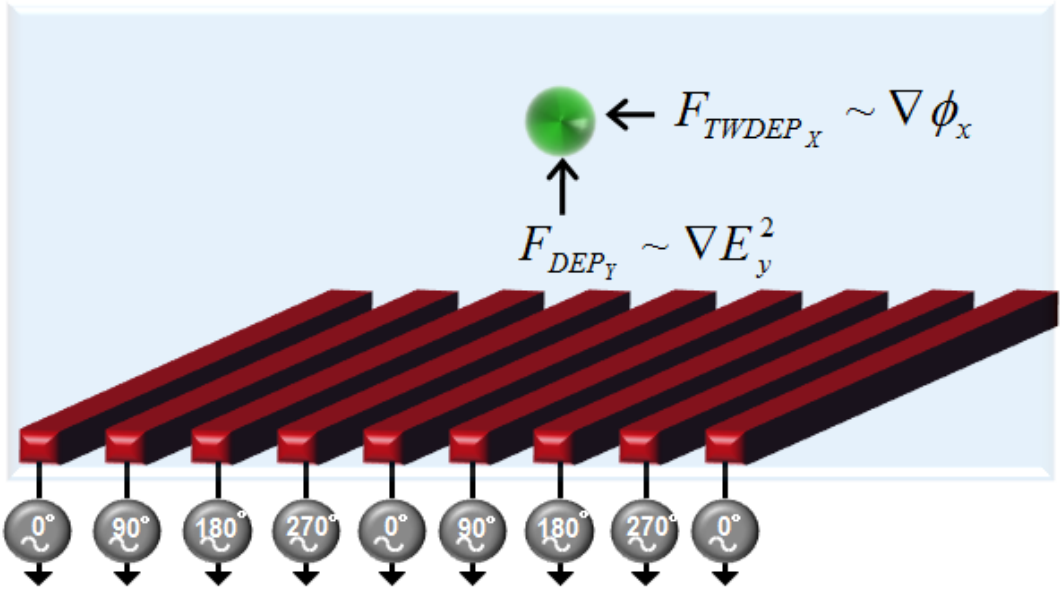

Figure 2.5 Electrode configuration used for traveling wave dielectrophoresis

Traveling-wave dielectrophoresis also has frequency dependence, encapsulated by the Clausius-Mossotti factor. The vertical component of force is proportional to the real part of K_{cm} and the horizontal component is proportional to its imaginary part. Figures 2.6 and 2.7 show typical spectrums for the real and imaginary parts of the Clausius-Mossotti factor for a homogenous particle. These spectrums will have unique features depending on particle type, but in general there are some characteristics to the imaginary part of the Clausius-Mossotti that make

it quite different than the real part. For most cases, the magnitude of the imaginary part tends towards zero at high and low frequencies, and the magnitude peaks at frequencies that correspond to points of inflection in the real part of the Clausius-Mossotti factor. These frequencies are commonly referred to as crossover frequencies. In terms of carrying out particle manipulations, this dictates that the frequency range in which the particles exhibit lateral movement on the x-axis is much narrower than with traditional dielectrophoresis. Also, unlike its real counterpart, in most cases, but not all, the imaginary part of the Clausius-Mossotti factor cannot change sign based on frequency, which means that for a given phase gradient, different particles will typically travel laterally in the same direction.

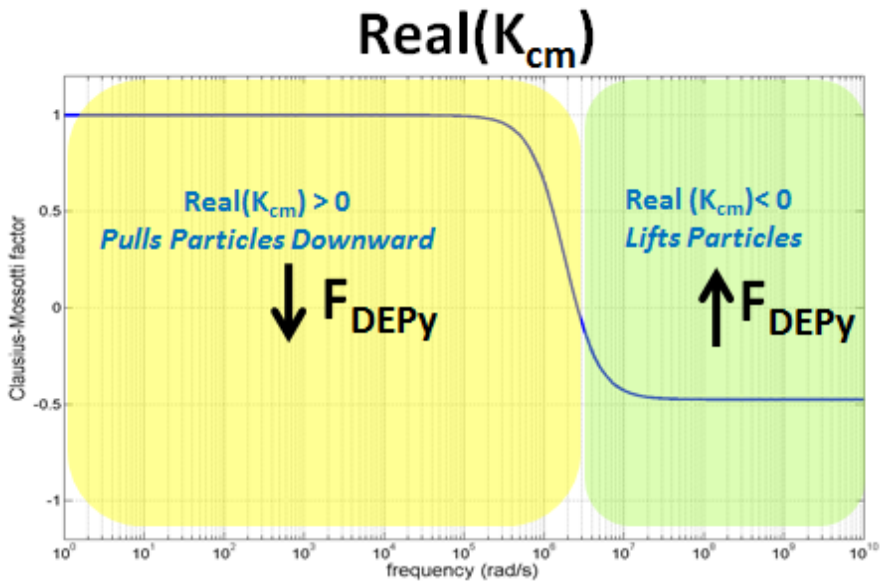

Figure 2.6 Typical spectrum for the real part of the Clausius-Mossotti factor for a homogenous particle

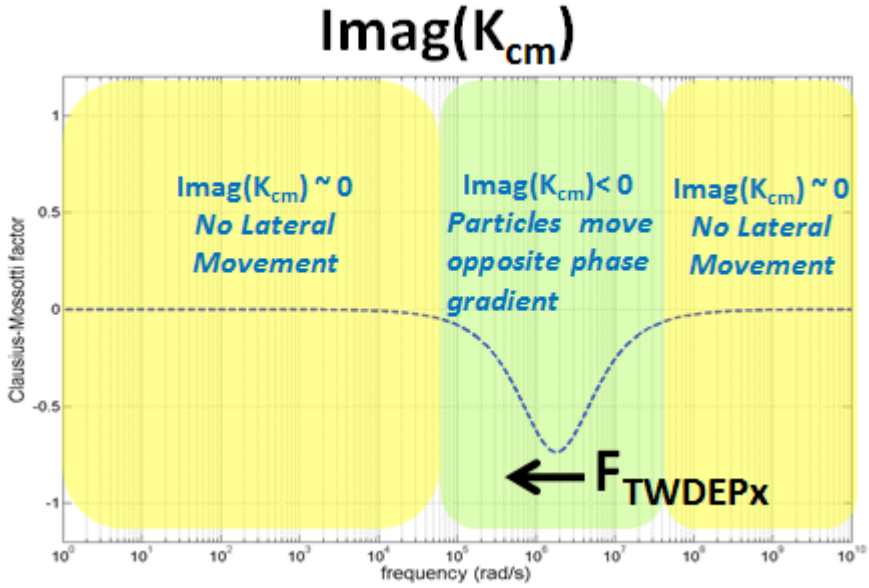

Figure 2.7 Typical spectrum for the imaginary part of the Clausius-Mossotti factor for a homogenous particle

Traveling-wave dielectrophoresis has a number of advantages over conventional AC dielectrophoresis. First, it offers a superior level of motion control. With traveling-wave dielectrophoresis, the in-phase and out-of-phase components of force are simultaneously exerted

on particles, allowing precise control of particle movement about two axes. Traveling-wave dielectrophoresis is also better suited for lab-on-chip implementations because manipulations require less switching electronics and therefore less power consumption than its counterpart. For example, if one were to use the electrodes of figure 2.5 and AC dielectrophoresis to move a particle across the width of the array, they would have to sequentially drive the voltage on each electrode while grounding the others (or vice-versa). In contrast, to accomplish that same traversal, a traveling-wave configuration would require no switching at all. Additionally, the magnitude of the electric-field used to transport those particles would be significantly less because the voltage potential between neighboring electrodes required for the same force is reduced by a factor of the number of phases used. Another advantage to traveling-wave dielectrophoresis is that, particle separations carried out using this method have a greater degree of selectivity in comparison to traditional AC dielectrophoresis because the incorporation of the imaginary part of the Clausius-Mossotti factor adds an additional differentiating factor.

There is a large body of work in the field of dielectrophoresis-based methods to separate particles. In the next section we provide a brief overview of work that has been done that is relevant to the research presented in this dissertation.

2.4 DIELECTROPHORESIS BASED METHODS FOR SEPARATING PARTICLES

There are numerous dielectrophoresis-based methods for separating particles in the literature, each with their own advantages and limitations [4,27]. The majority of techniques operate by simultaneously exerting forces of opposite sign on particles of different types, thereby causing them to be either attracted to or repelled from a particular location [28, 29, 30, 31 and 32]. These

techniques are known as differential dielectrophoresis affinity methods (figure 2.8). They operate by setting the frequency of the electric field at a value that is between the crossover frequencies of two dissimilar particle types. In the case of AC dielectrophoresis, that causes particles of one type to experience positive dielectrophoresis and move towards local field maxima, while the other type undergoes negative dielectrophoresis and is pushed away from the maxima. In the case of traveling-wave dielectrophoresis, affinity separations are carried out by operating at frequencies such that the imaginary part of the Clausius-Mossotti factor has different signs for the particle types, and travel laterally in opposite directions. In both cases, such frequencies do not always exist. Because of its simplicity, affinity methods can be very effective if the electrical properties of the two particle types are greatly dissimilar and have crossover frequencies that are significantly different. However, there are limitations if there is not a significant difference in particle electrical characteristics. Differential dielectrophoresis affinity methods rely heavily on careful selection of buffer solutions. Equations 2.6 and 2.7 show that it is necessary to adjust the permittivity and conductivity of the solution such that the frequency responses of particles of differing types will have different signs at a given frequency. This becomes impractical if the particles are too similar. In addition, in real applications, there may not be the freedom to adjust the conductivity of the buffer at all. For example, in many cellular assays, due to biocompatibility purposes it is necessary to place the cells in a buffer of very specific pH and/or ionic concentration. Another big disadvantage to dielectrophoresis affinity methods is that they cannot support separations with more than two types of particles for a given buffer.

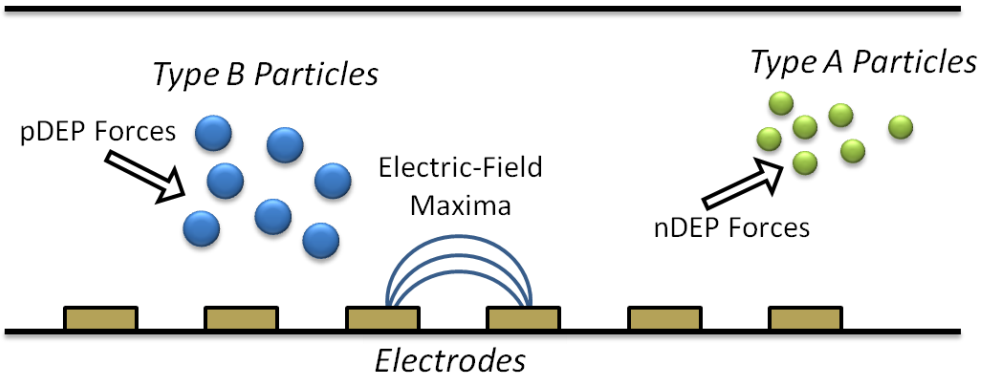

Figure 2.8 Particle separation by differential dielectrophoresis affinity. Type A particles are repelled from the local E-field maxima by negative dielectrophoresis forces while type B particles simultaneously undergo positive dielectrophoresis and are attracted to it.

Another popular class of dielectrophoresis separation techniques is based on field flow fractionation (figure 2.9), where dielectrophoretic forces are used in conjunction with fluidic drag forces to fractionate a sample [5, 33, 34 and 35]. A pressure-driven, continuous flow is used to transport samples above an electrode array. Dielectrophoresis forces are applied in conjunction with this flow and cause particles with different electrical properties to travel at different velocities. Over time, the particles migrate apart according to type. This approach has the disadvantage of requiring complex microfluidics. It is also unreasonable to use this technique for separating particles that are similar in composition. If the types are almost identical, then they will travel at nearly the same velocity which means they have to travel for a very long distance before any distinguishable separation can be observed. A consequence of this is that the size of the electrode array used has to grow as the relative electrical difference between particles decreases. If the differences are too small then the number of electrodes required would be unreasonable for a lab-on-chip implementation.

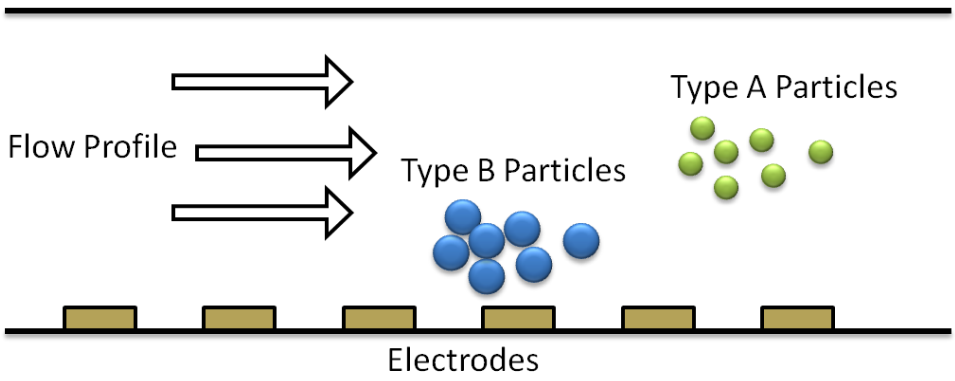

Figure 2.9 Particle separation by field-flow fractionation. Because of the differences in electrical characteristics, type A particles travel significantly faster than type B and separate from them.

In this research, we have devised a new method for separating particles that improves upon these current techniques and addresses some of their shortcomings. In chapter 4 we explain its operating principles in detail. However, since dielectrophoresis exerts force on nanoscale and microscale particles, the technique is susceptible to noise and the presence of noise can significantly disrupt the ability of the use of dielectrophoresis to separate particles. In the next section, we identify the primary noise sources that have to be taken into consideration when dealing with dielectrophoresis, and explain how their effects can be mitigated.

2.5 SOURCES OF NOISE IN DIELECTROPHORESIS MICROSYSTEMS

In addition to dielectrophoresis forces, there are other ancillary forces that affect particle motion [36,37]. The high intensity electric fields often needed to manipulate particles can induce electroosmotic flow to occur within the fluid. Joule heating of the fluid could cause temperature gradients that result in unwanted, thermally induced flow. Likewise, since the particles are small enough to be affected by impacts of water molecules, random Brownian motion is an effect that

needs to be considered. In this section we review models for each of these noise sources and discuss how their effects can be mitigated.

2.5.1 AC Electroosmosis

Recent work in the field of dielectrophoresis has shown that in addition to exerting force on particles, high intensity electric fields can induce motion in the fluid. This induced motion can under certain circumstances impose additional drag or propulsion forces on the particles [38]. This phenomenon is AC electroosmosis. It has been postulated that this electric-field induced fluid flow is the source of previously unexplained particle movements often reported in earlier dielectrophoresis work [39] and is now known to be the most disruptive noise source in dielectrophoresis microsystems.

AC electroosmosis is the result of an interaction that occurs at an electrode-fluid interface. When a charged object, such as an electrode, is placed into a liquid, an electrical double layer is formed [40]. The electrical double layer consists of two parallel layers of charge (figure 2.10). The first layer is the immobile surface charge of the solid object. The second layer is composed of oppositely charged free ions from the fluid. These counter-ions form a firmly attached, compact layer on the surface the electrode, known as the Stern layer. Additional counter-ions in the solution are still attracted by the electrode, but are also repelled by the Stern layer. When the ions reach equilibrium, they form mobile layer of counter-ions known as the diffuse layer. The concentration of counter-ions in the diffuse layer gradually decreases with distance from the electrode and depends on the type and concentration of ions in the solution. The thickness of the double layer is characterized by a parameter known as the Debye length, λ_d. It is the transport of the mobile diffuse layer that causes flow in the aqueous medium. If an

electric field is applied to the fluid, the charge in the diffuse part of the electrical double layer will move as a result of Coulombic attraction [41]. The attracted ions drag the fluid along with them and cause electroosmotic flow to occur (figure 2.11).

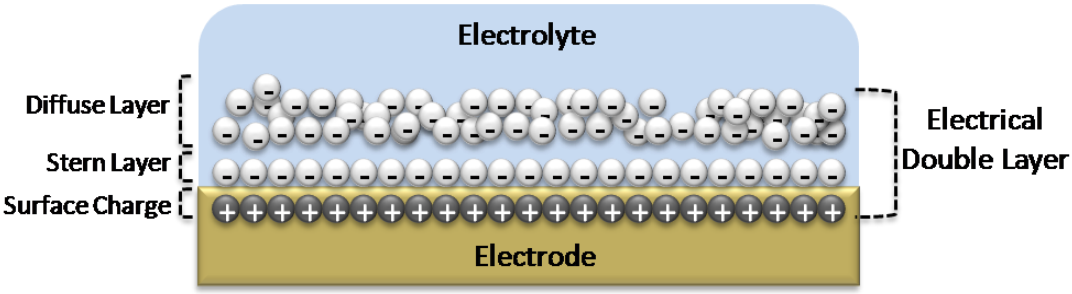

Figure 2.10 Electrical double layer created above an electrode that resides in a buffer solution

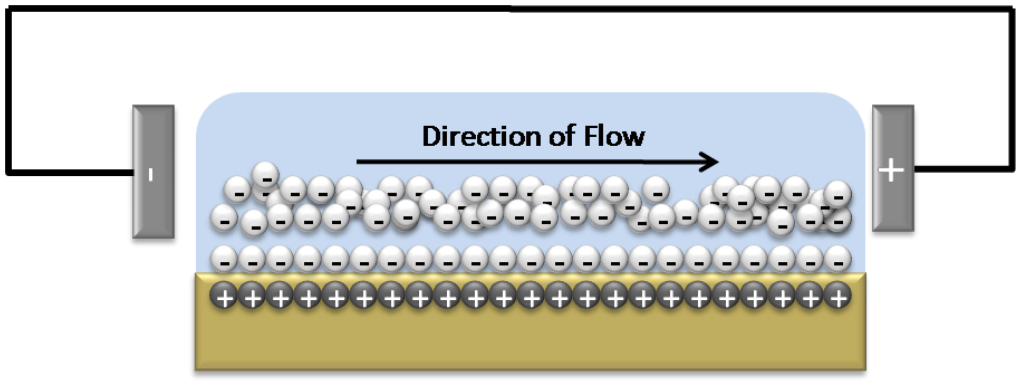

Figure 2.11 Mobile ions in double layer move under the influence of an electric field, dragging the fluid along with them and induce electroosmotic flow

AC electroosmosis can be modeled using a simplified linear circuit system [36, 38]. The equivalent circuit consists of parallel branches of resistors connecting neighboring electrodes, terminated at the end by distributed capacitors. The resistors represent the conductivity of the fluid and since the resistance between electrodes decreases the closer it moves towards gap between them, the resistance between the inner portions of the double layers is smaller than the outer portions. The capacitors model the electrical double layer and the charging of them

through the resistors represents the charging of the diffuse layers above the electrodes. Because the resistance values depend on location, each capacitor charges at different time. Using this model, the time averaged velocity of the fluid v_{slip} can be approximated as

$$\nu_{slip}(\omega) = \Lambda \frac{\varepsilon_m V^2}{8\eta z} \frac{\Omega^2}{(1+\Omega^2)^2} \tag{2.13}$$

where

$$\Omega = \Lambda \frac{\omega \varepsilon_m \pi z}{2\sigma_m \lambda_D} \tag{2.14}$$

$$\Lambda = \frac{C_s}{C_s + C_D} \tag{2.15}$$

In this model, z is the distance above the electrode plane while C_s and C_D are the Stern and diffuse layer capacitances. The time for the capacitances to charge is on the order of

$$\tau = \left(\varepsilon_m / \sigma_m\right)\left(\ell / \lambda_D\right) \tag{2.16}$$

with ℓ being the characteristic length of the system (the electrode gap). The magnitude of the velocity profile peaks at the characteristic frequency when $\Omega = 1$ and decays at low and high frequencies. At low frequency, the high impedance of the double layer capacitance has the effect of attenuating the electric field to be too small to generate flow while the velocity also tends to zero at high frequencies because there is not enough time for charge relaxation [41].

Net flow due to AC electroosmosis can be significant when traveling wave voltages are applied to an electrode array and recent work has carried out an analysis for that situation. [42,43]. Since the double layer cannot be charged instantaneously, there exists a delay between charging of the double layer and the maximum of the voltage signal. This phase difference is frequency dependent. As the frequency of the traveling-wave field approaches the characteristic

AC electroosmosis frequency, the phase difference between the double layer and the tangential component of the electric field decreases. As a result, a net flow occurs in the same direction as the traveling wave. Figure 2.12 is a simplified depiction of the traveling wave electric field when the signals are near the characteristic frequency. At this particular instant in time, the tangential field component between the electrodes with phase shifts of 0º and 90º point in the opposite direction of the field component between the 180º and 270º electrodes. Because the charge accumulated above these two sets of electrode pairs will be opposite in sign, all ions will be periodically "pumped" in the same direction, from left to right in this case

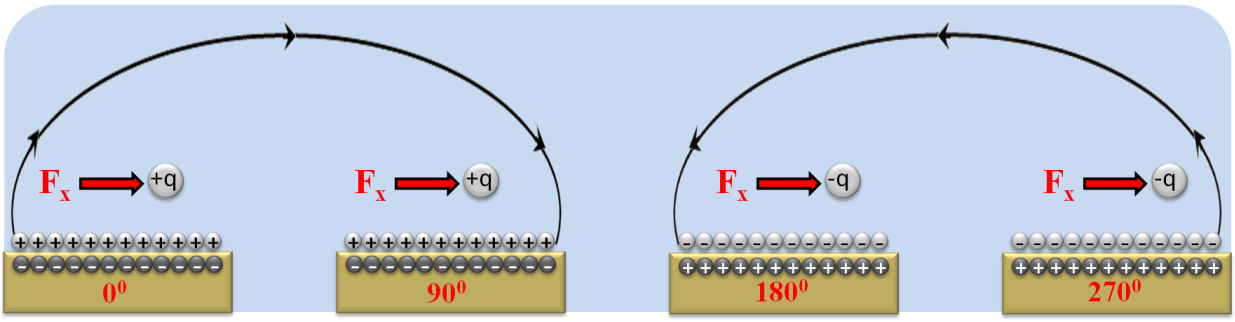

Figure 2.12 Traveling-wave electroosmotic pumping ions

This situation can be particularly problematic and disruptive when attempting to carry out traveling-wave dielectrophoresis separations. At frequencies near the AC electroosmotic characteristic frequency, configurations can arise such that the phase difference results in opposing drag forces strong enough to completely nullify traveling wave dielectrophoresis forces and render particles immobile. The best way to mitigate this negative effect is to operate at frequencies far away from the AC electroosmotic characteristic frequency, Ω. For ionic solutions used in dielectrophoresis, the characteristic frequency is typically in the low kHz range.

2.5.2 Electro-thermal forces

The high intensity electric fields needed to manipulate the particles have been observed to produce joule heating inside the fluidic medium [36]. This ohmic heating causes a temperature gradient in the fluid that in turn results a spatial conductivity and permittivity gradients within the suspending medium. The spatial variation of electrical properties within the medium results in columbic and dielectric body forces that will induce extra fluid flow. The time-averaged body force on the fluid is given by [36]

$$\left\langle \vec{F}_{thermal} \right\rangle = \frac{1}{2} Re\left[\frac{\sigma_m \varepsilon_m (\alpha - \beta)}{\sigma_m + i\omega\varepsilon_m} (\nabla T \cdot \vec{E}) \vec{E}^* - \frac{1}{2} \varepsilon_m \alpha \left| \vec{E} \right|^2 \nabla T \right] \tag{2.17}$$

where α and β are the linear and volumetric coefficients of thermal expansion and T is the absolute temperature. In practice, it has been found that the effects of elecetrothermal noise are negligible if the dielectrophoresis force components are made to be large enough in magnitude [36]. Dielectrophoresis forces can be made to dominate by increasing the voltage or reducing the electrode gap dimensions.

2.5.3 Random Brownian force

Brownian motion is the random movement of particles suspended in a fluid [36]. Since water molecules move at random, a suspended particle receives a random number of impacts of random strength and direction in any short period of time. Water molecules are about 1 nm in size; therefore particles such as viruses and cells are small enough to feel the effects of these impacts. Due to its random nature, no net movement results from these impacts.

Brownian motion can be modeled mathematically by the random walk theorem [36]. Unwanted Brownian motion will follow a Gaussian profile with a displacement given by

$$\Delta x = \sqrt{\frac{k_B T}{3\pi r_p \eta_m} t} \tag{2.18}$$

where k_B is Boltzman's constant and t is the period of observation. In order to move an isolated particle in a deterministic manner during this period, the displacement due to the dielectrophoretic force should be greater than Δx. As was the case for electrothermal noise, the Brownian force is typically small and its effects can be made to be relatively minor by increasing the magnitude of the dielectrophoretic forces exerted on the particle.

2.5.4 Buoyancy forces

Another force exerted on particles manipulated by dielectrophoresis is buoyancy [36]

$$F_{buoy} = V_p \left(\rho_p - \rho_m\right) g \tag{2.19}$$

where g is the acceleration due to gravity and the ρ_p and V_p represent the density and volume of the particle. Since the volume of a nano-particle is small, the magnitude of the buoyancy force is also small. Buoyancy not necessarily viewed as being noise in the traditional sense, however, the densities of the particle and the fluid may be such that $\vec{F}_{DEP}$ will have to overcome particles natural tendency to float or sediment over time.

In this chapter, we summarized all of the relevant forces that are exerted on particles undergoing dielectrophoresis. As a general rule, in order for dielectrophoresis to be controllable, the magnitude of the dielectrophoretic forces has to be greater than the summation of the noise sources presented in section 2.5. At the end of chapter 3, a brief summary is included

showing how the effects of noise can be avoided. Now that the general operating principles of dielectrophoresis are understood, in the next chapter we will take a look at electrical models for the specific particle types used in this dissertation and use those models to examine the unique dielectrophoretic response of each type of particle.

3.0 DIELECTROPHORETIC CHARACTERIZATION OF PARTICLES

The key to using dielectrophoresis as a means to separate particles is having accurate models of how particles of a certain type will respond in the presence of an AC electric field. This response is characterized by the Clausius-Mossotti factor, K_{CM}. The Clausius-Mossotti factor determines the magnitude and direction of the dielectrophoretic force exerted on particles as a function of the frequency and phase of the field. Since the properties of the field and medium are typically controlled, accurate knowledge of K_{CM} can be used as a way to characterize the individual frequency response of a particle.

There are a vast number of particle types and a large variety of analytical models that can be used to model their dielectric properties. For demonstration purposes in this dissertation, we selected a small library of 5 particle types that have differences in size, composition and surface chemistry in comparison to one another. The library of particles consists of two types of biological organisms and three types of manufactured microspheres including: 10μm polystyrene microspheres, 10μm and 6μm microspheres that have a conductive surface coating, live yeast cells and dead yeast cells. Examining every possible combination of two types of particles from this library gives us the ability to evaluate how effectively our method can separate based on variations in one or more of all of the major properties that make up the electrical models presented in this chapter (radius, conductivity, permittivity and internal structure). The result of this separation analysis is presented in chapter 7.

3.1 COMPLEX PERMITTIVITY PARTICLE MODELS

From equation (2.5) it can be see that K_{CM} depends on two values: the complex permittivity of the medium (ε_m^*) and the complex permittivity of the particle(ε_p^*). For the analyses presented in this chapter the electrical parameters of the reference medium are held constant when calculating K_{CM} (KCL solution of $\varepsilon_m = 78\varepsilon_0$, $\sigma_m = 5 \times 10^{-3}\, S/m$) so that the relative differences between particle types can be observed. A KCL buffer solution was selected in order to emulate the conductive mediums typically used in laboratory procedures dealing with cells. In this chapter, we will take a detailed look at K_{CM} for each of these particles by using variations of three established models to calculate ε_p^* : The homogenous dielectric sphere model, the ohmic-dielectric sphere model and the multi-layered shell model.

3.1.1 Polystyrene Microspheres (10um)

The first particle type included in our library is polystyrene microspheres (10μm PS, Polysciences, Inc.) with an average diameter of $d = 10.18\mu m$. One of the appealing features of polystyrene microspheres is that they can be manufactured with a relatively high degree of uniformity. As a result, these manufactured particles are used in a large number of commercial and research applications ranging from calibration of pharmaceutical assays to high precision spacers in LCD screens. Polystyrene is one of the most widely used plastics, therefore its electrical properties are well known

Since the microspheres consist of pure polystyrene throughout, their permittivity is best modeled as a homogenous dielectric sphere, such as what is shown in figure 3.1[25]. Polystyrene is an electrical insulator; therefore electrical conductivity of a PS particle, σ_p, is

equal to *0 S/m*. Polystyrene has a relatively small dielectric constant of ε *=2.55* due to its low degree of polarizability. The electrical characteristics of PS microspheres are such that the expression for complex permittivity is simply equal to its frequency independent relative permittivity

$$\varepsilon_p^* = \varepsilon_p \tag{3.1}$$

where $\varepsilon_p = 2.55\varepsilon_0$. The right side of figure 3.1 shows the real and imaginary parts of the Clausius-Mossotti factor that results from this model when in the reference medium and calculated using equations (2.5).

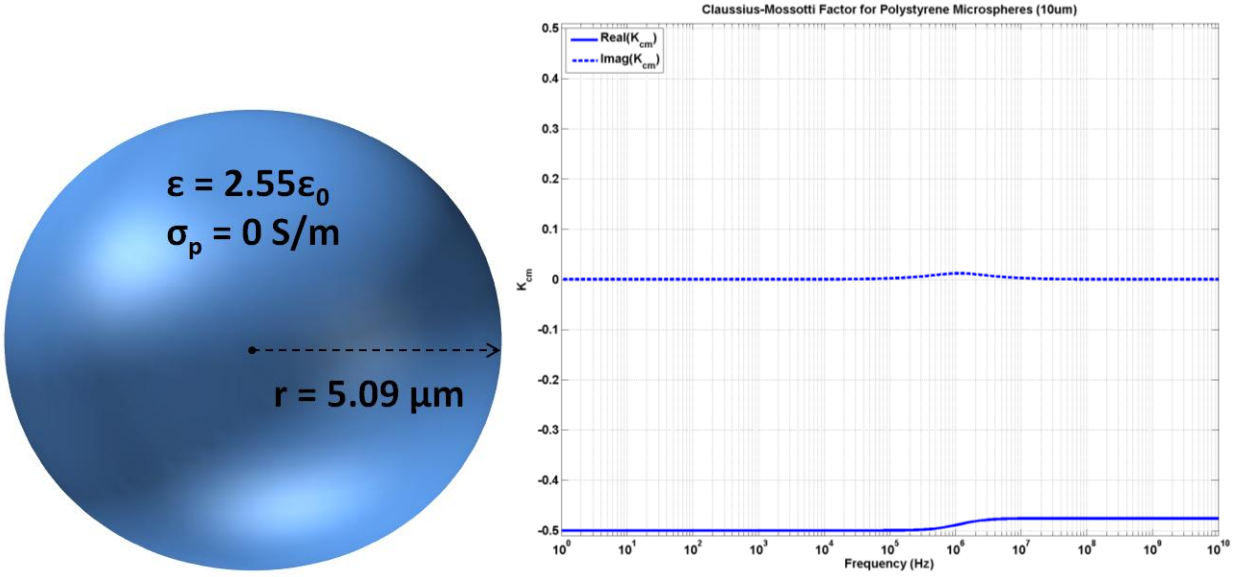

Figure 3.1 Homogenous dielectric sphere model for 10µm polystyrene microspheres and resulting Clausius-Mossotti factor when in a KCL medium of $\varepsilon_m = 78\varepsilon_0$ and $\sigma_m = 5 \times 10^{-3}\ S/m$

Figure 3.2 shows the real part of the Clausius-Mossotti factor for the 10µm PS microspheres. Since $Re\{\varepsilon_m^*\} \gg Re\{\varepsilon_p^*\}$ at all frequencies, *Re{K_{CM}}* for these particles will always be negative and near its lower bounds *-0.5*, the maximum negative value. The calculated range of *Re{K_{CM}}* is *-0.5 < Re{K_{CM}} < -0.476*. This indicates that particles of this type will always undergo negative dielectrophoresis (nDEP) and have a force component exerted on it in

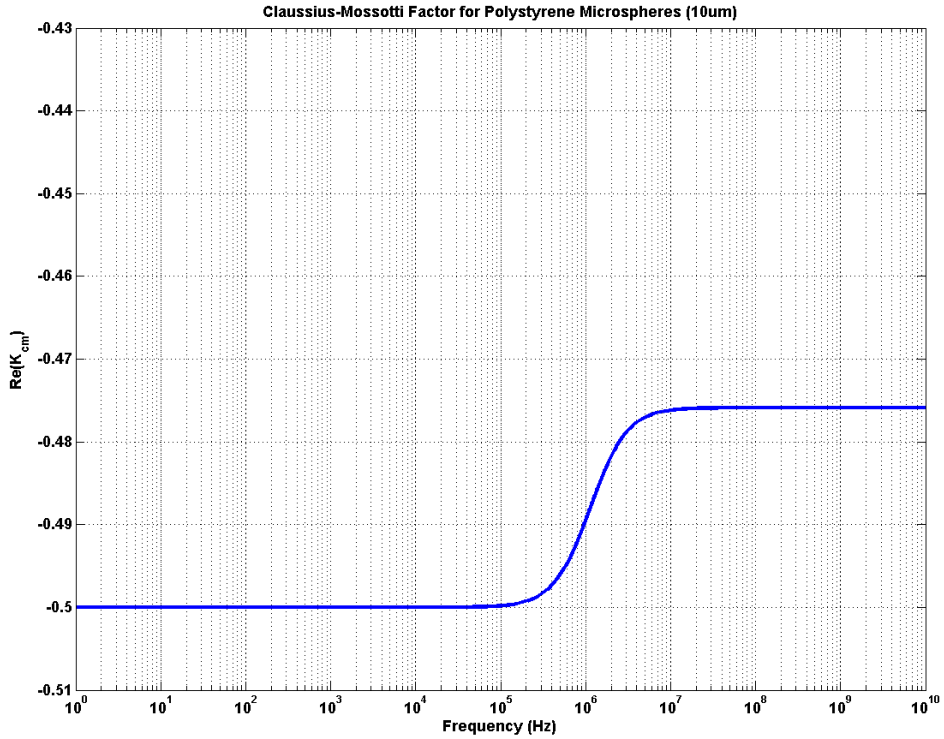

Figure 3.2 Real part of Clausius-Mossotti Factor for 10μm Polystyrene Microspheres

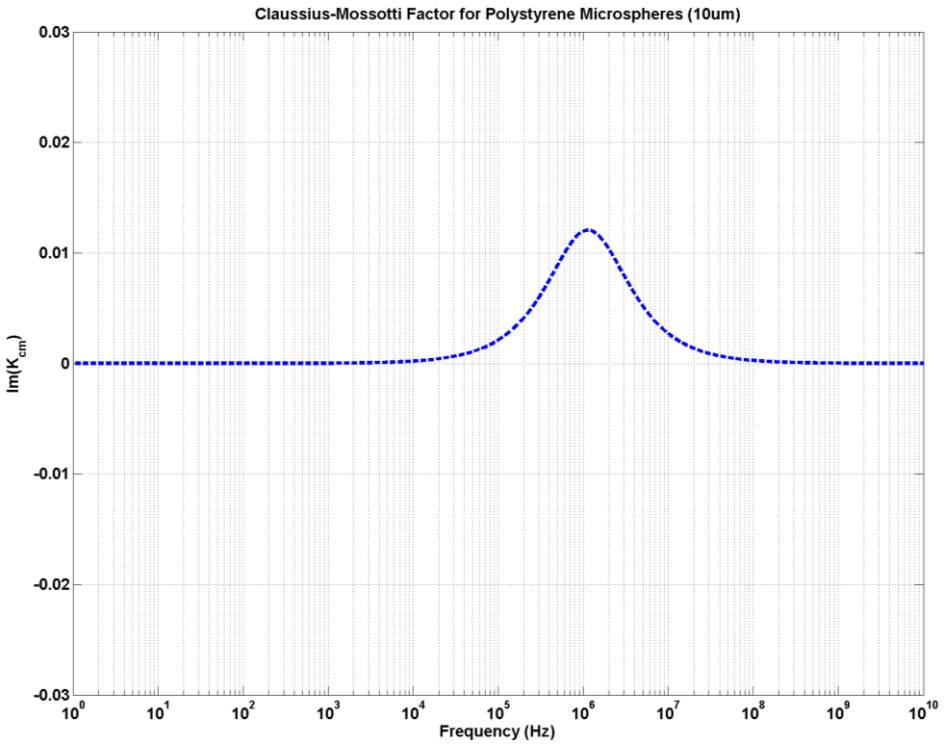

Figure 3.3 Imaginary part of Clausius-Mossotti Factor for 10μm Polystyrene Microspheres

the direction of decreasing field intensity. There is an inflection in the curve centered around $f = 1.17\ MHz$ where $Re\{K_{CM}\}$ becomes slightly less negative, approximately %5 smaller in magnitude. This is due the complex permittivity of the medium slightly decreasing at higher frequency. Figure 3.3 shows the corresponding imaginary part of the Clausius-Mossotti factor 10μm polystyrene microspheres. The point of inflection observed in $Re\{K_{CM}\}$ coincides with a peak in the magnitude of $Im\{K_{CM}\}$. At low frequencies and high frequencies $Im\{K_{CM}\}$ is zero and gradually increases to its maximum value of $Im\{K_{CM}\} = 0.012$, as the frequency approaches $f = 1.17\ MHz$. This peak value is ~1% of its maximum possible value of $Im\{K_{CM}\}$, and 40 times smaller than $Re\{K_{CM}\}$, indicating that TWDEP forces on these particles will be relatively small and DEP forces will dominate. Since the sign $Im\{K_{CM}\}$ is positive for all non-zero values, when TWDEP forces are exerted on the particles, the direction of the force components will be the same as the positive phase gradient.

In this dissertation, the electrode arrangement that will most often be referred to and used is the traveling-wave configuration shown in figure 2.5. For this combination of particles and medium, in such a configuration, the expectation is that there will be two primary regions of operation. At frequencies far away from $f = 1.17\ MHz$, 10μm polystyrene microspheres will feel a strong nDEP force component pushing it upwards with little to no lateral TWDEP forces exerted on them. As the frequency gets nearer to $f = 1.17\ MHz$, strong nDEP forces will still cause the particle to levitate while weak TWDEP forces will move the particles slowly, laterally across the electrode array.

3.1.2 Polystyrene-COOH Microspheres (10um)

The second particle type included in our library is polystyrene microspheres that have been functionalized by adding carboxylic acid surface coating (10μm PS-COOH, Polysciences, Inc.) and have an average diameter of $d = 10.18\mu m$. PS-COOH microspheres are used in applications where it is necessary to covalently couple proteins or molecules to the surface of a polystyrene bead. For the purposes of this work, it presents a particle group that differs from the 10μm PS particles only in its surface chemistry.

Polystyrene naturally has low electrical conductivity while carboxyl (COOH) ions have a net negative charge. The presence of negative ions on the surface of polystyrene beads makes them conductive and that significantly changes their dielectrophoretic behavior [44,45,46]. As a result, a model in which ohmic-losses are taken into account is best used to describe the complex permittivity of PS-COOH particles [44]. In this model, the overall conductivity of the particle (σ_p) is described by the sum of two parts, the particles internal electrical conductivity (σ_{bulk}) and surface conductivity $(\sigma_{surface})$ and is written as:

$$\sigma_p = \sigma_{bulk} + \sigma_{surface} \tag{3.2}$$

where

$$\sigma_{surface} = \frac{2K_s}{r} \tag{3.3}$$

for a particle of radius r with surface conductance K_s for the material. Since polystyrene is not a conductor, and the functionalization only occurs on the surface, the internal bulk conductivity σ_{bulk} remains equal to zero. Using equation 2.3, the complete expression for the complex permittivity of PS-COOH microspheres can be written as:

$$\varepsilon_p^* = \varepsilon_p - j\frac{2K_s}{\omega r} \tag{3.4}$$

The addition of a surface coating does not change the dielectric constant of the material, therefore the permittivity of PS-COOH microspheres is the same as for PS microspheres, $\varepsilon_p = 2.55\varepsilon_0$. In most applications where functionalized beads are used, knowledge of K_s is not needed; therefore it is typically an unknown parameter. As a result, in the dielectrophoresis research literature there has been a great amount of effort in experimentally determining the value to use for this parameter. It has been found that there is a linear relationship between K_s and r for PS-COOH microspheres and that the ratio K_s/r in most cases is a constant approximately equal to *0.25 nS/μm* [46]. This constant yields a value of K_s = *1.27 nS* for the PS-COOH particles examined here with radius r = 5.09μm. Figure 3.4 shows the ohmic-dielectric sphere model for 10μm PS-COOH microspheres and its corresponding Clausius-Mossotti factor spectrum when placed in the reference medium.

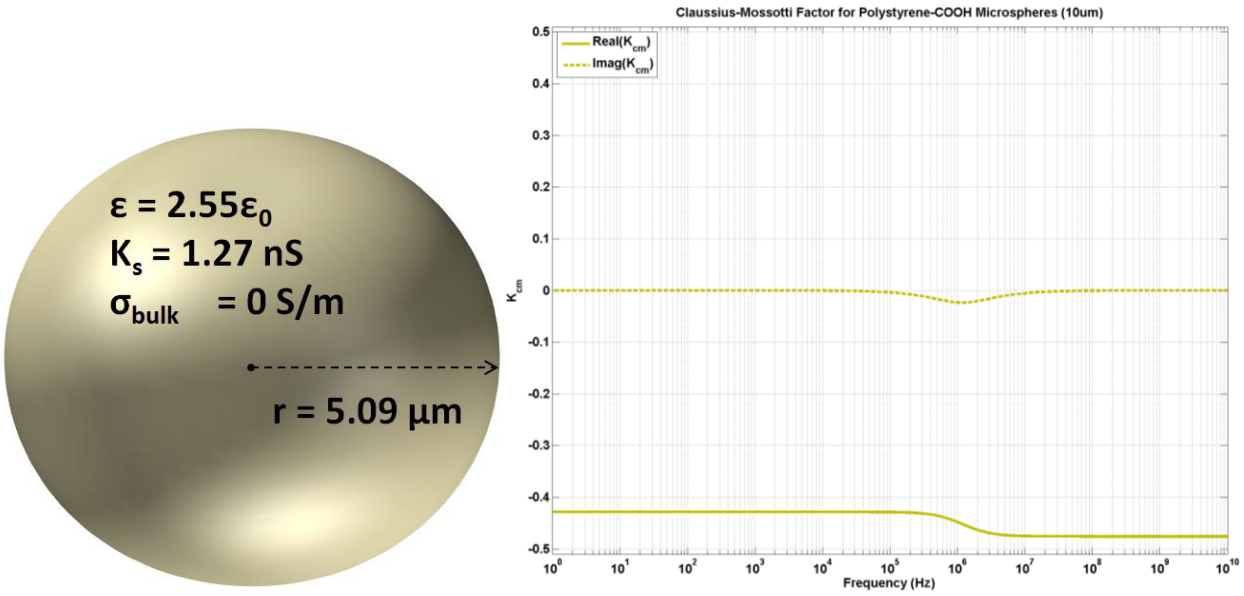

Figure 3.4 Ohmic-dielectric sphere model for 10μm polystyrene-COOH microspheres and resulting Clausius-Mossotti factor when in a KCL medium of $\varepsilon_m = 78\varepsilon_0$ and $\sigma_m = 5 \times 10^{-3}\ S/m$

Figure 3.5 shows the real part of the Clausius-Mossotti factor for the 10μm PS-COOH microspheres. Re$\{K_{CM}\}$ varies from $-0.476 < Re\{K_{CM}\} < -0.429$. As was the case for PS microspheres, Re$\{K_{CM}\}$ is negative at all frequencies and PS-COOH particles will always undergo negative dielectrophoresis in this medium. The inflection in the plot of figure 3.5 is centered on $f = 1.17$ *MHz*, the same frequency this occurs for PS microspheres. However, there are a few key differences. First, $Re\{K_{CM}\}$ for PS-COOH becomes more negative as frequency increases, as opposed to less negative for PS particles. The corresponding swing in magnitude is also larger, 11% for PS-COOH versus 5% for PS. In addition, at all frequencies the negative dielectrophoresis forces exerted on PS microspheres will be greater than or equal in magnitude to the negative forces exerted on PS-COOH microspheres. This is due to the fact that surface modification on the particles increases their conductivity, lessening the difference between the conductivity of the particle and the surrounding medium and making Re$\{K_{CM}\}$ smaller.

Figure 3.6 shows the corresponding imaginary part of the Clausius-Mossotti factor 10μm PS-COOH. Again, at low frequencies and high frequencies $Im\{K_{CM}\}$ is zero. $Im\{K_{CM}\}$ gradually decreases to a peak value of $Im\{K_{CM}\} = -0.024$, as the frequency approaches $f = 1.17$ *MHz* and remains negative for all non-zero values.

Even though $Re\{K_{CM}\}$ and $Im\{K_{CM}\}$ for PS-COOH particles share similarities with PS microspheres, there are key differences that will cause them to have different behaviors when introduced to a TWDEP field created by the electrode configuration in figure 2.5. Since the sign of $Im\{K_{CM}\}$ for PS-COOH is always negative, as oppose to positive for PS, while under the influence of TWDEP, PS-COOH and PS will travel in opposite lateral directions. Additionally, since the peak magnitude of $Im\{K_{CM}\}$ for PS-COOH is twice as large as the peak for PS, they will travel relatively faster.

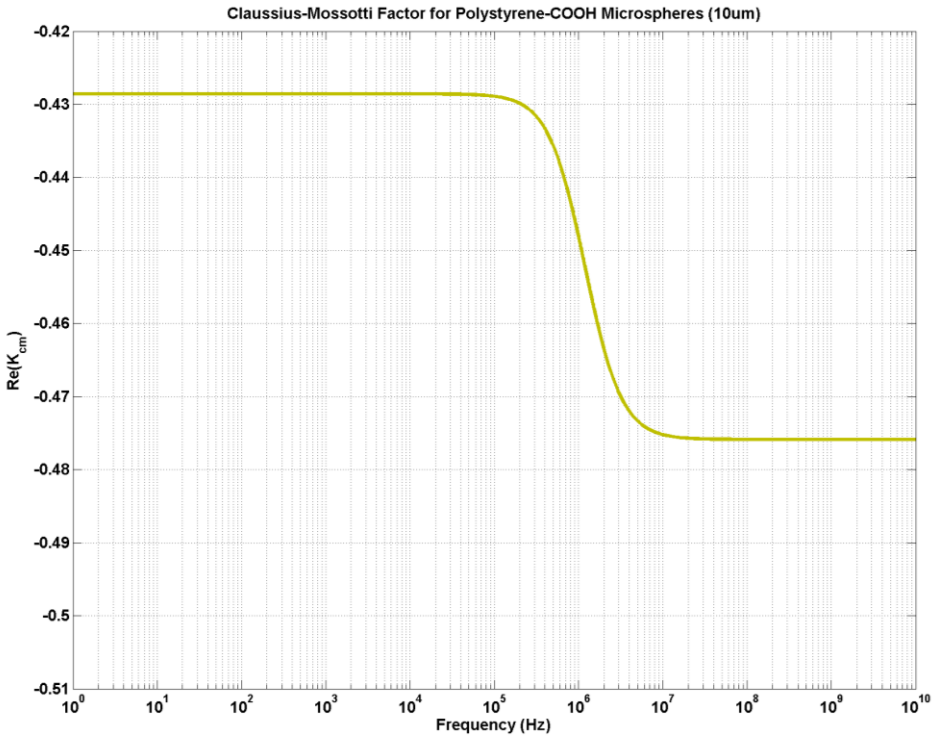

Figure 3.5 Real part of Clausius-Mossotti factor for 10µm Polystyrene-COOH Microspheres

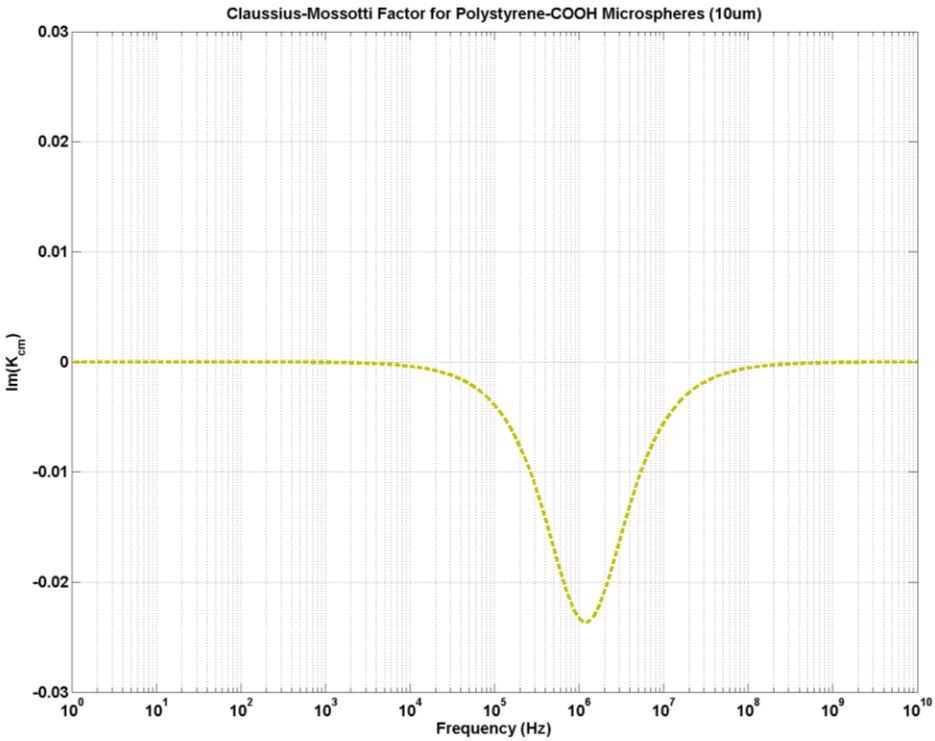

Figure 3.6 Imaginary part of Clausius-Mossotti factor for 10µm Polystyrene-COOH Microspheres

3.1.3 Polystyrene-COOH Microspheres (6um)

The third particle type included in our library is polystyrene microspheres that have also been functionalized with COOH. They differ from the particles described in section 3.2 only in their average diameter, $d = 6.22\mu m$ (6µm PS-COOH, Polysciences, Inc.). Since that is the only varying parameter, the complex permittivity of these particles can be described using the same ohmic-dielectric sphere model represented by equation (3.2). Figure 3.7 shows the ohmic-dielectric sphere model for 6µm PS-COOH microspheres and its corresponding Clausius-Mossotti factor spectrum when placed in the reference medium.

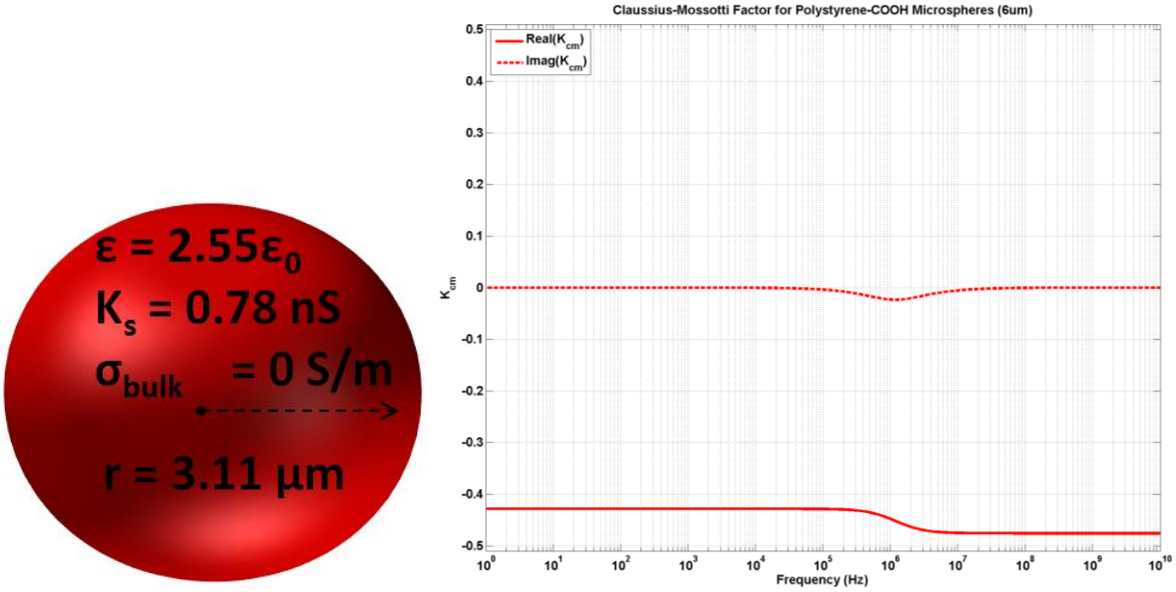

Figure 3.7 Ohmic-dielectric sphere model for 6µm polystyrene-COOH microspheres and resulting Clausius-Mossotti factor when in a medium of $\varepsilon_m = 78\varepsilon_0$ and $\sigma_m = 5 \times 10^{-3}\ S/m$

The plots of figures 3.8 and 3.9 show the real and imaginary parts of the Clausius-Mossotti factor for the 6µm PS-COOH microspheres. In this particular case, both

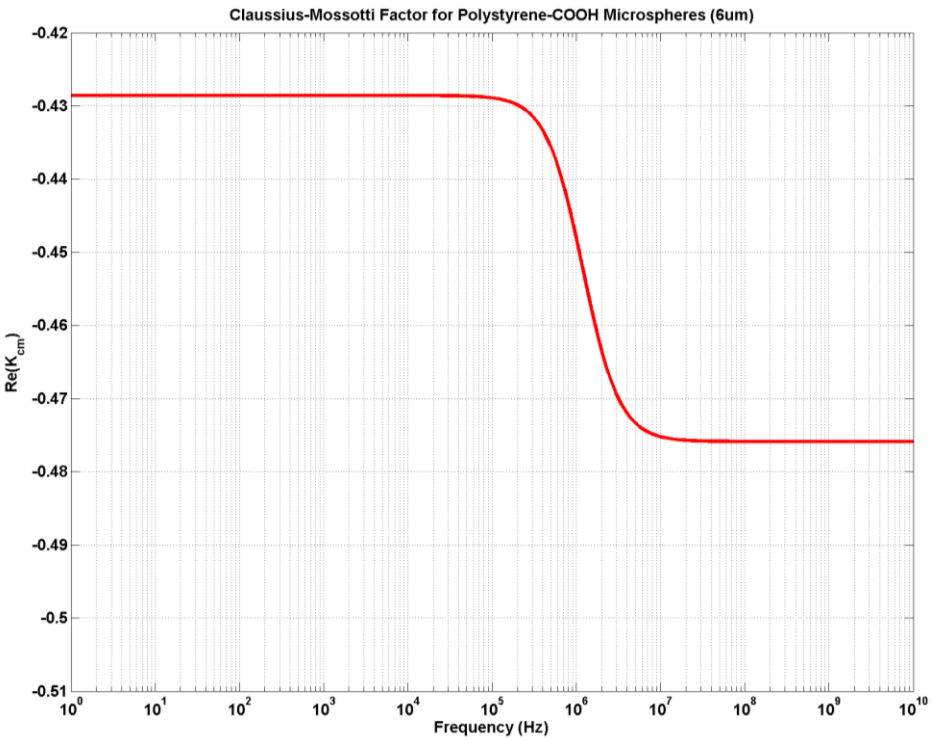

Figure 3.8 Real part of Clausius-Mossotti Factor for 6µm Polystyrene-COOH Microspheres

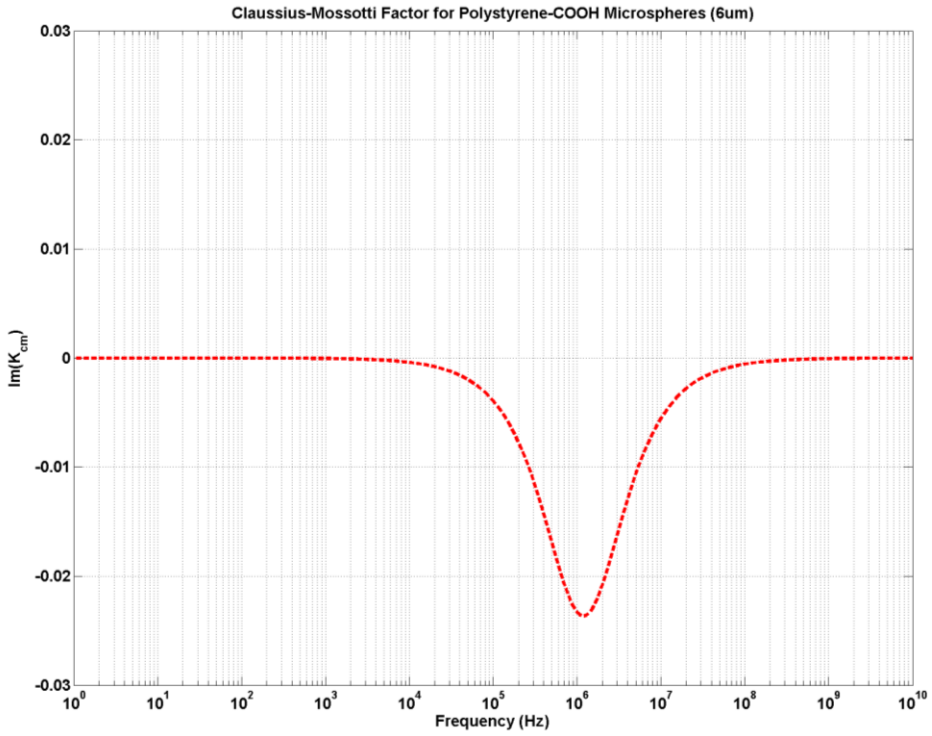

Figure 3.9 Imaginary part of Clausius-Mossotti factor for 6µm Polystyrene-COOH Microspheres

Re$\{K_{CM}\}$ *and* *Im*$\{K_{CM}\}$ have spectrums that are identical to that of 10μm PS-COOH microspheres. The reason for this is because the frequency response of COOH functionalized spheres do not have a dependency on radius since the ratio K_s/r is constant, making the overall conductivity of such particles the same, even though the surface conductance changes.

Even though 6μm PS-COOH and 10μm PS-COOH have identical spectra, they will not behave similarly when undergoing TWDEP in an environment like the one presented in figure 2.5. Equation 2.11 shows that the magnitude of the overall dielectrophoretic force exerted on a particle is proportional to r^3 therefore small differences in radius result in large differences in force. So while 6μm PS-COOH particles will move at its maximum and minimum velocities at the same frequencies as 10μm PS-COOH particles, and will travel in the same directions, they will do so at a much slower speed.

3.1.4 Live Yeast Cells

The fourth particle type included in our library is saccharomyces cerevisiae, more commonly known as yeast cells. Viable yeast cells are widely used in biological research and in the development and testing of technologies dealing biological particles because they are easy to culture in a laboratory and their internal structure and morphology is representative of a large class of cells [47,48]. Figure 3.10 shows a photograph of a typical yeast cell and a diagram of its internal structure. Yeast typically range from 1 to 10μm in diameter and are ellipsoidal in shape. Yeast is an enveloped cell and has many layers to its internal structure. The outer-most layer is a rigid cell wall followed by a periplasmic space. The periplasm separates the wall from a thin cellular membrane that typically measures a few nanometers in thickness. The cell membrane encapsulates the nucleus and many other sub-cellular components.

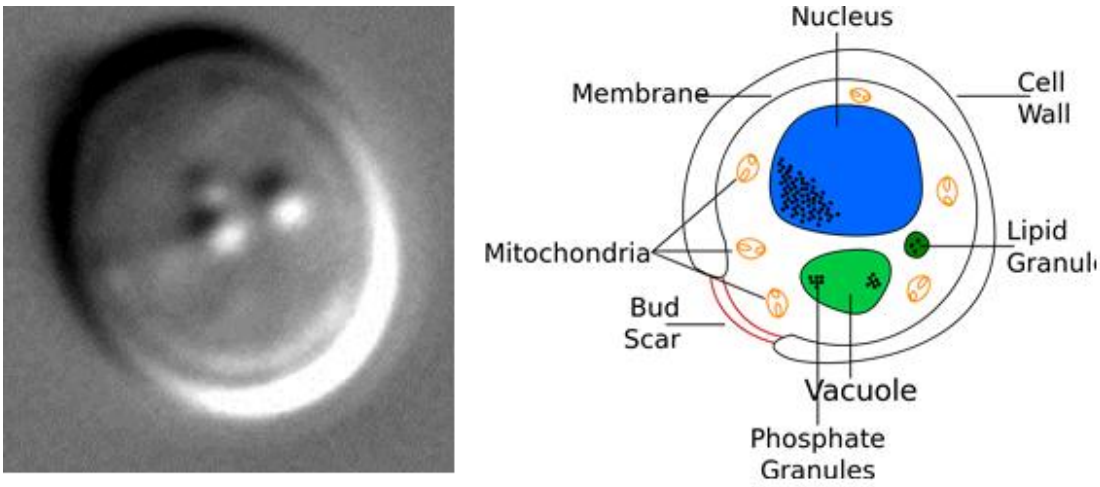

Figure 3.10 Microphotograph of a yeast cell and diagram of its internal structure [48]

Because of the structural complexity of yeast and many other cells, it is not sufficient to electrically model them using any of the permittivity models presented in this chapter thus far. There are many analyses of the dielectrophoretic forces exerted on biological particles in the published literature [25]. At the heart of these analyses is a concentric shell model for the effective complex permittivity, which in turn determines the Clausius-Mossotti factor [49]. In this model, particles are electrically modeled as concentric spheres of varying thickness, each layer having unique values for electrical conductivity and permittivity. The complex permittivity of a multi-layered particle can be calculated by using the 'smeared-out' sphere method [25] illustrated in figure 3.11. Given an inner shell (n^{th} layer) and an outer shell (n^{th} + 1 layer), an effective equivalent complex permittivity for the two layers ($\varepsilon^{*\prime}_{n+1}$) can be calculated using the expression:

$$\varepsilon_{n+1}^{*\prime} = \varepsilon_{n+1}^{*} \frac{\left[\left(\frac{\mathrm{r}_{n+1}}{\mathrm{r}_{n}}\right)^{3} + 2\left(\frac{\varepsilon_{n}^{*} - \varepsilon_{n+1}^{*}}{\varepsilon_{n}^{*} + 2\varepsilon_{n+1}^{*}}\right)\right]}{\left[\left(\frac{\mathrm{r}_{n+1}}{\mathrm{r}_{n}}\right)^{3} - \left(\frac{\varepsilon_{n}^{*} - \varepsilon_{n+1}^{*}}{\varepsilon_{n}^{*} + 2\varepsilon_{n+1}^{*}}\right)\right]} \tag{3.5}$$

which essentially averages the permittivities of the shells according to their relative dimensions. The result is a value for complex permittivity such that a homogenous sphere of that value would be electrically equivalent two the combination of the two shells. In general, this procedure can be used to calculate the effective permittivity for any arbitrary number of shells by successively reapplying equation 3.5 and using the equivalent homogenous sphere calculated in the previous step as the inner layer until the outermost layer has been incorporated into the effective permittivity.

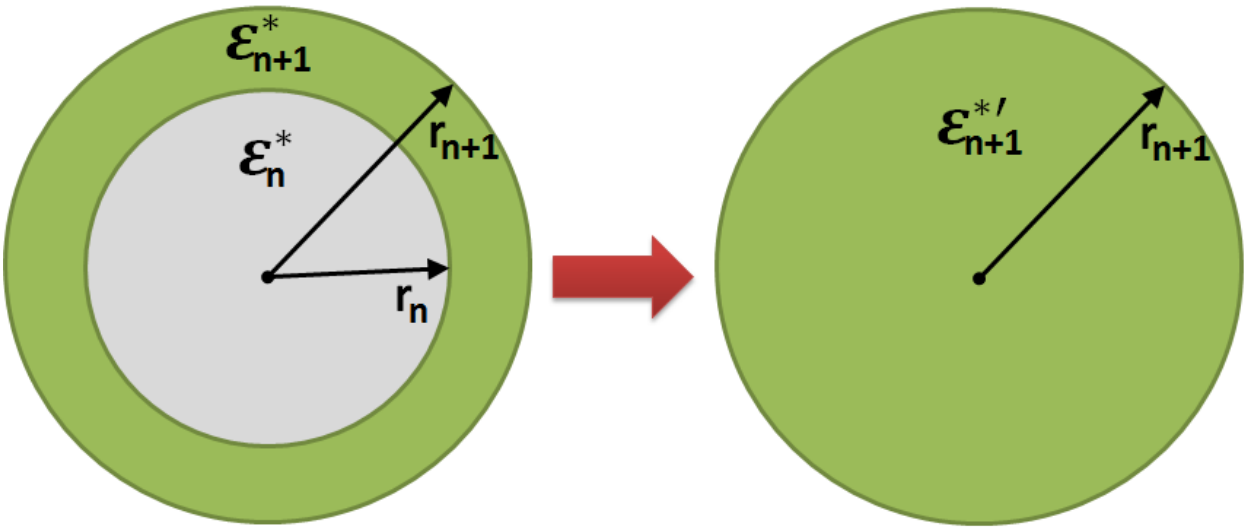

Figure 3.11 Approximating the effective complex permittivity of a two concentric spheres via use of the smearing method to determine the equivalent homogenous sphere complex permittivity.

Multi-shell models with various numbers of layers have been proposed to model the dielectric properties of viable yeast, and it has been shown that using 5 layers (figure 3.12) yields the most accurate results [50].

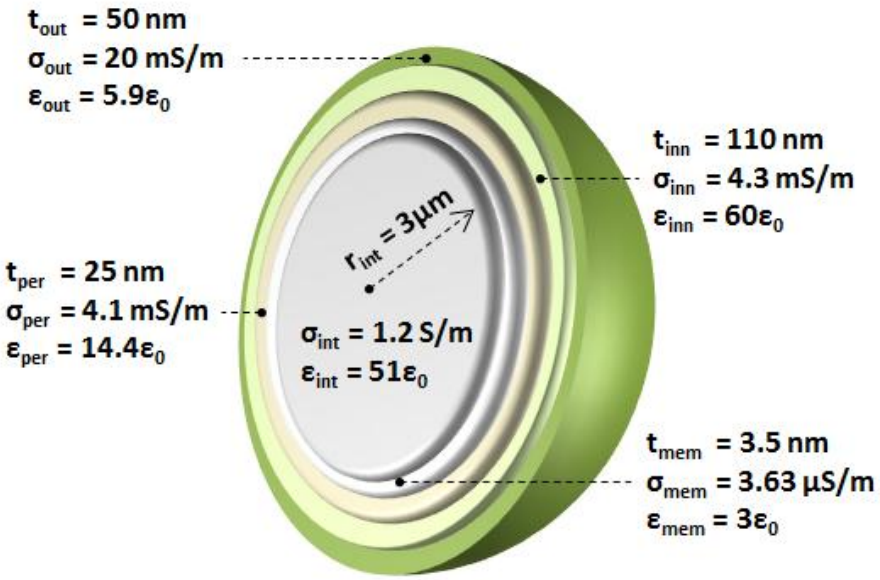

Figure 3.12 5-layer multi-shell models used for calculating the effective permittivity of viable yeast cells

In this model, it has been proposed that on average, viable yeast can best be represented by modeling the inner core and all the subcellular components as a sphere with radius of 3μm, conductivity σ_{int} = 1.2 S/m and with a dielectric constant of $\varepsilon_{int} = 51$. The cellular membrane is approximated to be 3.5 nm thick with a dielectric constant of $\varepsilon_{mem} = 3$. The conductivity of this layer depends greatly on the conductivity of the medium it resides in. The value that corresponds with our reference medium was calculated via a linear extrapolation using data points from [50], and results in a conductivity of σ_{mem} = 3.63 μS/m for our model. In the model, the membrane layer is followed by 25nm periplasmic space of σ_{per} = 4.1 mS/m and $\varepsilon_{per} = 14.4$. The multi-shell model better tracks the electrical characteristics of actual viable yeast by dividing

up the cell wall into inner and outer regions of thickness 50nm and 110nm respectively. The inner wall conductivity also depends on the medium (σ_{inn} = 4.3 mS/m for our reference medium) and an outer wall conductivity of σ_{out} = 20 mS/m. The inner and outer wall dielectric constants were determined to be $\varepsilon_{int} = 60$and $\varepsilon_{int} = 5.9$. Figure 3.13 shows the Clausius-Mossotti factor spectrum that results from this model in our reference medium and figures 3.14 and 3.15 show the real and imaginary parts of it.

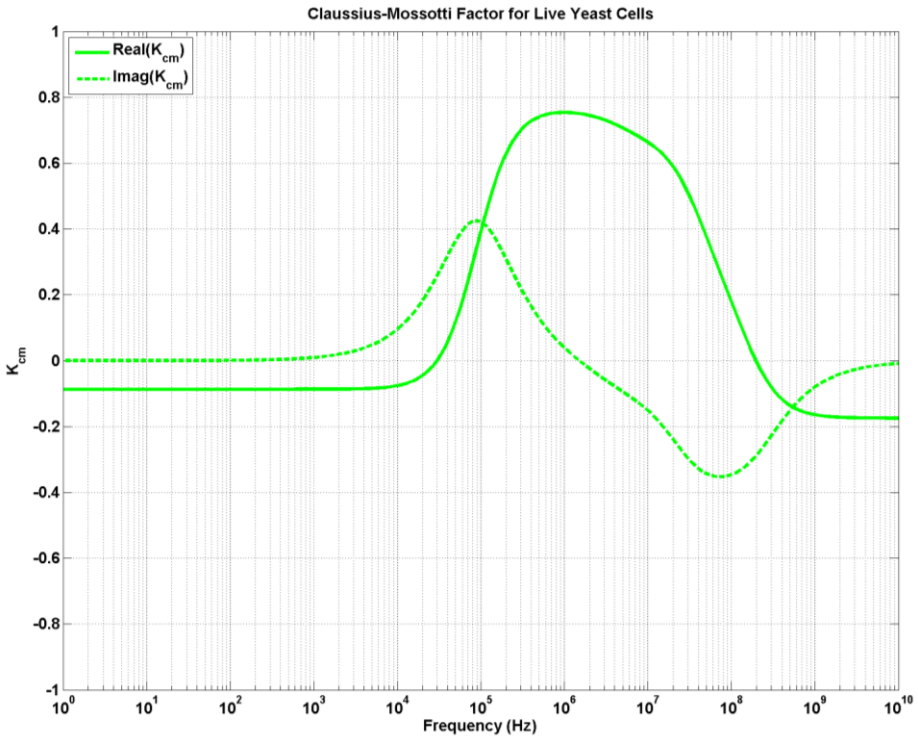

Figure 3.13 Clausius-Mossotti factor spectrum for 5-layer mutli-shell model of viable yeast cells in reference medium of $\varepsilon_m = 78\varepsilon_0$ and $\sigma_m = 5 \times 10^{-3}\ S/m$

The spectrum for $Re\{K_{CM}\}$ can be divided into 3 primary regions of operation. At lower frequencies ($0 < f < 30kHz$) $Re\{K_{CM}\}$ is negative and slowly increasing, indicating that viable yeast will undergo negative dielectrophoresis at these frequencies. From $30\ kHz < f < 200MHz$,

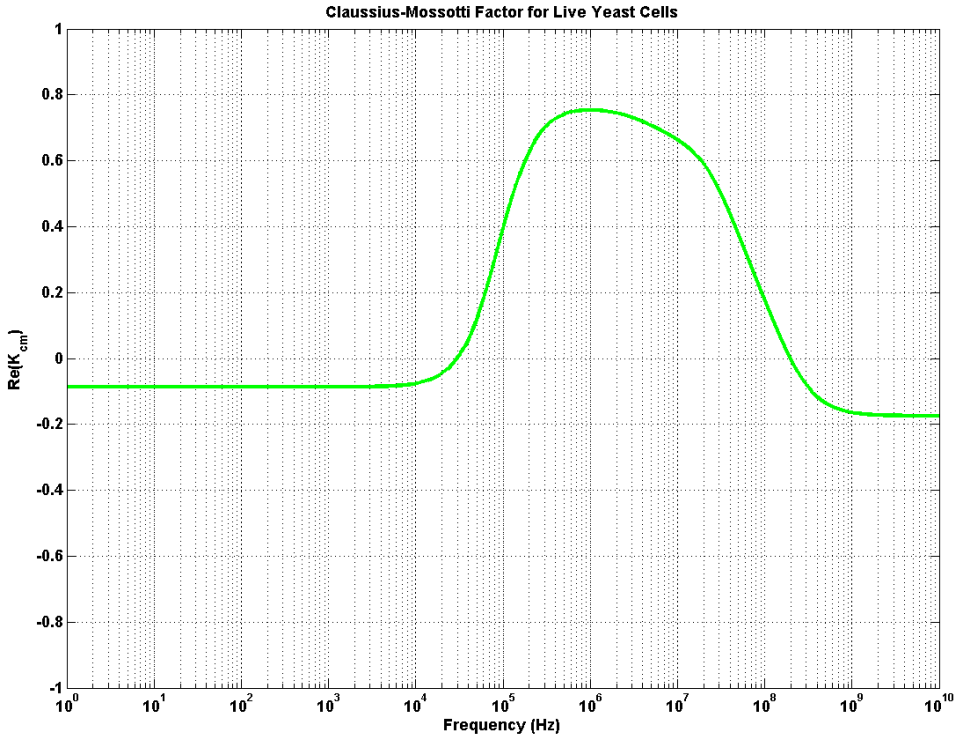

Figure 3.14 Real part of Clausius-Mossotti Factor for viable yeast cells

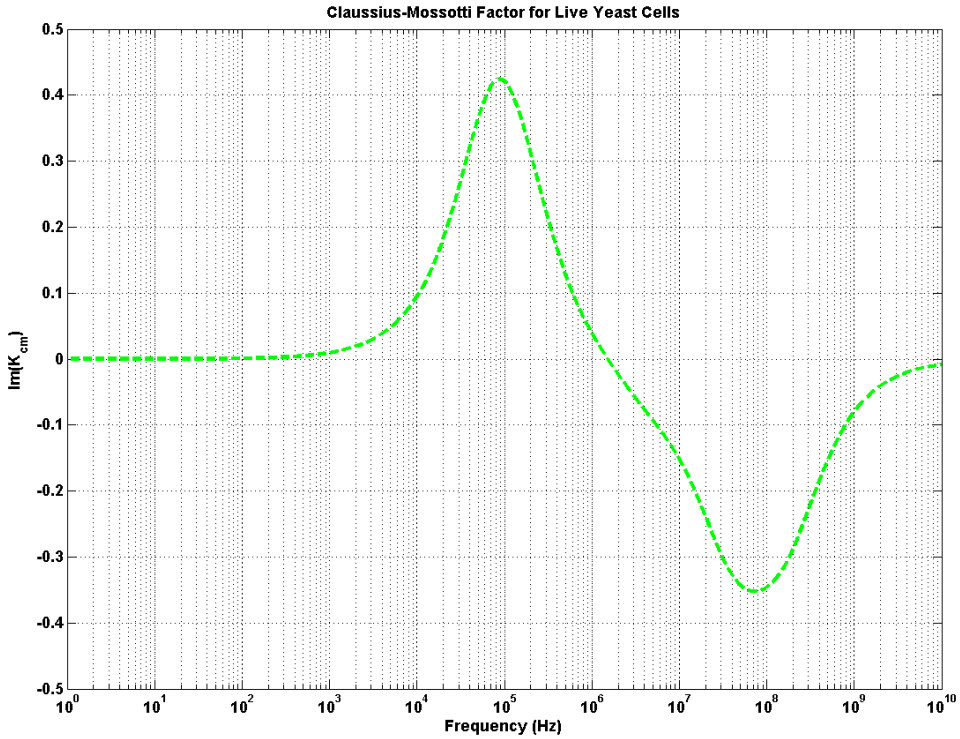

Figure 3.15 Imaginary part of the Clausius-Mossotti Factor for viable yeast cells

$Re\{K_{CM}\}$ is always positive, increases to its maximum value of $Re\{K_{CM}\} = 0.754$ at $f \approx 1MHz$ and then decreases towards zero at $f \approx 200MHz$. At very high frequencies ($f > 200\ MHz$), viable yeast behaving according to this model again exhibit negative dielectrophoresis. At these high frequencies, yeast can be made to feel its maximum possible negative dielectrophoresis forces when the Clausius-Mossotti factor saturates to a value of $Re\{K_{CM}\} = -0.174$, almost 3 times smaller in magnitude than the maximum negative forces that can be exerted on polystyrene spheres. The key difference to note here, in comparison to the manufactured particles described earlier, is that viable yeast cells can be made to have either strong positive dielectrophoresis forces exerted on it or relatively weak negative dielectrophoresis forces depending on frequency, whereas polystyrene spheres can only be made to have strong negative forces exerted on them in this medium.

Figure 3.15 shows the imaginary part of the Clausius-Mossotti factor viable yeast cells that results from using the multi-shell model. The primary distinguishing feature here is that the spectrum has two peaks: one that is positive and one that is negative. At low frequencies $Im\{K_{CM}\} = 0$ and then gradually increases to a peak of $Im\{K_{CM}\} = 0.43$ at $f = 88\ kHz$ and then descends back to zero at $f = 1.5\ MHz$. After that zero-crossing, the curve descends to a negative peak of $Im\{K_{CM}\} = -0.35$ at $f = 73\ MHz$. This reveals that viable yeast cells can have TWDEP forces exerted on them that are directed with or against the phase gradient, depending on frequency, as opposed to the polystyrene cases than can feel force vectors in one direction or the other, but not both. It is also of note that the maximum value of $Im\{K_{CM}\}$ for viable yeast cells can be up to 18 times larger in magnitude than the maximum value calculated for polystyrene beads (PS-COOH), meaning that TWDEP forces will have a much larger impact on their motion.

Based on this model and when introduced into the TWDEP configuration of figure 2.5, the expectation is that yeast cells will have 4 primary regions of operation. At very low frequencies, nDEP forces will cause the particle to levitate, with little to no lateral movement. As frequency increases, the particles will transition into a region where negative forces continue to elevate it, and but strong TWDEP forces will push the particle along the positive phase gradient. In the next band of frequencies where $Re\{K_{CM}\}$ is positive , strong pDEP forces will pull the particles down towards the electrode edges. If pDEP forces become too strong, the cells will be pinned to the electrodes and will not move laterally, even when $Im\{K_{CM}\}$ is non-zero. Eventually at high frequencies, when $Re\{K_{CM}\}$goes back to being negative, the cells will once again levitate and move laterally due to TWDEP forces. However since the sign of $Im\{K_{CM}\}$ is negative in this region, the particles will move in a direction opposite the phase gradient.

3.1.5 Dead Yeast Cells

The final particle type included in our library our yeast cells that are non-viable. This introduces a particle type that differs in a distinct physiological way from living yeast cells. For the purpose of carrying out experiments, one way to render living cells non-viable in a uniform way is to expose them to high temperatures for an extended duration of time [51]. Dead cells prepared in this manner have an additional benefit of being able to be selectively stained with dye, allowing them to be distinguished from living cells visually. Figure 3.16 shows a sample containing a mixture of living yeast cells and dyed cells that have been rendered non-viable via heating.

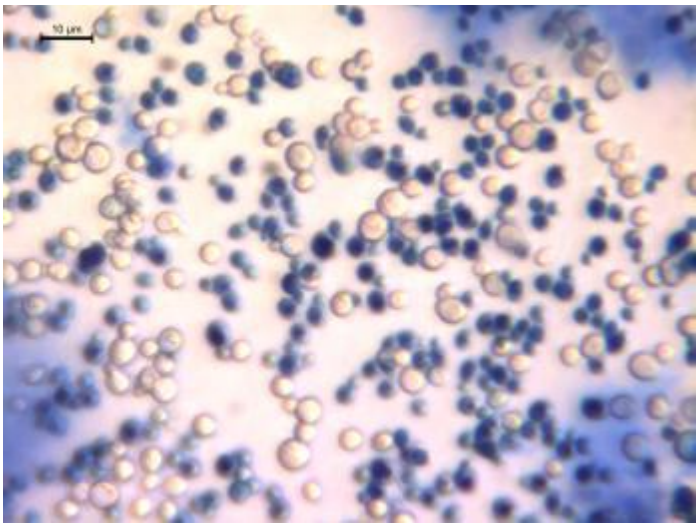

Figure 3.16 Mixture of living yeast cells and dead cells that have been stained with dye

Heat-treated yeast cells have been analyzed previously in the context of dielectrophoresis [51]. The multi-shell model has been found to be able to accurately model the electrical properties of yeast cells that have been rendered non-viable in this manner. The primary difference in the models used for dead versus living yeast is that dead yeast models have fewer layers. The model we use (figure 3.17), has 3 layers: a cell wall, membrane and inner core, 2 fewer layers than is used by our viable yeast model. Although 3-layer model has been empirically shown to be better fit for heat-treated cells, the physiological reasons as to why this is the case is not known. However, it would be reasonable to suggest that the application of extreme heat disrupts the cells internal structure to the point where the periplasmic space has been destroyed and there is no longer a significant difference between the inner and outer cell walls. In this model, the inner core has a radius of $r_{int} = 3$ μm, and the membrane and cell wall have respective thicknesses of $t_{mem} = 8$ nm and $t_{wall} = 250$ nm. The conductivities of the layers are $\sigma_{int} = 7$mS/m, $\sigma_{mem} = 160$ μS/m and $\sigma_{wall} = 1.5$ mS/m with corresponding dielectric constants

of $\varepsilon_{int} = 50$, $\varepsilon_{mem} = 6$ and $\varepsilon_{wall} = 60$. Figure 3.18 shows the Clausius-Mossotti factor that results when this model is placed in the reference medium.

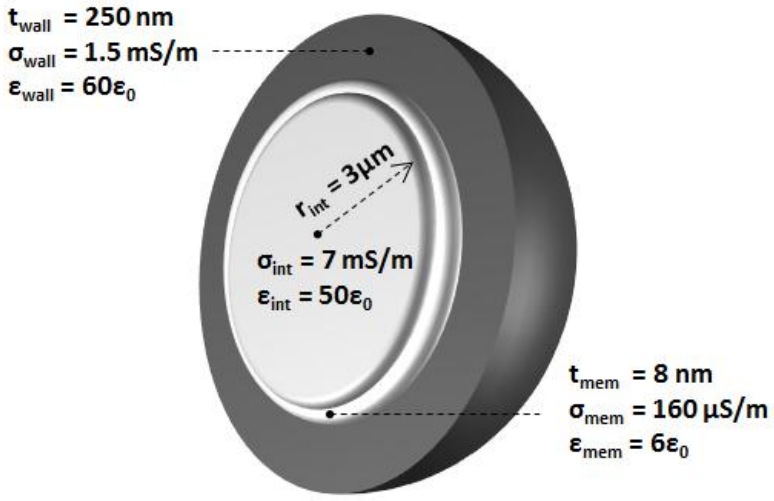

Figure 3.17 3-layer multi-shell models used for calculating the effective permittivity of non-viable yeast cells

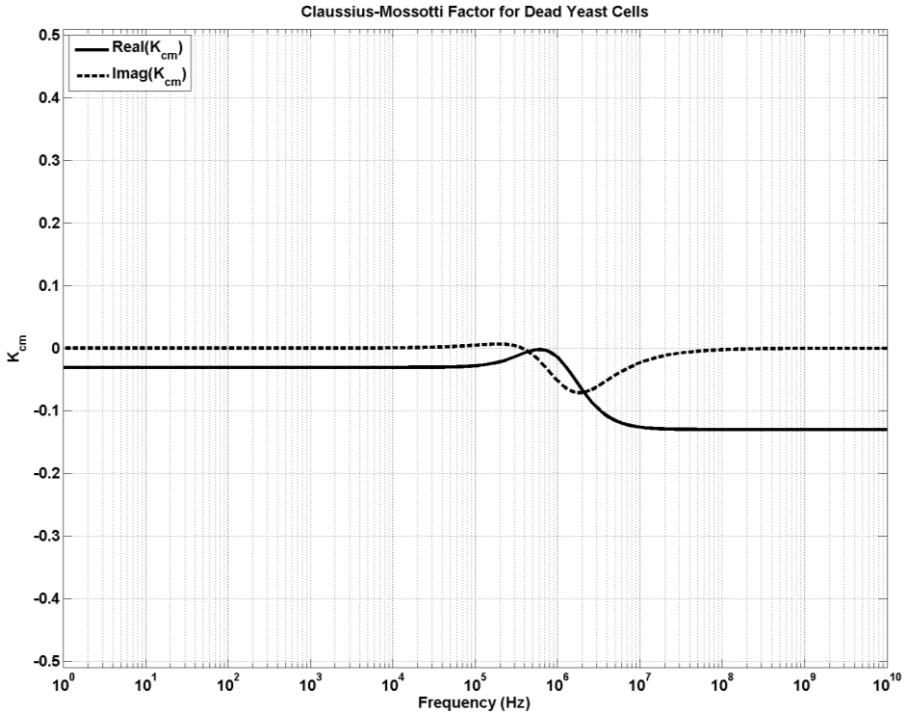

Figure 3.18 Clausius-Mossotti factor spectrum for 3-layer mutli-shell model of non-viable yeast cells in the reference medium of $\varepsilon_m = 78\varepsilon_0$ and $\sigma_m = 5 \times 10^{-3}\ S/m$

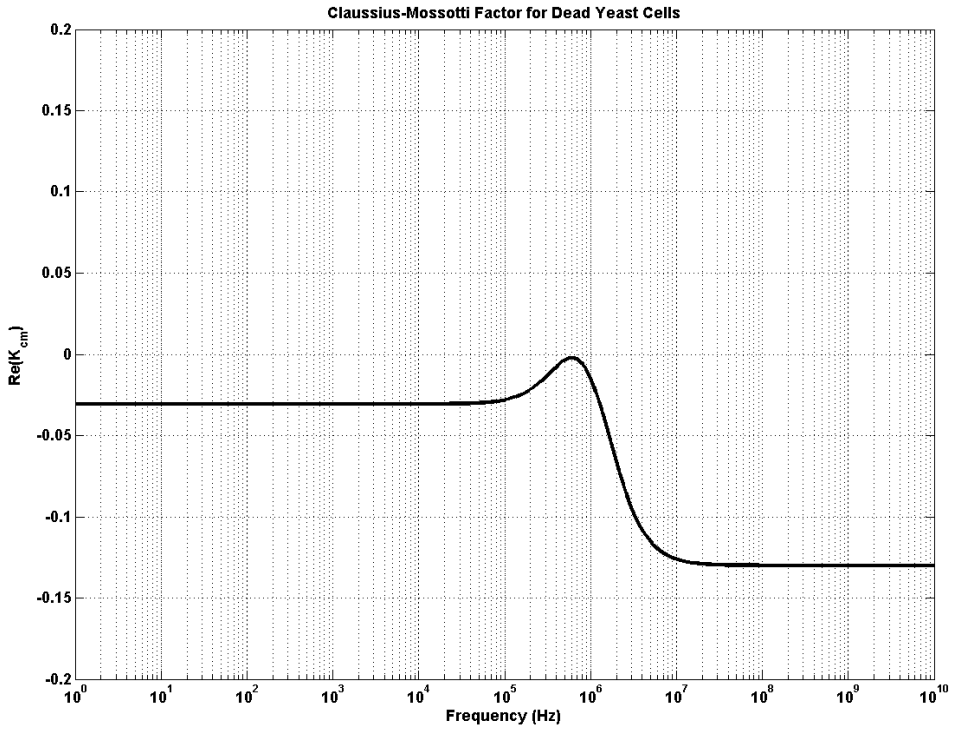

Figure 3.19 Real part of Clausius-Mossotti Factor for non-viable yeast cells

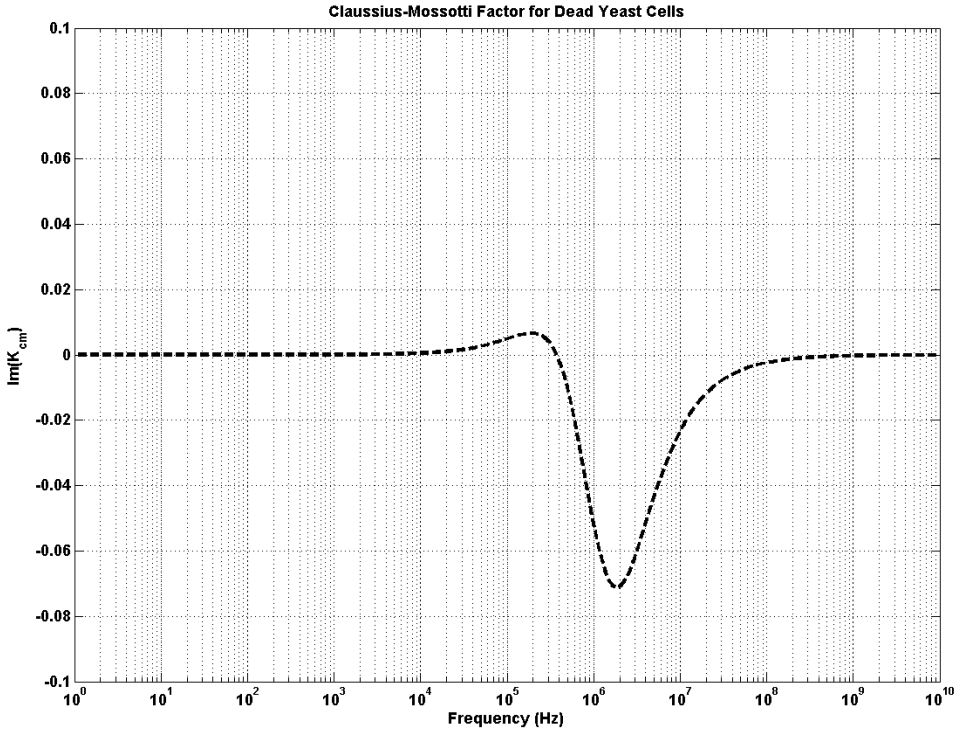

Figure 3.20 Imaginary part of Clausius-Mossotti Factor for non-viable yeast cells

Figures 3.19 shows a close up views of $Re\{K_{CM}\}$ for dead yeast cells. The plot shows that $Re\{K_{CM}\}$ is negative for all frequencies, meaning that they will always undergo negative dielectrophoresis in this medium. There is a point of inflection in the spectrum for $Re\{K_{CM}\}$, centered around $f = 285$ kHz, where $Re\{K_{CM}\}$ briefly increases towards zero, but never becomes positive. At frequencies shortly after that, the spectrum quickly declines and saturates to its maximum negative value. This is quite different from the behavior of living yeast cells that can exhibit both nDEP and pDEP depending on frequency. At lower frequencies, $Re\{K_{CM}\}$ has a constant value of -0.03 and at high frequencies a constant value of -0.13 . These peak values are such that the maximum negative dielectrophoresis force that can be exerted on dead yeast is on the same order of magnitude as living yeast cells but significantly less than the maximum for the polystyrene particles.

The imaginary spectrum for dead yeast cells is shown in figure 3.20. At low frequencies $Im\{K_{CM}\}$ is zero and then slowly increases to a small positive peak of 0.007 at approximately 195 kHz, where TWDEP forces will propel particles in the direction of the phase gradient. After that peak $Im\{K_{CM}\}$ descends to a negative value of -0.07 near 1.85 MHZ, where TWDEP forces will move the cell opposite the phase gradient. At high frequencies, $f > 100$MHz, $Im\{K_{CM}\}$ nears zero again and dead cells will not have TWDEP forces exerted on them

When this model is introduced into the TWDEP configuration of figure 2.5, it is predicts that dead cells will have 3 primary regions of operation. At very all frequencies, and in all 3 regions, nDEP forces will cause the particle to elevate above the array. In the first region of operation, occurring at very low and high frequencies, dead cells will not exhibit any lateral motion while remaining elevated above the electrode array due to nDEP. Near the frequency at which the small positive peak in $Im\{K_{CM}\}$ occurs (195 kHz), dead cells will be propelled laterally

in the same direction as the phase gradient, while they will move laterally in the opposite direction at frequencies near the negative peak (1.85MHz). Similar to the case for living yeast cells, the model for dead cells indicates that they will experience TWDEP in two directions. However, the response for dead yeast is distinctly different in that the maximum TWDEP forces will be an order of magnitude smaller than as for living yeast and their relative maximums happen at different frequencies.

3.2 COMPARISON OF DIELECTROPHORESIS FORCES TO NOISE SOURCES

In order for dielectrophoresis to be the controlling force, its magnitude must be greater than the summation of the unwanted noise sources presented in chapter 2. Among the selection of particles presented in this chapter, the dielectrophoresis force magnitude will be smallest for 6μm polystyrene-CCOH microspheres. These microspheres will feel the smallest amounts of force in the reference medium since they have a combination of the smallest radius and Clausius-Mosssotti factor component with the lowest magnitude ($Im\{K_{CM}\}$), and therefore represent the worst case for overcoming the effects of noise.

Figure 3.21 shows a plot of the of the traveling-wave dielectrophoresis force that will be exerted on 6μm PS-COOH microspheres versus frequency, along with the spectra for the primary noise components, AC electroosmosis, Brownian motion and electrothermal noise. The TWDEP force spectrum was calculated using expression 2.11 and using parameters from the electrode designs that will be presented in chapter 5. As can be seen from the plot of figure 3.21, the magnitude of Brownian and electrothermal noise forces are negligible in comparison to the traveling-wave force at all frequencies. The peak magnitude of the AC electrosmotic noise

spectrum is 31.5 pN at a frequency of f ≈ 1 kHz, while the peak for 6μm PS-COOH microspheres is 5.75 pN at a frequency of f ≈ 1 MHz. AC electroosmotic forces can be significantly larger than the TWDEP forces and disrupt the particles motion. However, AC electrosomosis does not have a significant role in affecting particle motion since at the higher frequencies where traveling-wave dielectrophoresis is used to manipulate particles, the AC electroosmosis spectrum tapers out.

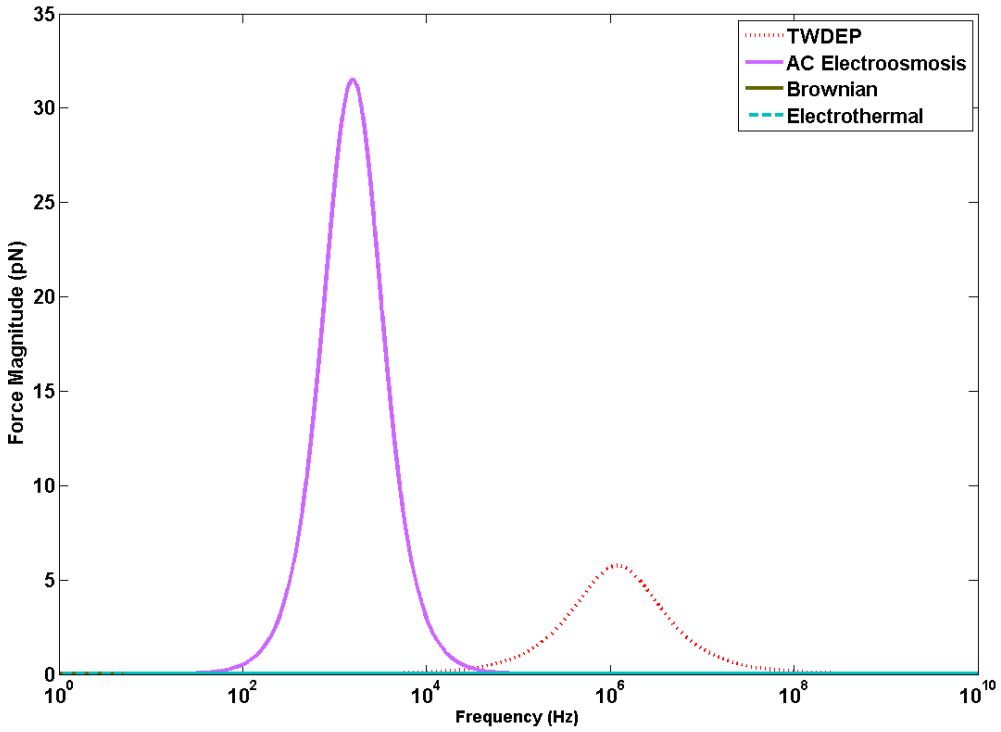

Figure 3.21 TWDEP force spectrum for 6μm PS-COOH microspheres plotted against the spectra for AC electroosmosis, Brownian motion and electrothermal noise.

In the next chapter, we will demonstrate how the insight gained from the various particle models about their phase and frequency dependent behavior can be exploited to identify specific sequences dielectrophoresis field configurations that generate net differential forces and result in particles types being separated from one another.

4.0 PROPOSED METHODOLOGY: SEPARATION OF PARTICLES BY TIME-MULTIPLEXED DIELECTROPHORESIS

The key insight we gain from the various electrical models for particles presented in chapter 3 is that particles with variations in electrical properties will have differences in Clausius-Mossotti factors. This is summarized in figure 4.1. As a result, they will experience either different amounts of force, forces in opposite directions, or no force at all, depending on the particular frequency of the AC field in the region of the particle. We exploit this property to separate particles using our technique, time-multiplexed dielectrophoresis.

In this chapter, we first explain the model we use for particle velocity and then provide a detailed derivation of the use of time-multiplexed dielectrophoresis to exert differential forces on particles according to their type. We then explain how those differential forces can be used to separate particles via an example based on multi-shell cell models and explain the benefits of our method through examples. In particular, we discuss the ability that time-multiplexing dielectrophoresis gives us to synthesize conditions in which particle types can be separated from one another, when other methods are not able to do so. We conclude this chapter with a summary of the practical benefits our method provides in terms of lab-on-chip implementations the and separation of particles in real-world scenarios.

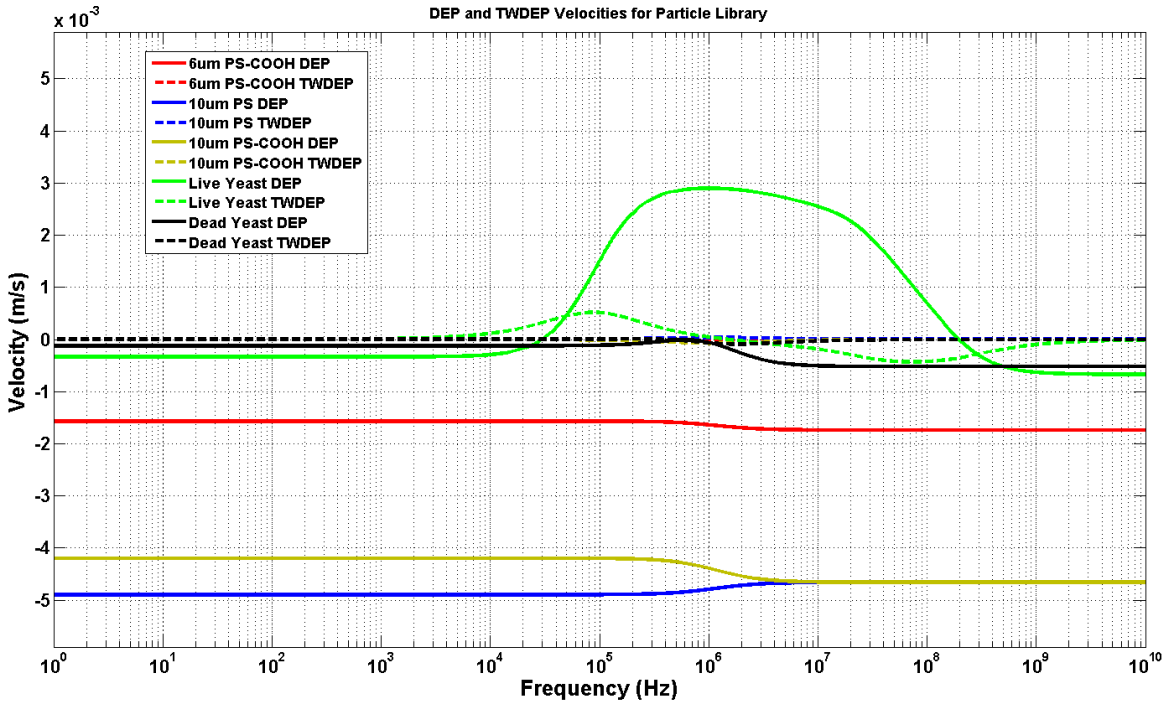

Figure 4.1 DEP and TWDEP velocity profiles for all the particles of chapter 3, showing the differences in velocity that occurs as a result of their relative differences in electrical properties.

4.1 GENERATING DIFFERENTIAL PARTICLE MOTION VIA TIME-MULTIPLEXING DIELECTROPHORESIS FIELDS

Particles undergoing dielectrophoresis move in a fluid, therefore their velocities will be significantly slowed by the resistance of drag forces. The net force on a particle undergoing traveling-wave dielectrophoresis as a result of the electrode configuration presented in figure 2.5 is

$$\vec{F}_p = \vec{F}_{TWDEP_X} + \vec{F}_{DEP_Y} + \vec{F}_{noise} + \vec{F}_{drag} \tag{4.1}$$

where $\vec{F}_{drag}$ represents opposing drag forces and $\vec{F}_{noise}$ is the sum of the noise components described earlier. In order to describe the separation of particles, it is best to analyze the system

in terms of particle velocities rather than forces since we are interested in controlling the motion of particles. But in order to determine velocity, we have to understand the nature of the drag forces that will be exerted on the particles.

In fluid mechanics, the Reynolds number is the ratio used to measure the relative importance of inertial forces to viscous forces and is defined as [52]

$$Re = \frac{\rho_m L v_m}{\eta} \tag{4.2}$$

where ρ_m is the fluid density, v_m is the velocity of the fluid, L is the characteristic length of the system and η is the dynamic viscosity of the fluid medium. The medium used in dielectrophoresis is typically of low viscosity like water, with a value of $\eta = 0.89 \times 10^{-3} Pa \cdot s$. At microfludic scales, the characteristic length is small, making the Reynolds number low; therefore micro and nanometer scale particles undergoing dielectrophoresis typically experience laminar Stokes flows in which inertia is negligible [52].

In general, the motion of an object in a fluid can be described by a set of partial differential equations known as the Navier-Stokes equations [53]. For the case of a small Reynolds number particle undergoing laminar flow in an incompressible, Newtonian fluid, these differential equations reduce to a simple closed form [52]. Micro and nanoscale particles undergoing dielectrophoresis meet the previously mentioned criteria (e.g., water or an electrolytic solution), therefore the drag force exerted on moving particles can be modeled using Stoke's law:

$$\vec{F}_{drag} = \gamma\left(\vec{v}_m - \vec{v}_p\right) \tag{4.3}$$

where $\vec{v}_p$ is the velocity of the particle and the friction factor term is $\gamma = 6\pi\eta r_p$.

Micro and nanoscale particles have extremely small mass (m_p), therefore their acceleration time constant, $\tau = m_p/\gamma$ is also very small and they reach steady state very quickly.

For example, an average sized yeast cell weighs $12 \times 10^{-12} g$ [54], which results in a time constant of τ = *238 ns*. The amount of dielectrophoretic force that can be generated using moderate voltages typically causes particles to move very slowly, at speeds on the order of μm/s. Therefore, the time period during which the particle is accelerating is negligible, and while the particle is moving, it can be assumed that it is not accelerating. Since the particle is not accelerating, there is no net force on the particle $\left(\vec{F}_p = m_p \vec{a}_p = 0\right)$. Therefore using equations 4.1 and 4.3, a particle undergoing motion can always be assumed to be traveling at its terminal velocity:

$$\vec{\boldsymbol{v}}_{\boldsymbol{p}} = \frac{\vec{\boldsymbol{F}}_{\boldsymbol{TWDEP_x}} + \vec{\boldsymbol{F}}_{\boldsymbol{DEP_y}} + \vec{\boldsymbol{F}}_{\boldsymbol{noise}}}{\boldsymbol{\gamma}} + \vec{\boldsymbol{v}}_{\boldsymbol{m}} \tag{4.4}$$

For our multiplexing method, it is desirable have control over both the x and y components of velocity. Assuming for a moment that noise is negligible and the fluid in the medium is not moving, using expressions 2.11 and 4.4 we can further express the x-component of particle velocity at a given frequency in terms of the key parameters of interest: TWDEP force magnitude, the sign of the electric field phase gradient along the x-axis and the sign of the imaginary part of the Clausius-Mossotti factor

$$v_{p_x}(\omega) = \frac{sgn(\nabla \phi_x) \cdot sgn[Im\{K_{CM}(\omega)\}] \cdot \left|\vec{F}(\omega)\right|_{TWDEP_x}}{\gamma} \tag{4.5}$$

Likewise, the y-component of particle velocity will be a function the DEP force magnitude, the sign of the electric field magnitude gradient along the y-axis and the sign of the real part of the Clausius-Mossotti factor:

$$v_{p_y}(\omega) = \frac{sgn\left(\nabla E_y^2\right) \cdot sgn[Re\{K_{CM}(\omega)\}] \cdot \left|\vec{F}(\omega)_{DEP_y}\right|}{\gamma} \tag{4.6}$$

At this point we define a new variable β, which is representative of the controllable sign of the force components. For the x-component of velocity, this directional variable has a value of

$$\beta_x = sgn(\nabla\phi_x) \cdot sgn[Im\{K_{CM}(\omega)\}] \tag{4.7}$$

The sign of the Clausius-Mossotti factor is fixed for a particle at a given frequency and the phase gradient can be externally used to control its sign. For the y-component of velocity, since in the configuration of figure 2.5 the electrodes are at the bottom of the chamber, the electric field intensity decreases as the height along the Y-axis increases. Therefore the sign of the electric field intensity gradient will always be negative and the overall sign of the y-component of velocity will be opposite the sign of the real part of the Clausius-Mossotti factor making

$$\beta_y = -sgn[Re\{K_{CM}(\omega)\}] \tag{4.8}$$

The sign of β_y can only be controlled via selection of frequency as phase has no bearing on its value. In terms of these new variables, the controllable, frequency dependent velocity components can be rewritten as

$$v_{p_x}(\omega) = \beta_x \cdot |v(\omega)|_{TWDEP} \tag{4.9}$$

$$v_{p_y}(\omega) = \beta_y \cdot |v(\omega)|_{DEP} \tag{4.10}$$

In addition to being able to control the directions of these velocity components, for our time-multiplexing dielectrophoresis method we wish to also be able to control the average value of the velocities over time. In our methodology, we require a supporting hardware platform (described in chapter 5) with the ability to change the field configuration at any given time, where the field configurations are defined in terms of their frequency ω and phase gradient $\nabla\phi$. For a field configuration of $\omega_1, \nabla\phi_1$ applied for time interval of T_1 that is then switched to a field

configuration of $\omega_2, \nabla\phi_2$ for duration of T_2, the time-averaged net differential velocity components particle becomes

$$\bar{v}_{p_x} = \langle v_{p_x}(\omega, t)\rangle = \left(\frac{T_1}{T_1 + T_2}\right) \cdot \beta_{x1} \cdot |v(\omega_1)|_{TWDEP} + \left(\frac{T_2}{T_1 + T_2}\right) \cdot \beta_{x2} \cdot |v(\omega_2)|_{TWDEP} \quad (4.11)$$

$$\bar{v}_{p_y} = \langle v_{p_y}(\omega, t)\rangle = \left(\frac{T_1}{T_1 + T_2}\right) \cdot \beta_{y1} \cdot |v(\omega_1)|_{DEP} + \left(\frac{T_2}{T_1 + T_2}\right) \cdot \beta_{y2} \cdot |v(\omega_2)|_{DEP} \quad (4.12)$$

The term $\left(\frac{T_1}{T_1+T_2}\right)$ can also be referred to as the duty cycle, *D* of the system, which will vary from $0 \leq D \leq 1$. Substituting in the variable for the duty cycle, the time-averaged velocity components that define the motion of a particle, in a time-multiplexing dielectrophoresis field are

$$\bar{\boldsymbol{v}}_{\boldsymbol{p_x}} = \boldsymbol{D} \cdot \boldsymbol{\beta_{x1}} \cdot |\boldsymbol{v}(\boldsymbol{\omega_1})|_{\boldsymbol{TWDEP}} + (\boldsymbol{1} - \boldsymbol{D}) \cdot \boldsymbol{\beta_{x2}} \cdot |\boldsymbol{v}(\boldsymbol{\omega_2})|_{\boldsymbol{TWDEP}} \quad \textbf{(4.13)}$$

$$\bar{\boldsymbol{v}}_{\boldsymbol{p_y}} = \boldsymbol{D} \cdot \boldsymbol{\beta_{y1}} \cdot |\boldsymbol{v}(\boldsymbol{\omega_1})|_{\boldsymbol{DEP}} + (\boldsymbol{1} - \boldsymbol{D}) \cdot \boldsymbol{\beta_{y2}} \cdot |\boldsymbol{v}(\boldsymbol{\omega_2})|_{\boldsymbol{DEP}} \quad \textbf{(4.14)}$$

In the next section we explain how these differential velocity components generated by time-multiplexing dielectrophoresis fields can be exploited to separate particles.

4.2 SEPARATING PARTICLES VIA TIME-MULTIPLEXED DIELECTROPHORESIS

In order to describe how time-multiplexing dielectrophoresis can be used to separate particles, we first we define conditions that must be met in order to separate particles using the electrode array of figure 2.5. The first condition that must be met is that the average net horizontal components of force for the particle types being separated from another must be opposite in direction. If it is the case that we wish to separate a mixture containing two particles types (e.g., type A and type B), then in terms of equation 4.13 the implication of this condition is that

$$\boldsymbol{sgn}\left(\bar{\boldsymbol{v}}_{\boldsymbol{A_x}}\right) \neq \boldsymbol{sgn}\left(\bar{\boldsymbol{v}}_{\boldsymbol{B_x}}\right) \tag{4.15}$$

This condition is necessary because in order for a separation between opposing particle types to take place, we wish to have them travel in opposite lateral directions and collect in distinct regions. There are also other practical implications of this constraint. The number of electrodes and the physical space in which the particles are contained in is finite, so even if particles are made to migrate apart while traveling in the same direction, eventually they would recombine once they reach the end of the electrode array.

The second condition that must be met is that the average net vertical component of force acting on the particle must be upwards, away from the electrode array. This occurs when the average DEP forces are negative. Therefore, in terms of equation 4.14, this implies that

$$\bar{\boldsymbol{v}}_{\boldsymbol{A,B_y}} < \boldsymbol{0} \tag{4.16}$$

over the duration of the separation period. This condition is critical to maintain. When positive dielectrophoresis forces are applied, particles are pulled down firmly to the electrode surfaces and are rendered completely immobile. As will be seen in the experimental section chapter 8,

this is particularly true in the case of cells, where the application of positive dielectrophoresis forces cause them to stick firmly to the electrode edges and lateral traveling-wave dielectrophoresis forces have no effect on their motion.

To best explain the use of time-multiplexing dielectrophoresis to separate particles, we will first look at an example. The bottom of figure 4.2 shows a mixture containing two theoretical particle types, type A and type B, over a dielectrophoresis electrode array. The plot of figure 4.2 shows the DEP and TWDEP velocity profiles for each particle type. Both types are based on the multi-shell cell model presented in chapter 3. They are identical in size and every electrical parameter except for one, their inner core conductivities. In this case, the inner core conductivity of type B particles is twice that of type A particles, causing a corresponding shift in the location of their crossover frequencies. The medium is significantly more conductive than the cells, therefore the cells always undergo negative dielectrophoresis and $Im\{K_{CM}(\omega)\} > 0$ for both cells at all frequencies where the traveling wave component of force is non-zero.

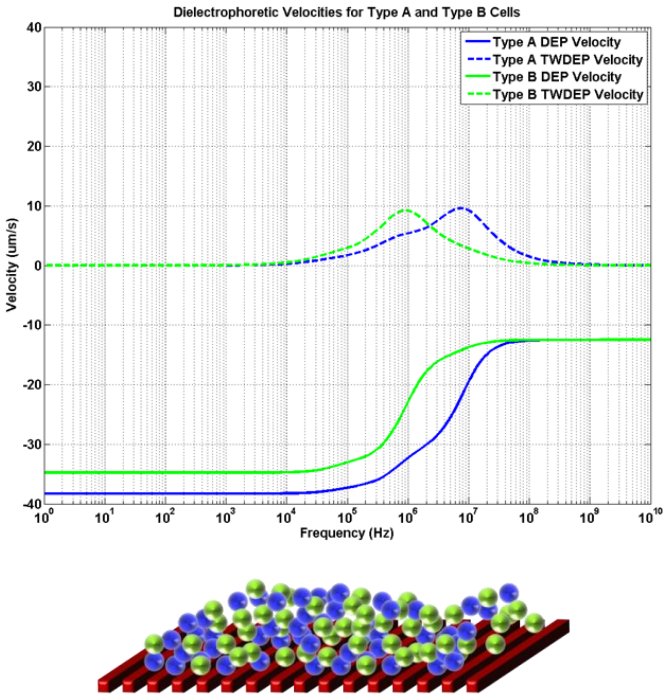

Figure 4.2 DEP and TWDEP velocity profiles for two theoretical particle types mixed above the electrode array

Figure 4.3 shows the DEP and TWDEP operating points for both particle types during the application of the first configuration, a traveling-wave field of frequency $\omega = \omega_1$, with a phase gradient across the electrodes such that $sgn(\nabla\phi_{x1}) = -1$. For this first example, the two configurations are applied for equal amounts of time, making $D = (1 - D) = 0.5$.

At frequency ω_1 $Re\{K_{CM}(\omega_1)\}$ is negative for both particle types so the condition of (4.16) is met as

$$\beta_{A_{y1}} = \beta_{B_{y1}} = -1 \tag{4.17}$$

and all cells are kept elevated above the electrode array.

Since the phase gradient is set to be negative (going from left to right in figure 4.3) and $Im\{K_{CM}(\omega_1)\}$ is positive for both particle types,

$$\beta_{A_{x1}} = \beta_{B_{x1}} = -1 \tag{4.18}$$

and all cells travel in the negative x-direction opposite the positive phase gradient.

In addition, during this first step a field configuration is selected such that one of the particle types will move at a faster x-velocity than the other particle type. At this frequency, this occurs for type A cells as

$$|v_A(\omega_1)|_{TWDEP} > |v_B(\omega_1)|_{TWDEP} \tag{4.19}$$

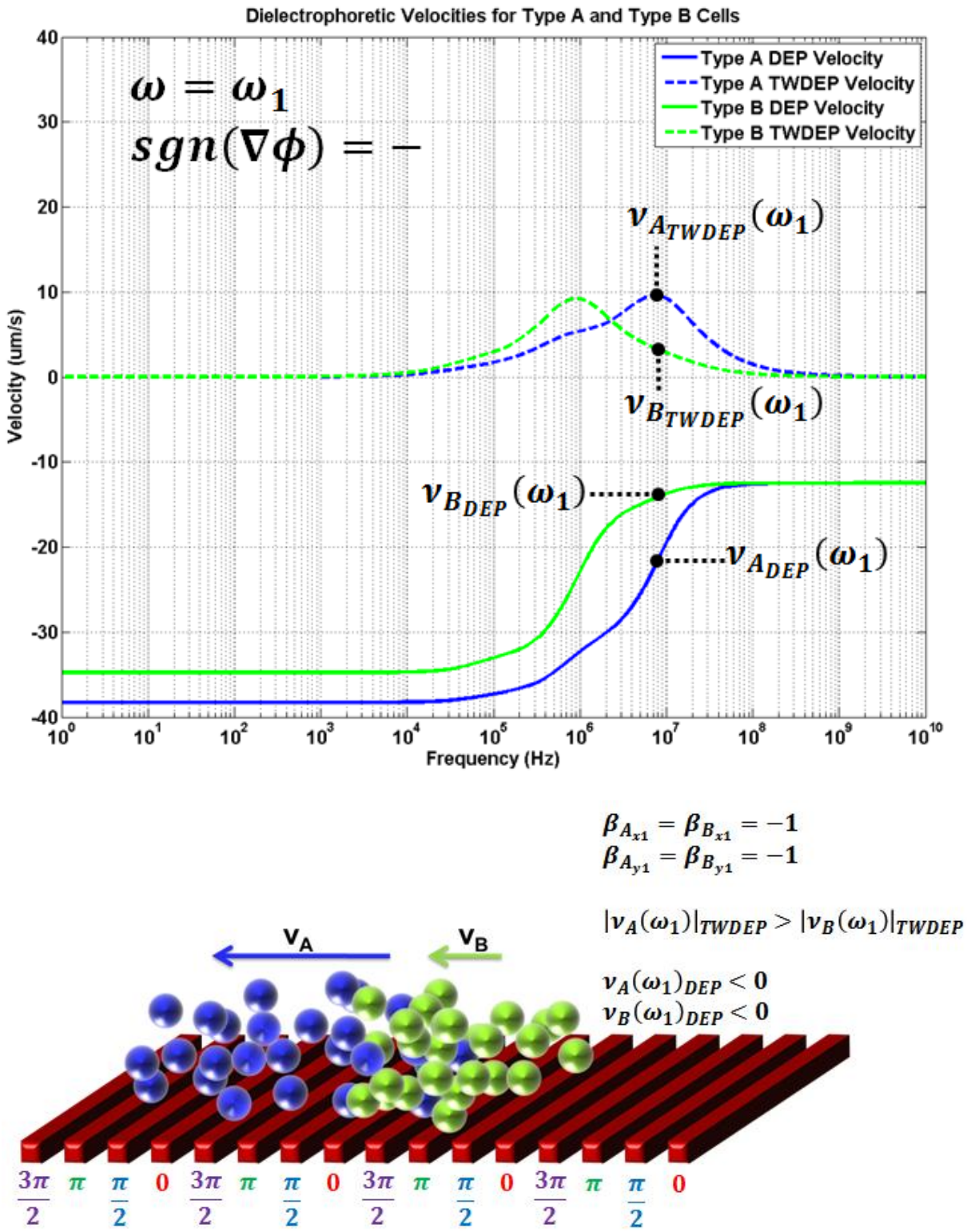

Figure 4.3 First field configuration where type A and type B cells are made to float above the electrode array and travel laterally in the direction opposite the phase gradient. A frequency is selected such that type A cells move faster than type B cells.

In the next step (figure 4.4), the configuration of the field is changed by selecting a new frequency $\omega = \omega_2$ and simultaneously changing the phase gradient such that $sgn(\nabla\phi_{x2}) = +1$. At this new frequency $Re\{K_{CM}(\omega_2)\}$ remains negative for both type A and type B cells, resulting in the variables that determine the y-velocity to be

$$\beta_{A_{y2}} = \beta_{B_{y2}} = -1 \tag{4.20}$$

and again satisfying condition of (4.16), keeping all the cells afloat above the array.

When the phase gradient is reversed in this second step, it has the effect of changing the directionality variables of for particle types, making

$$\beta_{A_{x1}} = \beta_{B_{x1}} = +1 \tag{4.21}$$

It is important to note here that $Im\{K_{CM}(\omega_2)\}$ does not change in sign for either particle type during this step, the imaginary part of the Clausius-Mossotti factor is purely a function of the particle makeup and the medium, the reversing of the phase gradient is what changes the direction of the two particle types.

Now that both type A and type B cells are traveling in the same direction, and opposite their direction of travel from the first step, the last parameter concern are the velocities at which they do so. For this second configuration, the frequency $\omega = \omega_2$ has to be carefully chosen such that

$$|v_A(\omega_2)|_{TWDEP} < |v_A(\omega_1)|_{TWDEP} \tag{4.22}$$

$$|v_B(\omega_2)|_{TWDEP} > |v_B(\omega_1)|_{TWDEP} \tag{4.23}$$

During this interval, the magnitude of the velocity for type A cells is less than it was during the previous step and the opposite is true for type B particles. By selecting such a frequency for the second configuration, we can see from equation (4.13) that requirement (4.15) has been fulfilled

during the period of time these two configurations were applied, as the average lateral velocities of the differing particle types have different signs.

To think of it in simpler terms, a sequence of fields are applied such that type A cells have a large negative x-component velocity for a specific time interval, followed by a smaller, positive x-component of velocity, making its average x-velocity over that period of time negative. The opposite occurs for type B cells, making its average x-velocity positive, thus causing the particles to have net displacements in opposite directions.

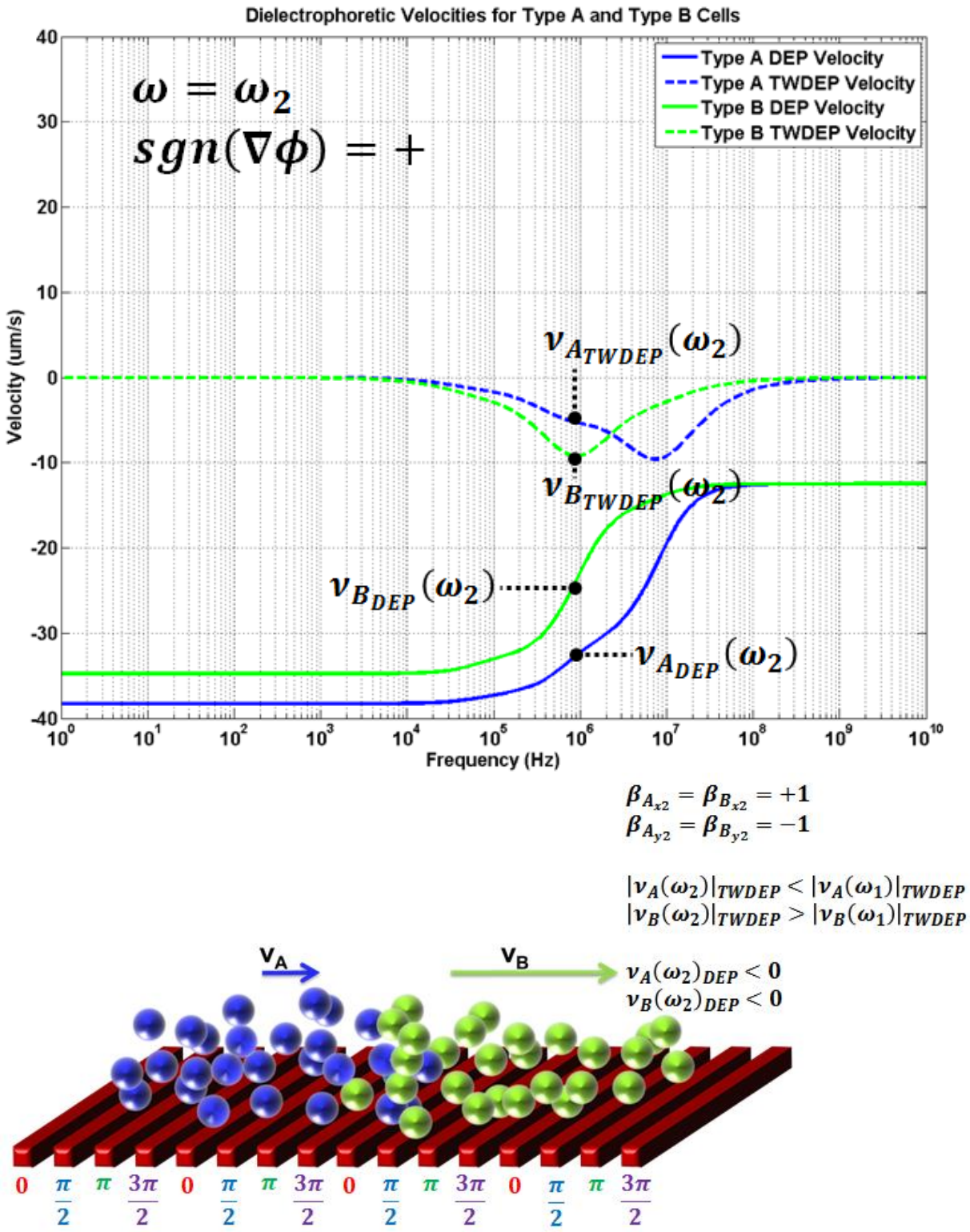

Figure 4.4 Second field configuration is applied where type A cells are made to move slower than the previous step, but in the opposite direction. Type B cells move faster than type A cells during the application of this configuration. Type B cells also move faster than they did in the previous step.

In time-multiplexing dielectrophoresis, the selected field configurations are repeatedly applied in sequence, for multiple periods. The net effect of repeatedly alternating between these electric field configurations is that the two particle types migrate over time in different directions (figure 4.5). The rate at which this migration occurs is determined by the average differential separation velocity,

$$\bar{v}_{diff} = \bar{v}_{A_x} - \bar{v}_{B_x} \tag{4.24}$$

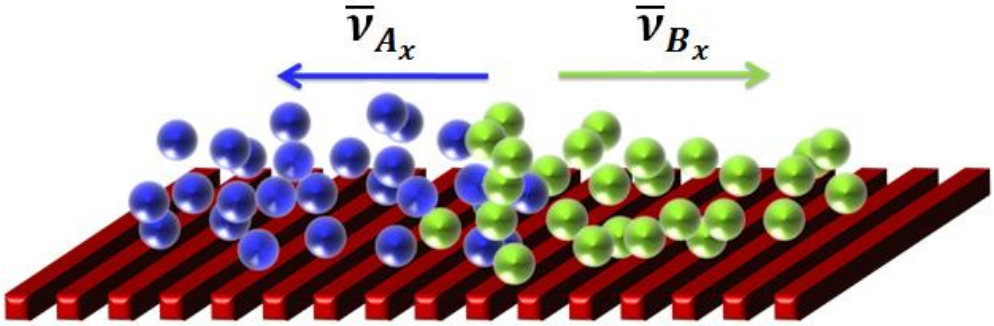

$$\bar{v}_{A_x} = D \cdot \beta_{A_{x1}} \cdot |v_A(\omega_1)|_{TWDEP} + (1 - D) \cdot \beta_{A_{x2}} \cdot |v_A(\omega_2)|_{TWDEP}$$
$$\bar{v}_{B_x} = D \cdot \beta_{B_{x1}} \cdot |v_B(\omega_1)|_{TWDEP} + (1 - D) \cdot \beta_{B_{x2}} \cdot |v_B(\omega_2)|_{TWDEP}$$

Figure 4.5 The net effect of repeatedly applying the two field configurations in sequence is that cells are made to have average net velocities in opposing directions causing them to separate from another

The actual lengths of time for which the configurations are applied (T_1 and T_2) do not have a bearing on the average differential velocity, only the ratio of them affects $\bar{v}_{diff}$ if the durations are significantly smaller than the time constants of motion for the particles. For example, in this case the *D = 50%* duty cycle used could be achieved by either having $T_1 = T2 = 1$ *ns* or with $T_1 = T2 = 1$ *s*. The minimum duration must be large enough such that the displacement of the particles due to dielectrophoresis is greater than the displacement due to the noise components described in chapter 2. In practice, this lower bound is set by the speed of the voltage switching circuitry, and is typically on the order of milli-seconds. If the duration for any

particular interval is too long, situations arise where the average lateral motion can be disrupted by horizontal component of the DEP force, which is assumed to be zero for very small distances. This issue is explored further the experimental results of chapter 8.

Particles of a particular type can be made to aggregate in a specific location by positioning dielectrophoretic trapping points near the ends of the array (figure 4.6). These traps are formed by spatially setting the phase gradient across all electrodes beyond the desired stopping point opposite to the gradient across the electrodes in the fractionation region. This creates a null region, where zero net lateral force is exerted on particles and particles that enter this region remain trapped upon entering.

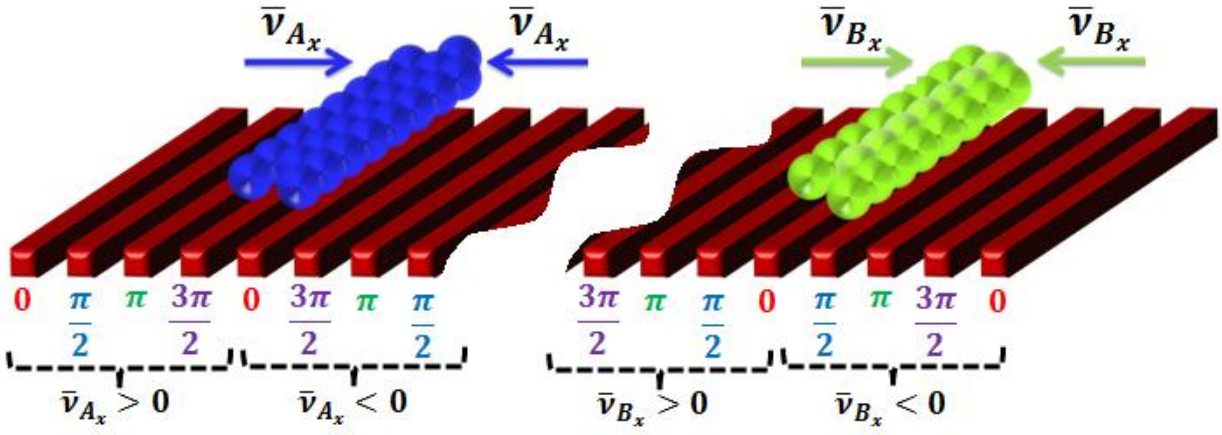

Figure 4.6 Traps for particle types are created by spatially reversing phase gradient in the trapping region with respect to the phase gradient across the electrodes used for separating. These traps are positioned at the ends of the array, so that only particles with a net velocity in the direction of a given trap collect in that region.

Looking at the advantages of our method in this case, the first becomes evident when compared to the use of dielectrophoresis affinity methods. If presented with the velocity profiles given above, or ones similar to it, it would be impossible to separate particle types by the use of an affinity method, as no frequency exists for which the signs (either the real or imaginary part of the Clausius-Mossotti factor) are opposite between particle types. There are also benefits to the time-multiplexing dielectrophoresis when compared to field-flow fractionation methods.

In this particular example the magnitude of the peak velocities due to TWDEP is on the order of 10μm/s. At the frequency for which the peak velocity occurs for each of the particles, the TWDEP velocity of the opposing cell type is approximately 5μm/s. If a field-flow fractionation method was applied, the maximum achievable differential velocity difference between the two is 5μm/s in any direction. By comparison for time-multiplexing dielectrophoresis, equation 4.13 with the duty cycle here of $D = 50\%$ reveals that time-multiplexing dielectrophoresis also achieves a separation velocity of 5μm/s. However there is one key difference, the cells are made to travel in opposing directions, which has the tangible benefits described earlier of allowing particles to remain separated and reducing the number of electrodes required to implement the device.

The ability to modulate the duty cycle provides an additional layer of control that can be taken advantage of. One may wish to separate a set of particles for which the velocity profiles do not exhibit the symmetry of the profiles presented in this example. It could be possible that a second field configuration for which conditions 4.22 and 4.23 are simultaneously met does not exist, the conditions that the first particle type moves slower during the application of the second configuration and the other particle type moves faster. For example, in this scenario if the second profile was such that type A cells moved slower than they did during the application of the first profile and in the opposite direction, but the relative speed type B cells did not increase, then the net average velocities of the two particle types would occur in the same direction. This situation can be remedied via adjustment of the duty cycle such that the durations for which the configurations are applied are not the same, adding weight to effects of one particular profile over the other. If in this scenario, the second configuration is applied for a relatively longer

amount of time, it could be that the average net velocity of type B cells could be made to change sign, while maintaining condition 4.22 for type A cells.

Another advantage of the ability to vary the duty cycle is that it can allow us to create conditions for which particles can be separated when they could not be separated using other dielectrophoresis techniques. In the example presented in this section, the cells exhibited negative dielectrophoresis at all frequencies, allowing them to remain suspended above the array while moving laterally. That will not always be the case if a particle has the ability to exhibit positive dielectrophoresis at certain frequencies and will significantly impact the ability of dielectrophoresis-based methods separate them. In the next section, we take a detailed look at this scenario via an example using models based on actual characterization data and show how time-multiplexing dielectrophoresis enables separations to still take place.

4.3 CREATING SEPARABLE CONDITIONS USING TIME-MULTIPLEXED DIELECTROPHORESIS

For some combinations of particles and mediums, there exist situations for which affinity methods or fractionation methods cannot be used to separate particles. We present such as case for the velocity profiles for live and dead yeast cells shown in figure 4.7. In this section we will first explain how our method can be used to separate these two cell types, and then explain the advantages of it over competing methods.

The velocity plots of figure 4.7 were calculated using the models for live and dead yeast cells presented in chapter 3. The parameters for the models were extracted from a best-fit analysis of experimental characterization data. The methods used to record measurements and match the data to the models is discussed in detail in chapters 5 and 6. The plotted DEP and TWDEP velocities are the expected values when the two types are cell are being manipulated by the 15μm separation electrode array using $2V_{pp}$ waveforms. The dashed lines in figure 4.7 show the TWDEP spectrums for the cells, while the solid lines show the DEP spectrums. For the profiles of figure 4.7, we wish to separate the cell types using the electrode arrangement of figure 2.5 in a space covering 16 electrodes, where each electrode is 15μm wide with a 15μm gap in between them (resulting in a total containment width of 480μm).

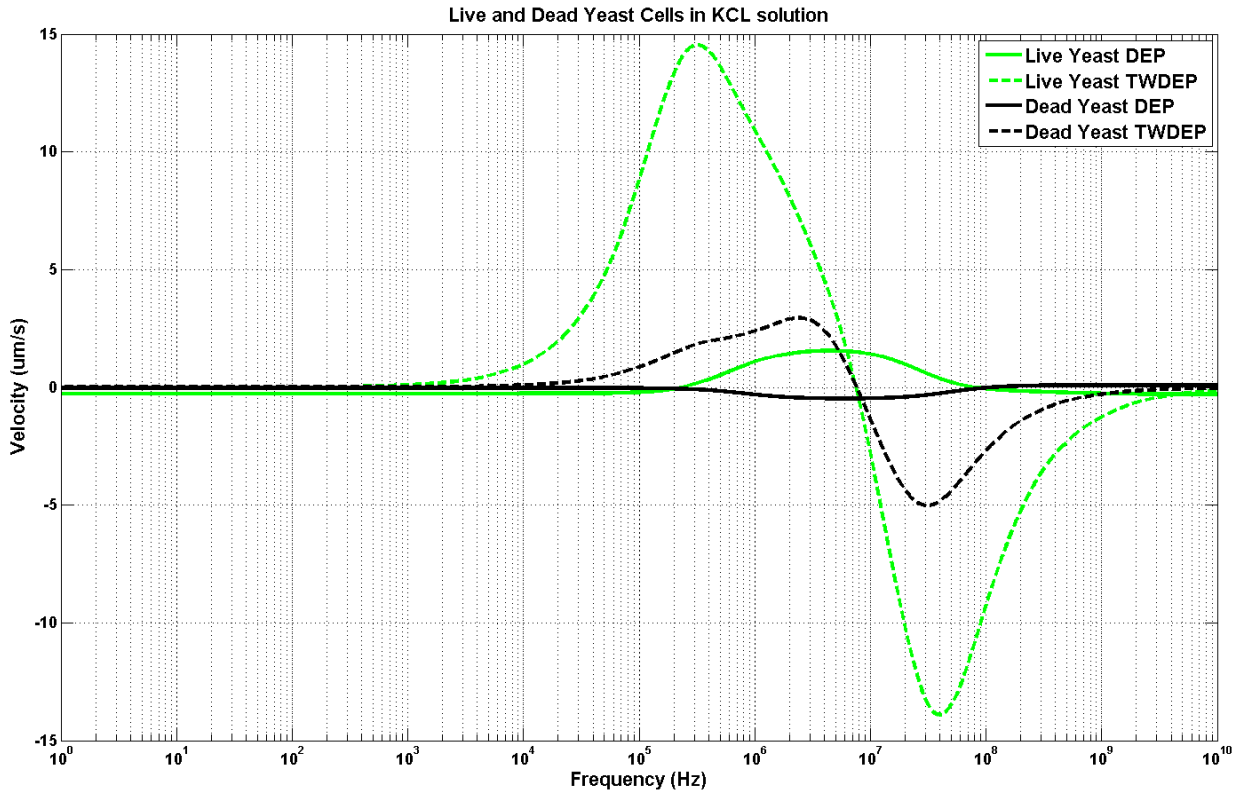

Figure 4.7 Comparison of TWDEP and DEP velocities for models of live and dead yeast cells in a 5mS/m KCL buffer solution. Models parameters for cells extracted from best-fit analysis of experimental data.

Based on these models, affinity methods could not be used to effectively separate these two cell types as there does not exist a frequency for which the TWDEP velocities are opposite in sign. There does exist a band of frequencies for which the DEP velocities differ in sign in the frequency range *200 kHz < f < 10 MHz*, where DEP velocities for live yeast are positive and DEP velocities for dead yeast are negative. However the sole application of a DEP field would not cause cells to effectively separate using the electrodes of figure 2.5. If a conventional DEP field was applied in that frequency range, living cells would be pulled firmly to the electrode surfaces and rendered immobile, and could not be directed to a specific region. Other researchers have overcome this issue by devising electrode arrangements with complex geometrical patterns that create horizontal components of DEP force [1,2,3]. However, not only

is this increase in complexity undesirable from a device implementation standpoint, these implementations also rely on careful selection of the medium and require a specifically calculated buffer that will have to be different for every pair of particle types one wishes to separate. Our methodology results in more general-purpose separation devices that accommodate changes in particle types via easily configurable parameters such as field frequency, phase and duty cycle. Additionally, in some real-world scenarios, changing the buffer may not even be an option.

Field-flow fractionation methods would also not be effective in this situation using only 16 electrodes at a 30μm center to center pitch. The maximum differential velocity for live and dead cells in a sole TWDEP field is 12.5μm/s at $f = 300kHz$, where live cells move at 14.5μm/s and dead cells at 2μm/s, in the same direction. Dead cells starting at the far end of the array could never be separated from the live cells moving toward them, and even in the best case of all the cells starting from the same position and at the beginning of the electrode array, all cells would have traversed the length of the 480μm long electrode array after a few minutes be re-mixed together. It is due to this type of limitation that fractionation electrode arrays have to be very long in length in order to effectively separate. In contrast, due to our multiplexing scheme and ability to cause directed, differential motion for each particle type, we have the capacity to carry out this separation in the 16 electrodes of this scenario.

In order to use time-multiplexing dielectrophoresis to separate the two types of figure 4.7, we have to first identify the field configurations we should multiplex between. With the objective of trying to satisfy our conditions for separability as set forth in equations (4.15) and (4.16), that the average x-velocities must be different in sign (cells types migrate apart) and that the average y-velocities must both be negative (cells elevated above array). This choice can be

made by carrying out a brute-force calculation of equations 4.13 and 4.14, the expressions for average net x and y velocities, for every possible pairwise-combination of frequencies and sequence of phase gradients at each duty cycle. One solution for the pair of cells presented in this section can be found when the multiplexing frequencies are 100 kHz and 25 MHz.

Figures 4.8 and 4.9 show close-up views of the DEP and TWDEP velocities for both cell types, evaluated at these frequencies. When the frequency of the traveling-wave field is at the frequency of the first muxing configuration $\omega_1 = 100\ kHz$, live cells travel laterally at an order of magnitude faster than dead cells ($8.78\,\mu m/s$ vs $0.85\,\mu m/s$) and in the same direction ($\beta_{live_{x1}} = \beta_{dead_{x1}} = +1$). Also at this frequency, live and dead cells both exhibit relatively weak negative dielectrophoresis velocity magnitudes of $0.23\,\mu m/s$ and $0.04\,\mu m/s$ directed upwards from the electrodes ($\beta_{live_{y1}} = \beta_{dead_{y1}} = -1$), keeping them afloat. For the second configuration frequency, $\omega_2 = 25\ MHz$, live and dead cells have lateral traveling-wave velocities of $12.15\,\mu m/s$ and $4.88\,\mu m/s$ in the direction opposite that of the first muxing configuration $\left(\beta_{live_{x2}} = \beta_{dead_{x2}} = -1\right)$. The magnitude of the vertical dielectrophoresis velocities at 25 MHz are $0.78\,\mu m/s$ and $0.38\,\mu m/s$ for live and dead yeast. The direction of the dielectrophoresis forces on dead yeast is negative at *25MHz* $\left(\beta_{dead_{y2}} = -1\right)$, elevating them above the array. However, the direction of the vertical force component on live yeast is positive

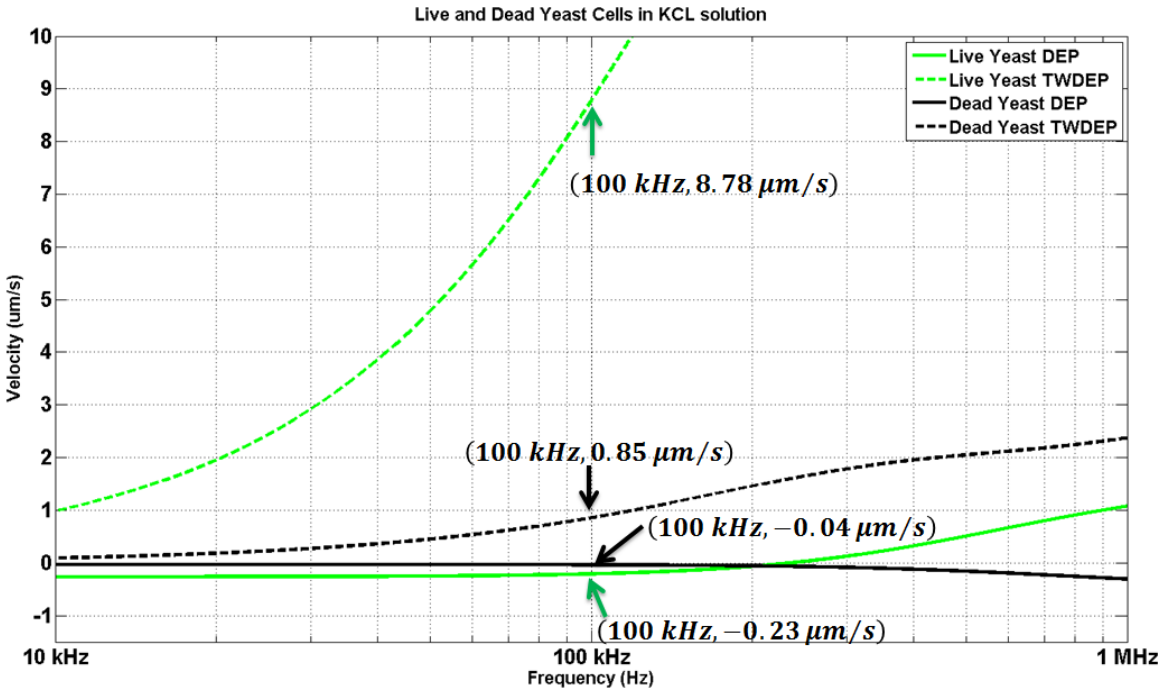

Figure 4.8 Close-up view of DEP and TWDEP spectrums for live and dead yeast cells. The plot is centered around the frequency chosen for configuration #1, *f = 100 kHz*, and shows the velocities evaluated at this frequency

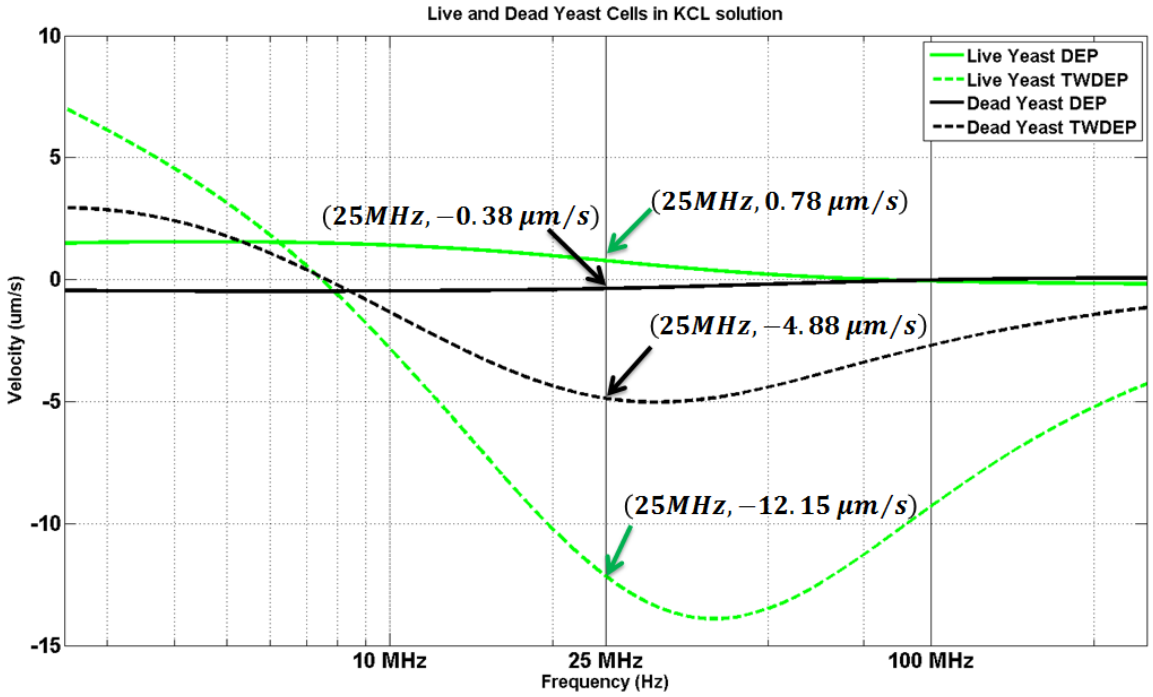

Figure 4.9 Close-up view of DEP and TWDEP spectrums for live and dead yeast cells. The plot is centered around the frequency chosen for configuration #2, *f = 25 MHz*, and shows the velocities evaluated at this frequency

at *25 MHz* $\left(\beta_{dead_{y2}} = +1\right)$, causing cells of that type to be attracted towards electrodes at the bottom of the chamber.

The primary point of interest for this combination of frequencies is that at *25 MHz*, as well as for the majority of the DEP spectrum of live yeast, the cells have strong positive dielectrophoresis forces exerted on them that disrupt their ability to be separated. By using our technique, we can multiplex and adjust the duty cycle *D* such that the weak negative forces exerted on live yeast at 100 kHz can be made to average out the effects of the positive forces exerted on them at *25 MHz*, thereby keeping them afloat at all times. Figure 4.10 shows the average net DEP velocity on live and dead yeast cells when multiplexing between these two configurations as a function of the duty cycle.

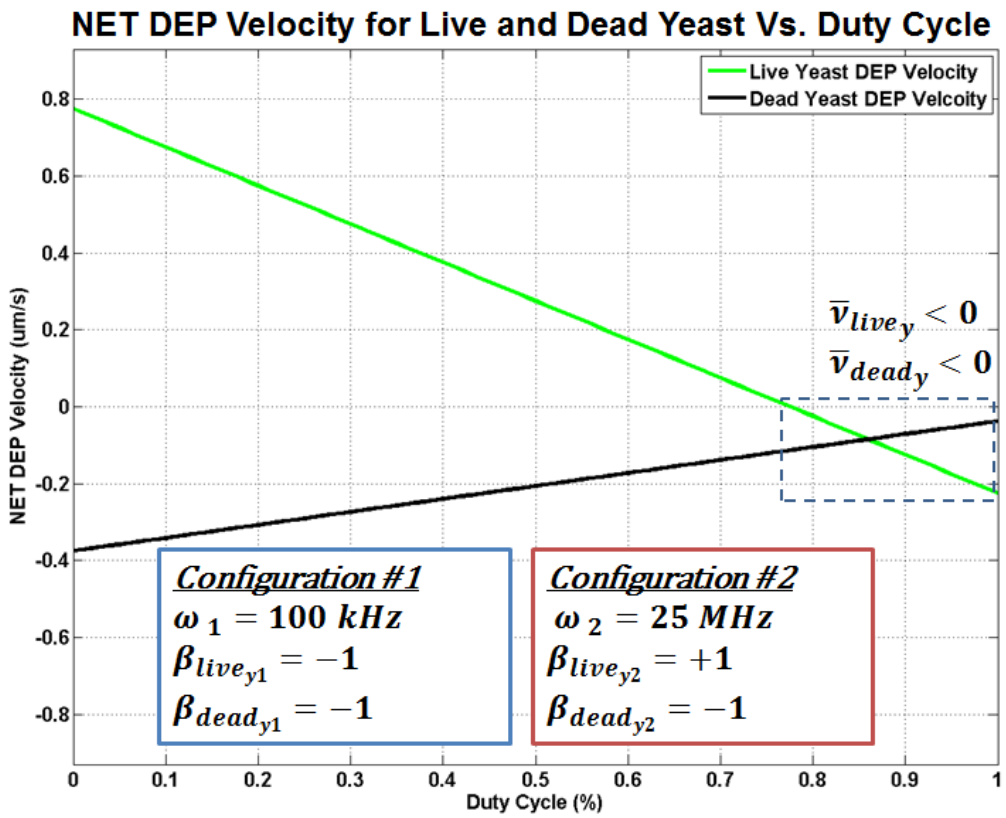

Figure 4.10 Average y-velocity after multiplexing as a function of duty-cycle. The average velocity due to DEP for live yeast is negative when the duty cycle ranges for 75% < D < 100%.

Not until the duty cycle reaches $D = 0.78$ (i.e. *100 kHz* field applied 78% of the time and *25 MHz* field applied 22% of the time) are the negative forces are able to average out the positive forces exerted on live yeast, making the average y-component of velocity $\bar{v}_{live_y} \leq 0$. Since the average y-component for dead cells is negative at all frequencies, condition 4.16 can be said to be fully satisfied when $0.78 < D < 1$, making both cell types simultaneously levitate above the array.

Figure 4.11 shows average net velocity due to TWDEP for live and dead yeast when multiplexing between the same two frequencies, 100 kHz and 25 MHz, as a function of duty cycle. As duty cycle increases, the effects of the first configuration become more pronounced and both average x-velocities increase towards $0\,\mu m/s$. Since the rate at which the TWDEP

velocity increases is higher for live cells, it reaches a zero-crossing sooner than the dead cells, when $D = 58\%$, giving the average net velocities the cell types different signs. The average x-velocity for dead cells remains negative until $D = 85\%$, after which it has the same sign as the average x-velocity for dead cells. Therefore, the range of duty cycles for which condition 4.15 is satisfied, that the average net x-velocities are opposite in sign so that particles migrate apart, is satisfied for the range of duty cycles covering $58\% < D < 85\%$.

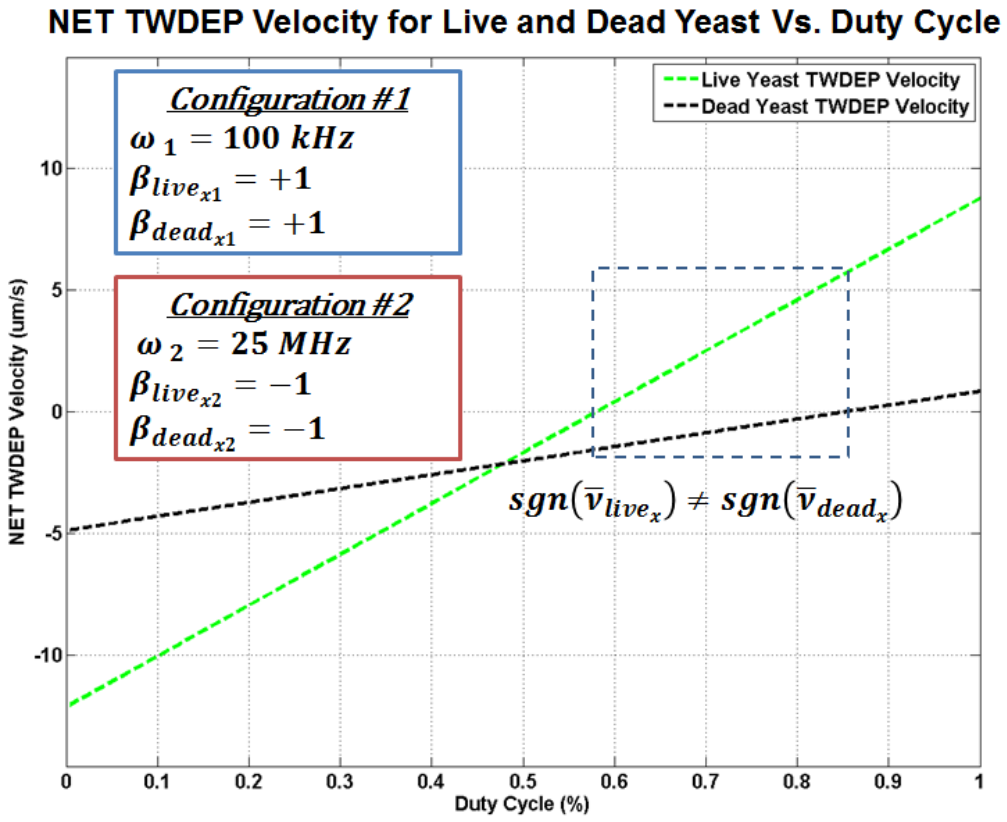

Figure 4.11 Average net x-component of velocity after multiplexing, plotted as a function of duty-cycle. The net TWDEP velocity of live yeast cells and dead yeast cells are made to be opposite in sign when the duty cycle ranges for 58% < D < 85%. The overlap of this range and the duty cycle range of figure 4.10 yield values of D for which the particles can be separated, 58% < D < 78%. .

The duty cycle is parameter that when varied cannot independently affect either just the the average net x or y-velocity. Therefore, the duty cycles for which both conditions for separability are met lie within the overlap of the previous two calculated ranges, $58\% < D <$

78%. From this example, it can be seen that conditions in which the two cell types were inseparable could be overcome by time-multiplexing dielectrophoresis fields and allow them to be separated from one another.

This set of particles has an unique feature in that their lateral directions of movement, β_{live_x} and β_{dead_x}, can be made to change sign not only by changing the phase gradient, but also by changing the frequency. This feature can be taken advantage, making it only necessary to multiplex frequency and not phase in order to change particle directions. It should also be noted that the particular solution of muxing configuration parameters presented in this section is not the only possible solution that satisfies the conditions for separability. Other solutions for this pair of particles and for every combination of particles included in our library are presented in chapter 7. However, as shown in the results of chapter 7, the only solutions where the separation criteria can be met are when time-multiplexing dielectrophoresis is applied, further highlighting the utility of our method. In the next section, we take a look few more additional advantages and practical benefits of time-multiplexing dielectrophoresis.

4.4 ADDITIONAL ADVANTAGES OF TIME-MULTIPLEXING DIELECTROPHORESIS

There are a number of practical advantages to carrying out separations using time-multiplexing dielectrophoresis. The first of which is that time-multiplexing dielectrophoresis allows for the realization of lab-on-chip platforms that can discriminate between species with finer resolution and using fewer electrodes than other devices. Devices that separate particles based on field flow fractionation techniques are electrode limited. If the difference between particle types is very small, then their velocities are similar. Therefore, when using conventional methods, the number of electrodes they would have to traverse before they achieve any reasonable separation distance between them occurs could turn out to be so large that it would be impractical to implement on a lab-on-chip.

For example, we can consider a hypothetical lab-on-chip technology in which electrodes can be fabricated with a center to center pitch of 100 μm used to realize a field flow fractionation device. If the two particle types we wish to fractionate are very similar, and have have nominal x-component velocities of 10 μm/s and 11 μm/s, a 10% difference, the differential speed between them would be 1 μm/s. If for this scenario the requirement is that there is at least 1 mm of separation between the two particle types, it would take 1,000 seconds of travel before that requirement is met. After 1,000 seconds, the faster of the particles will have traversed a distance of 11mm, requiring at least 110 electrodes. In contrast, using our proposed technique, the two particle types can meet the separation requirement using as few as 12 electrodes, 4 for muxing, and 8 to generate traps on each side. This advantage is demonstrated further by way of examples in chapter 7. In addition, field flow fractionation methods are not scalable; so as the difference

between the particles gets smaller, more electrodes have to be added in order to accommodate the time it takes for them to separate.

Another clear advantage to our technique is that it removes restrictions on the buffer solution used to contain the samples. As discussed in the previous chapter, dielectrophoresis affinity separation methods require that the conductivity of the buffer solution be adjusted such that the Clausius-Mossotti factor will have opposite signs for the two types. We eliminate this limitation by making travel in opposite directions occur by modulation of phase gradients. If the differences between types is too small, it would be extremely difficult to prepare a solution with enough precision such that its conductivity will be greater than one particle type and less than the other (i.e. $\sigma_A > \sigma_m > \sigma_B$) since it would be such a narrow range.

Even if one could titrate such a solution, it would be impossible to sort a sample that contains more than two particle types. If we think of a case of three particles where $\sigma_A > \sigma_B > \sigma_C$, then the solution conductivity, σ_m, cannot meet the requirement of simultaneously being in between both ranges (i.e., the ranges $\sigma_A > \sigma_m > \sigma_B$ and $\sigma_B > \sigma_m > \sigma_C$ can never be satisfied for a single value of σ_m in the aforementioned case). In contrast, our technique can be extended to accommodate such complex particle mixtures by concatenating additional array segments for each type introduced and then reapplying the separation method after each bifurcation. Figure 4.7 shows the imaginary parts of the Clausius-Mossotti factor for four different particle types that reside in the same buffer, resulting in four different crossover frequencies (ω_A, ω_B, ω_C and ω_D). In this case, at frequency ω_{AB} particle types A and B travel near the same velocity and faster than particle types C and D. The opposite is true at frequency ω_{CD} which means that these two frequencies could be used with our technique to bifurcate the four particles types into two

groups. Reapplying the technique on the separated groups will allow them to be further fractionated into subgroups.

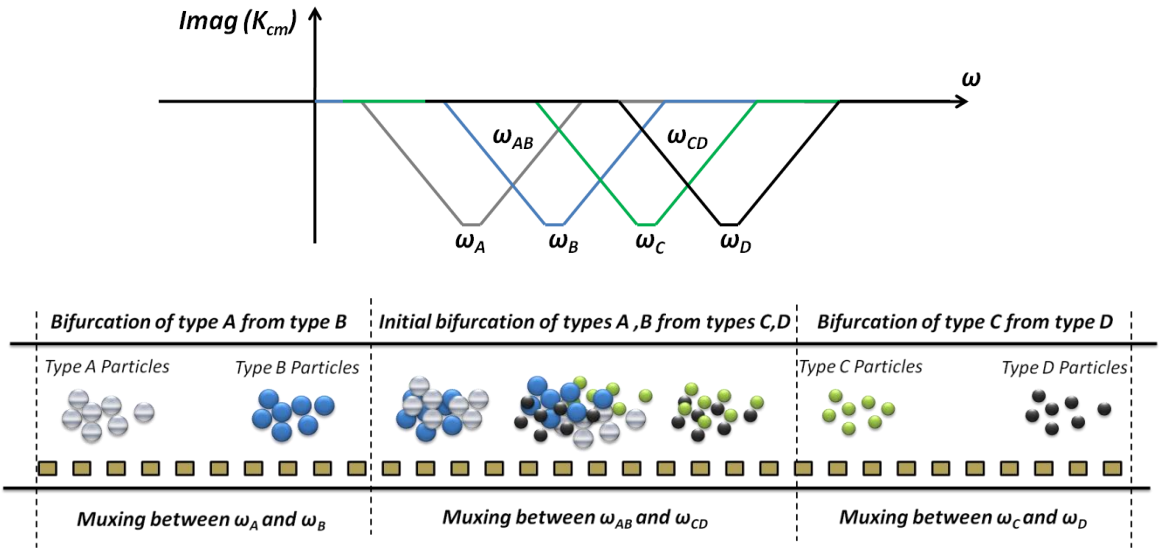

Figure 4.12 Time-multiplexing dielectrophoresis use to fractionate sample containing more than just two distinguishable particle types, a case that is impossible using affinity methods.

One final benefit to the technique comes from it being based on differential forces. Since the particles being separated from one another reside in the same medium, they feel the effects of fluid velocity, v_m, equally. Therefore, due to the differential nature of the forces exerted, unwanted effects that occur from externally imposed flows or imbalances in the device are mitigated to a certain extent, loosening the requirements on the microfluidics. In like manner, any common-mode noise components in the system that act on all particles equally, such as noise from the voltage supplies, have less bearing on separations as they are effectively canceled out.

Figure 4.13 shows the plan we used to experimentally demonstrate our technique and its effectiveness. After we established our preferred models and theory, we designed a corresponding hardware lab-on-chip platform to validate the models and implement our technique. This platform required two types of devices: one device to characterize particles and

measure their responses and one device with the capacity to carry out the time-multiplexing of dielectrophoresis fields. Both designs were primarily driven by finite element-analysis simulations of the electrodes and the forces that could be generated by them. As a result of these simulations, we finalized the desired electrode geometries had the electrodes fabricated. These microelectrode structures then had to be packaged and interfaced to microfluidic structures to deliver and contain the samples under test. After the devices were ready for testing, we first used the characterization device to measure the responses for the five particle types included in our library, and carried out a best-fit analysis on the results to extract accurate model parameters. Using these refined models we carried out a detailed analysis of the ability of our technique to separate each pairwise combination of particles. Finally, as a result those analyses, time-multiplexing field configurations with the ability to exert differential forces on particles were identified and tested.

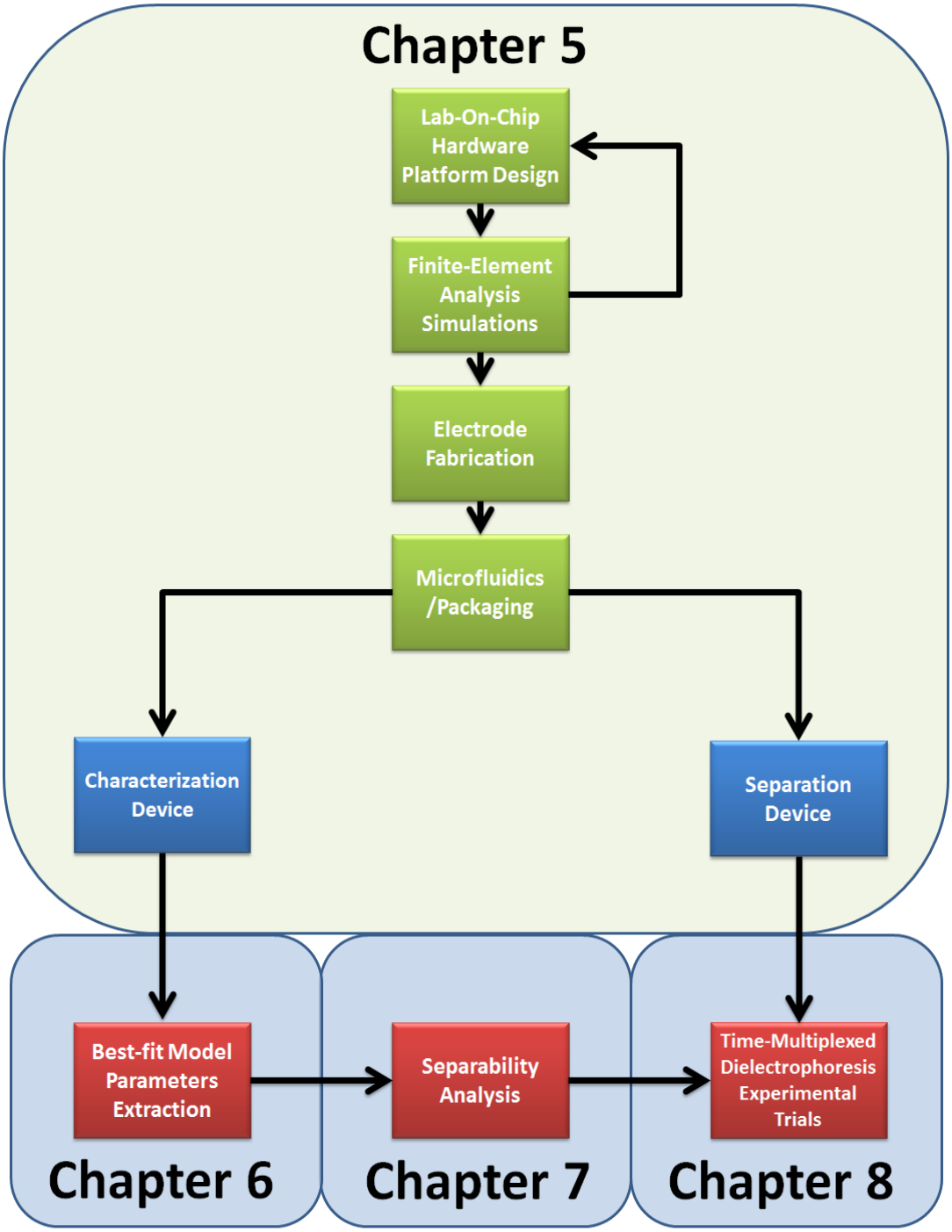

Figure 4.13 Experimental work plan used to evaluate the time-multiplexing dielectrophoresis methodology

Now that we have presented our technique and the advantages it has to offer over conventional dielectrophoresis separation methods, in the next section will show our designs for a hardware lab-on-chip platform that can be used to carry out time-multiplexing dielectrophoresis.

5.0 EXPERIMENTAL DESIGN: LAB-ON-CHIP HARDWARE PLATFORM

In order to experimentally evaluate our technique, we designed and implemented a custom lab-on-chip hardware platform. Figure 5.1 is a conceptual illustration of the platform, and shows some of the higher-level key features we set forth as goals during the design process. The two main functions of the platform are to be able to first, characterize the dielectrophoretic responses of particles and then secondly, use that information to carry out separations on particle mixtures.

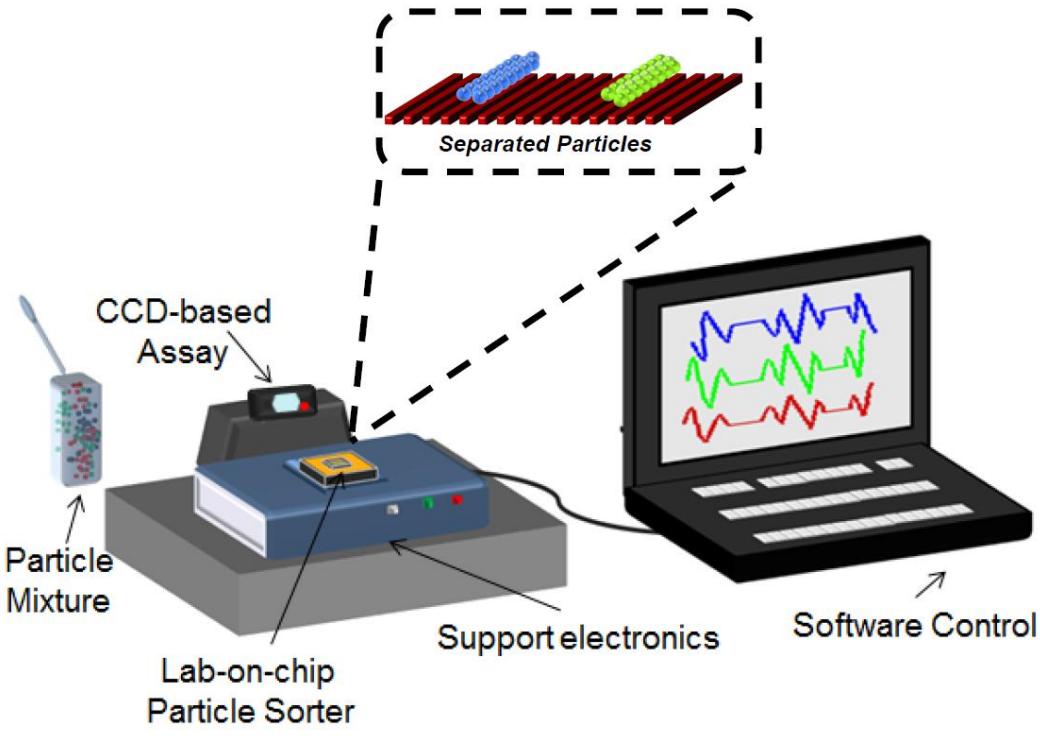

Figure 5.1 Conceptual depiction of lab-on-chip hardware platform. Lab-on-chip device is used to characterize and separate particle samples delivered via a microfluidic interface. Signal generation electronics are used to create time-multiplexing dielectrophoresis fields and results of separations are captured by a digital imager.

The central hardware component necessary for either characterizing or separating particles are the electrodes which require interfaces in order to drive the voltages on them. In addition, the particle samples we wish to experiment with reside in liquid mediums and have very little volume. In order to accommodate these small samples, microfluidic structures have to be designed that allow their transport and containment. Since the voltages used to drive electrodes are not static, it is also necessary that the supporting electronics have the ability to generate voltages of varying frequency, phase and amplitude. To implement the time-multiplexing scheme, these waveforms have to be able to be switched very quickly and the spatial assignment of waveforms to electrodes has to configurable within the array. The data that results from experiments using this platform is visual in nature so a mechanism for imaging particle motion taking place within the region around the electrodes is also necessary. Finally, while not critical to the operation of the design, we wish to design a platform that has straight-forward graphical user-interface that masks the complicated time-multiplexing dielectrophoresis details from the end user.

All of the requirements above constitute the primary design goals we set out to achieve for our lab-on-chip platform. In the sections of this chapter, we describe in detail how we met these goals and give the implementation details for each part, starting with the electrode structures.

5.1 DIELECTROPHORESIS ELECTRODES

The electrodes used for dielectrophoresis are the central components to the platform and everything else in the design stems from them. One of the large appeals of dielectrophoresis lab-

on-chip devices is their simplicity. The primary components are electrodes, which are nothing more than conductors patterned onto a substrate. In this first subsection, we discuss the operating principles behind both electrode structures and the design features we chose. The hardware platform uses electrodes of two types: quadrupole electrode structures for characterizing particles, and linear electrode arrays for separating them. In the following sections we give the design and fabrication details for them

5.1.1 Quadrupole Characterization Electrodes Design

The electrode geometry we selected for characterizing the response of particles is commonly referred to as polynomial or quadrupole electrodes [25,51] and is shown in figures 5.2 and 5.3. The quadrupole structure consists of 4 electrodes with chamfered edges, equally arranged on four sides and separated by gaps of equal spaces. What makes this structure ideal for characterizing particles is that the same device can be used to characterize both the DEP and TWDEP responses of a particle, with only a change of the phases of the voltages on the electrodes.

Figure 5.2 shows the phase configuration used to measure the DEP velocity spectrum of particles. In this configuration, two out-of-phase voltage signals are required and are assigned to drive the four electrodes such that any two neighboring electrodes are 180^{o} apart. Simulations of the fields generated from this configuration are shown in the next subsection. However in general, this configuration creates an electric field pattern in which the field strength becomes increasingly intense in the directions toward the electrode gaps. As a result of the gradient of the field, particles undergoing positive dielectrophoresis will be pulled towards the gaps, and particles undergoing negative dielectrophoresis will pushed towards the center of the quadrupole,

where the field gradient is zero (figure 5.2). Observing the velocity at which particles move towards the gaps or center of the quadrupole versus frequency provides an indirect way of measuring the DEP force exerted on each particle.

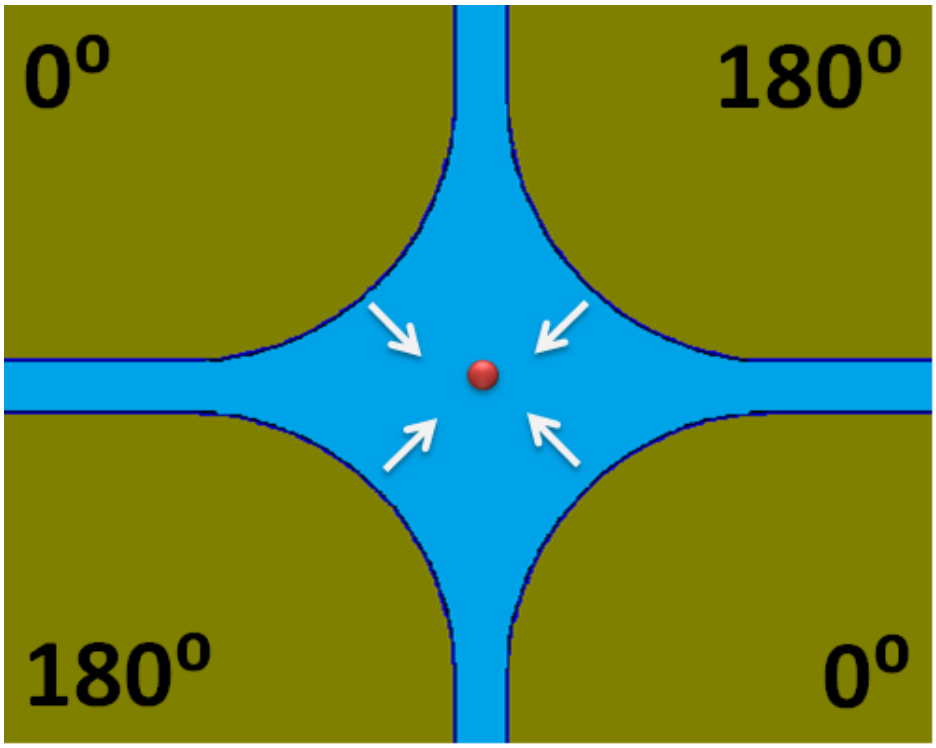

Figure 5.2 Quadrupole electrodes with voltages configured to make a DEP characterization field. Particles undergoing nDEP will be pushed towards the center, while particles undergoing pDEP will be pulled towards the gaps. The DEP force exerted on a particle can be measured indirectly by observing its velocity.

Figure 5.3 shows the voltage phase assignment used to measure the TWDEP velocity spectrum of particles. In this configuration, voltage signals are assigned to drive the four electrodes such that neighboring electrodes are 90° apart in phase. This configuration creates a rotating electric field pattern. The dipole moment of a particle place in this field is circularly polarized and this circularly polarized moment rotates in synchronization with the field. The polarization of the particle lags behind the rotation of the field, generating a torque on the particle and causing it to rotate. This effect is also commonly known as electro-rotation, and the

velocity due to electro-rotation is directly proportional to the TWDEP force. Measuring the time a particle takes to orbit around its axis of rotation provides an indirect way of measuring its TWDEP velocity.

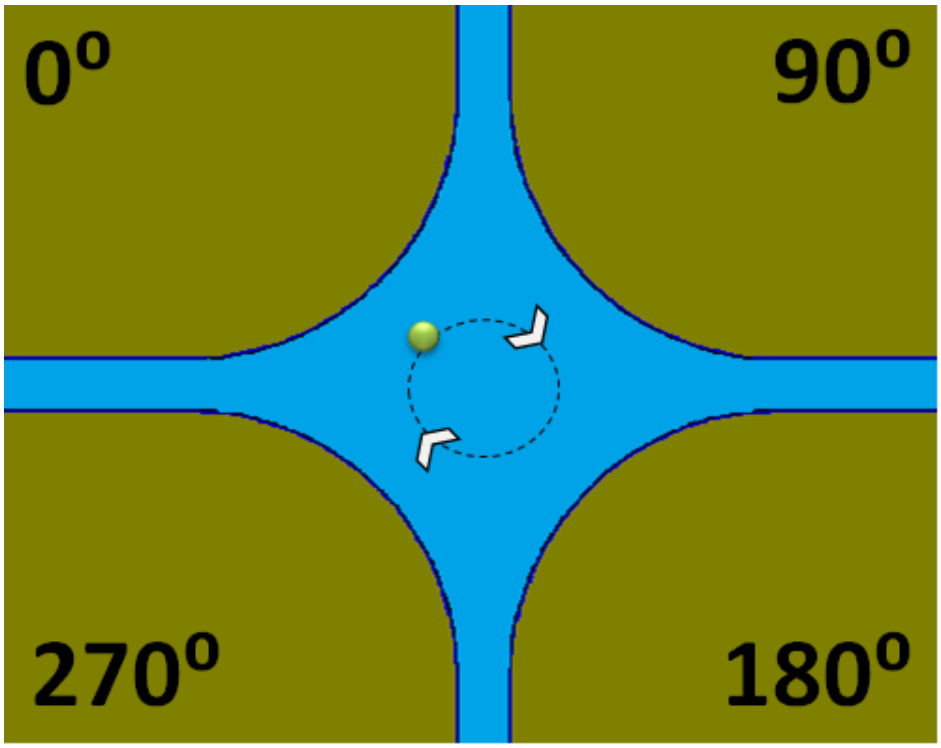

Figure 5.3 Quadrupole electrodes with voltages configured to make a TWDEP characterization field. Particles become circularly polarized and rotate. Measurement of the particles orbital velocity allows TWDEP forces to be indirectly observed.

Before having these quadrupole electrode devices fabricated, we verified our designs by using commercial finite-element analysis simulation software to calculate the fields the electrodes could generate and the forces they could exert on particles. Knowledge of these forces allows us to determine what the critical electrode dimensions should be in order to be able to successfully characterize particles. In the subsection to follow, we present simulation results for the quadrupole electrodes.

5.1.1.1 Finite-Element Analysis Simulations of Quadrupole Characterization Electrodes

Figure 5.4 shows the 2D simulation model for the quadrupole electrodes we created using the ANSYS (formerly ANSOFT [55]) Maxwell electromagnetic field simulation software. Maxwell uses the finite element method to solve for static fields. There are two critical design parameters when designing the quadrupole, the gap spacing between neighboring electrodes and the filet distance starting from the corner of the electrode.

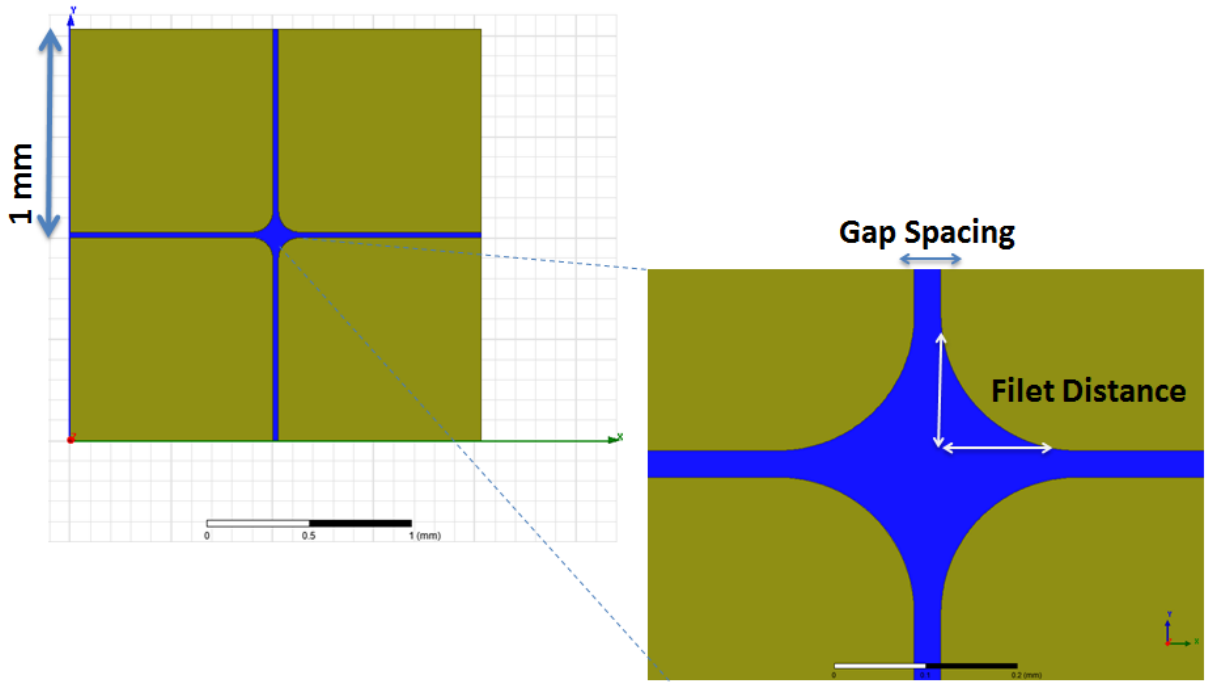

Figure 5.4 Quadrupole electrodes with voltages configured to make a DEP characterization field. Particles undergoing nDEP will be pushed towards the center, while particles undergoing pDEP will be pulled towards the gaps. The DEP force exerted on a particle can be measured indirectly by observing its velocity.

Equation 2.4 reveals that the DEP force exerted on a particle is proportional to the cube of its radius. Since these particles are very small, the force has to be made large via the electric field intensity. There are two ways to increase the intensity of a field created by electrodes: decrease the gap size or increase the voltage. We desire to use in our design readily available,

high bandwidth, low voltage signals on the order $2V_{pp}$ to $4V_{pp}$ and this requirement determines the upper bound on the maximum gap spacing. The other requirement for the dielectrophoresis electrodes is that the gap spacing be bigger than the particles themselves, otherwise the degree to which the field magnitude changes over the diameter of the particle is large and the dipole approximation no longer holds true [56]. Figure 5.5 shows simulation results of one of the quadrupole devices when the electrode voltages are in a two-phase DEP characterization configuration and the filet distance is varied.

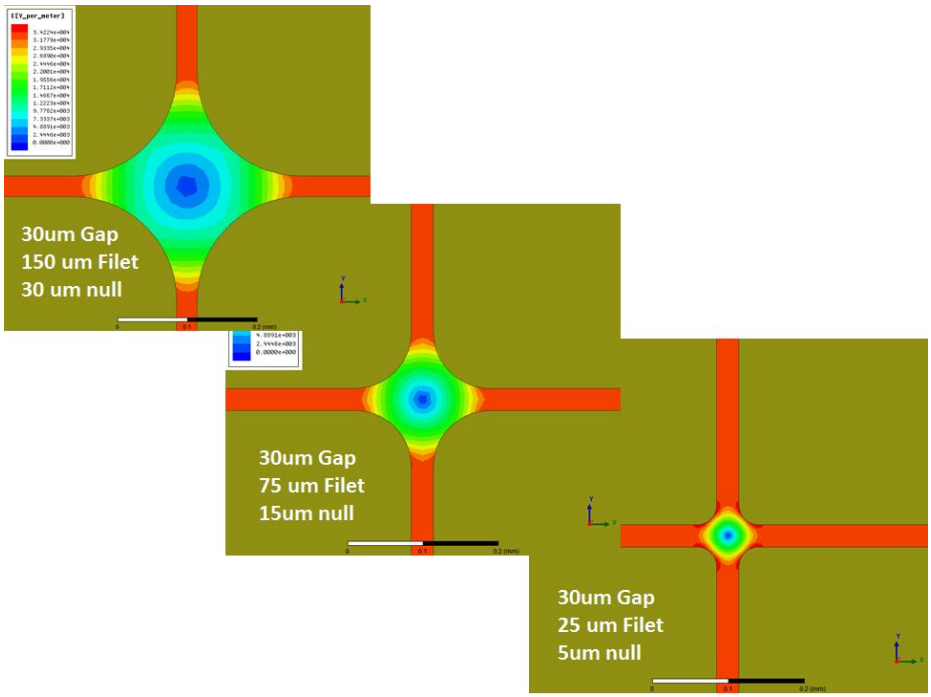

Figure 5.5 Simulations of quadrupole electrodes electric field magnitude with 30μm gap and varying filet distances when configured to characterize DEP velocities of particles

We desire particles move at a minimum of approximately 1μm/s when placed in the field. This threshold value was selected based on experimental observations that velocities much slower than that are difficult to visually discern in a reasonable amount of time. We based the requirements of our simulations on the 6μm PS-COOH microspheres models of chapter 3 as particles of that type will feel the lowest amount of force out of our those in our particle library.

Using the previously mentioned requirements and the velocity equation of 4.4 to drive the simulations, we determined from the simulations that an appropriate field magnitude could be generated by using electrode gap spaces in the range of 15μm to 30μm using the given voltages of 2 V_{pp} to 4 V_{pp}. Figure 5.5 also shows the effect of varying the filet distance. As the filet distance becomes larger, the electric field null region in the center of the electrodes also becomes larger, increasing the size of the location particles undergoing nDEP are directed to. The importance of this null region is that it determines how many particles can be stably held in the center region by nDEP forces. If the null is too large, it is difficult to accurately characterize individual particles as large numbers of them will clump together when drawn in. Using the low-end voltage range and the electrode gap size corresponding to the weakest fields (30μm), this null region varies from approximately 5μm to 30μm in diameter as the filet distance goes from 25μm to 150μm. This can only contain a few particles if they are of the size range of the ones included in our particle library.

Figure 5.6 shows simulations results when the quadrupole electrodes are placed in their TWDEP characterization mode. When characterizing TWDEP, the phase difference between neighboring electrodes is smaller (90^0 vs 180^0), therefore the voltage difference across gaps is smaller and the field magnitude is less, however for the electrode dimensions selected, enough force can be generated to manipulate 6μm PS-COOH microspheres.

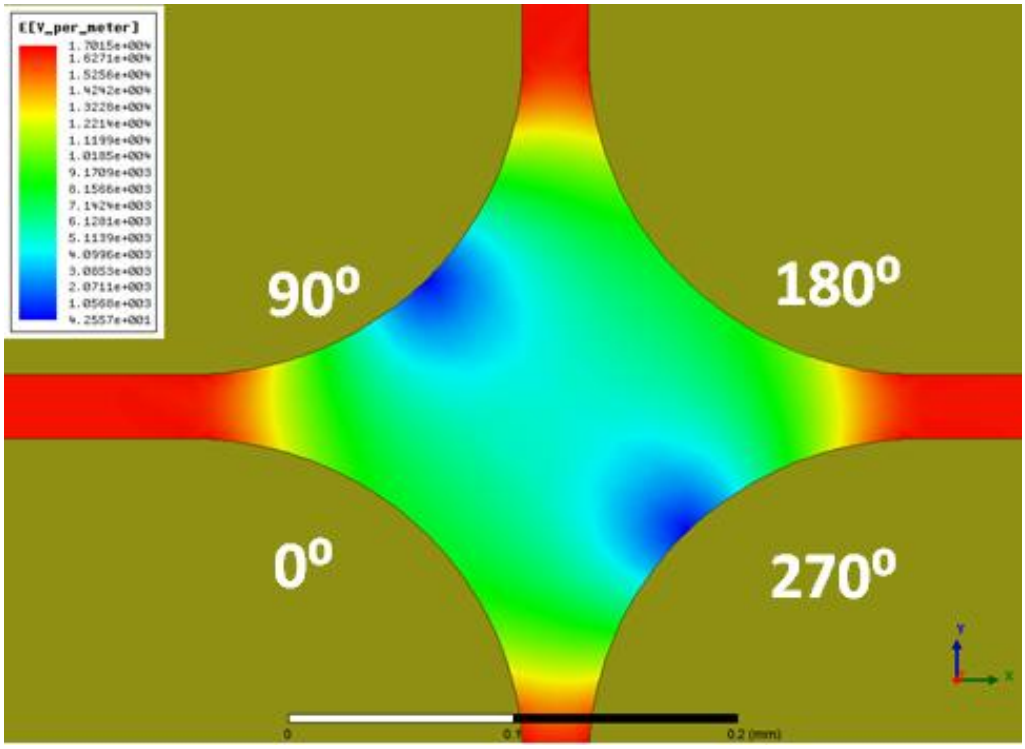

Figure 5.6 Simulations of quadrupole electrodes electric field magnitude with 30μm gap and 150μm filet distances when configured to characterize TWDEP velocities of particles

In addition to the use of simulated field-magnitudes to estimate force using analytical equations, we also wish to have an accurate expectation of the transient behavior of particles being manipulated by these fields. In order to do so, we employ the use of another commercial simulation package, COMSOL [57]. The COMSOL particle tracing module uses the finite-element method to predict the motion of particles due to dielectrophoresis. Figure 5.7 shows the 3D COMSOL model we constructed for the purposes of observing particle motion while in a DEP characterization field. The COMSOL software currently only calculates DEP forces exerted on particles using the homogenous particle model, which is not sufficient for our needs. As a result, we added custom modifications so that the software could incorporate the effects of other permittivity models.

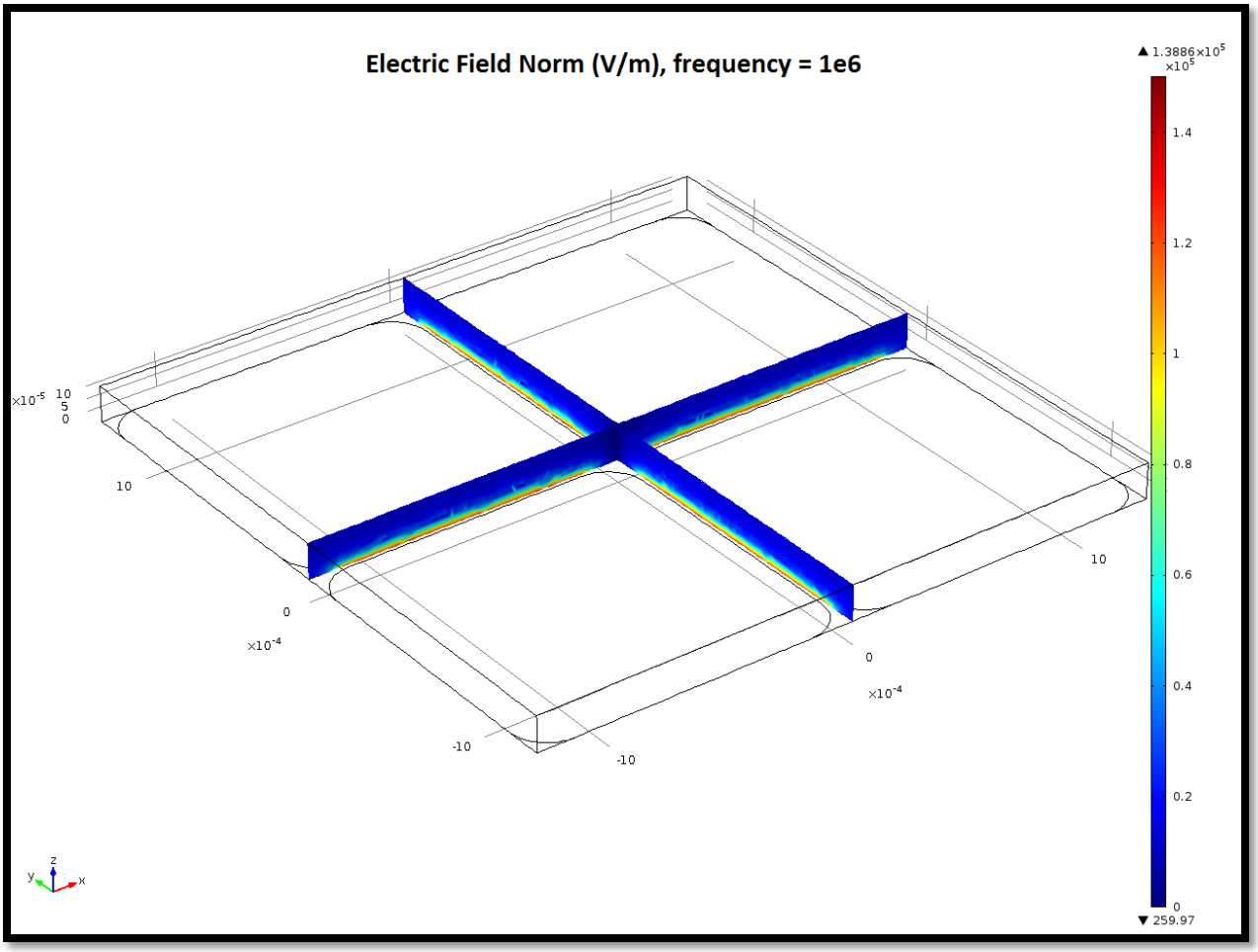

Figure 5.7 3D simulation model of quadrupole electrodes. Slice-plot shows electric field magnitude when device is configured in DEP characterization mode.

The parameters used for these simulations were voltage magnitudes of $2V_{pp}$ @ 1MHz, 30µm gap spaces, 150µm filet distances. The multi-slice surface plots of figure 5.7 show the electric field magnitude profile. Figure 5.8 shows the initial random distribution of particles for the transient part of the simulation. The particle models used was the 6µm PS-COOH model of chapter 3 in the same 5mS/m reference medium. This combination of parameters represents the worst-case conditions for generating enough force to manipulate these particles using our device.

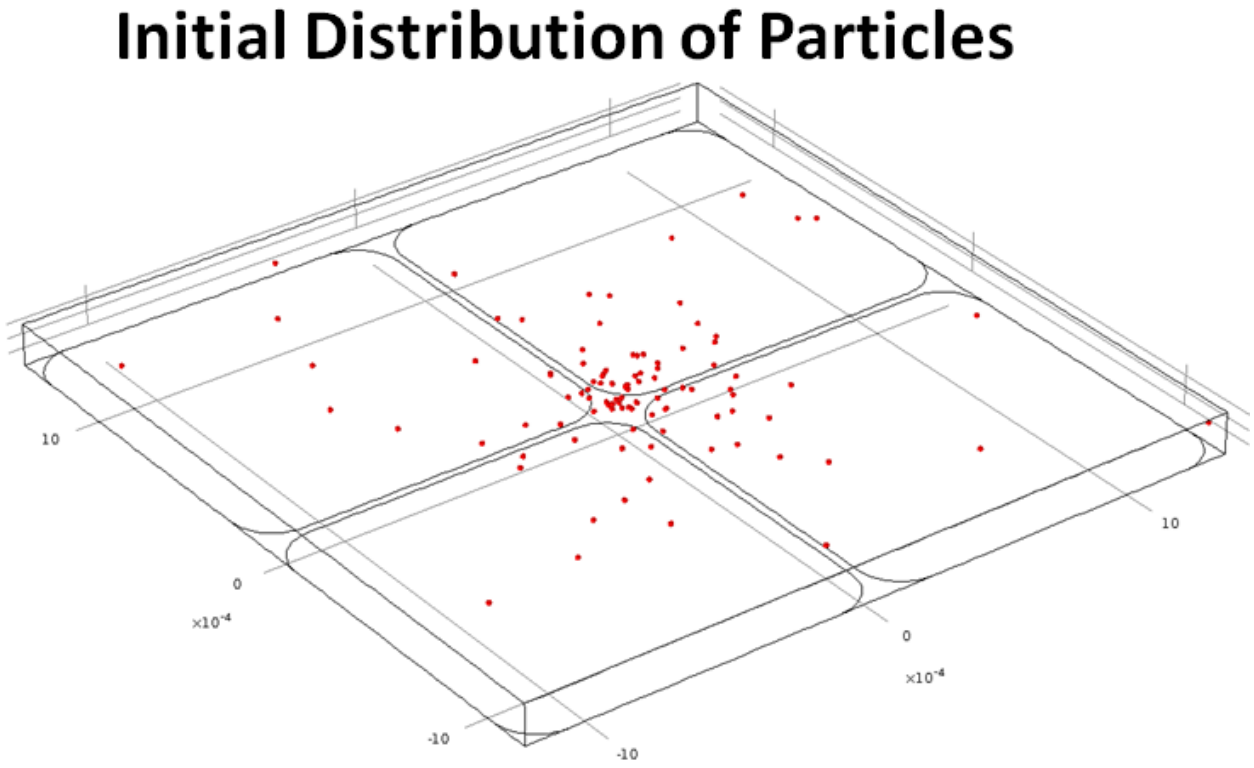

Figure 5.8 Initial distribution of 6μm PS-COOH microsphere models at time t = 0

Figure 5.9 shows the distribution of particles after a 60 second application of the 1 MHz DEP characterization field. At this frequency, 6μm PS-COOH microspheres undergo negative dielectrophoresis. As a result, particles whose location is initially near the center of the quadrupole are pushed further inwards until they reach the null region and remain trapped. Particles outside of the center region or initially at too high of a depth, are repelled by the intense fields generated between the gaps. It is not possible to determine how many particles can stably be trapped in the center using this software as particle-particle interactions are not included. Particles that are initially far away from both the gaps and center have no DEP exerted on them and just sink due to gravity. However from this simulation, we can get an accurate prediction of whether or not a reasonable amount force can be exerted on these particles using the selected

geometries. The average velocity of the particles depends highly on their initial location in the DEP field, but it was confirmed that particles on average do not travel at less than 1μm/s when starting near the center region. In addition, these simulations revealed that while for the quadrupole the primary design parameters are the gap spacing and filet distance, the overall size of the electrode cannot be ignored as well. If the electrodes are made too small, then the opposing corners of an individual electrode are close enough to the gap to change the shape of the field. As a result, we arrived at electrode of sizes 5mm x 5mm that are sufficiently large enough to prevent those unwanted effects. In chapter 6 we show how we use these devices to characterize the particles in our library.

In the next section, we present the design and simulation results for the other main device in our lab-on-chip hardware platform, the separation electrode array.

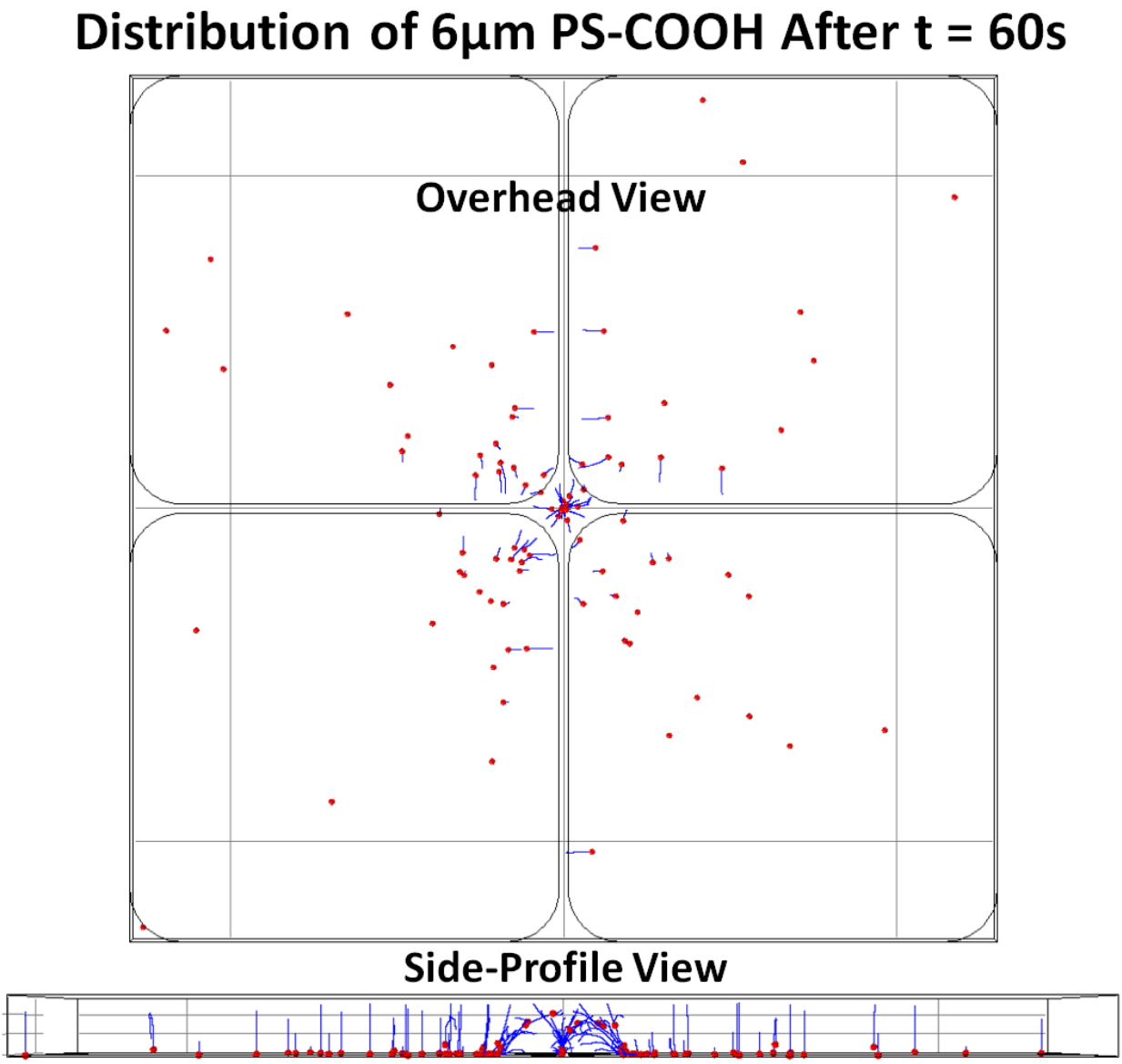

Figure 5.9 Distribution 6µm PS-COOH microspheres after 60 seconds of application of DEP characterization field. The voltages used were 2Vpp at a frequency of 1MHz. At this frequency, the particles undergo negative dielectrophoresis. Particles near the center are pulled in to the null region in the center, while particles are repelled from the high intensity field regions near the gaps.

5.1.2 Linear Separation Electrode Array Design

The electrode arrangement used to carrying out time-multiplexing dielectrophoresis is the same as for the traveling-wave dielectrophoresis electrodes described in section 2.3. The electrodes consist of a linear array of equally spaced conductors. Based on our experience with earlier prototypes we concluded that an array of 32 electrodes would provide a good balance between experimental testing flexibility and packaging complexity. We used the simulations of this section to verify whether or not the previously determined maximum electrode dimensions of 30μm would be sufficient to generate enough force to carry out time-multiplexing dielectrophoresis.

5.1.2.1 Finite-Element Analysis Simulations of Separation Electrode Array

Since the COMSOL particle tracing software can only calculate DEP forces exerted on particles, we made custom modifications to it so that the effects of TWDEP forces could be included. The electrode array is symmetric about the axis that runs the length of the electrodes thus it is only necessary to simulate the fields in two dimensions. Figure 5.10 shows the 2D finite-element model we created for the separation electrode array. The electrodes in this model are 30μm wide with equally sized gap spaces. The surface plot shows the electric-field magnitude profile that is generated in the fluid containment region when voltage magnitudes are $2V_{pp}$ @ 1MHz and the phase of the signals on each electrode is increased by 90^0 with respect to its neighbor (going from left to right), resulting in a positive phase gradient of $\nabla\phi_x = \frac{2\pi}{240}\left(\frac{\text{rads}}{\mu\text{m}}\right)$. The buffer in the containment area is assumed to be the 5mS/m reference medium and the containment dimensions are determined by the microfluidic designs described later in section 5.2.

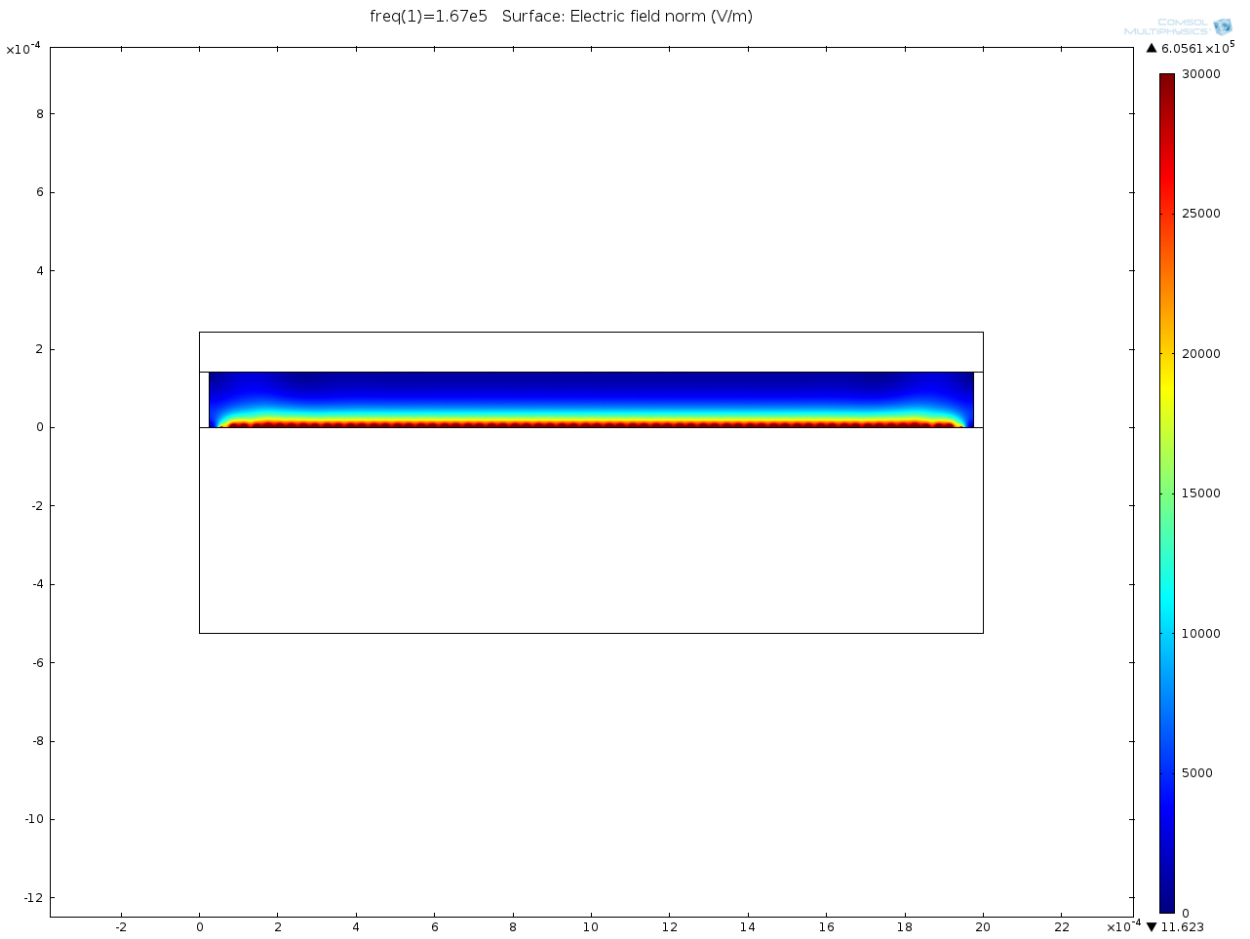

Figure 5.10 Simulation results of electric field magnitude profile generated in fluid containment region when traveling-wave voltages are applied. The electrode gaps and spacing are 30μm and the voltages are 2Vpp, 1MHz signals. The phase of each electrode is shifted 90^0 with respect to its neighbor (going left to right), resulting in a positive phase gradient.

Figure 5.11 shows the results of the transient particle motion simulation. The top of figure 5.11 shows the initial random distribution of particles in a zoomed in region of the array. The bottom of figure 5.11 shows that after 60 seconds, all particles almost reach their steady state levitation depth of 60μm, the point at which the vertical DEP forces balance out with gravity, and travel in the negative x-direction. The particles travel opposite the phase gradient (right to left) because $Im\{K_{CM}\}$is negative for these particles at 1 MHz. The average TWDEP x-velocity for the particles is approximately 0.5 μm/s which is

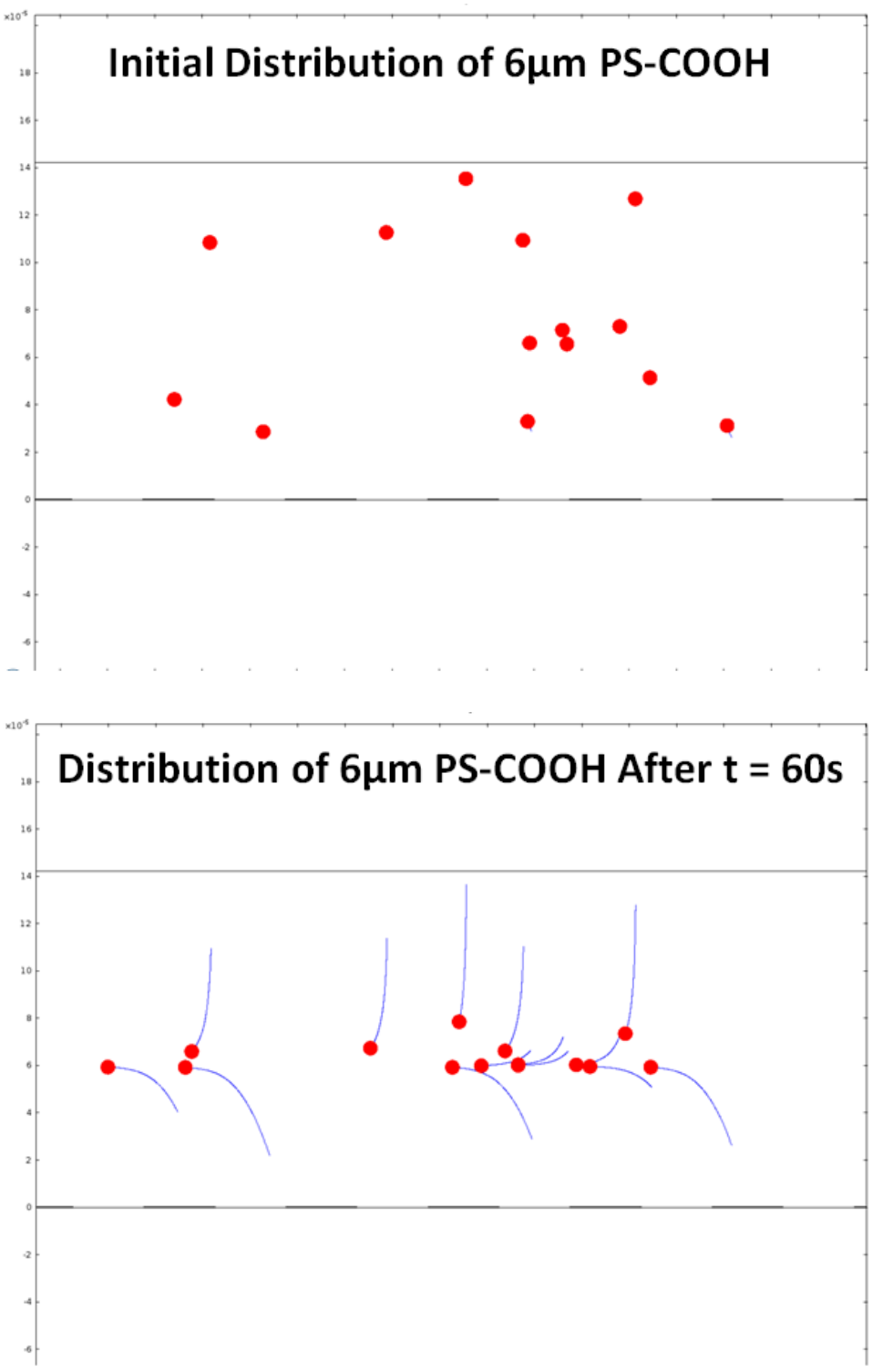

Figure 5.11 Top shows 2D particle motion simulation model and initial random distribution of particles. Bottom shows particles reaching a steady-state levitation height of 60µm due to DEP forces balancing out with gravity and traveling in the negative x-direction due to the TWDEP field created by the electrodes.

slightly below our desired threshold of 1μm/s. However the difference in velocity is well within the range of being able to be compensated for by slightly increasing the voltage or switching to the 15μm electrode array.

As a result of these simulations we were able to determine the electrode geometries and dimensions that give us a reasonable ability to test our methodology. We made the decision to fabricate multiple devices, covering the size ranges we determined to be operable via simulation. Sets of 5mm x 5mm quadrupole electrodes with gaps of 15μm and 30μm and filet distances ranging from of 25μm to 150μm were fabricated as well as linear electrode arrays with gaps and widths of 15μm and 30μm. In the next section we provide the fabrication details of our electrode designs.

5.1.3 Electrode Fabrication and Packaging

The electrodes were fabricated in batch, using a metal on glass photolithography process (TRICR Corp.). The minimum electrode dimension fabricated was 5μm, allowing the use of a simple metal lift-off process. Two sample wafers that have been fully processed are shown in figure 5.12.

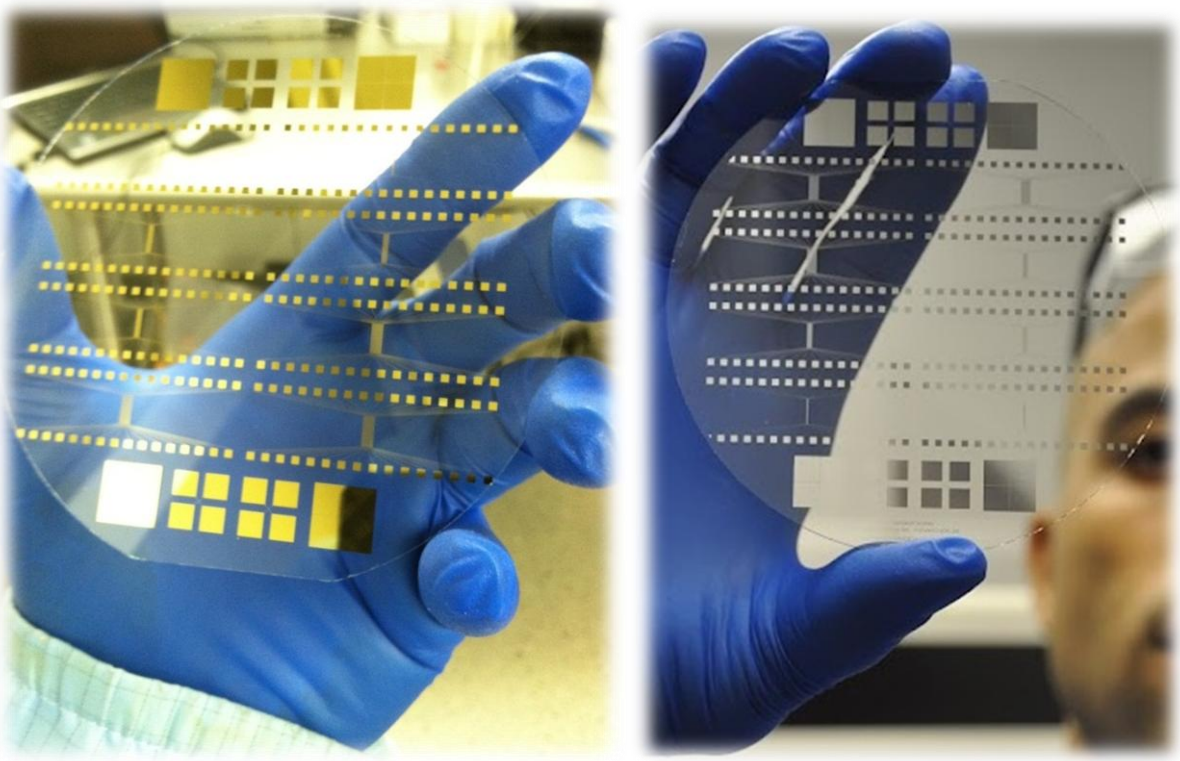

Figure 5.12 Gold and aluminum processed wafers with multiple copies of both electrode structure types

Four-inch soda lime glass wafers were selected for substrates, as glass has a number of desirable qualities in this application. Since there are no active circuit components at this level, expensive silicon substrates are not needed. In addition, the transparency of glass allows for illumination of the electrode region from many different angles, which is critical for recording data. During the metal lift off fabrication process, a sacrificial layer of photoresist is deposited onto the wafers and photolithographically patterned according to our electrode designs, using a chrome photo-mask. Vapor deposition is then used to pattern a 200 Å adhesion layer of titanium, followed by a 200nm metal electrode layer. Wafers with electrode layers made of both gold and aluminum were fabricated. The tradeoff between the two metals is cost versus durability. After experimenting, it was found that gold electrodes were better suited for this

platform in the long run, as one gold chip can be reused for weeks if properly cleaned, whereas the aluminum devices oxidized after a few uses.

However the most critical fabrication parameter in this process is the thickness of the electrode layer. If this layer is made to be too thin, the manufactured device becomes unreliable. However if it is too thick, the electrodes become difficult to use for dielectrophoresis. When the electrodes heights are on the same order of magnitude as the size of the particles, then dielectrophoresis 'dead zones' will be created between electrodes, as there is little to no electric field gradient in that region, if particles fall into those valleys they remain trapped, as no dielectrophoretic forces can be exerted on the particles.

Each processed wafer contains 8 separation electrode arrays and 8 sets of characterization electrodes of varying sizes. A wet-saw is then used to dice the wafer into individual chips. Figure 5.13 shows a close up view of one of the gold quadrupole electrode chips that had a gap spacing of 15μm and filet radius of 75μm. Figure 5.14 shows a close-up view of one of the gold 30μm separation electrode arrays after processing.

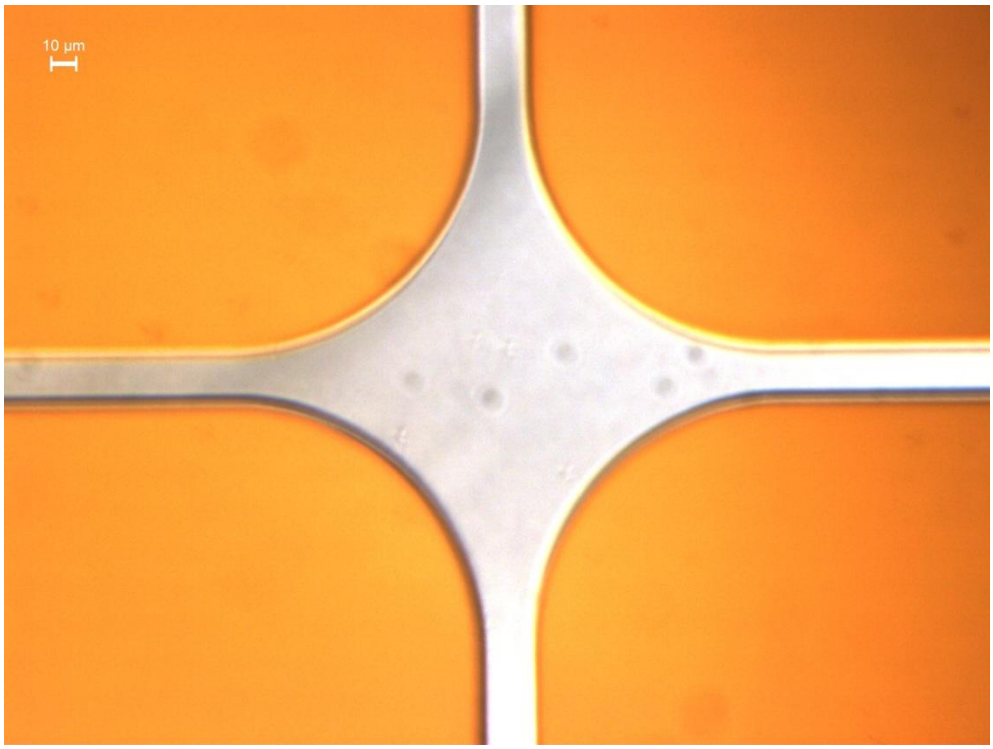

Figure 5.13 Close-up view of one of the gold quadrupole characterization chips after processing

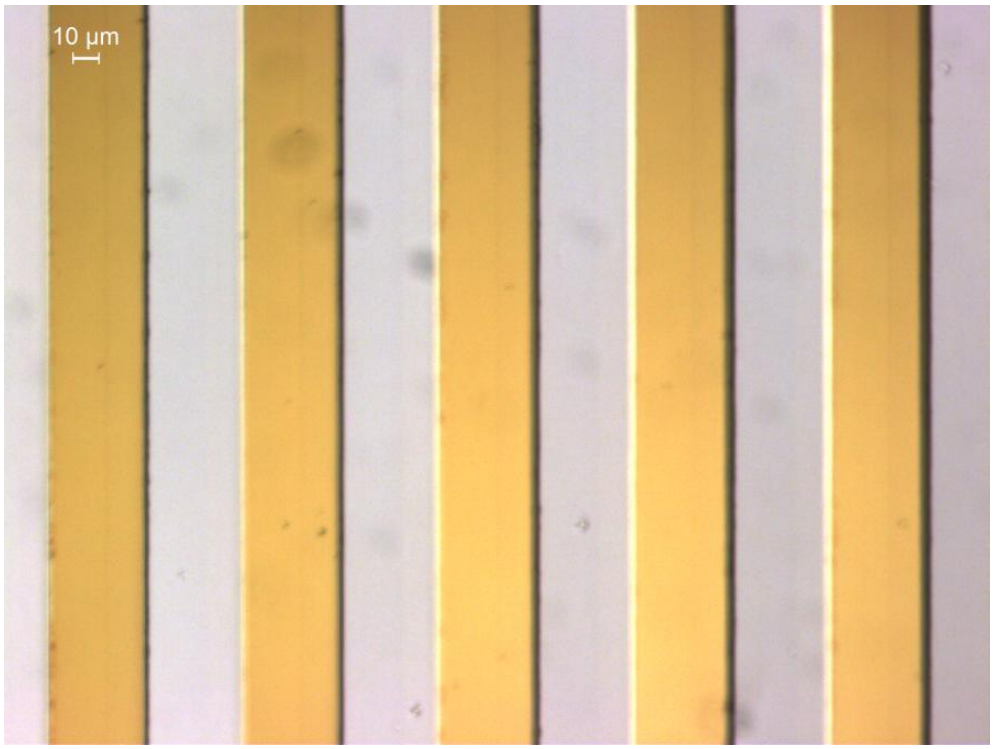

Figure 5.14 Close-up view of one of the gold separation electrode arrays after processing

5.1.3.1 Packaging of Quadrupole Electrodes

After the wafers were fabricated, the next step in the process was to have them diced into chips and packaged. The finished glass wafers are 500μm thick and devices were cut out using a diamond wet-saw (Golden Altos Corp.). After being cut, quadrupole devices were bonded directly to a FR4 printed circuit board using super-glue. A photograph of one chip is shown in figure 5.15. Electrical connections to the four electrodes of the quadrupole were made by manually soldering very thin wires to the chips. Extra care had to be taken as the metal layers are extremely thin and can easily scrape off when heated. So as to prevent this from occurring, the corners of the electrodes were covered in flux and used in conjunction with low-temperature solder paste.

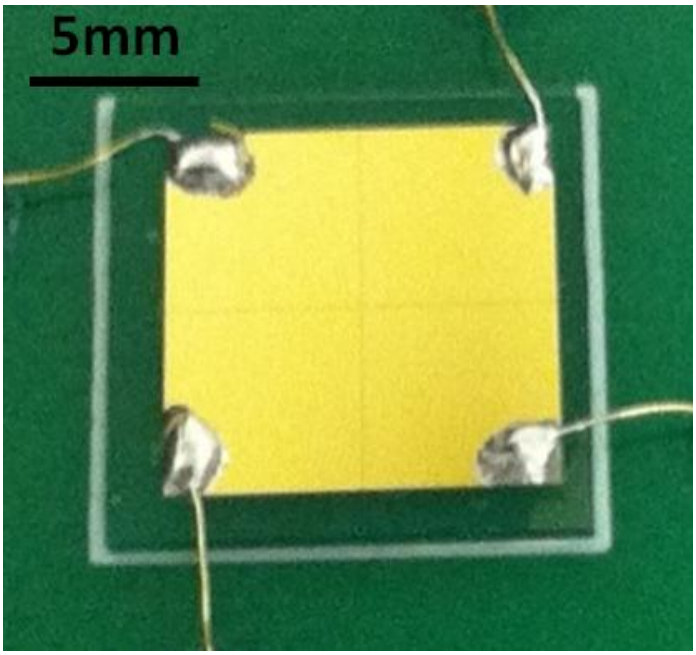

Figure 5.15 Quadrupole electrode chip after being diced, bonded to the surface of a PCB, and soldered

5.1.3.2 Packaging of Separation Electrode Array

Figure 5.16 is a photograph of one the separation electrode arrays after fabrication, showing the fan-out pattern from the electrodes to the connection pads. In order to implement our technique, it is necessary that the voltages on each of these electrodes are individually controllable. So as to make this possible, the diced chip is bonded into a dual-inline package using an epoxy (Golden Altos Corp.).

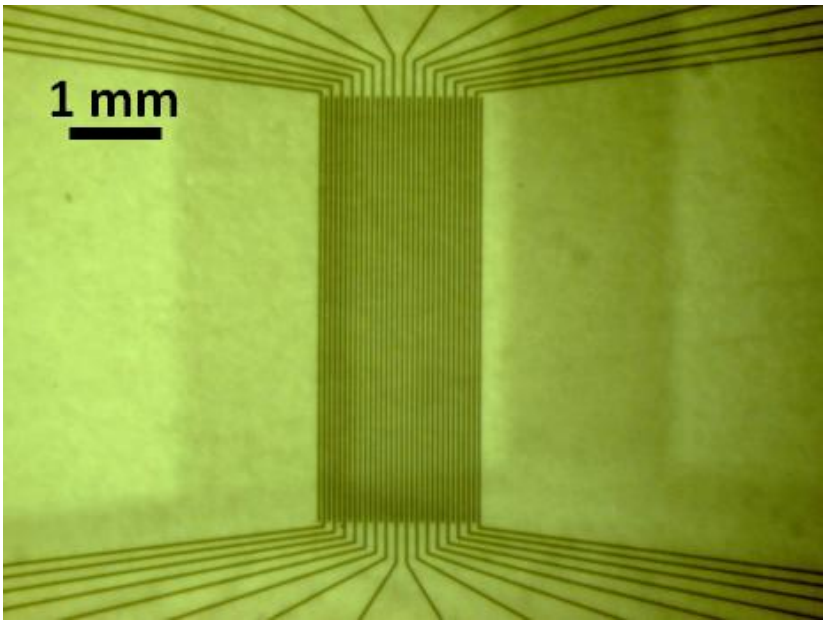

Figure 5.16 Separation electrode electrode array. A chip with 32, 30μm electrodes is shown

After the die is attached, a wedge wire bonder is used make connections between the electrode contact pads and the package pins (figure 5.17). After initial testing, it was observed that the reflective surface of the electrodes made obtaining a good microscope image difficult. In addition particles, such as transparent cells, were difficult to see when they were in between electrodes due to lack of sufficient illumination. To remedy these issues, a ¼" hole was drilled into the center of the package so that the chip could be illuminated from its underside as seen in figure 5.18.

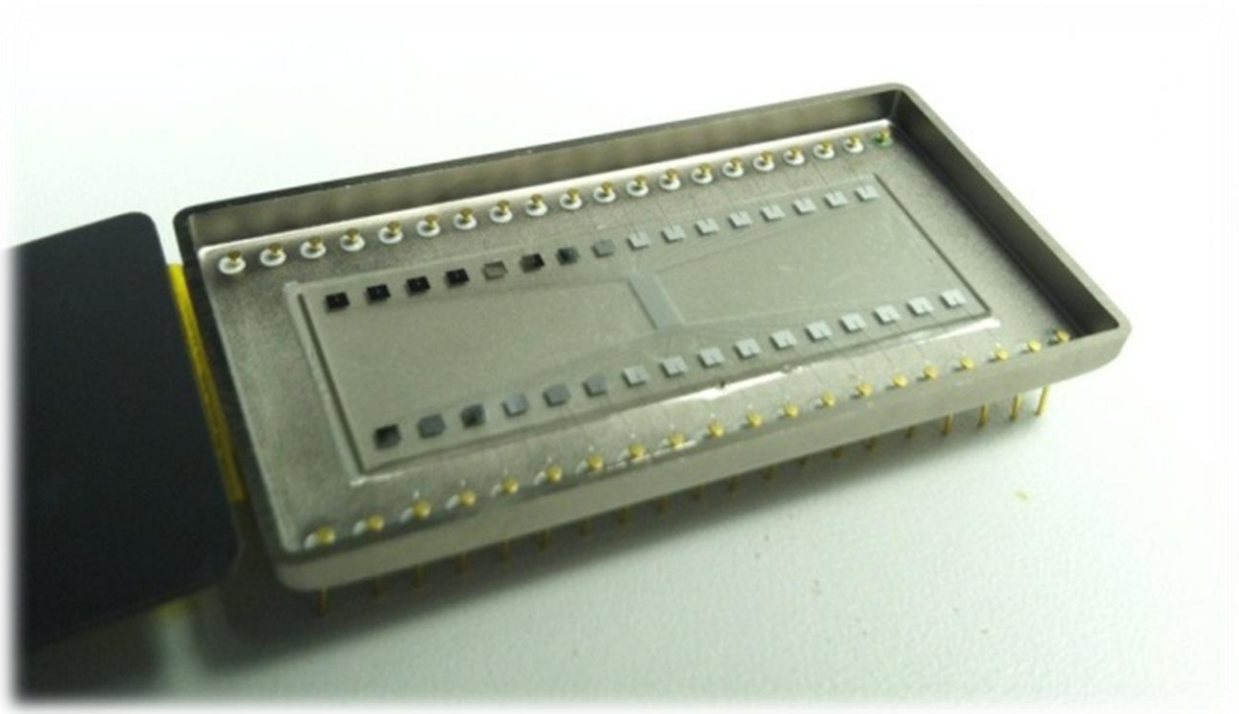

Figure 5.17 Separation electrode chip after dicing, attachment to a dual-inline package and wire-bonding

Figure 5.18 Hole drilled in back of package so that separation electrode array could be illuminated from its underside

After both devices are packaged, the next fabrication step is to make it possible to contain and deliver microfluidic samples to the electrodes. The microfluidic interfaces we designed and built in order to achieve this task this are discussed in the next section.

5.2 MICROFLUIDIC INTERFACES

One of the challenging aspects of this hardware platform is that very minute samples, on the order of a few microliters or smaller, have to be precisely delivered to a specific location, the region directly above the dielectrophoresis electrodes. As a result, facilities for microfluidic transport and containment have to be designed. Currently, the most common approach to prototyping microfluidic structures is to use PDMS molds [58] which requires the use of photolithographic techniques that are carried out in a clean-room environment and difficult to implement for the inexperienced. For our designs, we used a simpler, more rapid, lower cost approach of creating microfluidic structures using a desktop digital craft cutter [59].

The setup that we used is shown in figure 5.19. Using this approach, fluid channels and reservoirs are created by first entering the desired fluid channel geometry into the craft CAD software and then patterning a sheet of double-sided adhesive accordingly. The minimum possible feature size of this approach is 200μm. The same is then done for a transparency sheet that acts as the coverslip layer, and also provides inlet/outlet ports to the channels. The bottom of figure 5.19 shows one of the channel designs used with the separation electrode array. The complete microfluidic chip is assembled by removing one side of the adhesive protective layers (shown in white), aligning it to the transparency layer and then applying it. The other side of the adhesive can then be applied to the device with the electrodes.

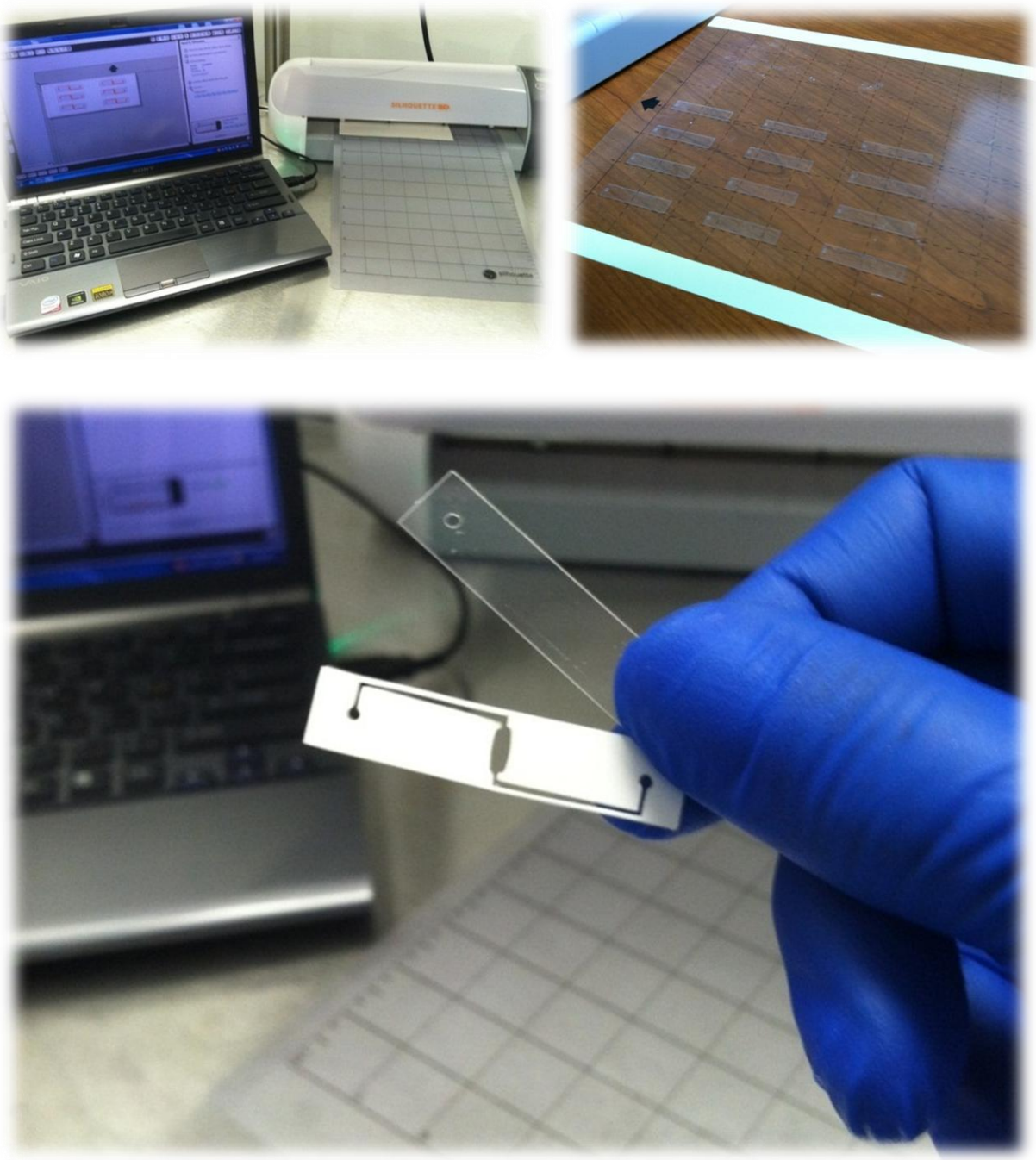

Figure 5.19 Setup for creating microfluidic prototypes using a digital craft cutter. The top left shows the CAD software and cutting device. The top right hand side shows a transparency coverslip layer shortly after being patterned. The bottom shows a patterned double-sided adhesive layer (white) and its corresponding coverslip

Figure 5.20 is a depiction of the cross-section of the assembled microfluidic devices. The depths of the channels and reservoirs are determined by the thickness of the double-sided adhesive layer. We used a polyester adhesive that was 142µm thick (Adhesives Research ARcare 92712) in our designs. The thickness of the transparent coverslip layer is not critical, in terms of fluidic transport, however its function is critical as microfluidic samples evaporate in a matter of minutes if not properly covered. Another consideration for the transparency layer is to select a material that is fairly rigid (Grafix clear dura-lar film) so as to facilitate easier application of microfluidic device to the substrate.

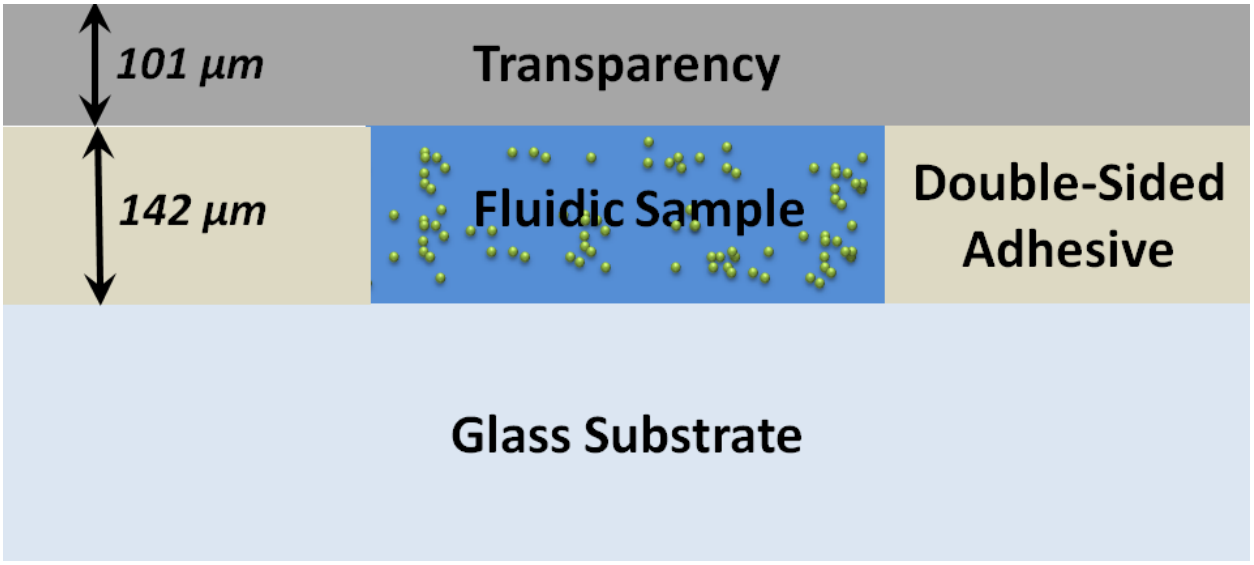

Figure 5.20 Cross section view of microfluidic devices after application of transparency and adhesive layers to the substrate. The height of the fluid channels formed is determined by the thickness of the adhesive layer.

In the following subsections, we give the details of the final microfluidic designs used to support sample transport and delivery for both the quadrupole characterization electrodes and separation electrode array.

5.2.1 Quadrupole Characterization Chip Microfluidic Interface

Figure 5.21 shows the transparency and adhesive layers used to deliver samples to the quadrupole characterization electrodes. A very simple reservoir structure was used. The a rectangle of 2.54mm x 7.27mm rectangle that was patterned into the adhesive layer providing a total sample containment volume of 2.6µl. The coverslip layer included a semi-circle inlet of 2.54 mm in diameter and a 1.27mm x 2.54mm rectangular outlet for air flow. The inclusion of the outlet allows the device to be filled via pipetting small samples onto the inlet and allowing capillary action to fill the chamber. Figure 5.22 shows the application of the microfluidic interface to one of the quadrupole electrode sets.

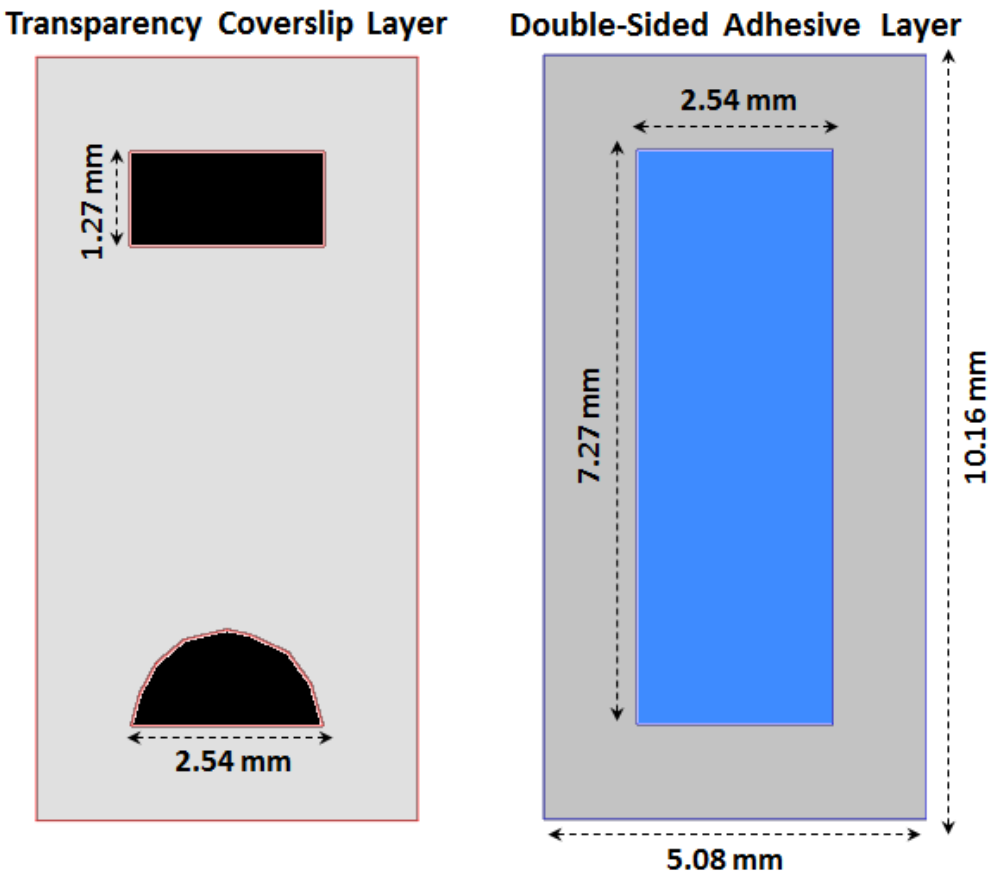

Figure 5.21 Microfluidic containment designed to interface to quadrupole electrodes

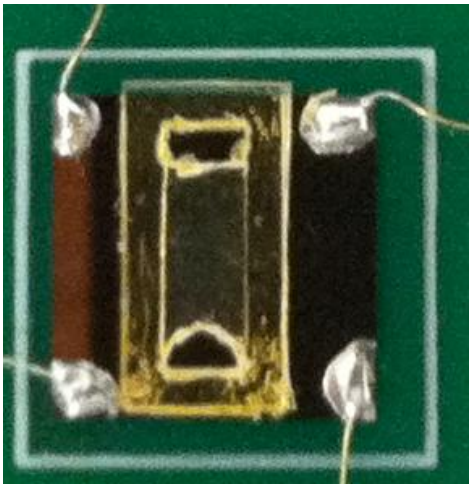

Figure 5.22 Microfluidic interface applied to a set of quadrupole electrodes

5.2.2 Separation Chip Microfluidic Interface

The quadrupole microfluidics are not sufficient for the separation electrode array because of additional requirements. For the separation device, we wish to be able to flush and clean the device between uses, and also deliver samples using a common, standard syringe. To meet these requirements, a microfluidic interface was designed that consisted of inlet/outlet ports, connected to long channels that deliver the samples to a containment region above the array.

Figure 5.23 shows the evolution of the microfluidics for the separation electrodes. A final designed was arrived to by trial and error and observation. The initial design consisted of a rectangular chamber, similar to that of the quadrupole, fed by 2 channels that fed the center of the containment. This was found to have the tendency to create large air-bubbles that prevented the containment from being completely filled. In the next design iteration, the channels were moved to feed the chamber from its top and bottom ends so that the path of the airflow from inlet to outlet would pass through the entirety of the chamber. The corners of the chamber were also rounded so as to prevent air bubbles being trapped in the corner. The channels were then widened from the minimum possible width supported by the craft cutter to 500μm. The final modification was to angle the channels away from the outer edge of the cutout, as it was found that the larger the adhesive surface area surrounding the channels were made, the less likely leakage would occur. Figure 5.24 shows the measurements of the final design for the microfluidic interface for the separation electrode array.

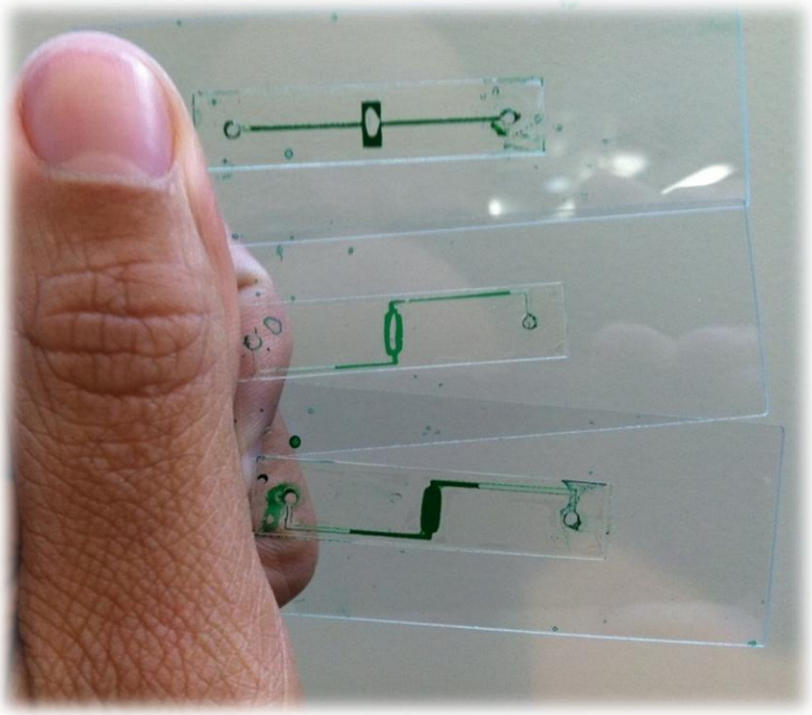

Figure 5.23 Evolution of microfluidic interface for separation electrode array

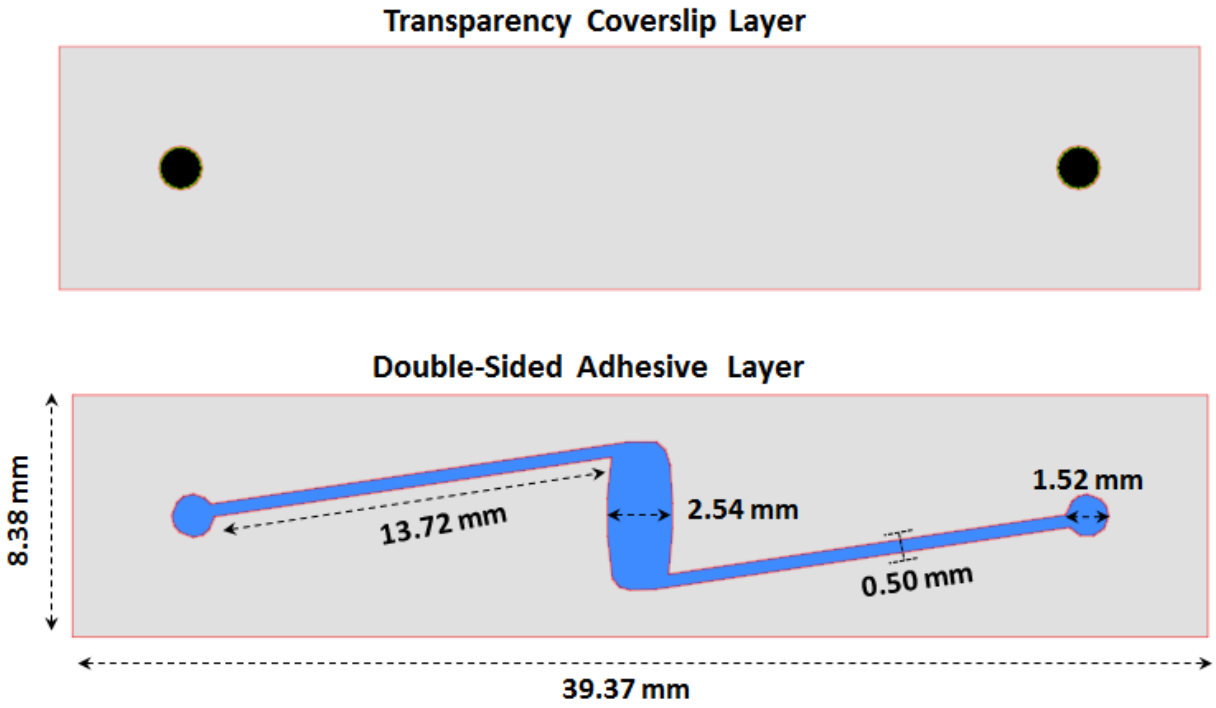

Figure 5.24 Microfluidic channels and containment designed to interface to separation electrode array

In addition to containing the sample, the separation electrode chip requires an effective way to deliver the sample using commonly available methods, such as syringes. This design requirement was met by acquiring commercially available microfluidic assemblies (IDEX Health and Science, NanoPort 6-32). The top of figure 5.25 shows NanoPort assemblies affixed to the areas above microchannel inlets and outlets on one of the packaged separation devices. For this assembly, small micro-gaskets are affixed directly above the inlet/outlet cut-outs (not shown) and a threaded port is placed over top of them and then bonded to the top of the craft-cutter microfluidic device. Extra epoxy is placed around the port to prevent leakage and prevent the structure from becoming undone due to the high pressure that occurs when a syringe forces flow through such a small channel. The bottom of figure 5.25 show the luer-lock syringe connected to 1/32" outer-diameter tubing. Alignment and securing of the tubing occurs via a matching conical fitting that screws into the NanoPort. With this setup, samples can easily be delivered to the region above the electrode via a pressured driven flow in a controlled manner.

The setup of figure 5.25 shows the packaged device plugged into a printed circuit board that was used in conjunction with the electronics used to implement the time-multiplexing of dielectrophoresis fields. In the next section, we give the implementation details of the board and of all the supporting electronics included the design of our lab-on-chip hardware platform.

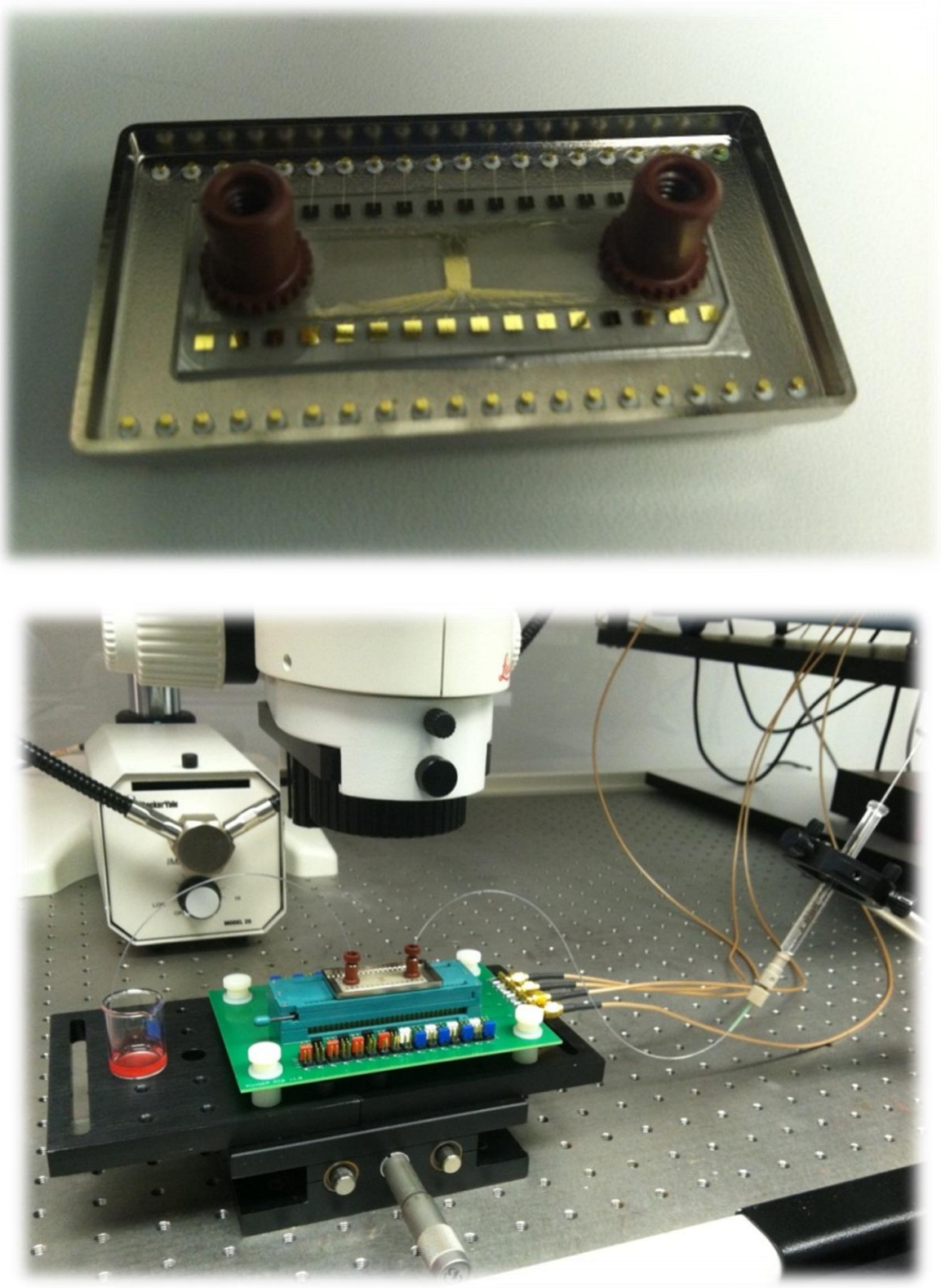

Figure 5.25 Top shows separation electrode chip with microfluidic channels and access ports affixed on top. Bottom shows syringe and tubing setup used to deliver samples to the region near the electrodes

5.3 ELECTRONIC DESIGN

Both the quadrupole characterization chip and the separation electrode array are primarily voltage driven devices, therefore a supporting electronic infrastructure has to be designed to facilitate the assignment of voltage waveforms to them. In this section, we present the designs for the circuitry associated with the two chips and the software user interface used to control the devices.

5.3.1 Electronic Design for Quadrupole Characterization Electrodes

The quadrupole requires four AC signals that vary in phase. This this is accomplished by externally driving them by independent, programmable voltage sources. The top of figure 5.26 shows the schematic and the bottom of figure 5.26 shows the assembled characterization device mounted to the printed circuit board implementation. The leads soldered to the corners of the quadrupole electrodes are soldered to landing pads on the PCB and the pads are then directly wired to SMA connectors. The board is a 2-layer FR4 PCB, where signals are routed using 6 mil traces and a ground plane is included to reduce electrical noise.

While extremely simple in nature, the schematic and board highlight one of the appealing features of dielectrophoresis for lab-on-chip applications. The path from source to electrode to ground is an open circuit, thus there is no DC power consumption. In addition, the low impedance electrodes dissipate very little power when in operation.

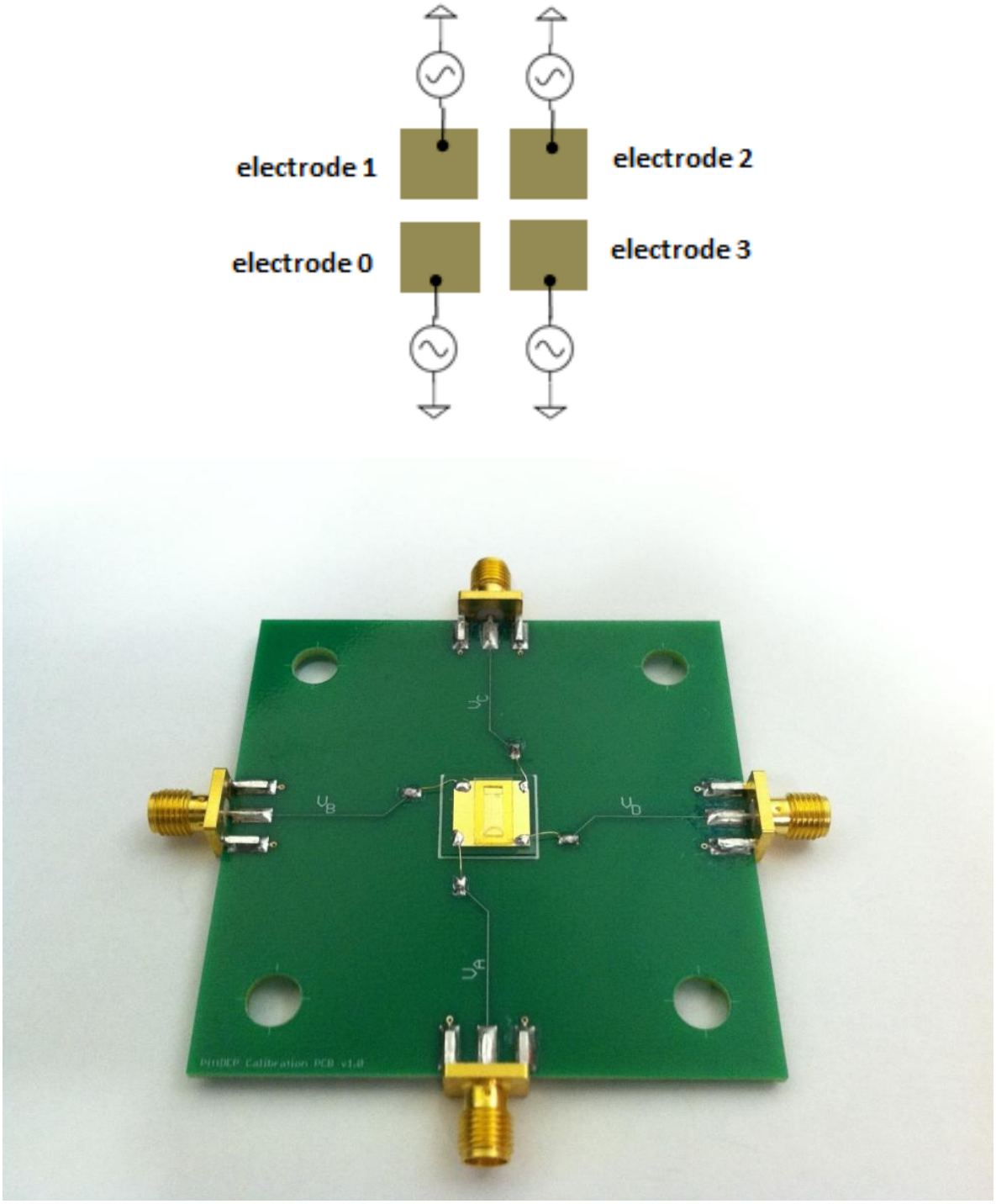

Figure 5.26 Top shows schematic for quadrupole electrodes. Bottom shows completely assembled quadrupole characterization device.

Figure 5.27 shows a preliminary test of the quadrupole chip being directly driven by voltages configured to create the DEP calibration field presented in the simulations of section 5.1.1. In this preliminary test, a sample containing 6μm PS-COOH microspheres was used. The top of figure 5.27 shows the experimental results and the bottom shows the corresponding simulations at the same points in time. The experimental results are in good agreement with the simulations, after the DEP characterization field has been applied for 2. In both cases, particles initially near the center get further compressed into the middle, while particles near the electrode gaps move further away from the gaps. This test provides initial verification of the electrode designs and further characterization results will are included in chapter 6.

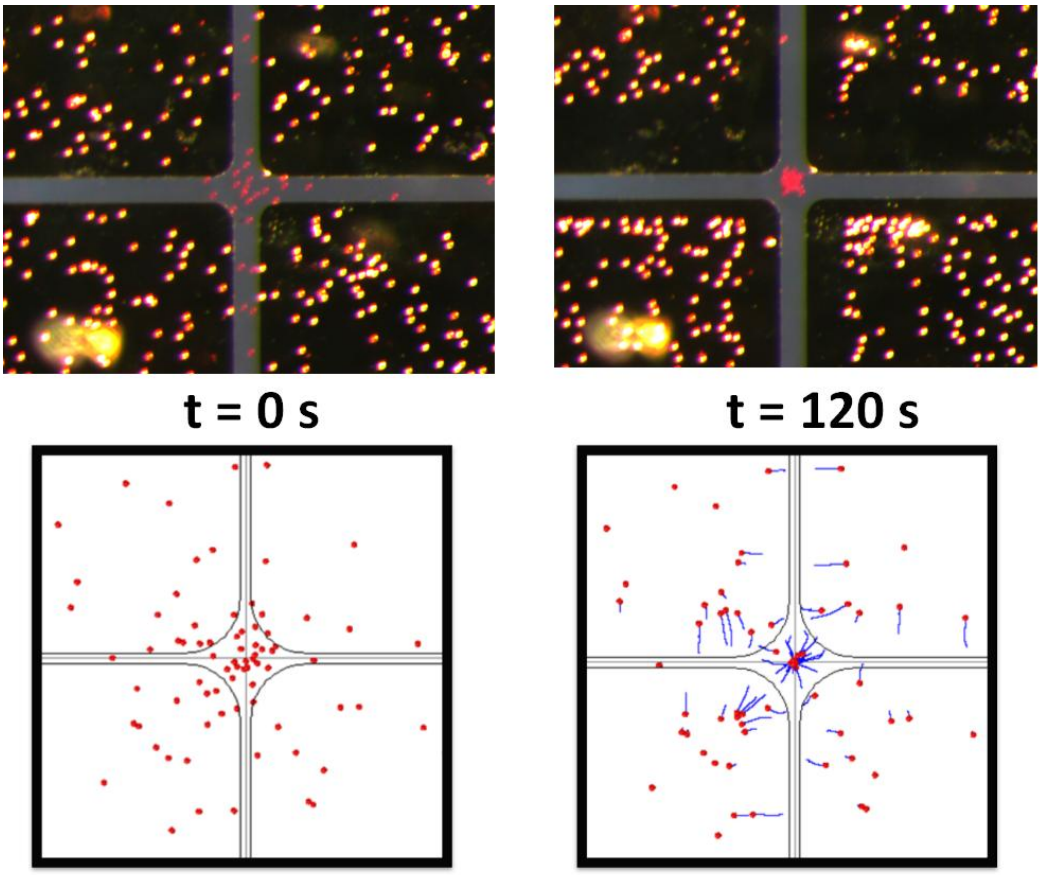

Figure 5.27 Top shows microspheres being manipulated by quadrupole at t = 0s and t = 120s. Bottom shows shows simulations at same times.

5.3.2 Electronic Design for Separation Electrodes

The electronic design for the separation electrodes requires a slightly higher level of complexity than the characterization chip. The separation electrodes are used to generate the time-multiplexing dielectrophoresis fields. Figure 5.28 shows the schematic for the circuitry associated with the electrode array and the corresponding printed circuit board used to implement it. An arbitrary waveform generator is used to carry out the time multiplexing and create voltage waveforms that quickly alternate between signal patterns. Four time-multiplexing source channels, each shifted 90° in phase, are used to drive bus traces on the PCB via SMA connectors. There is a 2x4 set of pins associated with each electrode. The pins in the first column are all directly connected to the electrode via PCB traces. Each of the four rows in the second column of pins connects to one of the four time-multiplexing voltage sources. The connection from electrode to source is made via a jumper. This setup allows us to spatially reverse the phase gradient of groups of electrodes with respect to others. This feature is particularly needed when creating the dielectrophoretic 'traps' shown in figure 4.6. For example, for the phase assignment shown there, starting from left to right, the trap can be created by reversing the order of the source assignments on the first four electrodes with respect to the next four electrodes. Even though in that case the signal phase on a particular electrode will vary over time as multiplexing takes place, the phase gradient between the two groups will always be opposite, thereby creating the trap. One additional feature we added to the PCB design shown in figure 5.28 is a zero-insertion force (ZIF) socket for the dual-inline package that holds the chip is placed in. This provides the benefit of only having to have one PCB, and chips can easily be swapped out when they need to be replaced. In the next section we describe how patterns are controlled via a software user interface.

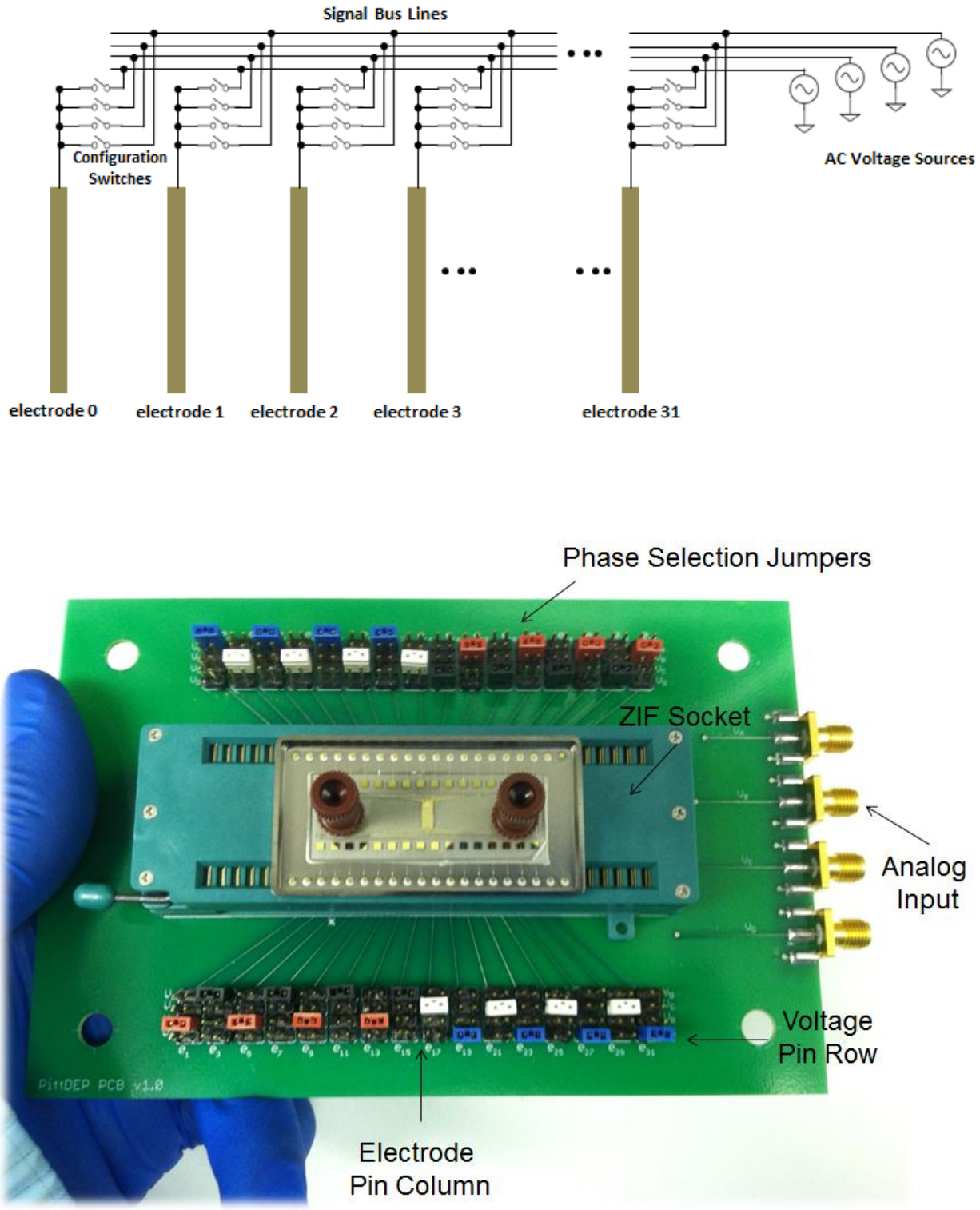

Figure 5.28 Top shows schematic for connectivity of electrodes in the separation array. Bottom shows corresponding printed circuit board.

5.3.3 Software User Interface

A custom software interface was designed to provide control of the device. The software being used on a touch-screen tablet computer is shown at the top of figure 5.29. The software provides the user with the ability to select two particle types from among those in the particle library described in chapter 3 via a pull down menu. The model parameters can be adjusted by the user and the resulting frequency profiles are displayed so as to give the user an expectation of how each particle type should individually respond to the fields. For the two configurations that will be multiplexed, the user has the ability to select the relative phase gradient, voltage amplitude (ranging from 0 V_{pp} to 4 V_{pp}), frequency, and duration of each configuration that is applied before switching, providing the ability to control all of the time-multiplexing parameters necessary in equations 4.13 and 4.14. In order to implement the time multiplexing, four channels from a digital arbitrary waveform generator (Tetronix AWG520) are used. The waveform generator is controlled by the software user interface over via a TCP/IP network.

The digital waveform generator provides 2,048 samples per channel, sampled at a rate of 1GS/s. Since 4 relative phases are required between the channels, the minimum possible signal period is determined by its relation to the duration of 4 samples at a given sampling rate. This gives the ability to create patterns with frequencies up to 250 MHz. Once a user selects the duty cycle and phase gradients, the software selects from a set of preconfigured patterns and adjusts the sampling rate of the generator accordingly. The bottom of figure 5.29 is a photograph of the result of the software controller being used to multiplex waveforms of 100 kHz and 1 MHz with opposite phase gradients being displayed on an oscilloscope.

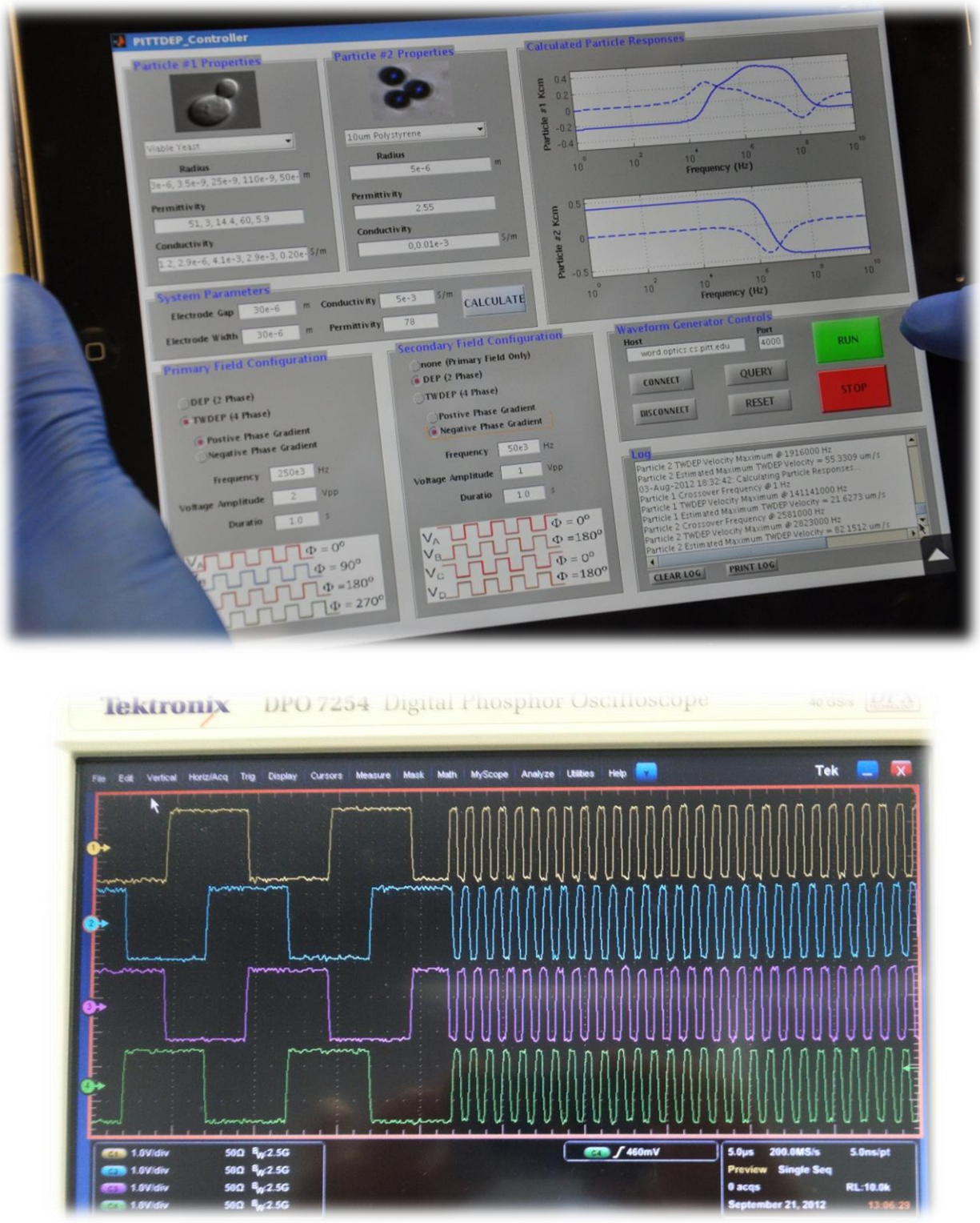

Figure 5.29 Top shows the custom software interface developed to control multiplexing voltage waveforms being operated via a touchscreen tablet computer. Bottom shows signals of 100 kHz with a positive phase gradient and 1 MHz with a negative phase gradient being time-multiplexed.

The final component of the hardware platform is a mechanism to visually record data from the behavior of the particles. This was accomplished via the combination of a 15 fps CCD camera and microscope, seen in the background of figure 5.30. Figure 5.30 shows the complete lab-on-chip hardware platform with all the major elements and features of our original design goals depicted in figure 5.1 included. This platform was not our only hardware implementation approach and brief descriptions of our other design prototypes are included in Appendix A.

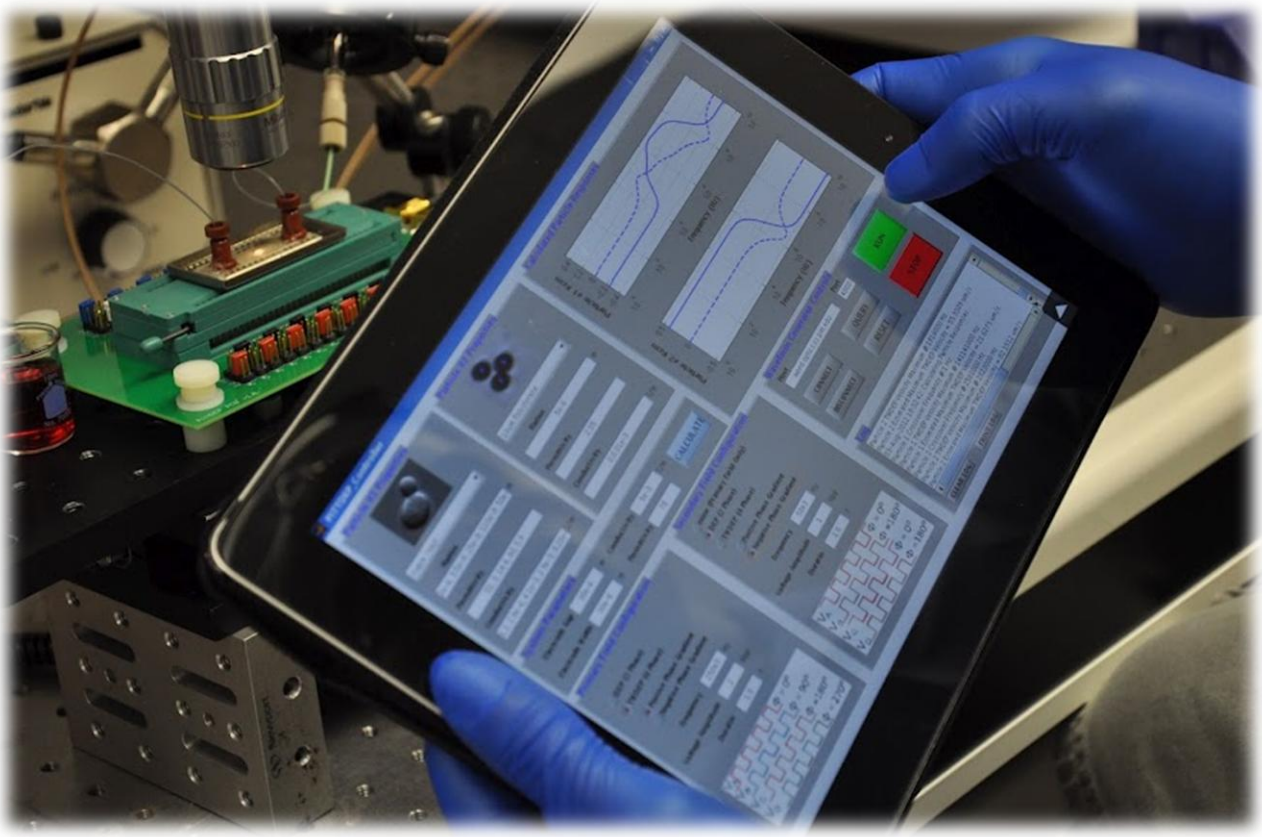

Figure 5.30 Completed lab-on-chip hardware platform, including packaged dielectrophoresis chip, microfluidic interface, electronic control and software interface.

Successful completion of this hardware platform gives us the ability to experimentally characterize particles and verify our library models as well as demonstrate our time-multiplexing dielectrophoresis method. In the next chapter we show the results of our characterizations.

6.0 EXPERIMENTAL CHARACTERIZATION OF PARTICLE LIBRARY

In order to be able to use time-multiplexing dielectrophoresis to separate particles, we first need to have accurate models for their dielectrophoretic response. In this chapter, we present the results of using the quadrupole device to characterize the five particle types included in our library.

Figure 6.1 shows how the quadrupole electrodes were used to measure the DEP velocity of particles. A dilute sample of particles was first pipetted onto the inlet of the microfluidic containment. After the particles settled, signals were applied to the electrodes at the given frequency and the phases of the signals so as to create the DEP characterization field described in section 5.1.1. After the application of the fields, particles move due to dielectrophoresis, particles undergoing pDEP are pulled towards the electrode gaps while particles undergoing nDEP are concentrated to the center of the quadrupole. The example of figure 6.1 shows 6μm polystyrene-COOH microspheres undergoing nDEP. Accurate, consistent velocity measurements were made by adding a calibrated distance overlay to the recorded video data, consisting of concentric circles equally spaced apart, and then using open-source, manual video tracking software (Kinovea, [1]) to measure the time it took to traverse a particular pair of concentric circles. Velocity measurements at frequencies where particles underwent positive dielectrophoresis were made by first applying a nDEP field and frequency, forcing them to the

center, and then switching to the pDEP test frequency and measuring the speed at which they are pulled out towards the electrodes.

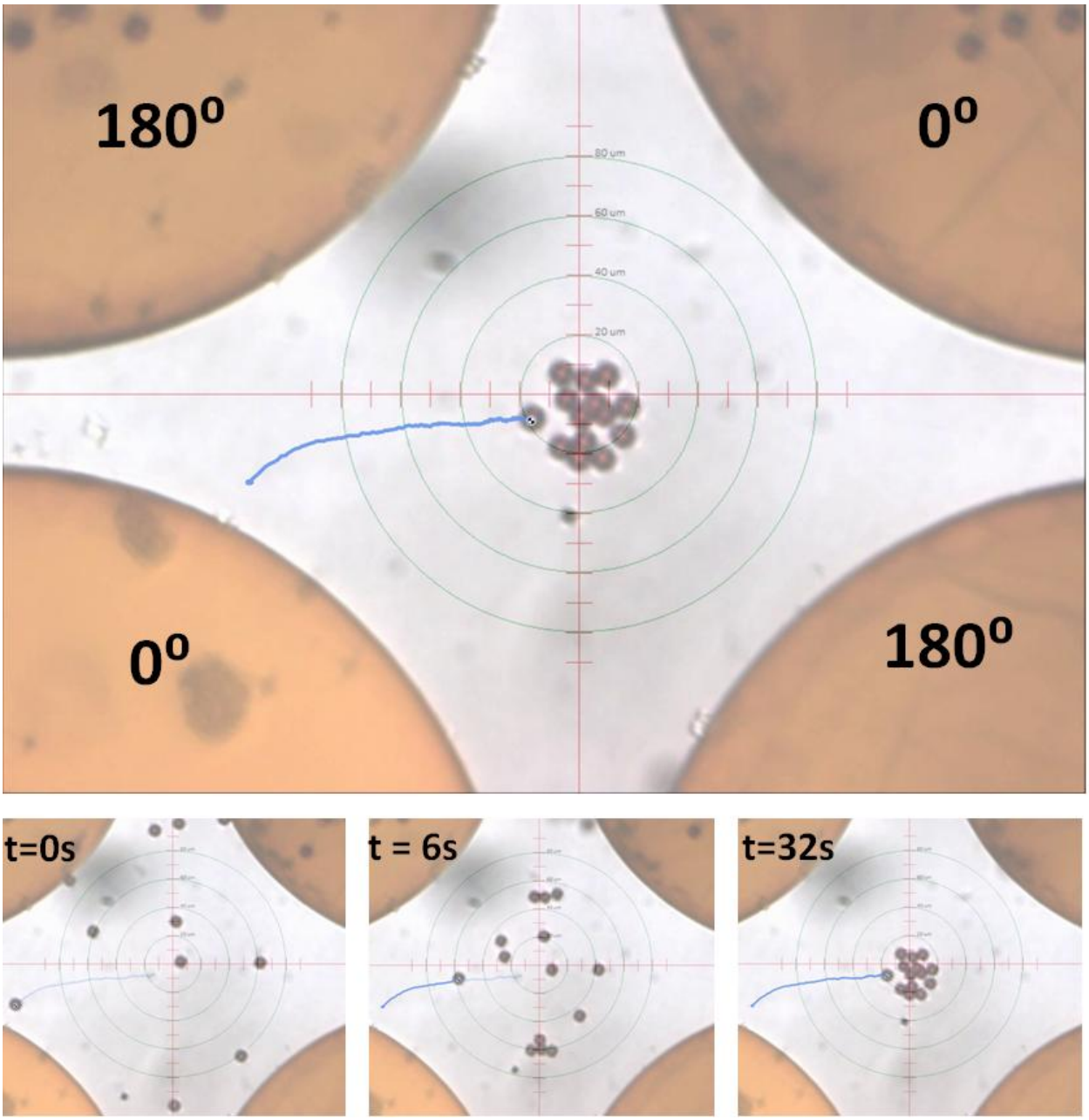

Figure 6.1 Example DEP velocity measurement for 6µm polystyrene microspheres. Measurement was taken by applying an nDEP field and observing the time it takes for a particle to traverse a set of concentric circles as it moves towards the center. pDEP measurements were taken by recording time it takes to travel from center outward.

Figure 6.2 shows how the quadrupole was used to take measurements of the velocity of particles due to TWDEP. The four-phase voltage configuration described in chapter 5 was applied to the electrodes causing the particles to orbit around this axis of rotation. TWDEP velocity measurements were taken by observing the time it took for an individual particle to rotate around its orbital axis and the distance traveled. The direction of rotation (clockwise versus counter-clockwise) indicates whether or not particles are traveling in the direction of the phase gradient or opposite to it.

In the example of figure 6.2, a quadrupole device with 30μm gaps and 150μm filet distances is used to characterize live yeast cells. Since the size of the electric-field null region in the center created by this device is much larger in diameter than the particles being characterized, large numbers of particles are held in the center, forming clusters that determine the axis of rotation. However, our goal is to accurately characterize the individual response of a particular particle type, and large numbers of particles simultaneously rotating together can mask their true dielectrophoretic behavior. As a result, we carried out the final characterization experiments using the smaller 15μm gap/75μm filet distance quadrupole chips with a voltage magnitude of $2V_{pp}$, in order to decrease the diameter of the null region. In addition, before conducting each experiment set, we repeatedly applied nDEP and pDEP fields so as to position as few particles as possible in the center, allowing us to characterize a single, isolated particle. The DEP and TWDEP data shown for each particle type were taken using the same particle. The medium selected for the experiments was a standard 5mS/m KCL solution, the same as was selected in the model discussion of chapter 3. Measurements were not made at frequencies below 100 Hz where the effects of electrolysis were observed to dominate the motion of the particles. In addition, the bandwidth of the signal generator set the maximum test frequency to be 250 MHz.

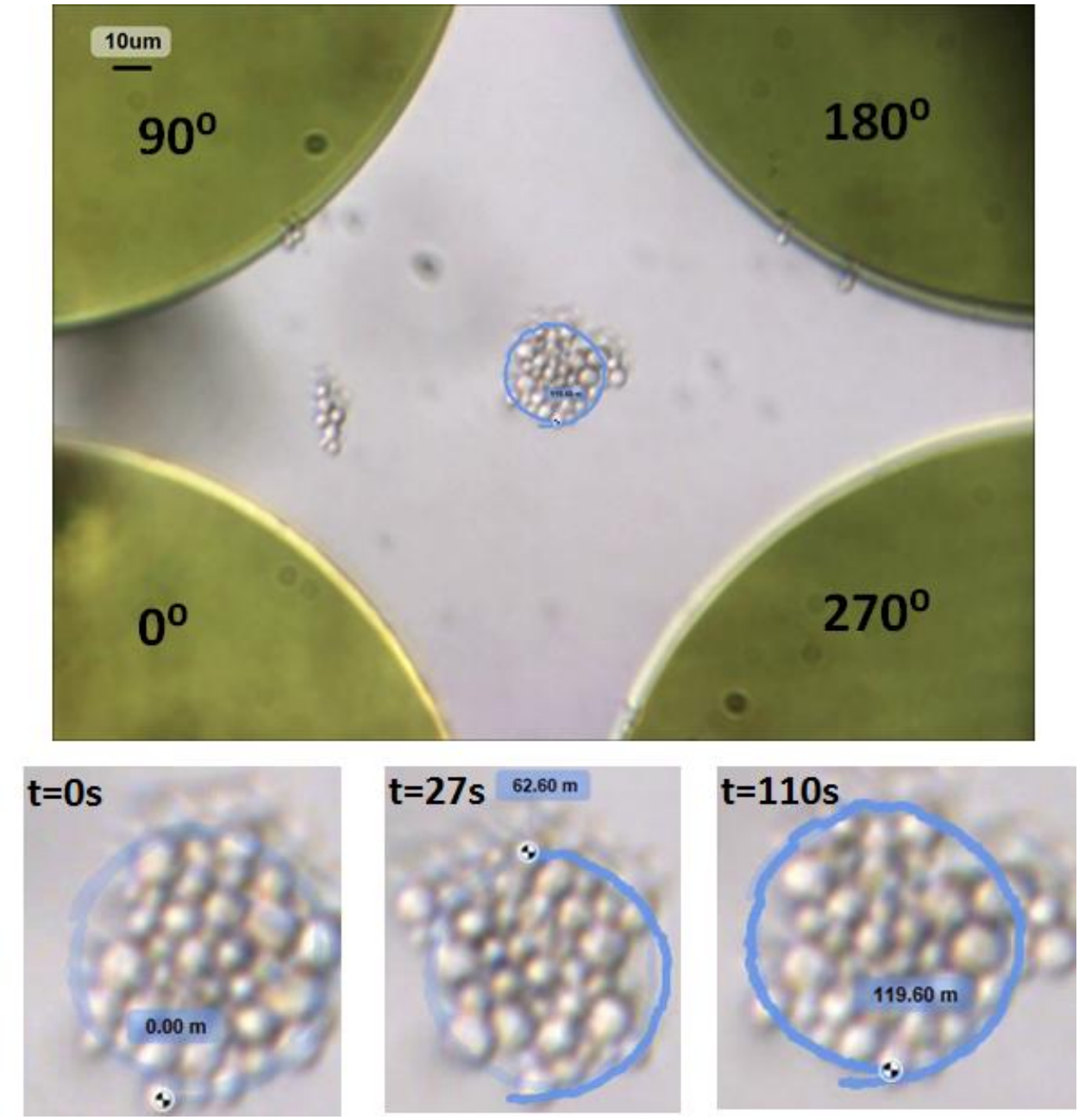

Figure 6.2 Example TWDEP velocity measurement for live yeast cells. Measurement was taken by applying a TWDEP field configuration and observing the time it takes for the cell to travel around its axis of rotation and the distance traveled.

6.1 CHARACTERIZATION RESULTS

In the subsections to follow, we present the results of the characterization experiments for each particle type. After recording observations, we carried out a best-fit analysis between the measured data and the appropriate model of chapter 3 to refine our model parameters.

6.1.1 Polystyrene Microspheres (10um)

The first particle type characterized were the 10μm polystyrene microspheres shown in figure 6.3. The data points in the plots of figure 6.4 are the DEP and TWDEP velocity measurements. The measured TWDEP velocity spectrum peaked at 2.5 MHz at a velocity of 1.02 μm/s and decreased for all measurements at frequencies above and below 2.5 MHz At frequencies below 500 kHz and above 5 MHz, there was little to no observable particle rotation. All rotations observed occurred in the clockwise direction, the same direction as the positive phase gradient. These observations are in reasonably good agreement with the predicted results using the homogenous dielectric sphere model of section 3.1. Both TWDEP profiles are positive at all frequencies where motion was observed. The location of the two peak frequencies were different, 1.17 MHZ versus 2.5 MHz, but are reasonably close.

The DEP velocity measurements showed a large degree of variability. The DEP velocity increased from -4.08 μm/s to -1.57 μm/s in the range of 10 kHz to 100 kHz. The DEP velocity then decreased to its maximum negative value of -7.91 μm/s at 10 MHz and then increased again to -2.62 μm/s at 250 MHz. There are a key similarities to the original model. The model and data are in agreement that these particles always undergo negative dielectrophoresis in this medium, as the DEP velocities were negative at all observed frequencies. In addition, the

magnitudes of the DEP forces are generally much larger than the TWDEP forces. There also occurred a point of inflection in the DEP profile that coincided with the TWDEP peak velocity. However, the drop off was much larger than the model predicted and went more negative as frequency increased instead of less negative.

In order to refine the model parameters, a best-fit analysis was carried between the observed data and the homogenous dielectric sphere model described in section 3.1 using the Matlab curve-fitting toolbox. The two plot lines shown in figure 6.4 show the results the curve-fit for the DEP and TWDEP velocity measurements. The curve-fitting engine used does not have the capacity to simultaneously fit two functions that have the same dependent variables, in this case the parameters used in calculating complex permittivity. Therefore curve-fits were carried out separately on the two sets of measurements, and the model parameters extracted from the fits were averaged together in order to provide our refined model parameters.

Figure 6.5 shows the best-fit curves after averaging and table 6.1 shows the extracted parameters. The particle radius differed by 53nm from the original model, which is well within the 5% tolerability range provided by the manufacturer. In the original model, the microspheres were said to have no conductivity, but these results show that they are indeed slightly conductive, which in turn accounts for the slight shift the peak TWDEP frequency. While the main features of the DEP measurements were in agreement with the models, the curve-fit for the did not capture all of the details of the DEP spectrum and converged to parameters that result in the average DEP velocity across the spectrum.

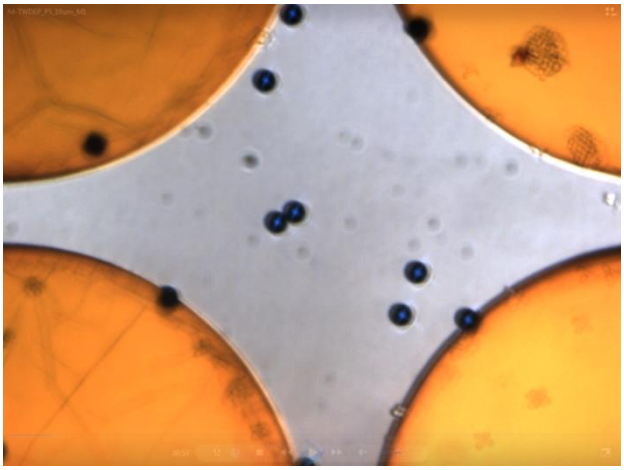

Figure 6.3 10μm Polystyrene microspheres characterized by quadrupole characterization chip

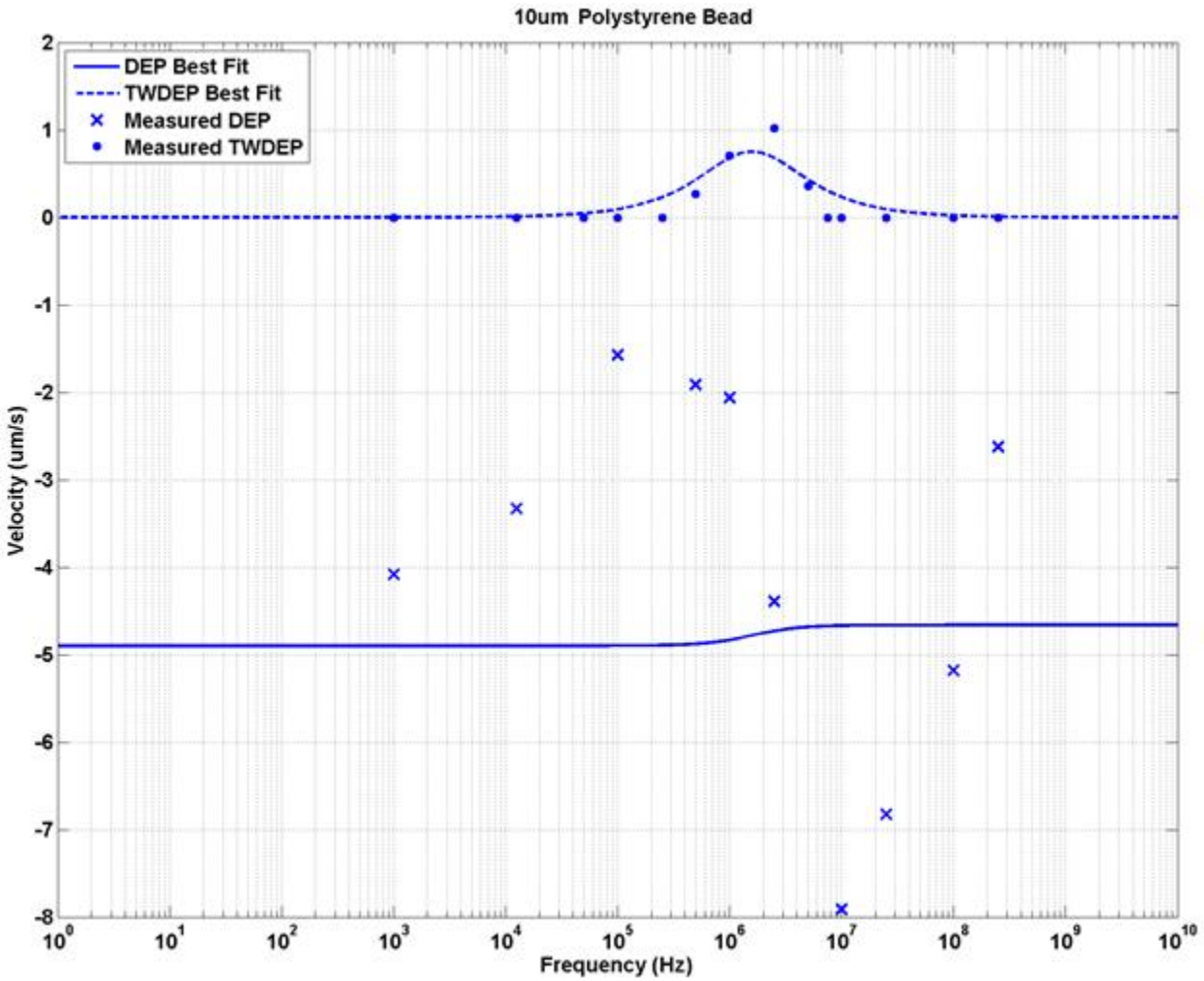

Figure 6.4 Measured DEP and TWDEP velocities for 10μm Polystyrene microspheres and best-fit curves

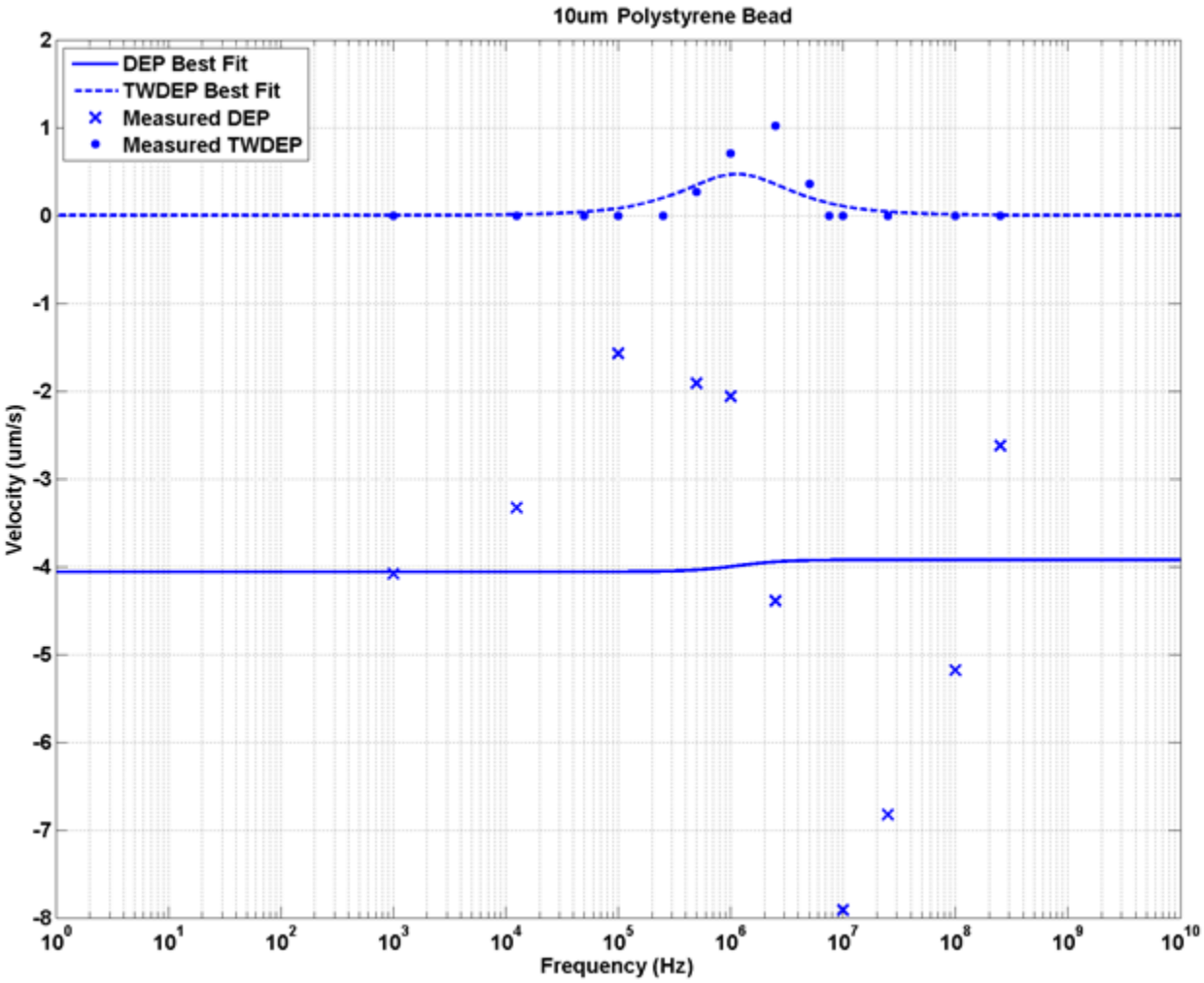

Figure 6.5 Measurements for 10μm Polystyrene microspheres and models with averaged best-fit parameters

Table 6.1 10μm Polystyrene microspheres model parameters extracted from measurements

	10um PS
r	5.143×10^{-6} m
σ_p	5.03×10^{-5} S/m
ε_p	$2.55\varepsilon_0$

6.1.2 Polystyrene-COOH Microspheres (10um)

The second particle type characterized were the 10μm polystyrene-COOH microspheres shown in figure 6.6. The data points in the plots of figure 6.7 are the DEP and TWDEP velocity measurements. The measured TWDEP velocity spectrum peaked at 2.5 MHz at a velocity of -0.81 μm/s and decreased for all measurements at frequencies above and below 2.5 MHz. At frequencies below 500 kHz and above 50 MHz, there was little to no observable particle rotation. All rotations observed occurred in the counter-clockwise direction, the direction opposite the positive phase gradient. These observations are in reasonably good agreement with the predicted results using the ohmic-dielectric sphere model of section 3.2. Both TWDEP profiles are negative at all frequencies where motion was observed. The location of the two peak frequencies were different, 1.17 MHZ versus 2.5 MHz, but are again reasonably close when considered on a logarithmic scale.

The DEP measurements were again in agreement with some of the key features from the original model. The particles always undergo negative dielectrophoresis in this medium, as the DEP velocities were negative at all observed frequencies. The magnitudes of the DEP forces are also much larger than the TWDEP forces. There also occurred a point of inflection in the DEP profile that coincides with the TWDEP peak velocity. In this case the negative dielectrophoresis forces became more negative as frequency increases, just as the model predicts.

The plot lines of figure 6.7 show the best-fit curves for the TWDEP and DEP measurements to the ohmic-dielectric sphere model from section 3.2. Figure 6.8 shows the fitted curves after averaging the extracted parameters from the two fits and table 6.2 displays the averaged parameter values. The extracted models parameters were generally in good agreement

with the original model of chapter 3 and the model with refined parameters reasonably predicts the behavior of the observed measurements. The biggest difference from the original model was in surface conductivity, and the measured data resulted in a surface conductance parameter value that is approximately twice what was originally thought (1.27 nS versus 2.93 nS). However, this shift in conductivity is what accounts the slight shift in TWDEP peak frequency.

The models and data show good agreement as well when the results of the 10μm PS microspheres of section 6.1 are compared to the results of the 10μm PS-COOH microspheres presented in this section. The models predict and measurements agree that both particle types would exhibit their peak TWDEP velocity at the same frequency, which occurred for both at 2.5 MHz. In addition, the models and data are in agreement that the direction of the TWDEP rotational velocity would be opposite for the two particles. The models also predicted that the forces exerted on the two particle types would be approximately the same in magnitude which was observed as well, peak TWDEP velocities for both were on the order of ~1μm/s and the average DEP velocity for both was much larger in magnitude.

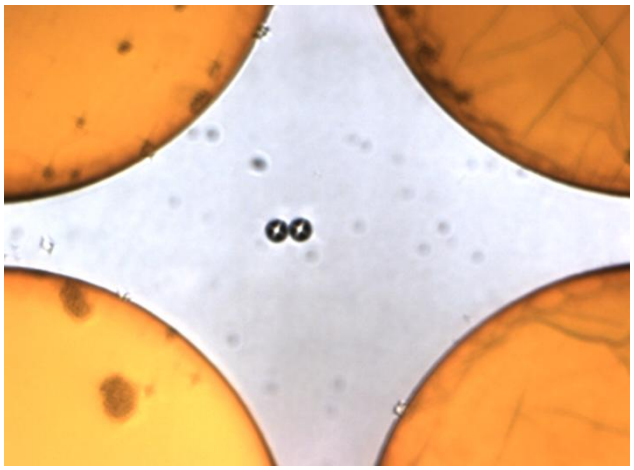

Figure 6.6 10µm Polystyrene-COOH microspheres characterized by quadrupole characterization chip

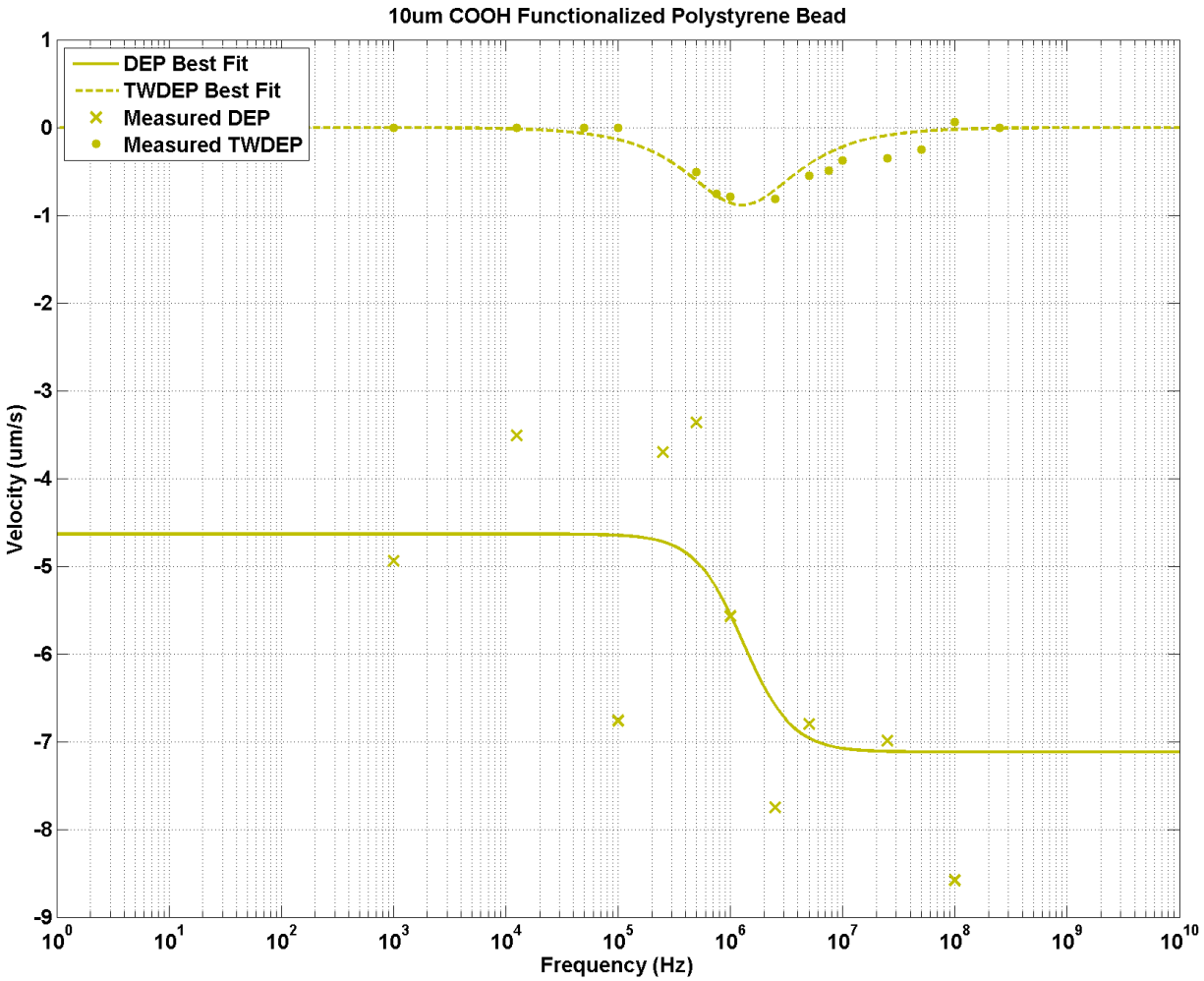

Figure 6.7 Measured DEP and TWDEP velocities for 10µm Polystyrene-COOH microspheres and best-fit curves

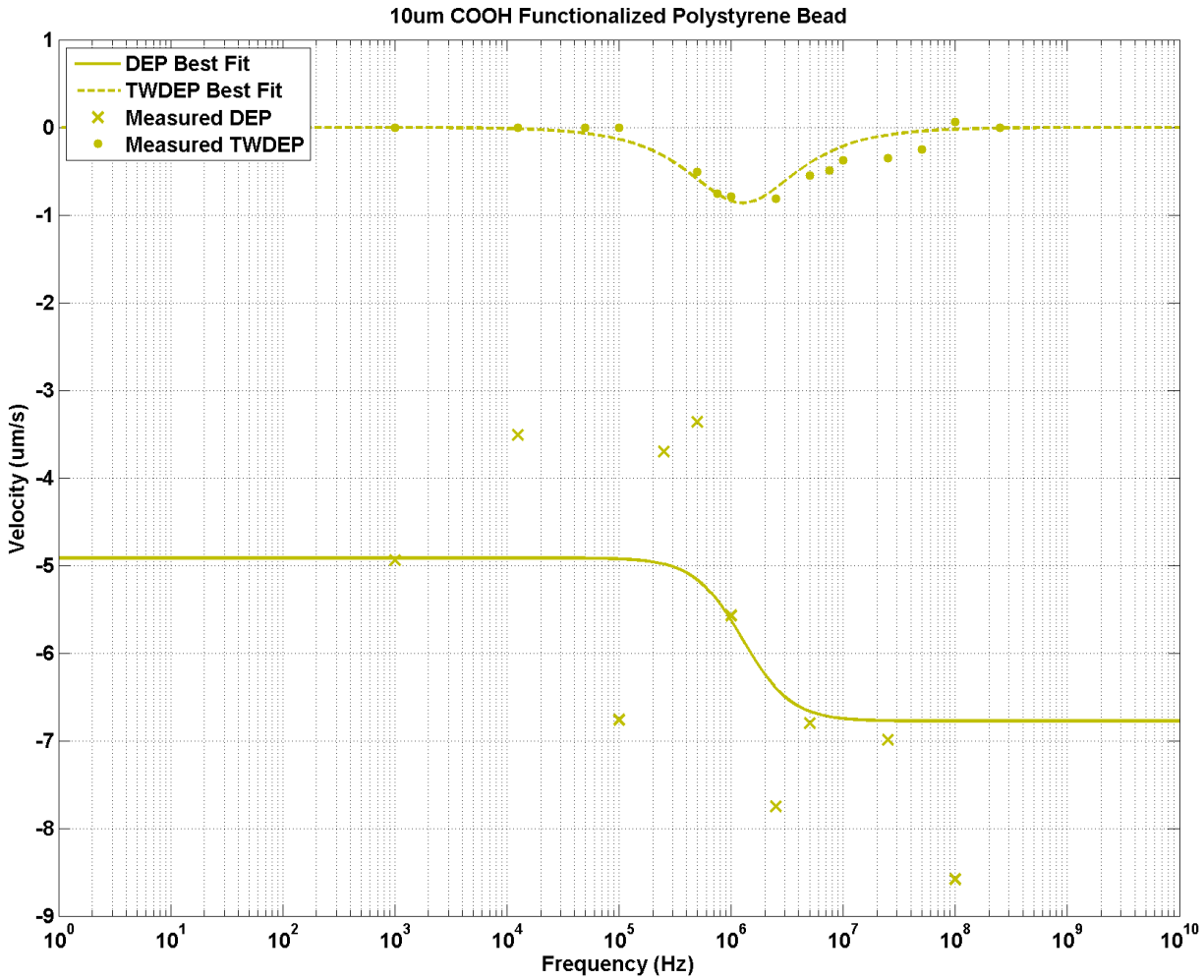

Figure 6.8 Measurements for 10µm Polystyrene-COOH microspheres and models with averaged best-fit parameters

Table 6.2 10µm Polystyrene-COOH microspheres model parameters extracted from measurements

	10um PS-COOH
r	5.088×10^{-6} m
K_s	$2.93 \times 10^{-9}\ S$
σ_{bulk}	$2.22 \times 10^{-14}\ S/\mathrm{m}$
ε_p	$2.55\varepsilon_0$

6.1.3 Polystyrene-COOH Microspheres (6um)

The third particle type characterized were the 6μm polystyrene-COOH microspheres shown in figure 6.9. The data points in the plots of figure 6.10 are the DEP and TWDEP velocity measurements. The measured TWDEP velocity spectrum peaked once again at 2.5 MHz with a velocity of -0.55 μm/s and decreased in magnitude for all measurements at frequencies above and below 2.5 MHz. At frequencies below 50 kHz and above 50 MHz, there was little to no observable particle rotation. All rotations observed occurred in the counter-clockwise direction, the direction opposite the positive phase gradient. These observations are again in reasonably good agreement with the predicted results using the ohmic-dielectric sphere model of section 3.3. Both TWDEP profiles are negative at all frequencies where motion was observed. The location of the two peak frequencies between the model and data were again different, 1.17 MHZ versus 2.5 MHz..

The DEP measurements were in agreement with the key features from the original model, as was the case for the 10μm PS-COOH. The particles always undergo negative dielectrophoresis in this medium, the magnitudes of the DEP forces are also much larger than the TWDEP forces, and there is a point of inflection in the DEP profile that coincides with the TWDEP peak velocity that decreases with increasing frequency.

The plot lines of figure 6.10 show the best-fit curves for the TWDEP and DEP measurements to the ohmic-dielectric sphere model from section 3.3. Figure 6.11 shows the fitted curves after averaging the extracted parameters from the two fits and table 6.3 displays the averaged parameter values. The extracted models parameters were in good agreement with the

original model of from section 3.3. As was the case for the 10μm PS-COOH microspheres, the extracted surface conductance was higher than the expected (0.78 nS versus 3.5 nS).

The models and data show good agreement as well when the results of the 10μm PS-COOH microspheres of section 6.2 are compared to the results of the 6μm PS-COOH microspheres presented in this section. The models predict that both particle types will travel at their maximum TWDEP velocity at the same frequency and always in the same direction, which the measurements reflected. The key difference between the two particle types is radius, which in turn affects the velocity magnitude. Since the 6μm PS-COOH microspheres have a smaller radius than the 10μm PS-COOH microspheres the expectation is that they will travel slower, which was the case for the measurements (-0.55 μm/s peak versus -0.81 μm/s peak).

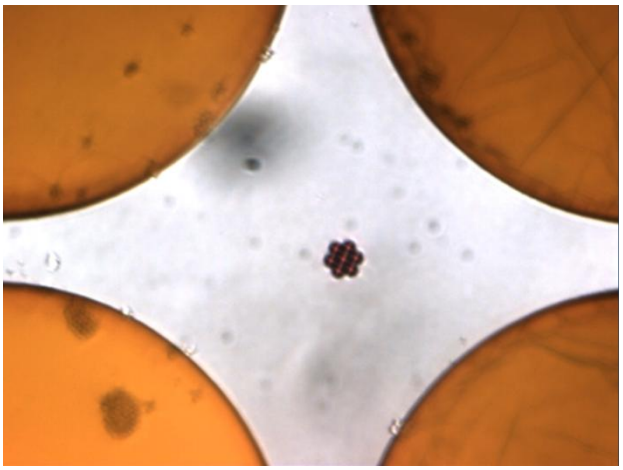

Figure 6.9 6μm Polystyrene-COOH microspheres characterized by quadrupole characterization chip

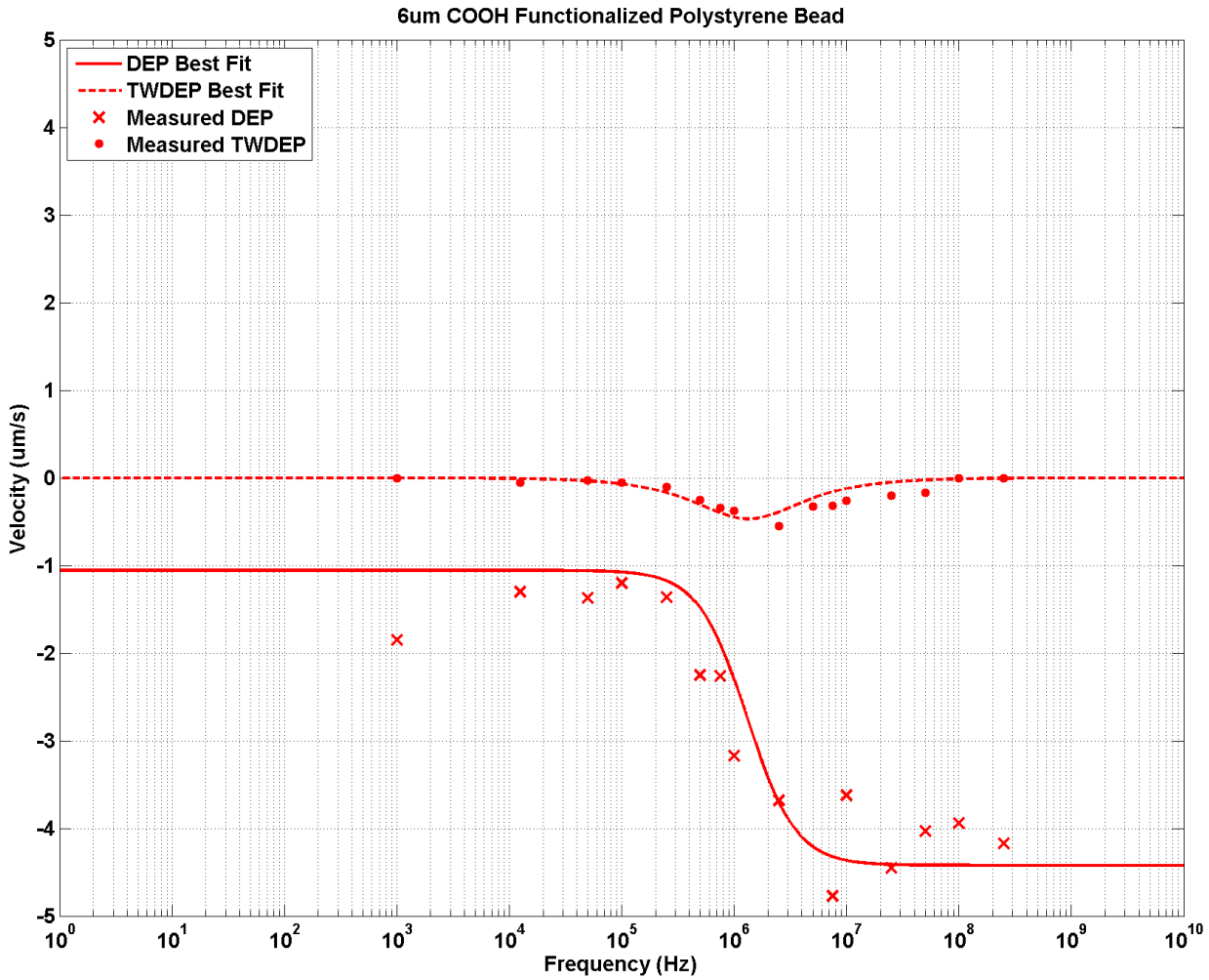

Figure 6.10 Measured DEP and TWDEP velocities for 6μm Polystyrene-COOH microspheres and best-fit curves

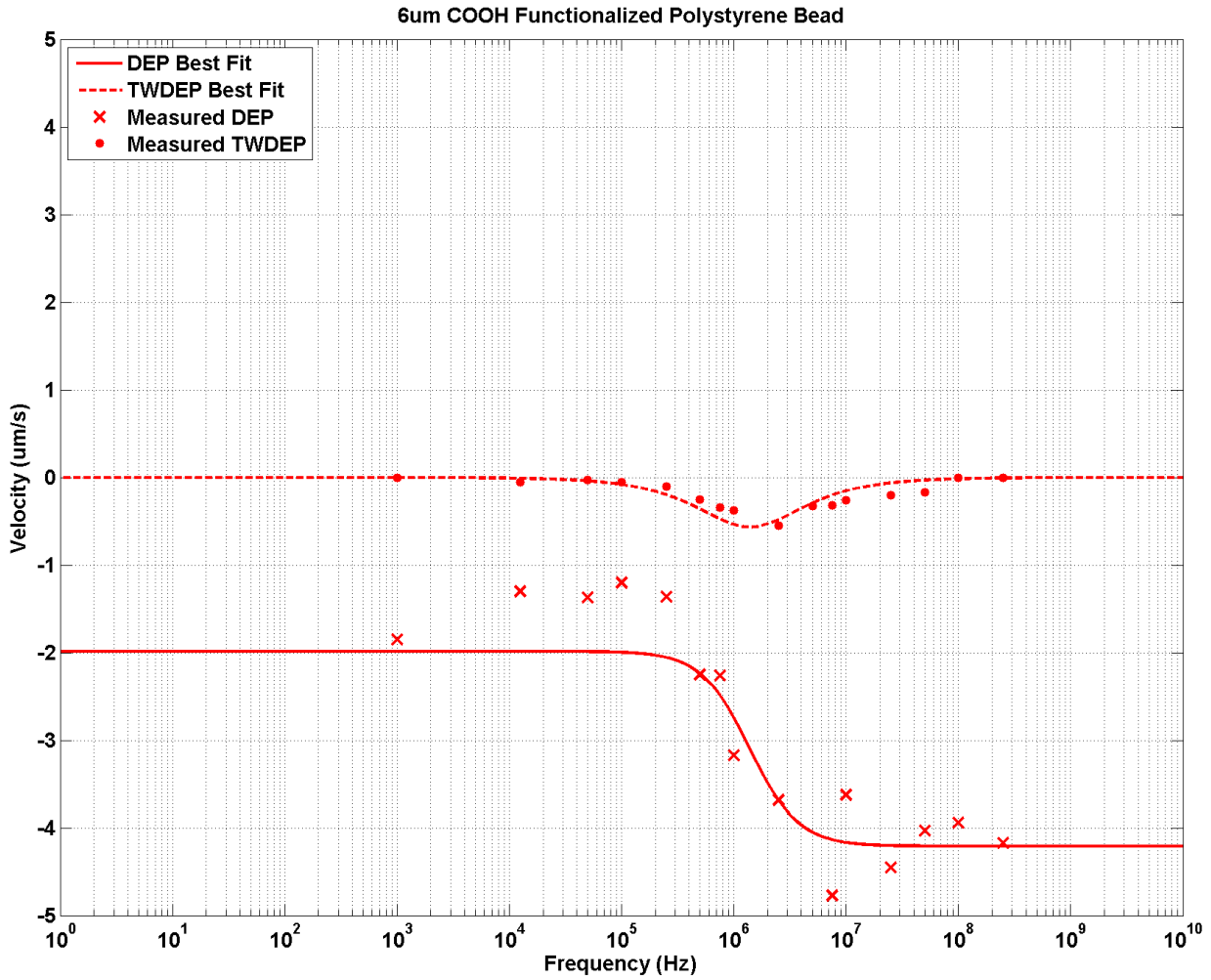

Figure 6.11 Measurements for 6μm Polystyrene-COOH microspheres and models with averaged best-fit parameters

Table 6.3 6μm Polystyrene-COOH microspheres model parameters extracted from measurements

	6um PS-COOH
r	3.11×10^{-6} m
K_s	$3.5 \times 10^{-9}\ S$
σ_{bulk}	$2.59 \times 10^{-10}\ S/\mathrm{m}$
ε_p	$2.55\varepsilon_0$

6.1.4 Live Yeast Cells

The fourth particle type characterized is the living yeast cells shown in figure 6.12. The particles characterized thus far are manufactured and do not occur naturally, therefore there tends to be a low amount of variability between particles of a given type. However, that is not the case for biological specimens, as there is a continuous spectrum of particle types within a given subtype, such as is the case for living yeast cells. It would not be possible to characterize a sample size that is truly representative of all the possibilities within a reasonable amount of time and is a subject matter for research on its own. Therefore, the decision was made to accurately characterize an individual cell that we would take to be representative of the majority. The living yeast cells used in experiments were always taken from cell cultures that were no less than 24 hours old, and less than 48 hours old, while still in the budding stage of their life cycle[48]. A cell was selected that also had an average radius approximately equal to what was used in the original models, 3μm.

The data points in the plots of figure 6.13 are the DEP and TWDEP velocity measurements. The measured TWDEP velocity spectrum had two peaks, a positive one at 250 kHz where the TWDEP velocity was 14.3 μm/s and negative peak at 50 MHz where the measured velocity was -18.14 μm/s. The measured spectrum has a zero-crossing near 7.5MHz where no rotation was observed. At frequencies below 250 kHz and above 50 MHz the TWDEP velocity trended towards zero. These observations are in good agreement with the predicted results using the 5-layer multi-shell model sphere model of section 3.4. The measured results displayed the same unique feature the 5-layer model had of having two TWDEP magnitude peaks, one at a lower frequency that occurs in the same direction as the phase gradient and one at

high frequency that causes the cell to rotate opposite the phase gradient. The multi-shell model parameters originally used predicted that the positive peak, zero-crossing and negative peak frequencies would occur at 88 kHz, 1.5 MHz and 73 MHz respectively and the actual measured frequencies occurred at 250kHz, 7.5 MHz and 50 MHz, which is reasonably close considering the large variation that could occur using biological specimens.

The DEP measurements of the cell also had good agreement with the frequency dependent behavior of the original model from section 3.4. At low frequencies, the cell exhibited negative dielectrophoresis, and then gradually positive dielectrophoresis as the frequency increased. The observed crossover frequency occurred around 200 kHz while the model predicted a crossover at 30 kHz. Just as was the case with the model, the peak magnitudes of the observed positive dielectrophoresis forces were significantly larger than the negative dielectrophoresis forces. The model predicted that the positive dielectrophoresis forces would reach its peak at 1 MHz, while the observed positive dielectrophoresis peak occurred at 5 MHz. The model predicted that live yeast would again exhibit weak negative dielectrophoresis forces after 200MHz. The DEP velocity of our sample also rapidly declined after its positive dielectrophoresis peak, however at our maximum possible test frequency of 250 MHz, the yeast cell had no observable movement due to DEP indicating that was the frequency nearest its second zero crossing frequency. One key difference between the model and observations is that for the model, the magnitude of the DEP forces are generally larger than the magnitude of the TWDEP forces however the opposite was true for the measurements and is accounted for via adjustment of the model parameters.

The plot lines of figure 6.13 show the best-fit curves for the TWDEP and DEP measurements to the 5-layer multi-shell model from section 3.4. Figure 6.14 shows the fitted

curves after averaging the extracted parameters from the two fits and table 6.4 displays the averaged model parameter values.

The models and measured data show good agreement when compared to the results of the polystyrene microspheres characterized in the previous sections. As the models predicted, the peak magnitude of the forces exerted on living cells was much larger than the peak magnitudes for polystyrene spheres. The largest observed velocity magnitude for live yeast was 18.14 μm/s versus 1.02 μm/s for 10μm polystyrene microspheres.

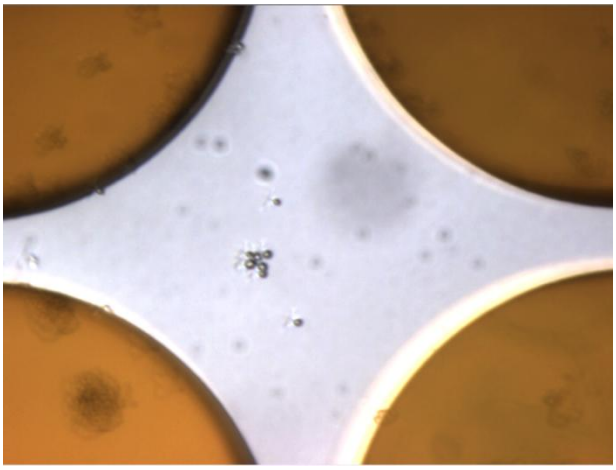

Figure 6.12 Live yeast cells characterized by quadrupole characterization chip

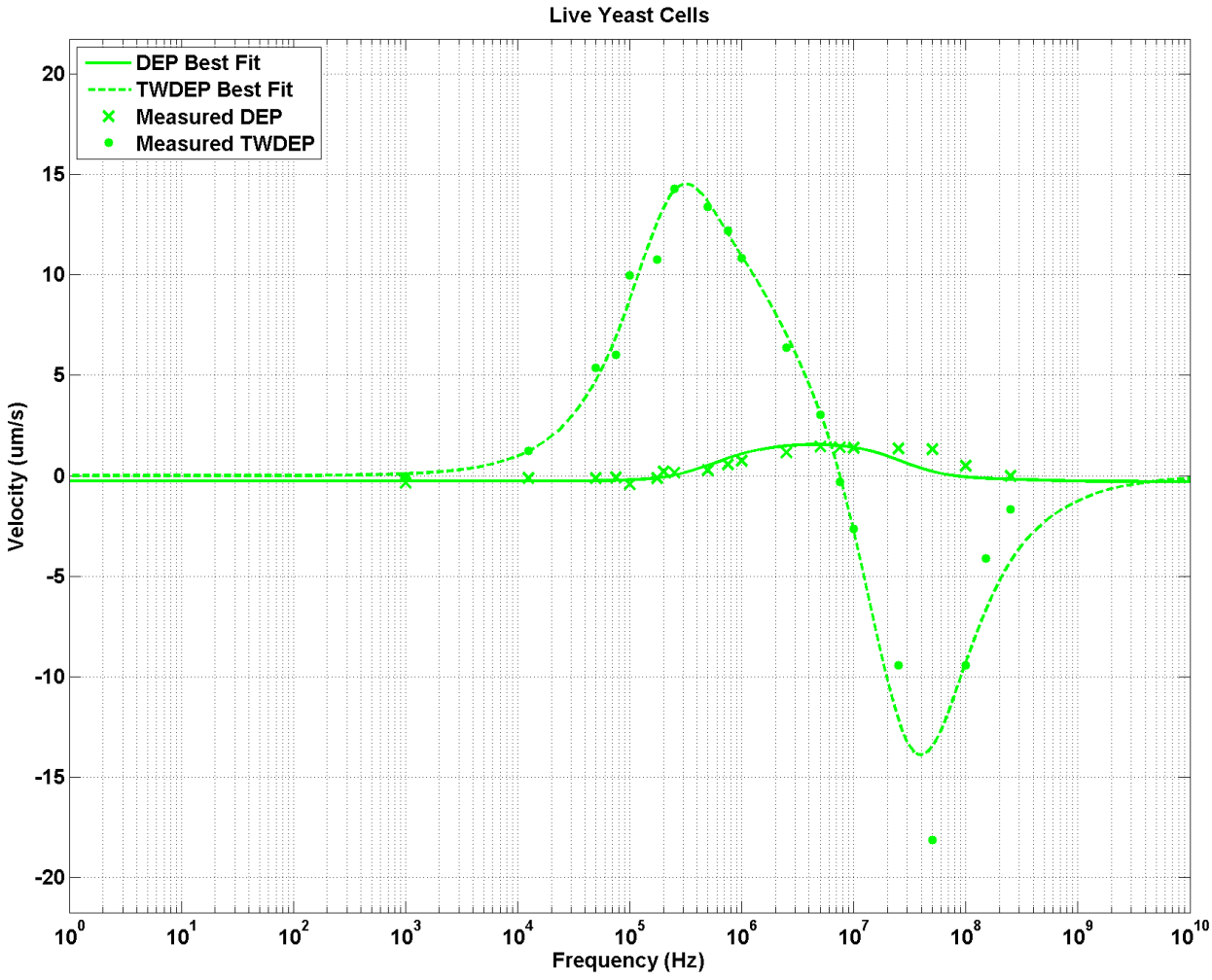

Figure 6.13 Measured DEP and TWDEP velocities for live yeast cells and best-fit curves

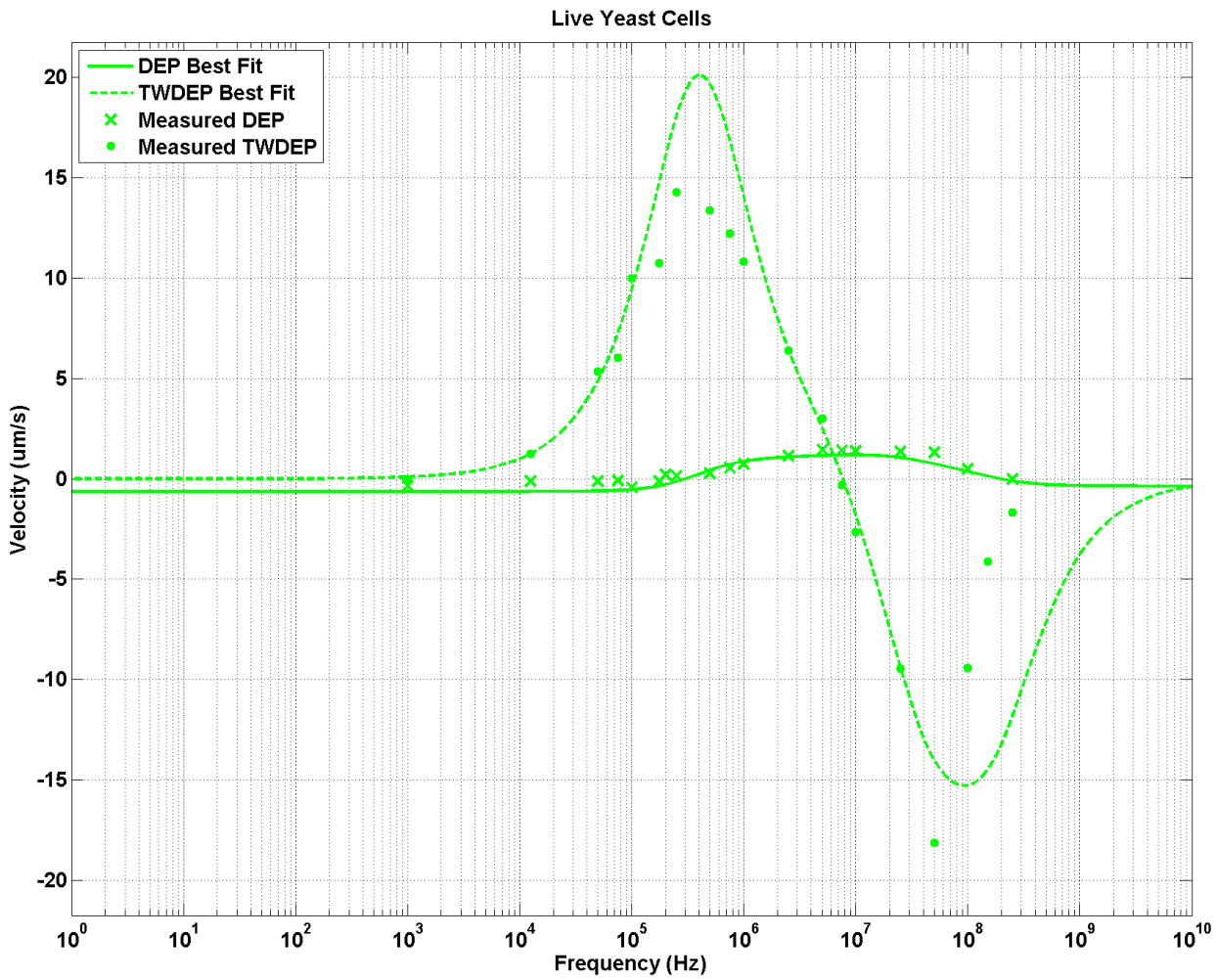

Figure 6.14 Measurements for live yeast cells and models with averaged best-fit parameters

Table 6.4 Live yeast cell model parameters extracted from measurements

	Live Yeast Cells				
	Inner Core	**Membrane**	**Periplasm**	**Inner Wall**	**Outer Wall**
t	$3.01 \times 10^{-6}\ m$	$1.5 \times 10^{-9}\ m$	$3.3 \times 10^{-8}\ m$	$1.02 \times 10^{-7}\ m$	$6.45 \times 10^{-8}\ m$
σ	$2.77 \times 10^{-1}\ S/m$	$7.65 \times 10^{-7}\ S/m$	$3.90 \times 10^{-3}\ S/m$	$4.40 \times 10^{-3}\ S/m$	$2.23 \times 10^{-1}\ S/m$
ε	$51.0\varepsilon_0$	$2.5\varepsilon_0$	$15.9\varepsilon_0$	$69.7\varepsilon_0$	$6.6\varepsilon_0$

6.1.5 Dead Yeast Cells

The fifth and final particle type we characterize is dead yeast cells and the sample characterized is shown figure 6.15. As is the case for live yeast cells, what can be categorized as a dead yeast cell can span a wide spectrum of possibilities in itself. So as to ensure a measure of uniformity amongst the tested samples, dead yeast cells were prepared in the laboratory instead of using cells that have died due to natural causes. In order to prepare dead cells, live yeast cells from a culture that was older than 24 hours but less than 48 hours were taken and heated to 90° C for 20 minutes, rendering the entire sample non-viable.

The data points in the plots of figure 6.16 are the DEP and TWDEP velocity measurements. The measured TWDEP velocity spectrum had two peaks, a positive one at 2.5 MHz where the TWDEP velocity was 2.75 μm/s and negative peak at 25 MHz where the measured velocity was -5.53 μm/s. The measured spectrum has a zero-crossing at a frequency between 5MHz and 7.5MHz. At frequencies below 2.5 MHz and above 25 MHz the TWDEP velocity trended towards zero. The frequency dependent observations made here are not in good agreement with the predicted results from the 3-layer multi-shell model sphere model of section 3.5, suggesting that the parameters require significant refinement.

The DEP measurements of the cell had moderate agreement with the frequency dependent behavior of the original model from section 3.5. At low and high frequencies, both the model and data exhibit negative dielectrophoresis. Both also displayed a small increase in the DEP spectrum before decreasing at high frequency. However, this small peak was observed at 10 MHz in the recorded data and 1.5 MHz for the original model. Also, weak positive

dielectrophoresis effects were observed in the measurements at this peak, whereas the model did not show an increase to the degree that would cause positive dielectrophoresis to be observed.

The plot lines of figure 6.16 show the best-fit curves for the TWDEP and DEP measurements to the 3-layer multi-shell model from section 3.5. Figure 6.17 shows the fitted curves after averaging the extracted parameters from the two fits and table 6.5 displays the averaged model parameter values. The most significant difference between the original model parameters and the extracted parameters is that all of the extracted conductivity values are significantly larger than their model counterparts, accounting for the difference in shapes and locations of the peak frequencies.

Whatever the physiological source of the discrepancy between the original model at the extracted parameters may be, the key finding from these results is that the measured DEP and TWDEP responses have unique features, as do all the particles from our library that we characterize in this chapter and our time-multiplexing dielectrophoresis method can be used to exploit those differences in separations.

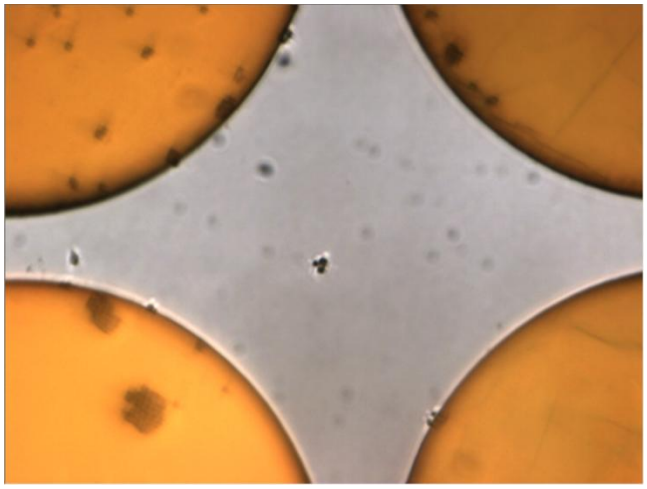

Figure 6.15 Dead yeast cells characterized by quadrupole characterization chip

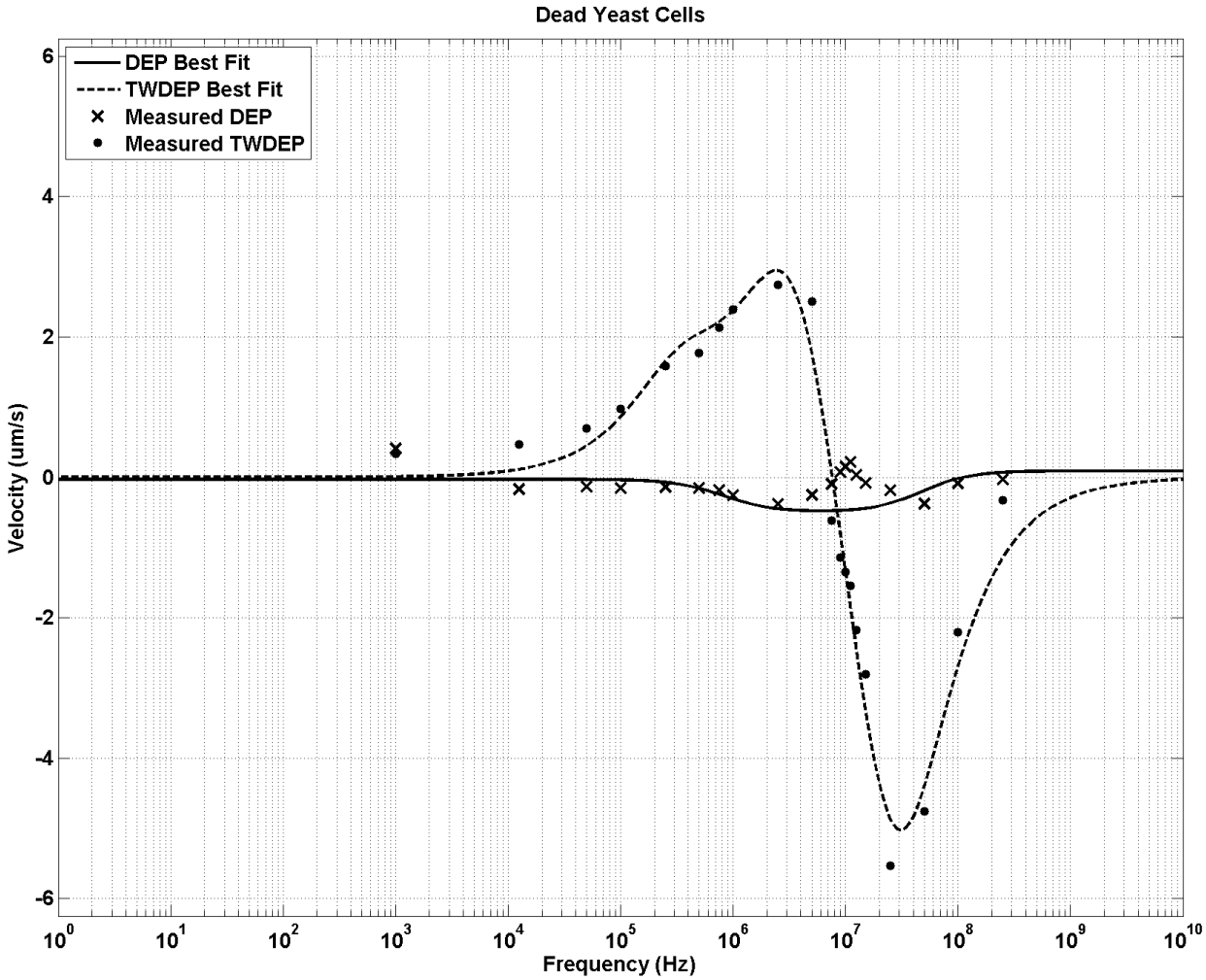

Figure 6.16 Measured DEP and TWDEP velocities for live yeast cells and best-fit curves

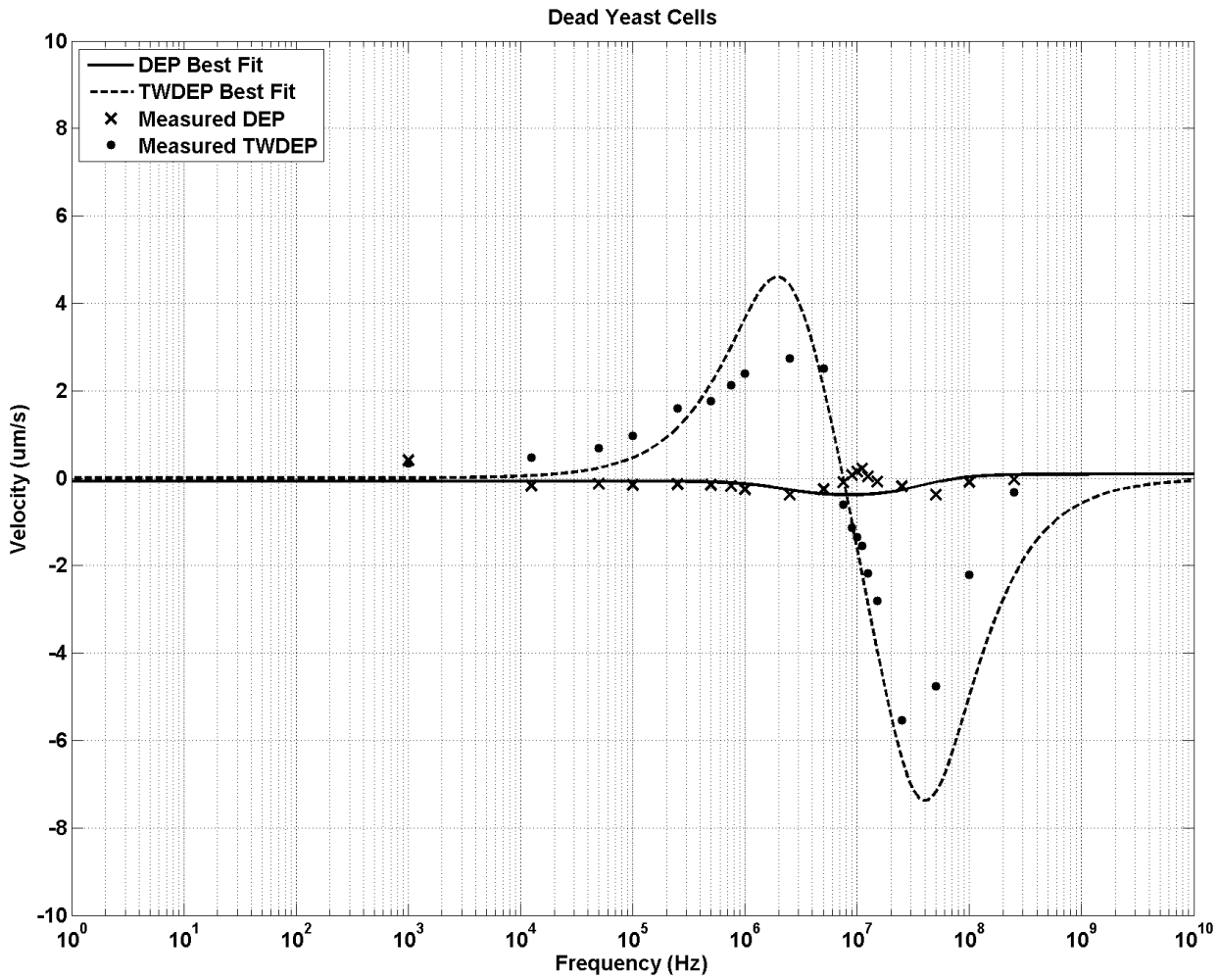

Figure 6.17 Measurements for dead yeast cells and models with averaged best-fit parameters

Table 6.5 Dead yeast cell model parameters extracted from measurements

	Dead Yeast Cells		
	Inner Core	**Membrane**	**Wall**
t	$3.0 \times 10^{-6}\ m$	$2.0 \times 10^{-9}\ m$	$2.53 \times 10^{-7}\ m$
σ	$3.56 \times 10^{-1}\ S/m$	$2.45 \times 10^{-4}\ S/m$	$4.50 \times 10^{-3}\ S/m$
ε	$50\varepsilon_0$	$6\varepsilon_0$	$60\varepsilon_0$

6.2 DISCUSSION OF RESULTS

This technique presented in this dissertation based on the fact that particles that vary in type and composition have different electrical characteristics will have unique responses when placed in the presence of a dielectrophoresis field. Our library consists of particles that have differences in size, composition and surface chemistry in comparison to one another. Table 6.6 is a summary of the results of this chapter and presents all the extracted parameters together for comparison. The results show that the differences in makeup and type can be mapped backed to differences in electrical characteristics. In turn, those electrical differences resulted in differences in their response to dielectrophoresis fields. It is these differences in responses that we exploit in using time-multiplexing dielectrophoresis to separate particles.

The majority of the models provided good fits to the measured data. However, there was a considerable amount of variation between the best-fit curves and measured data for the DEP spectra of 10μm PS and 10μm PS-COOH. The source of the variation is unknown. However, as will be demonstrated in the next chapter, specific knowledge of the DEP spectrum is less critical if it is known that the DEP spectrum remains negative at all frequencies, as it does in this case. A DEP spectrum that is always negative allows the particle to levitate regardless of frequency and have the particle's lateral direction be guided by the TWDEP spectrum.

In the next chapter we use the characterization results shown in table 6.6 to carry out a detailed analysis of the separability of the particle types using our time-multiplexing dielectrophoresis method.

Table 6.6 Summary of Experimental Characterization Results

	10um PS
r	5.143×10^{-6} m
σ_p	$5.03 \times 10^{-5}\ S/\mathrm{m}$
ε_p	$2.55\varepsilon_0$

	10um PS-COOH
r	5.088×10^{-6} m
K_s	$2.93 \times 10^{-9}\ S$
σ_{bulk}	$2.22 \times 10^{-14}\ S/\mathrm{m}$
ε_p	$2.55\varepsilon_0$

	6um PS-COOH
r	3.11×10^{-6} m
K_s	$3.5 \times 10^{-9}\ S$
σ_{bulk}	$2.59 \times 10^{-10}\ S/\mathrm{m}$
ε_p	$2.55\varepsilon_0$

	Dead Yeast Cells		
	Inner Core	Membrane	Wall
t	$3.0 \times 10^{-6}\ m$	$2.0 \times 10^{-9}\ m$	$2.53 \times 10^{-7}\ m$
σ	$3.56 \times 10^{-1}\ S/m$	$2.45 \times 10^{-4}\ S/m$	$4.50 \times 10^{-3}\ S/m$
ε	$50\varepsilon_0$	$6\varepsilon_0$	$60\varepsilon_0$

	Live Yeast Cells				
	Inner Core	Membrane	Periplasm	Inner Wall	Outer Wall
t	$3.01 \times 10^{-6}\ m$	$1.5 \times 10^{-9}\ m$	$3.3 \times 10^{-8}\ m$	$1.02 \times 10^{-7}\ m$	$6.45 \times 10^{-8}\ m$
σ	$2.77 \times 10^{-1}\ S/m$	$7.65 \times 10^{-7}\ S/m$	$3.90 \times 10^{-3}\ S/m$	$4.40 \times 10^{-3}\ S/m$	$2.23 \times 10^{-1}\ S/m$
ε	$51.0\varepsilon_0$	$2.5\varepsilon_0$	$15.9\varepsilon_0$	$69.7\varepsilon_0$	$6.6\varepsilon_0$

7.0 SEPARABILITY OF PARTICLES USING TIME-MULTIPLEXED DIELECTROPHORESIS

Once the dielectrophoretic behaviors of specific particle types are known, via experimental data or accurate models, as was done in the previous chapter, then it is possible to determine how time-multiplexing dielectrophoresis can be used to separate particles from one another and the effectiveness with which we can do so. In this chapter, we carry out a detailed analysis on the separability of every combination of particles included in our library.

The DEP and TWDEP force spectra of particles depends on a wide range of variables (e.g., permittivity, conductivity, structure, etc.). These spectra are in most cases extremely non-linear and both force components must be considered simultaneously when evaluating the separability between particle types. Therefore, finding an optimal set of time-multiplexing dielectrophoresis configuration parameters to separate particle types is not trivial. For any pair of particles we wish to separate, it must be determined which two frequencies should be multiplexed (ω_1, ω_2), what the phase gradients associated with those frequencies should be set to $(\nabla\phi_{x1}, \nabla\phi_{x2})$ and how long the relative duration of the application of the fields should be (the duty cycle, *D*).

In order to determine what that these multiplexing parameters should be, we wrote a custom software program in MATLAB to find solutions within this multi-dimensional space using a brute-force approach. For every particle in our library, we evaluated its average net

velocities $\left(\bar{v}_{p_x}, \bar{v}_{p_y}\right)$, according to the derived time-multiplexing expressions of equations 4.13 and 4.14, for a wide selection of frequency pairs, across the entire range of possible duty cycles $(0 \leq D \leq 1.0)$ and for every combination of phase gradient sequences $[(-\nabla\phi_{x1}: -\nabla\phi_{x2}), (-\nabla\phi_{x1}: +\nabla\phi_{x2}), (+\nabla\phi_{x1}: -\nabla\phi_{x2}), (+\nabla\phi_{x1} + \nabla\phi_{x2})]$. The frequency sequences selected for evaluation included every combination of frequencies for which we had taken experimental measurements. This choice was made because at those points the extracted models are the most accurate, it allows us to directly compare results using both models and measured data, and significantly reduces the computational cost. At each calculated configuration the separability conditions of 4.15 and 4.16 (that the particles move in opposite directions and remain levitated) were checked to see whether or not the particles would be separable. The metric used to determine if a separable parameter configuration is better than another is the rate at which the configuration would cause particle types to migrate apart, the magnitude of the differential lateral velocity $\bar{v}_{diff}$.

Whenever a solution is found, there is a range of duty cycles associated with it under which the particles will be separable. In order to reduce the complexity of the solution space by one dimension, the mean duty cycle within that range was selected. The mean duty cycle was used rather than simply selecting the duty cycle at which the maximum differential velocity occurs because situations arise where the differential velocity is maximized by a duty cycle that forces the lateral net velocity of one particle type to zero. We wish to avoid this situation and apply field configurations that will cause each type to be guided towards a particular location as oppose to having one type be stagnant while the other type moves. Finding a truly optimal solution is a matter for future research, and could be developed if additional constraints were formulated.

7.1 ANALYTICAL SEPARABILITY RESULTS

In the subsections to follow, two results are presented for each pair of particles: the first show the calculated multiplexing parameters based on the actual recorded observations and the other result shows parameters based on the extracted and averaged best-fit models from chapter 6. Comparisons of these results give us an indication of how sensitive our method is to variation and also a range of configuration parameters to use when carrying out separation experiments on our lab-on-chip hardware platform.

Each result in this section is presented as a three-dimensional plot of separation velocity versus the two multiplexing frequencies. A fourth dimension is included on each plot via a colored surface that maps the average separation duty cycle required to separate. The final muxing parameters selected for each pair of particles correspond to the peak of each plot, where the separation velocity is maximized. In section 7.2 we give a table summary of results.

7.1.1 Live Yeast and Dead Yeast

The first case analyzed is the separation of live and dead yeast cells. The plots of figure 7.1 show their DEP and TWDEP velocity spectra based on the extracted models from chapter 6. This combination of particles presents a case where the particles primary difference is of a physiological nature.

The surface plot of figure 7.2 shows the separation velocity between live and dead cells based on the experimental data. The peak differential velocity is 6.55 μm/s and occurs when $\omega_1 = 100\ kHz$ and $\omega_2 = 25\ MHz$ and only the frequencies are multiplexed (not the phases) at a duty cycle of 81%.

Figure 7.3 shows the separation velocity between live and dead cells based on the extracted models. At the same frequency pair the measured data predicted its peak differential velocity, the models also predict that the cells will be separable using time-multiplexed dielectrophoresis. When multiplexing between those frequencies at a duty cycle of *D = 80%*, the models predict a differential velocity of *6.57* μm/s. The maximum separation velocity based on the extracted models for live and dead yeast cells is 13.33 μm/s. This maximum occurs when multiplexing between $\omega_1 = 250\ kHz$ and $\omega_2 = 50\ MHz$ at a duty cycle of 85%.

For this combination of live and dead yeast cells, a separable solution does not exist if only a single frequency is applied. Both the calculations based off of models and data indicate that the cells can only be separated when time-multiplexing frequency or frequency and phase.

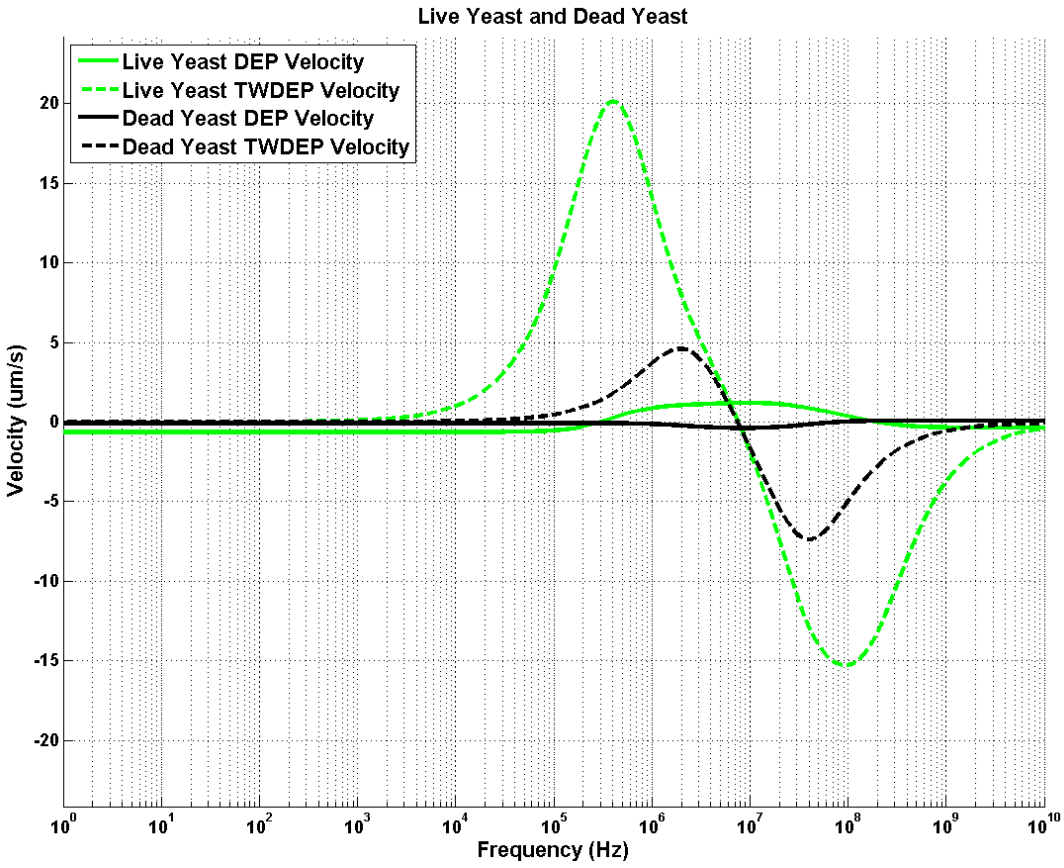

Figure 7.1 DEP and TWDEP velocity spectra for live and dead yeast cells

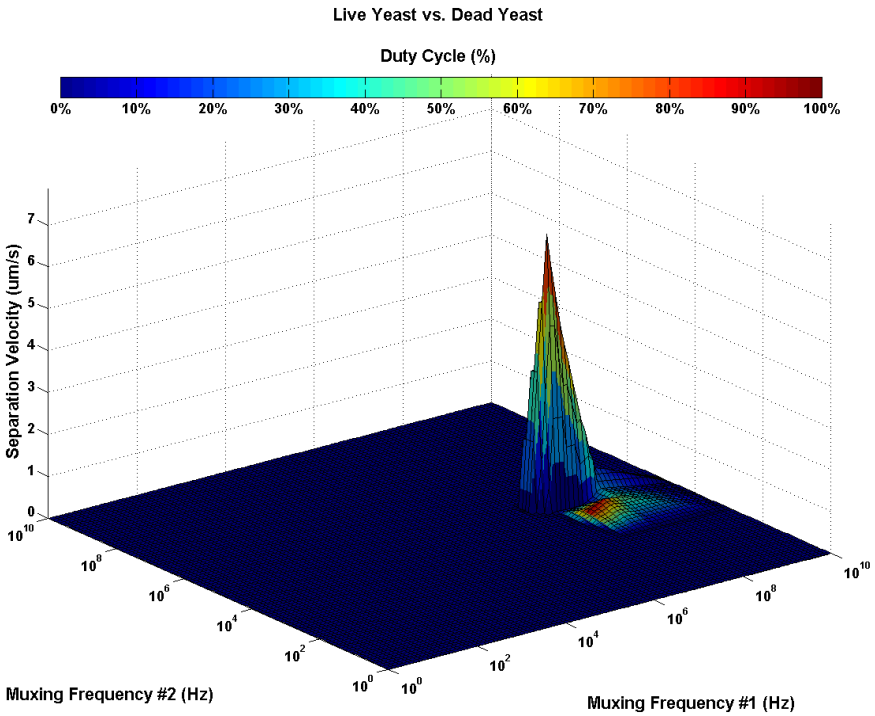

Figure 7.2 Separation velocity for live and dead yeast cells when field configurations are frequency multiplexed. $max(v_{diff}) = 6.55\mu m/s$ when $\omega_1 = 100\ kHz$, $\omega_2 = 25\ MHz$, and $D = 0.81$

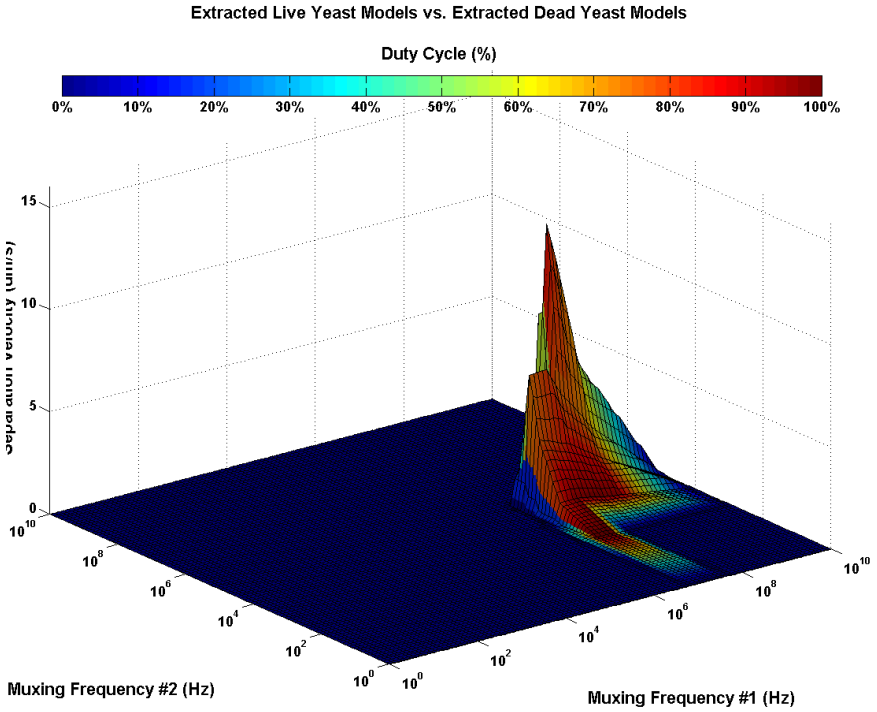

Figure 7.3 Separation velocity for extracted live and dead yeast cell models when field configurations are frequency multiplexed. $max(v_{diff}) = 13.33\mu m/s$ when $\omega_1 = 250\ kHz$, $\omega_2 = 50\ MHz$, and $D = 0.85$

7.1.2 Polystyrene-COOH (10um) and Live Yeast

The second separation case is 10μm polystyrene-COOH microspheres (10μm PS-COOH) versus live yeast cells. The plots of figure 7.4 show their DEP and TWDEP velocity spectra based off the extracted models. This combination of particles presents a case where the particles have major differences in size and internal composition.

The surface plot of figure 7.5 shows the separation velocity between 10μm PS-COOH and live yeast cells based on the experimental data. The peak differential velocity is 11.16 μm/s and occurs when $\omega_1 = 100\ kHz$ and $\omega_2 = 500\ kHz$ and only the frequencies are multiplexed at a duty cycle of 70%.

Figure 7.6 shows the separation velocity between 10μm PS-COOH and live yeast cells based on the extracted models. The peak differential velocity based off the models and data occur at the same exact frequency pair, $\omega_1 = 100\ kHz$ and $\omega_2 = 500\ kHz$. The models predicts a maximum separation velocity of 12.50 μm/s when these frequencies are multiplexed at a duty cycle of D = 72%.

For this combination of 10μm PS-COOH microspheres and live yeast cells, a separable solution based on the experimental data does not exist when only a single frequency is applied. Calculations on data indicate that the particles can only be separated when time-multiplexing frequency or frequency and phase.

However, the models reveal that a constant frequency, non-multiplexing solutions exists in the low frequency range where both particles undergo negative dielectrophoresis and have traveling-wave dielectrophoresis velocities that are opposite in sign. The maximum separation velocity in this region is 9.56 um/s when $\omega = 100\ kHz$. However, this maximum velocity is

less than what the same models calculate when multiplexing with the previously mentioned configuration, showing that time-multiplexing dielectrophoresis would actually increase separation efficiency in this case.

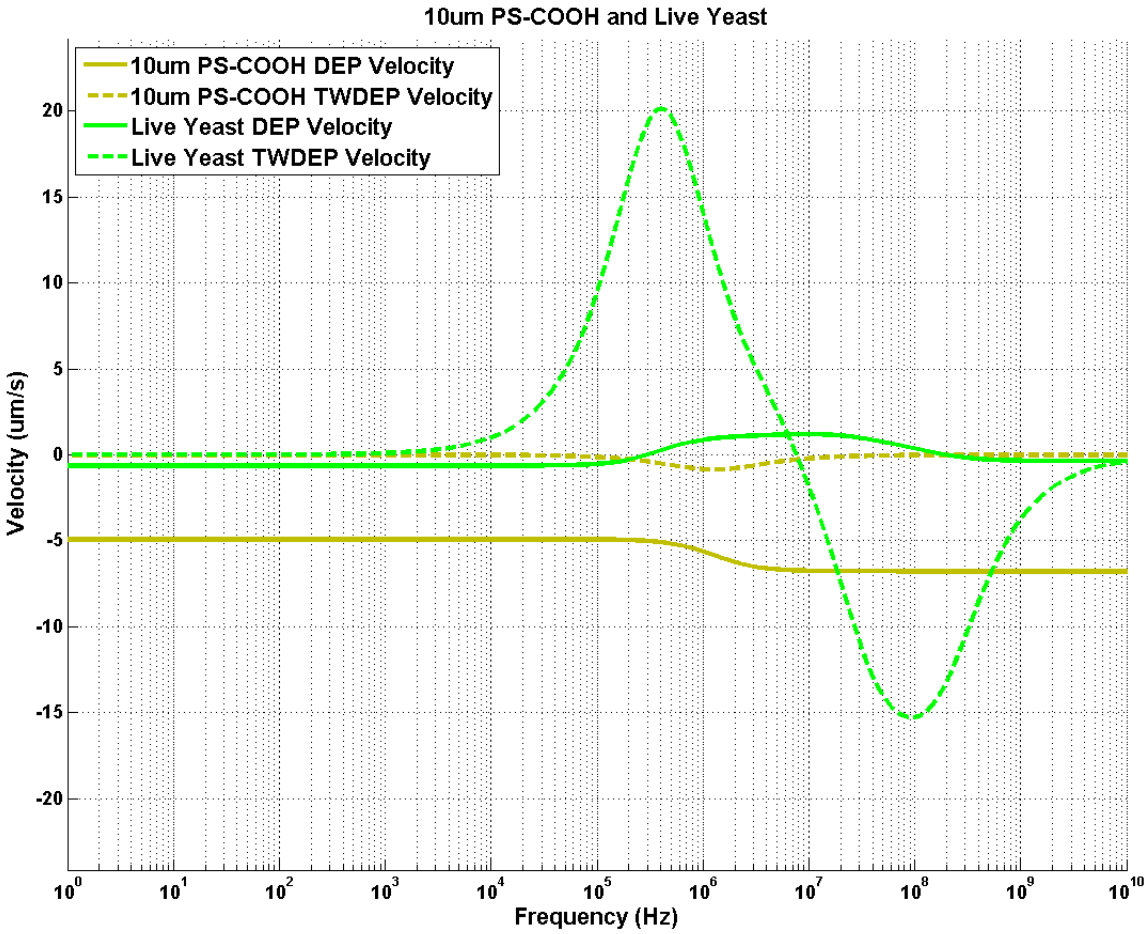

Figure 7.4 DEP and TWDEP velocity spectra for 10μm PS-COOH microspheres and live yeast cells

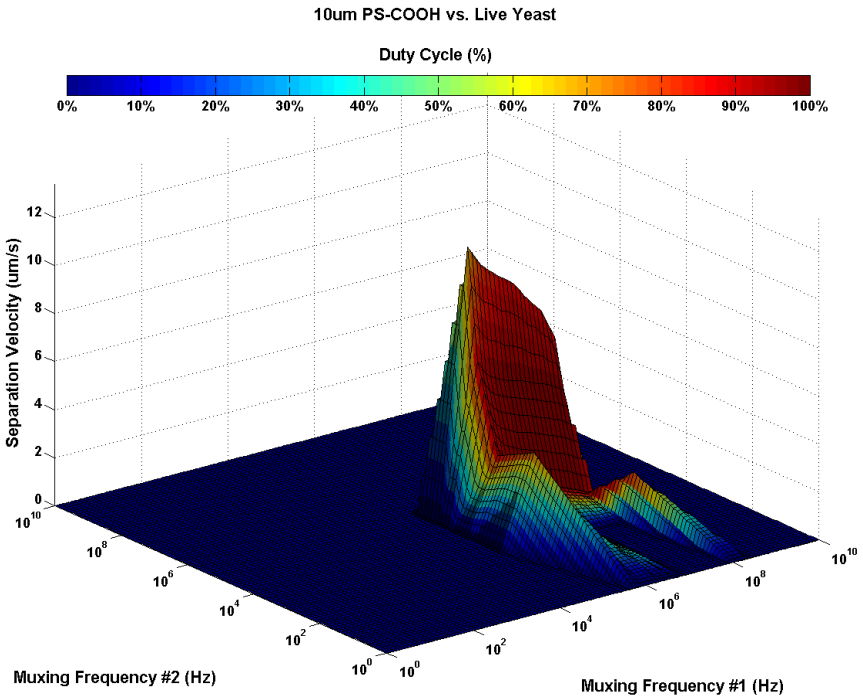

Figure 7.5 Separation velocity for 10μm PS-COOH and live yeast cells when field configurations are frequency multiplexed. $max(v_{diff}) = 11.16\mu m/s$ when $\omega_1 = 100\ kHz$, $\omega_2 = 500\ kHz$, and $D = 0.70$

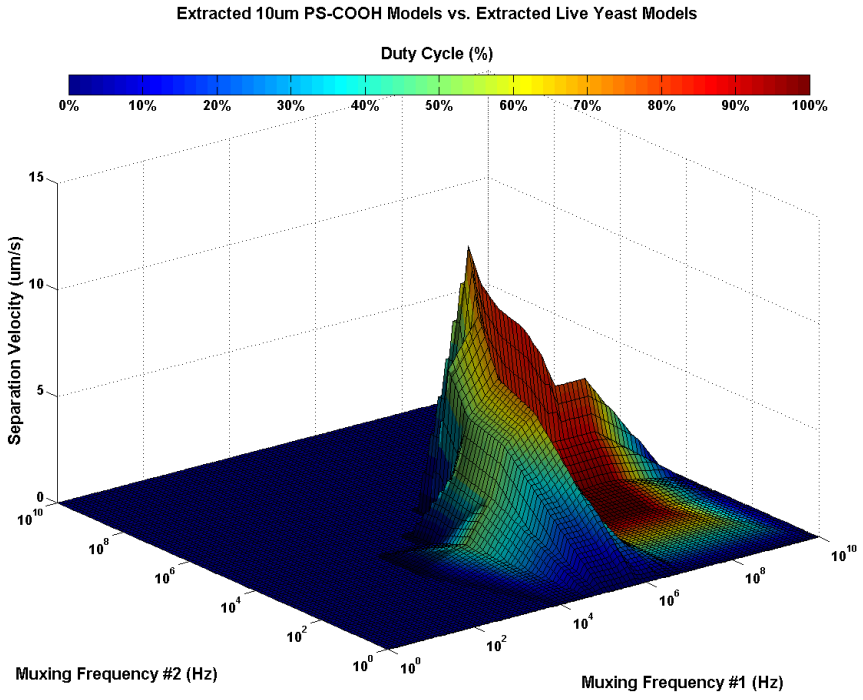

Figure 7.6 Separation velocity for extracted 10μm PS-COOH and live yeast cell models when field configurations are frequency multiplexed. $max(v_{diff}) = 12.50\mu m/s$ when $\omega_1 = 100\ kHz$, $\omega_2 = 500\ kHz$, and $D = 0.72$

7.1.3 Polystyrene-COOH (10um) and Dead Yeast

The third separation case is 10μm polystyrene-COOH microspheres (10μm PS-COOH) versus dead yeast cells. The plots of figure 7.7 show their DEP and TWDEP velocity spectra based on the extracted models. This combination of particles presents the case where the particles have major differences in size and internal composition.

The surface plot of figure 7.8 shows the separation velocity between 10μm PS-COOH and dead yeast cells based on the experimental data. The peak differential velocity is 4.12 μm/s and occurs when $\omega_1 = 25\,MHz$ and $\omega_2 = 250\,MHz$ and both the frequencies and phase gradients are multiplexed at a duty cycle of 66%.

Figure 7.9 shows the separation velocity between 10μm PS-COOH and dead yeast cells based on the extracted models. At the same frequency pair the measured data predicted its peak differential velocity, the models also predict that the cells will be separable using time-multiplexed dielectrophoresis. When multiplexing between those frequencies at a duty cycle of *D = 62%*, the models predict a differential velocity of *4.01* μm/s. The maximum separation velocity based off the extracted models for live and dead yeast cells is 6.06 μm/s. This maximum occurs when multiplexing between $\omega_1 = 2.5\,MHz$ and $\omega_2 = 50\,MHz$ at a duty cycle of 53%.

For this combination of 10μm PS-COOH microspheres and dead yeast cells, separable solutions based on both the experimental data and models do exist for constant, non-multiplexing frequencies. This separation region occurs for a brief range in the low megahertz range where both particles undergo nDEP but have TWDEP velocities that differ in sign. However, the data and models predict respective maximum constant frequency separation velocities of 3.56 μm/s

and 5.11 μm/s at 2.5 MHz, both of which are lower than their phase/frequency multiplexing counterparts. Therefore, time-multiplexing dielectrophoresis would be the more efficient separation technique to use in this case.

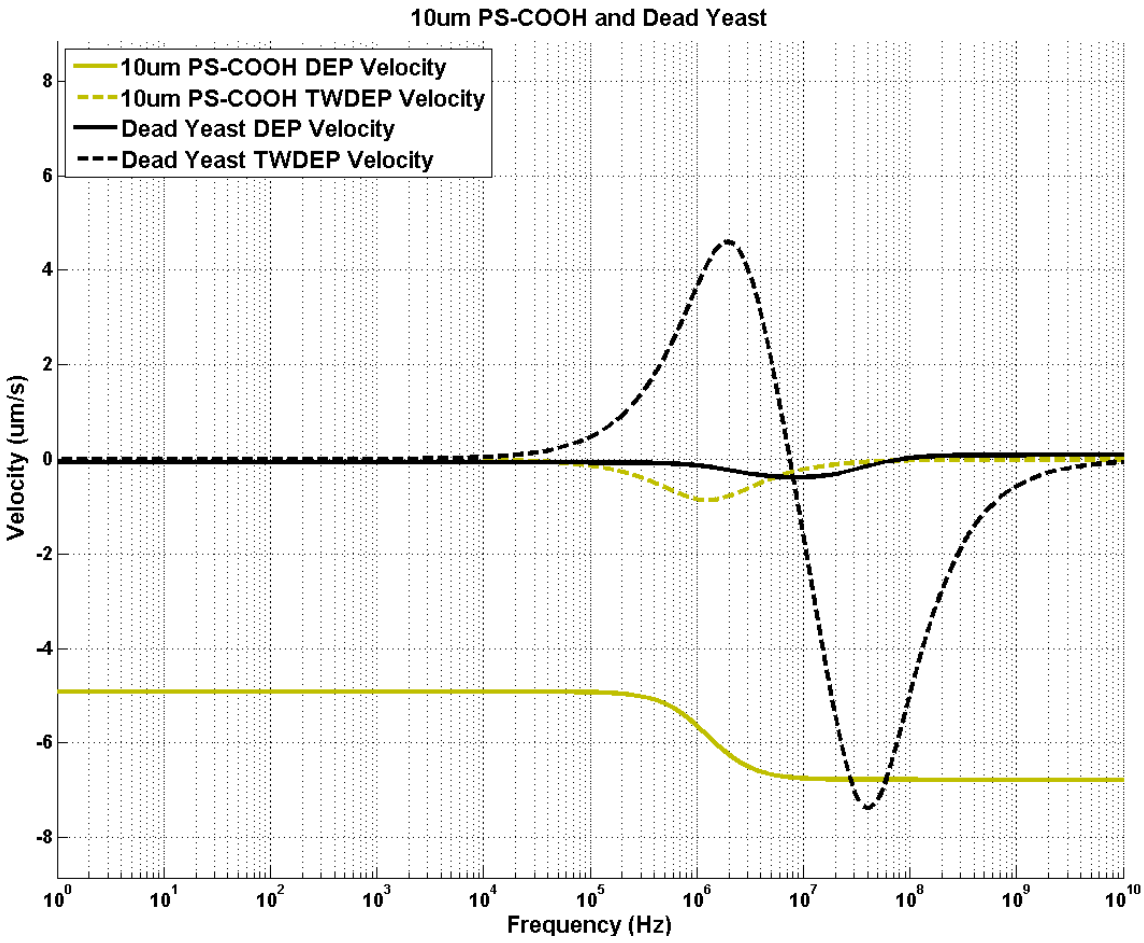

Figure 7.7 DEP and TWDEP velocity spectra for 10μm PS-COOH microspheres and dead yeast cells

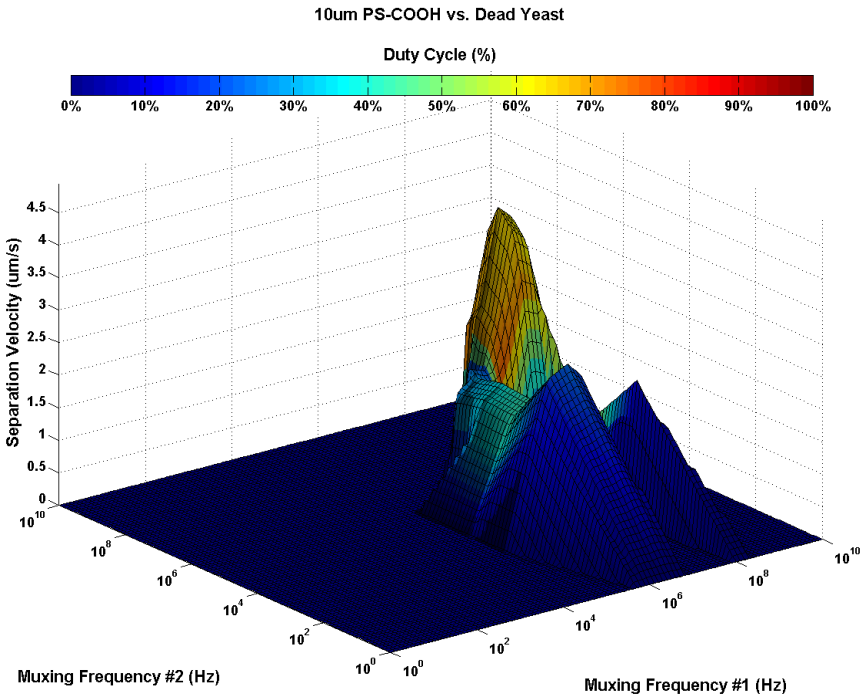

Figure 7.8 Separation velocity of 10µm PS-COOH and dead yeast cells when field configurations are phase and frequency multiplexed. $max(v_{diff}) = 4.12\mu m/s$ when $\omega_1 = 25\ MHz$, $\omega_2 = 250\ MHz$, and $D = 0.66$

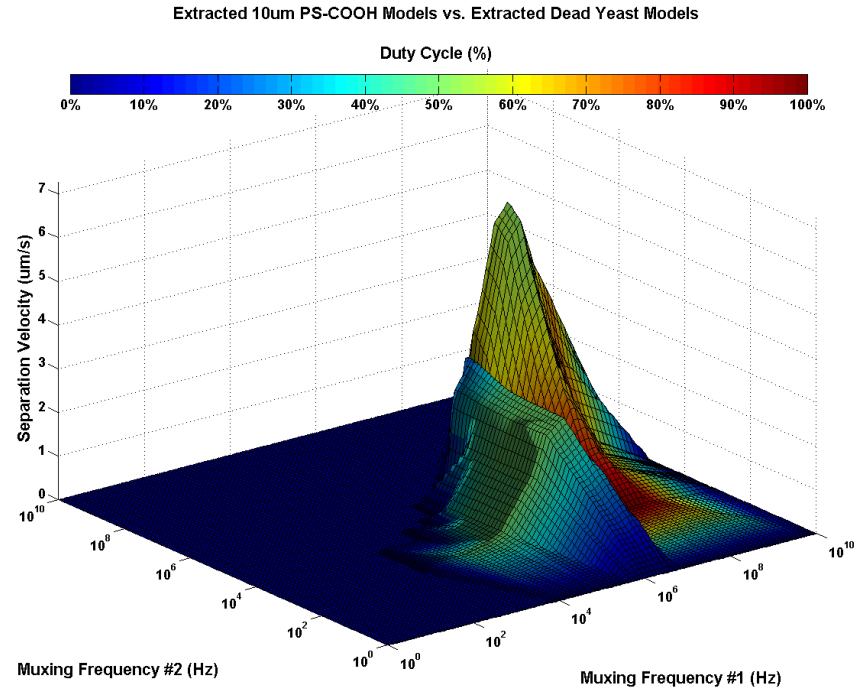

Figure 7.9 Separation velocity of extracted 10µm PS-COOH and dead yeast models when field configurations are phase and frequency multiplexed. $max(v_{diff}) = 6.06\mu m/s$ when $\omega_1 = 2.5\ MHz$, $\omega_2 = 50\ MHz$, and $D = 0.53$

7.1.4 Polystyrene-COOH (10um) and Polystyrene (10um)

The fourth separation case is 10μm polystyrene-COOH microspheres (10μm PS-COOH) versus 10μm polystyrene microspheres (10μm PS). The plots of figure 7.10 show their DEP and TWDEP velocity spectra based on the extracted models. This combination of particles presents case where the particles are on average the same size but vary only in their surface chemistry.

The surface plot of figure 7.11 shows the separation velocity between 10μm PS-COOH and 10μm PS microspheres based on the experimental data. The peak differential velocity is 1.83 μm/s and occurs when $\omega_1 = 2.5MHz$ and $\omega_2 = 2.5MHz$ and the frequencies are multiplexed at a duty cycle of 50%.

Figure 7.12 shows the separation velocity between 10μm PS-COOH and 10μm PS microspheres based off of the extracted models. The peak differential velocity is 1.31 μm/s and occurs when $\omega_1 = 1MHz$ and $\omega_2 = 1MHz$ and the frequencies are multiplexed at a duty cycle of 50%.

For this combination of 10μm PS-COOH and 10μm PS microspheres the maximum separation velocities resulting from both the data and models occur when the two multiplexed frequencies are the same and have a duty cycle of %50, which makes the configuration identical to just applying a constant frequency. Therefore, time-multiplexing dielectrophoresis would not be a more efficient separation method in this case.

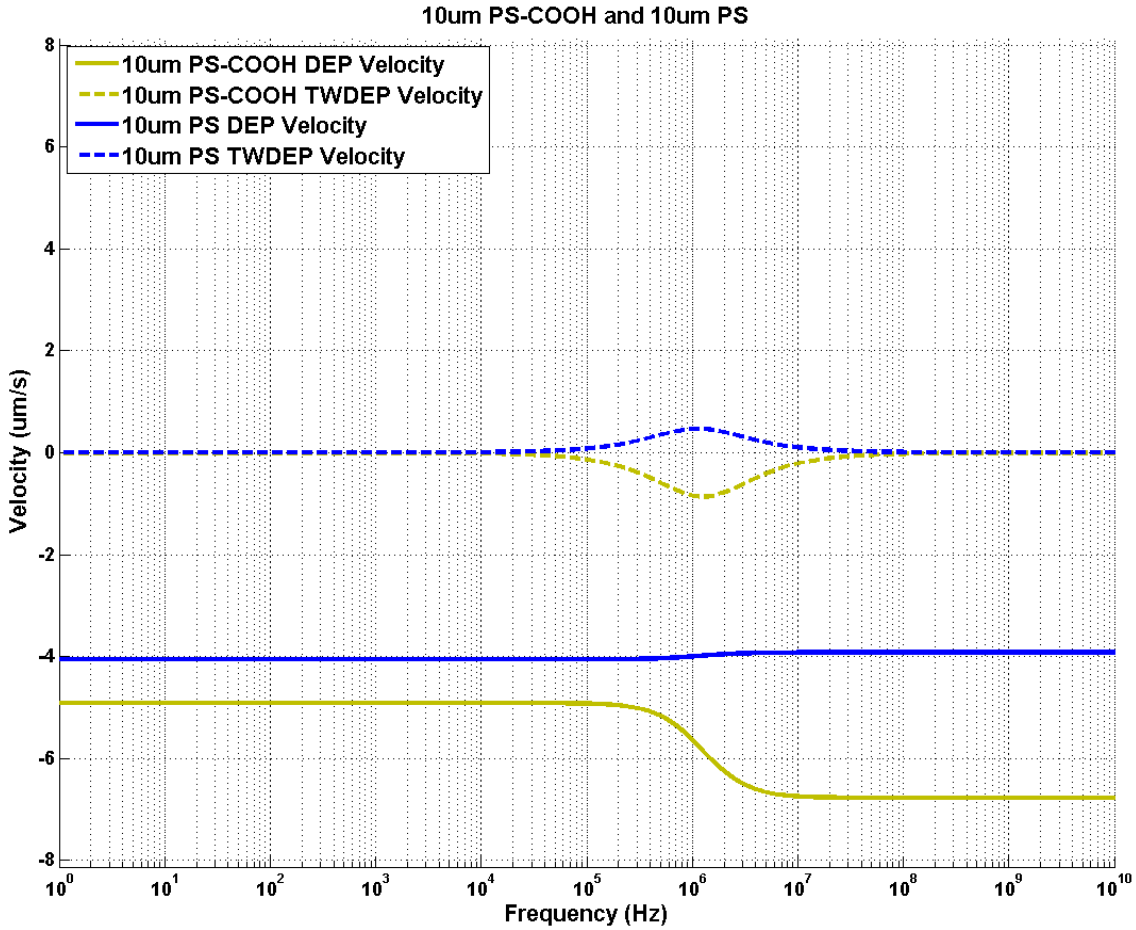

Figure 7.10 DEP and TWDEP velocity spectra for 10µm PS-COOH and 10µm PS microspheres

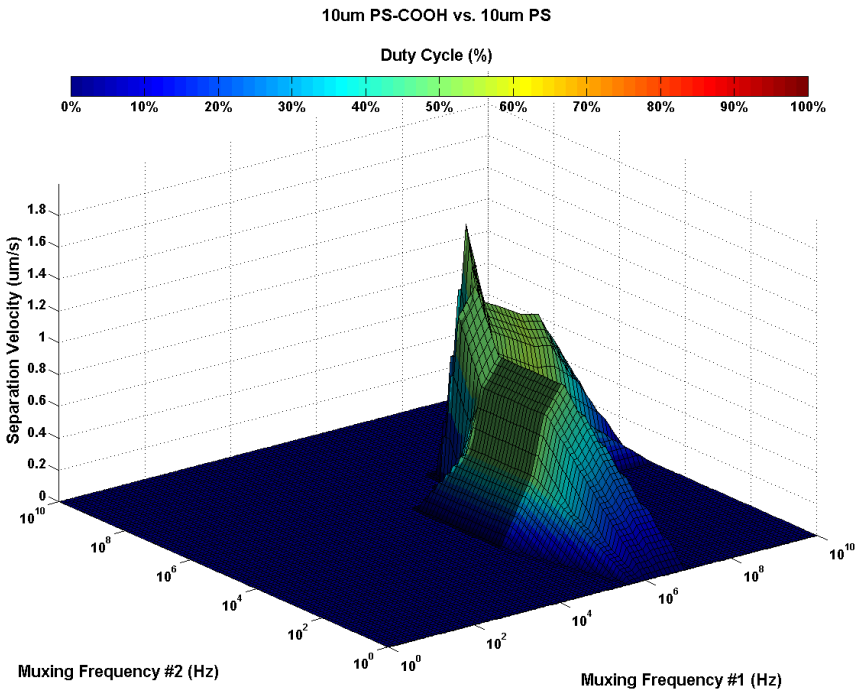

Figure 7.11 Separation velocity between 10μm PS-COOH and 10μm PS microspheres when field configurations are frequency multiplexed. $max(v_{diff}) = 1.83\mu m/s$ when $\omega_1 = 2.5\ MHz$, $\omega_2 = 2.5\ MHz$, and $D = 0.50$

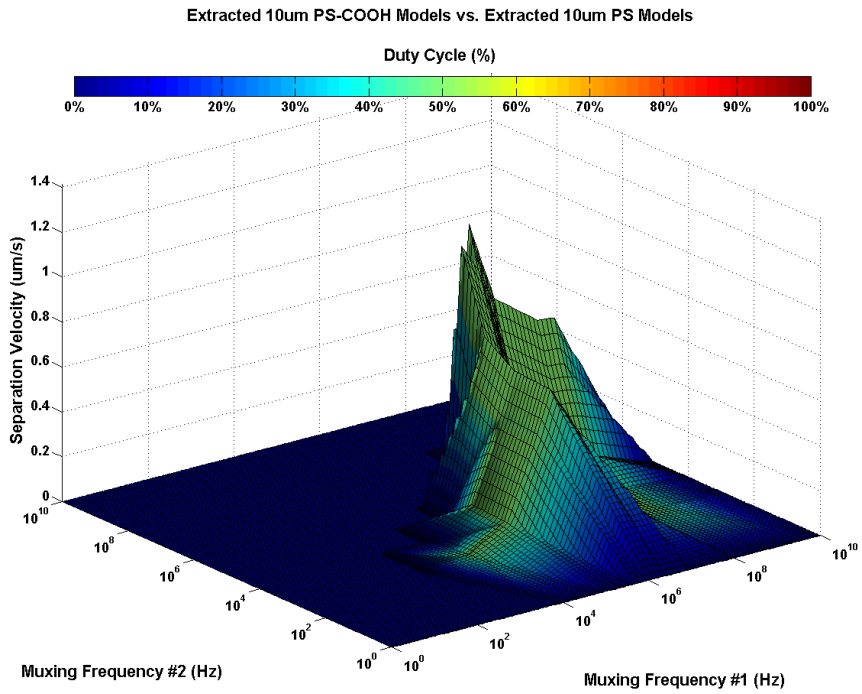

Figure 7.12 Separation velocity between extracted 10μm PS-COOH and 10μm PS models when field configurations are frequency multiplexed. $max(v_{diff}) = 1.31\mu m/s$ when $\omega_1 = 1\ MHz$, $\omega_2 = 1\ MHz$, and $D = 0.50$

7.1.5 Polystyrene (10um) and Live Yeast

The fifth separation case is 10μm polystyrene microspheres (10μm PS) versus live yeast cells. The plots of figure 7.13 show their DEP and TWDEP velocity spectra based on the extracted models. This combination of particles presents case where the particles have major differences in size and composition.

The surface plot of figure 7.14 shows the separation velocity between 10μm PS microspheres and live yeast cells based on the experimental data. The peak differential velocity is 7.91 μm/s and occurs when $\omega_1 = 100\ kHz$ and $\omega_2 = 2.5\ MHz$ and both the frequencies and phase gradients are multiplexed at a duty cycle of 86%.

Figure 7.15 shows the separation velocity between 10μm PS and live yeast cells based on of the extracted models. At the same frequency pair the measured data predicted its peak differential velocity, the models also predict that the cells will be separable using time-multiplexed dielectrophoresis. When multiplexing between those frequencies at a duty cycle of *D = 75%*, the models predict a differential velocity of *5.40* μm/s. The maximum separation velocity based off the extracted models for 10μm PS microspheres and live yeast cells is 11.85 μm/s. This maximum occurs when multiplexing between $\omega_1 = 500\ kHz$ and $\omega_2 = 250\ MHz$ at a duty cycle of 1%.

For this combination of 10μm PS microspheres and live yeast cells, separable solutions based on the experimental data only exists when both the phase gradient and frequencies are multiplexed. Solutions based on the extracted models exist for constant frequency, frequency multiplexing and frequency/phase multiplexing configurations, however the maximum

separation velocity occurs when a time-multiplexing method is applied, making time-multiplexed dielectrophoresis the more efficient separation method to use in this case.

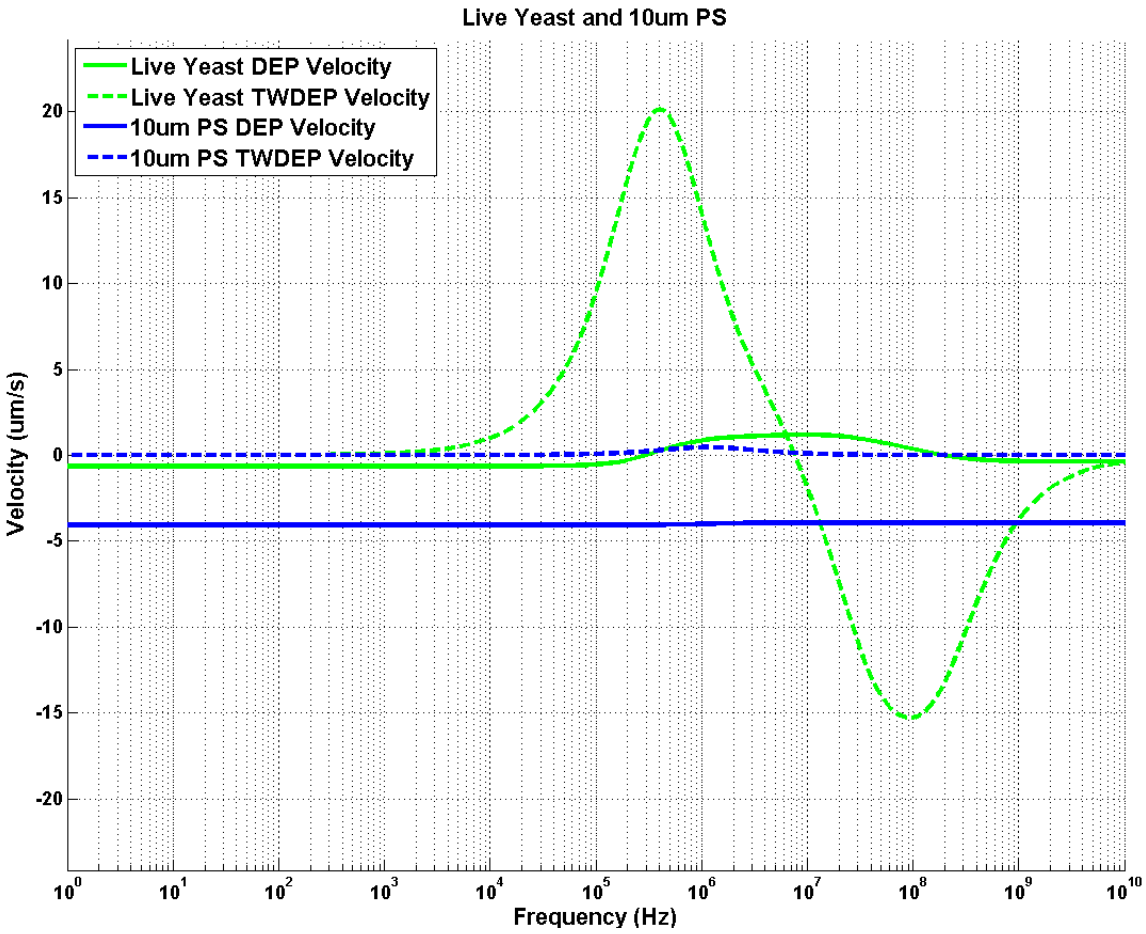

Figure 7.13 DEP and TWDEP velocity spectra for 10μm PS microspheres and live yeast cells

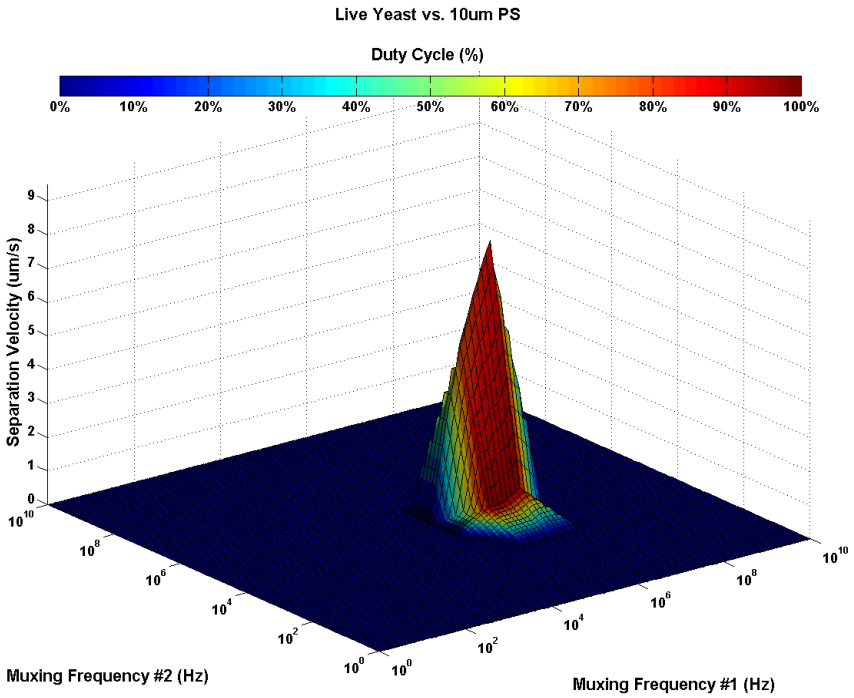

Figure 7.14 Separation velocity of live yeast cells and10μm PS microspheres when field configurations are phase and frequency multiplexed. $max(v_{diff}) = 7.91\mu m/s$ when $\omega_1 = 100\ kHz$, $\omega_2 = 2.5\ MHz$, and $D = 0.86$

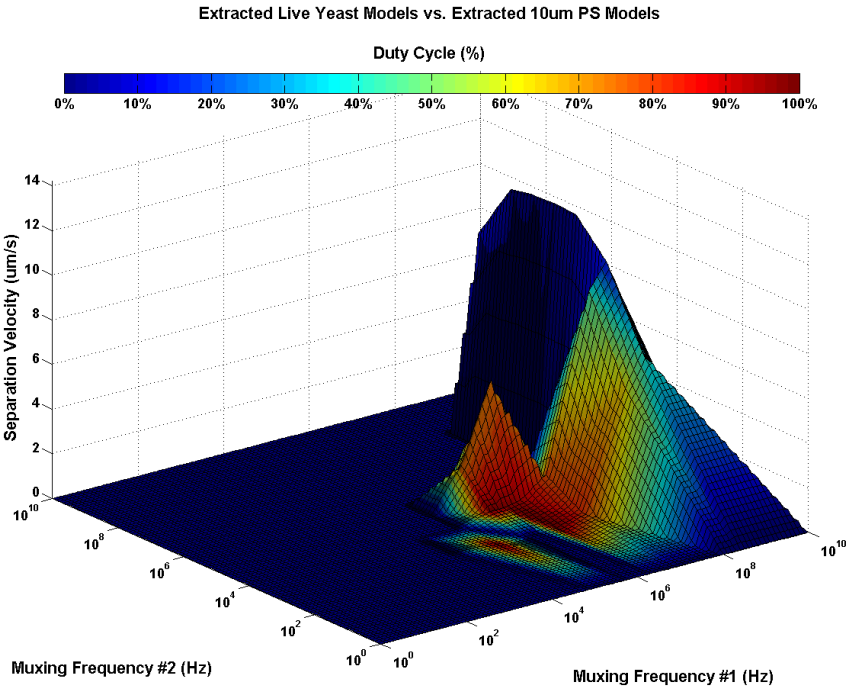

Figure 7.15 Separation velocity of extracted live yeast and10μm PS models when field configurations are phase and frequency multiplexed. $max(v_{diff}) = 11.85\mu m/s$ when $\omega_1 = 500\ kHz$, $\omega_2 = 250\ MHz$, and $D = 0.01$

7.1.6 Polystyrene (10um) and Dead Yeast

The sixth separation case is 10μm polystyrene microspheres (10μm PS) versus dead yeast cells. The plots of figure 7.16 show their DEP and TWDEP velocity spectra based on the extracted models. This combination of particles presents another case where the particles have major differences in size and composition.

The surface plot of figure 7.17 shows the separation velocity between 10μm PS microspheres and dead yeast cells based on the experimental data. The peak differential velocity is 1.32 μm/s and occurs when $\omega_1 = 2.5\,MHz$ and $\omega_2 = 100MHz$ and only the frequencies are multiplexed at a duty cycle of 23%.

Figure 7.18 shows the separation velocity between 10μm PS and live yeast cells based on the extracted models. At the same frequency pair the measured data predicted its peak differential velocity, the models also predict that the cells will be separable using time-multiplexed dielectrophoresis. When multiplexing between those frequencies at a duty cycle of *D = 32%*, the models predict a differential velocity of *2.15* μm/s. The maximum separation velocity based off the extracted models for 10μm PS microspheres and dead yeast cells is 3.24μm/s. This maximum occurs when multiplexing between $\omega_1 = 10\,MHz$ and $\omega_2 = 100\,MHz$ at a duty cycle of 54%.

For this combination of 10μm PS microspheres and live yeast cells, separable solutions based on the experimental data only exist when either frequency multiplexing or phase/frequency multiplexing is used. Solutions based on the extracted models exist for constant frequency, frequency multiplexing and frequency/phase multiplexing configurations, however the maximum

separation velocity occurs when a time-multiplexing method is applied, making time-multiplexed dielectrophoresis the more efficient separation method to use in this case.

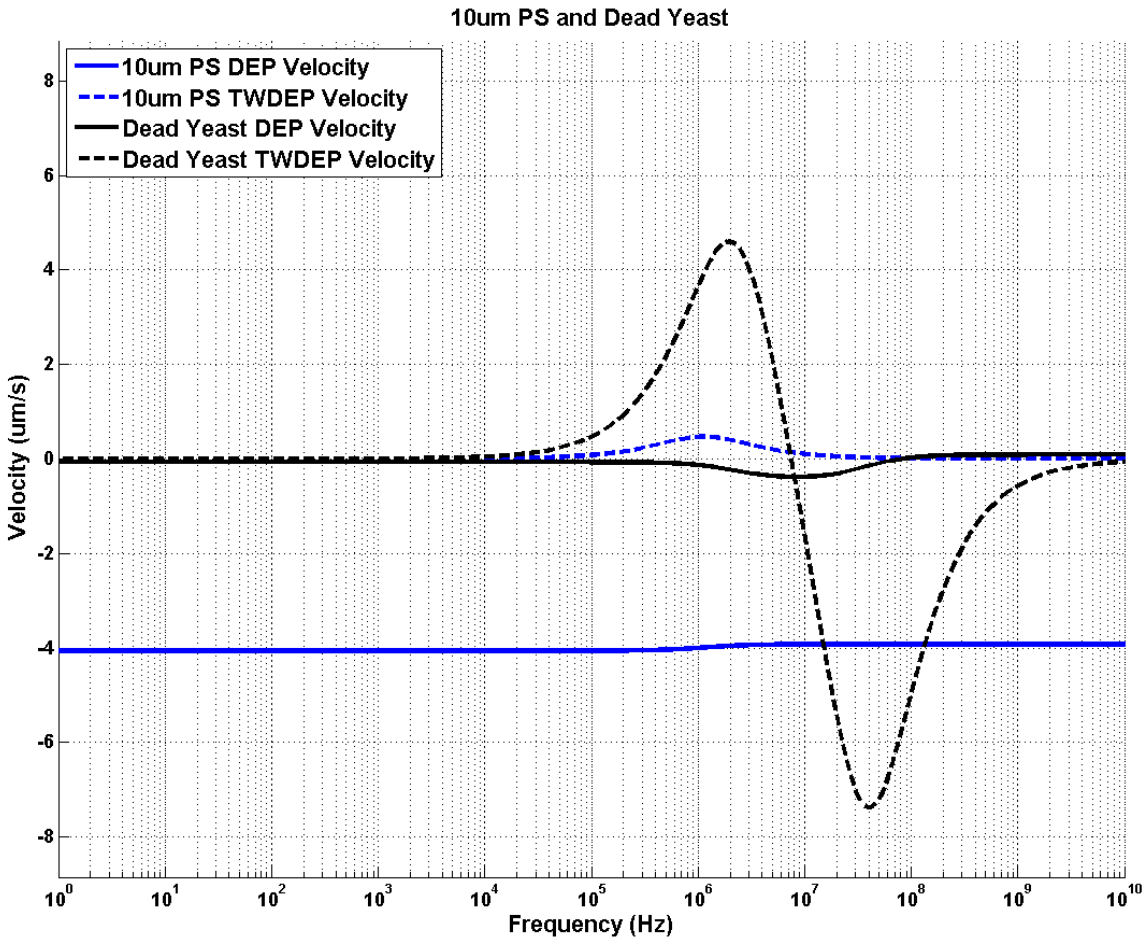

Figure 7.16 DEP and TWDEP velocity spectra for 10μm PS microspheres and dead yeast cells

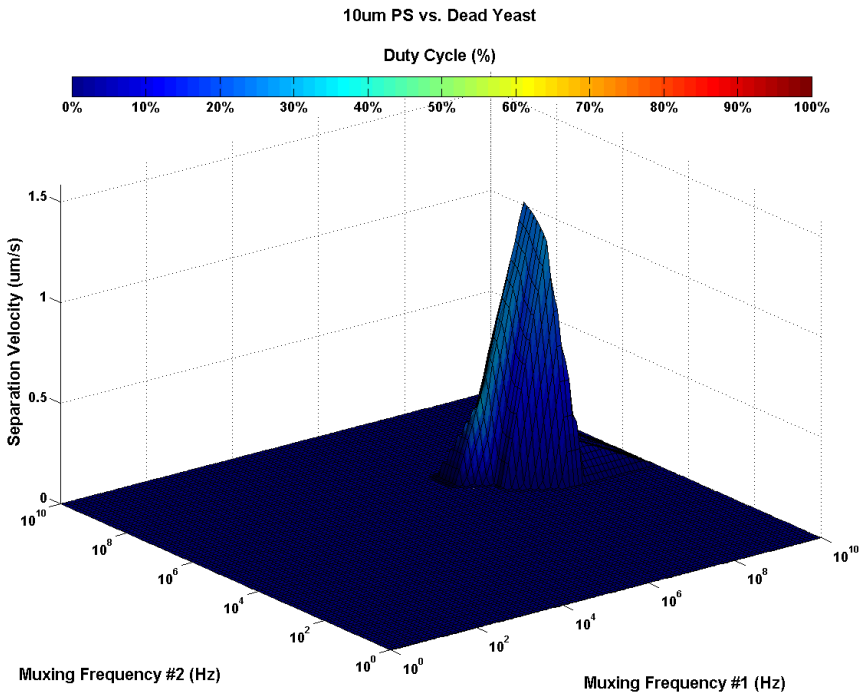

Figure 7.17 Separation velocity of 10μm PS and dead yeast cells when field configurations are frequency multiplexed. $max(v_{diff}) = 1.32\mu m/s$ when $\omega_1 = 2.5\ MHz$, $\omega_2 = 100\ MHz$, and $D = 0.23$

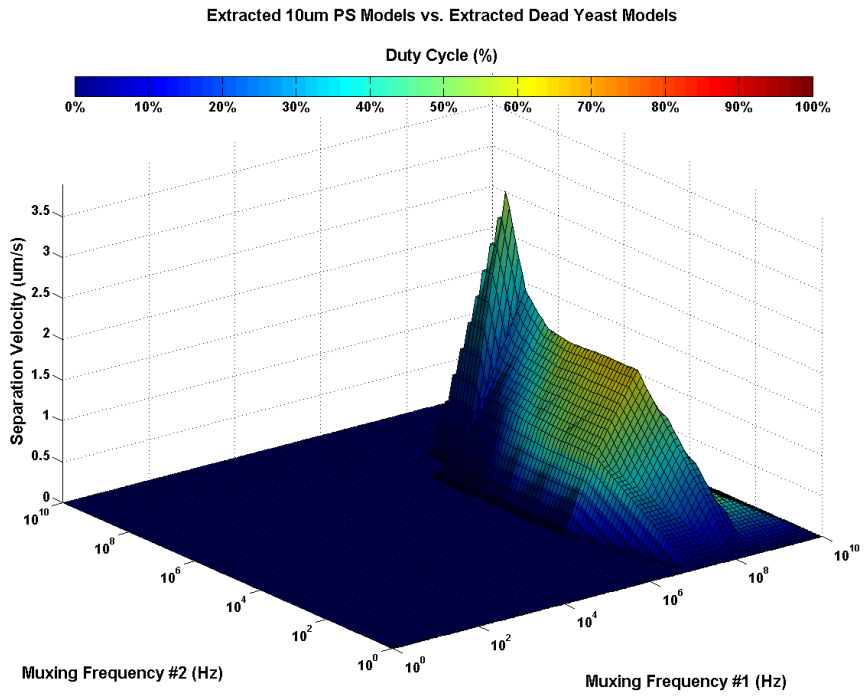

Figure 7.18 Separation velocity of extracted 10μm PS and dead yeast cells models when field configurations are frequency multiplexed. $max(v_{diff}) = 3.24\mu m/s$ when $\omega_1 = 10\ MHz$, $\omega_2 = 100\ MHz$, and $D = 0.54$

7.1.7 Polystyrene-COOH (6um) and Live Yeast

The seventh separation case is 6μm polystyrene-COOH microspheres (6μm PS-COOH) versus live yeast cells. The plots of figure 7.19 show their DEP and TWDEP velocity spectra based on the extracted models. This combination of particles presents a case where the particles are on average approximately the same size but have major differences in internal composition.

The surface plot of figure 7.20 shows the separation velocity between 6μm PS-COOH microspheres and live yeast cells based on the experimental data. The peak differential velocity is 11.60 μm/s and occurs when $\omega_1 = 100\ kHz$ and $\omega_2 = 250\ kHz$ and only the frequencies are multiplexed at a duty cycle of 64%.

Figure 7.21 shows the separation velocity between 10μm PS and live yeast cells based on the extracted models. At the same frequency pair the measured data predicted its peak differential velocity, the models also predict that the cells will be separable using time-multiplexed dielectrophoresis. When multiplexing between those frequencies at a duty cycle of *D = 50%*, the models predict a differential velocity of *13.87* μm/s. The maximum separation velocity based on the extracted models for 6μm PS-COOH microspheres and live yeast cells is 18.46μm/s. This maximum occurs when multiplexing between $\omega_1 = 250\ kHz$ and $\omega_2 = 500\ kHz$ at a duty cycle of 88%.

For this combination of 6μm PS-COOH microspheres and live yeast cells, separable solutions based on the experimental data and extracted models exist for all possible field configurations, including constant frequencies. However in each case, the separation velocity is maximized when a multiplexing method is used.

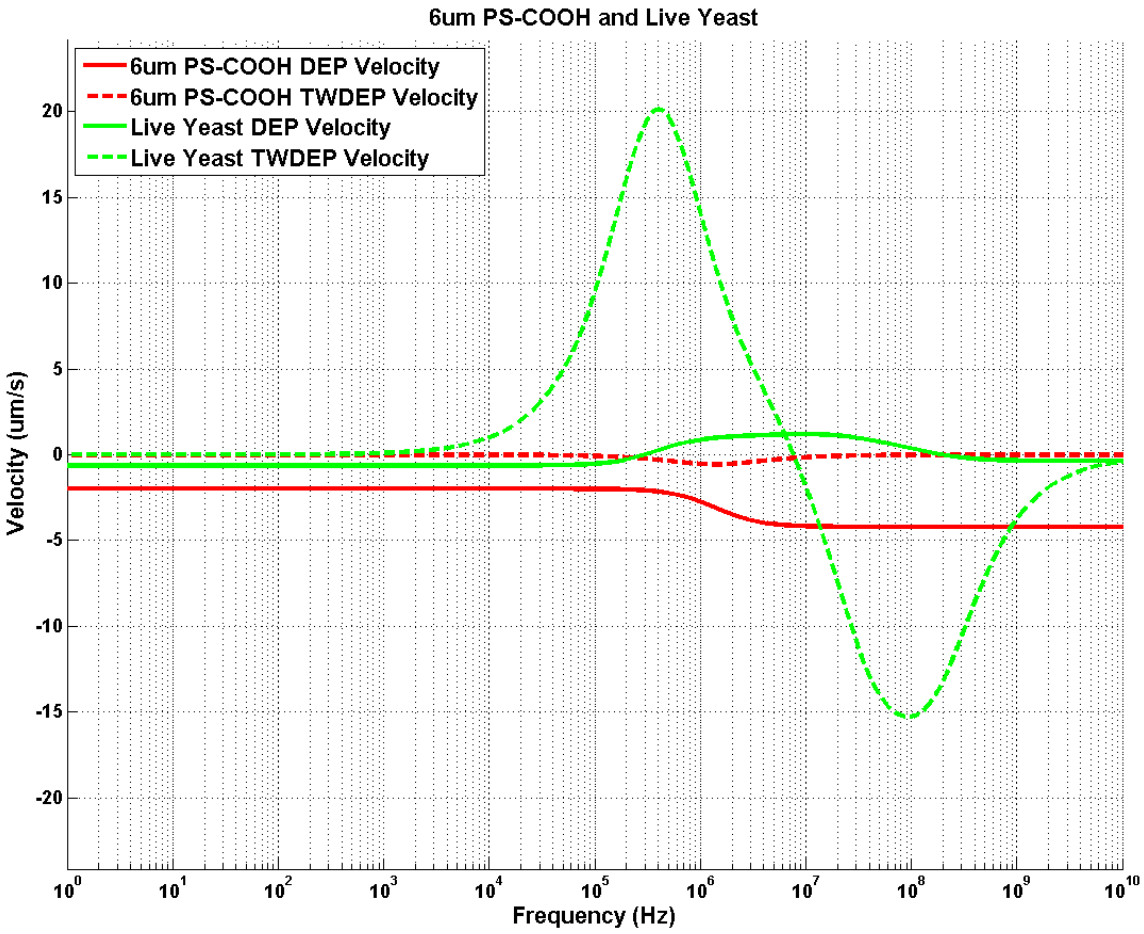

Figure 7.19 DEP and TWDEP velocity spectra for 6µm PS-COOH microspheres and live yeast cells

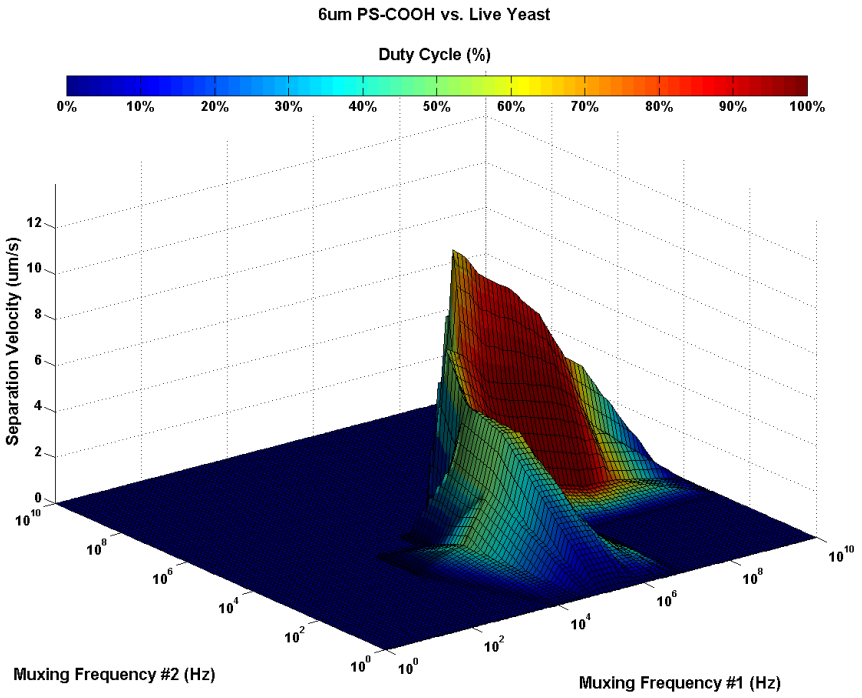

Figure 7.20 Separation velocity between 6μm PS-COOH and live yeast cells when field configurations are frequency multiplexed. $max(v_{diff}) = 11.6\,\mu m/s$ when $\omega_1 = 100\,kHz$, $\omega_2 = 250\,kHz$, and $D = 0.64$

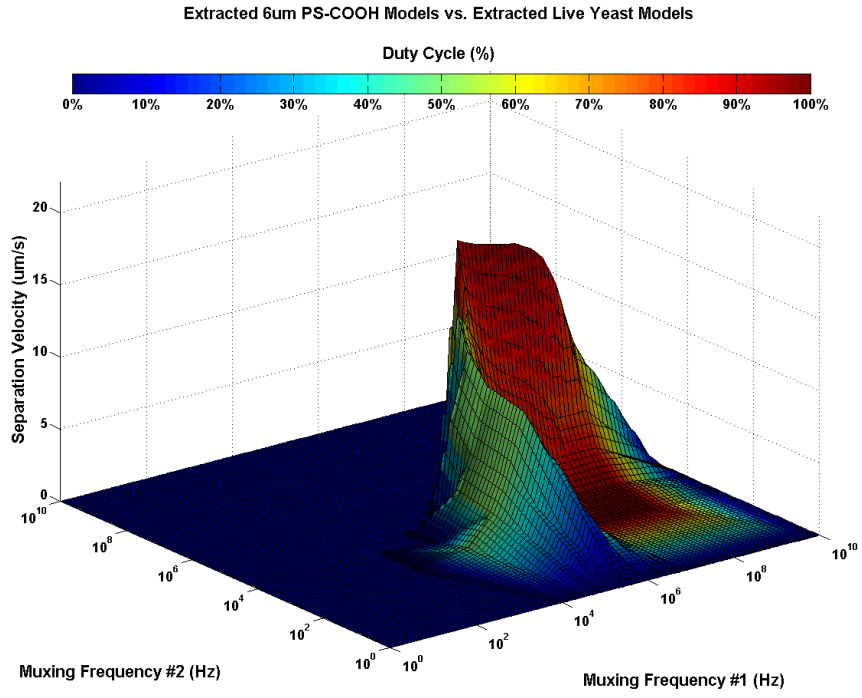

Figure 7.21 Separation velocity of extracted 6μm PS-COOH and live yeast cell models when field configurations are frequency multiplexed. $max(v_{diff}) = 18.46\mu m/s$ when $\omega_1 = 250\,kHz$, $\omega_2 = 500\,kHz$, and $D = 0.88$

7.1.8 Polystyrene-COOH (6um) and Dead Yeast

The eighth separation case is 6μm polystyrene-COOH microspheres (6μm PS-COOH) versus dead yeast cells. The plots of figure 7.22 show their DEP and TWDEP velocity spectra based on the extracted models. This combination of particles presents another case where the particles are on average approximately the same size but have major differences in internal composition.

The surface plot of figure 7.23 shows the separation velocity between 6μm PS-COOH microspheres and live dead cells based on the experimental data. The peak differential velocity is 4.04 μm/s and occurs when $\omega_1 = 25\ MHz$ and $\omega_2 = 250\ MHz$ and the frequencies and phase gradients are multiplexed at a duty cycle of 64%.

Figure 7.24 shows the separation velocity between 6μm PS-COOH and dead yeast cells based on the extracted models. At the same frequency pair the measured data predicted its peak differential velocity, the models also predict that the cells will be separable using time-multiplexed dielectrophoresis. When multiplexing the selected frequencies and phase gradients at a duty cycle of $D = 62\%$, the models predict a differential velocity of *3.88* μm/s. The maximum separation velocity based off the extracted models for 6μm PS-COOH microspheres and dead yeast cells is 5.94μm/s. This maximum occurs when multiplexing between $\omega_1 = 2.50\ MHz$ and $\omega_2 = 50\ MHz$ at a duty cycle of 54%.

For this combination of 6μm PS-COOH microspheres and live yeast cells, separable solutions based on the experimental data and extracted models exists for all possible field configurations, including constant frequencies. However in each case, the separation velocity is maximized when a multiplexing method is used.

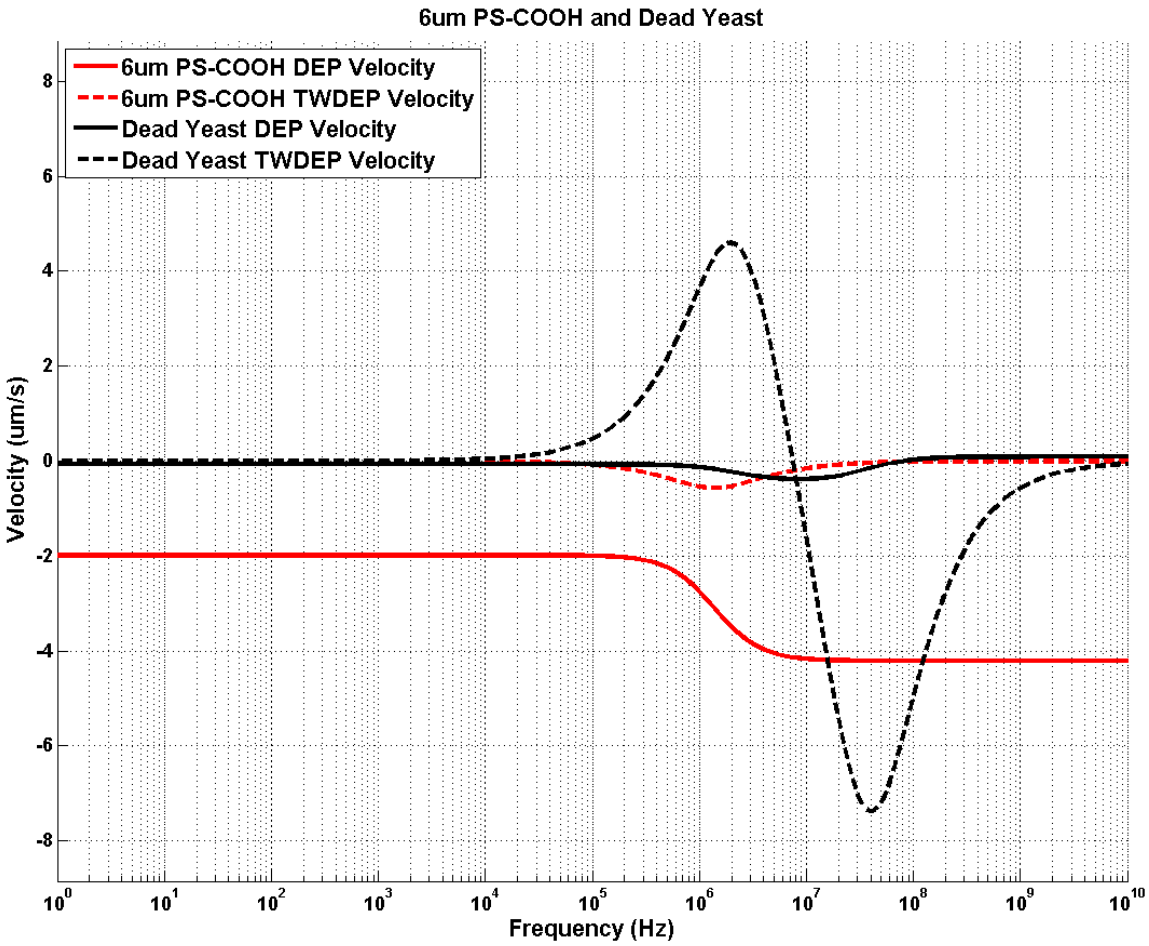

Figure 7.22 DEP and TWDEP velocity spectra for 6μm PS-COOH microspheres and dead yeast cells

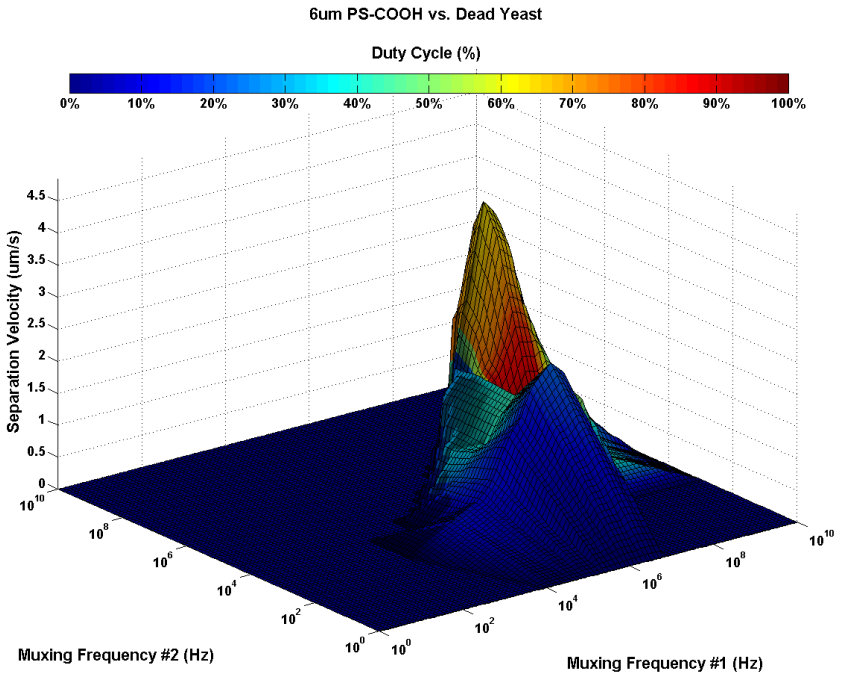

Figure 7.23 Separation velocity of 6µm PS-COOH and dead yeast when field configurations are phase and frequency multiplexed. $max(v_{diff}) = 4.04\,\mu m/s$ when $\omega_1 = 25\,MHz$, $\omega_2 = 250\,MHz$, and $D = 0.64$

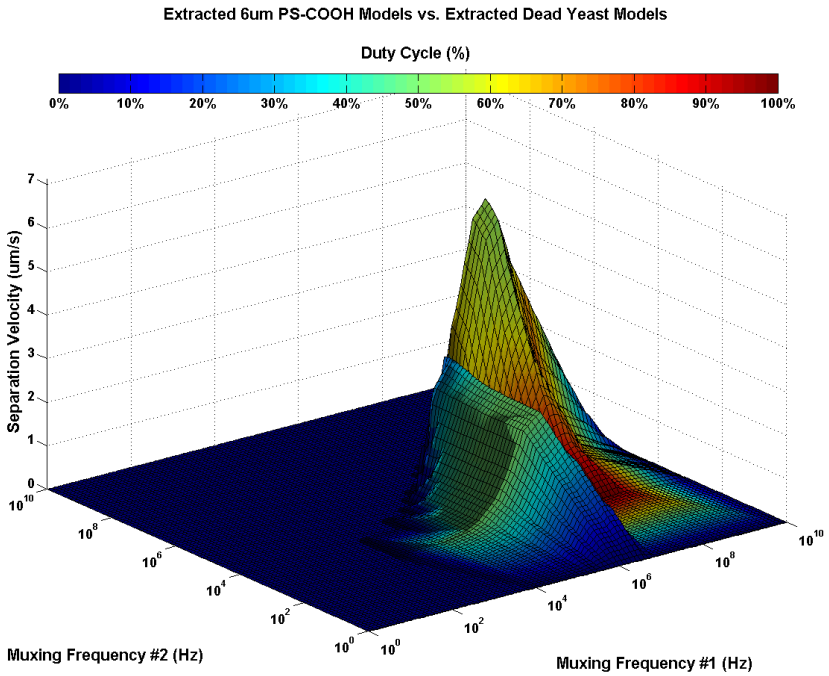

Figure 7.24 Separation velocity of extracted 6µm PS-COOH and dead yeast models when field configurations are phase and frequency multiplexed. $max(v_{diff}) = 5.94\mu m/s$ when $\omega_1 = 2.5\,MHz$, $\omega_2 = 50\,MHz$, and $D = 0.54$

7.1.9 Polystyrene-COOH (6um) and Polystyrene-COOH (10um)

The ninth separation case is 6μm polystyrene-COOH microspheres (6μm PS-COOH) versus 10μm polystyrene-COOH microspheres (10μm PS-COOH). The plots of figure 7.25 show their DEP and TWDEP velocity spectra based on the extracted models. This combination of particles presents case where the particles have the same surface chemistry modification, but vary significantly in size.

The surface plot of figure 7.26 shows the separation velocity between 6μm PS-COOH microspheres and 10μm PS-COOH based on the experimental data. The peak differential velocity is 0.12 μm/s and occurs when $\omega_1 = 750\ kHz$ and $\omega_2 = 2.5\ MHz$ and the frequencies and phase gradients are multiplexed at a duty cycle of 56%.

Figure 7.27 shows the separation velocity between 6μm PS-COOH and 10μm PS-COOH based on the extracted models. At the same frequency pair the measured data predicted its peak differential velocity, the models also predict that the cells will be separable using time-multiplexed dielectrophoresis. When multiplexing between the selected frequencies and phase gradients at a duty cycle of *D = 49%*, the models predict a differential velocity of *0.03* μm/s. The maximum separation velocity based off the extracted models for 6μm PS-COOH microspheres and 10μm PS-COOH is 0.03μm/s. This maximum occurs when multiplexing between phase gradients and frequencies of $\omega_1 = 500\ kHz$ and $\omega_2 = 2.5\ MHz$ at a duty cycle of 56%.

For this combination of 6μm PS-COOH and 10μm PS-COOH microspheres, separable solutions based on both the experimental data and extracted models only exists when a multiplexing technique is applied.

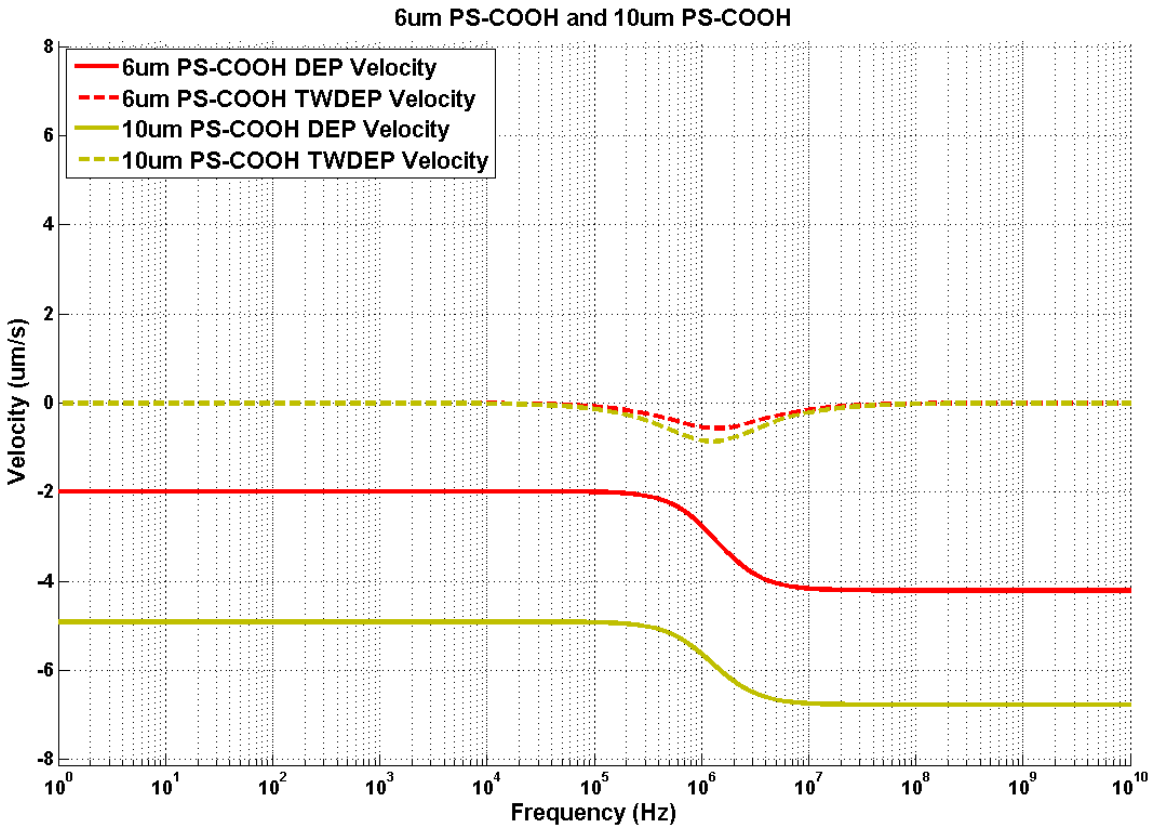

Figure 7.25 DEP and TWDEP velocity spectra for 6µm PS-COOH and 10µm PS-COOH microspheres

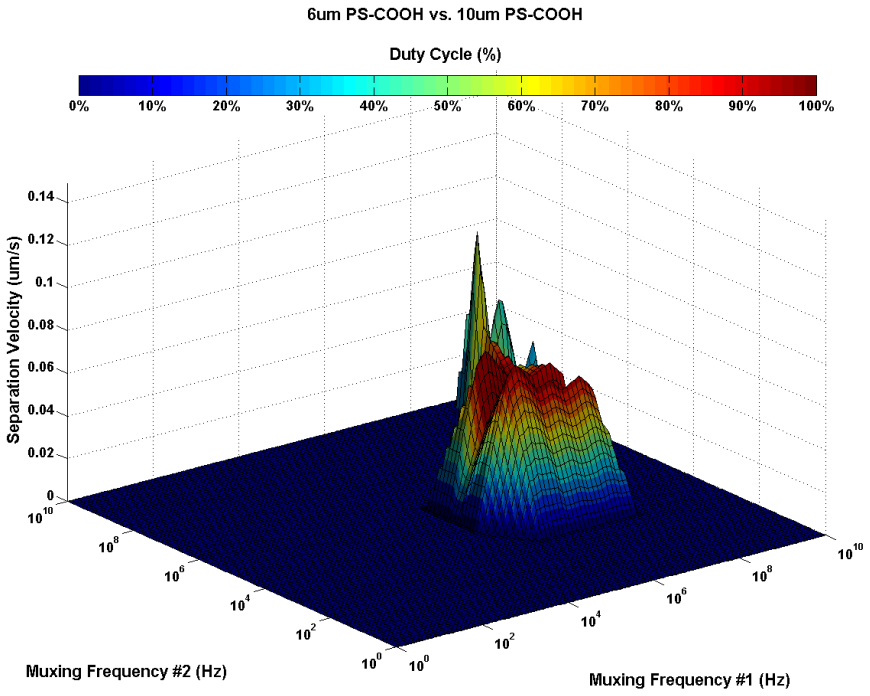

Figure 7.26 Separation velocity of 6µm PS-COOH and 10µm PS microspheres when field configurations are phase and frequency multiplexed. $max(v_{diff}) = 0.12\ \mu m/s$ when $\omega_1 = 750\ kHz$, $\omega_2 = 2.5\ MHz$, and $D = 0.56$

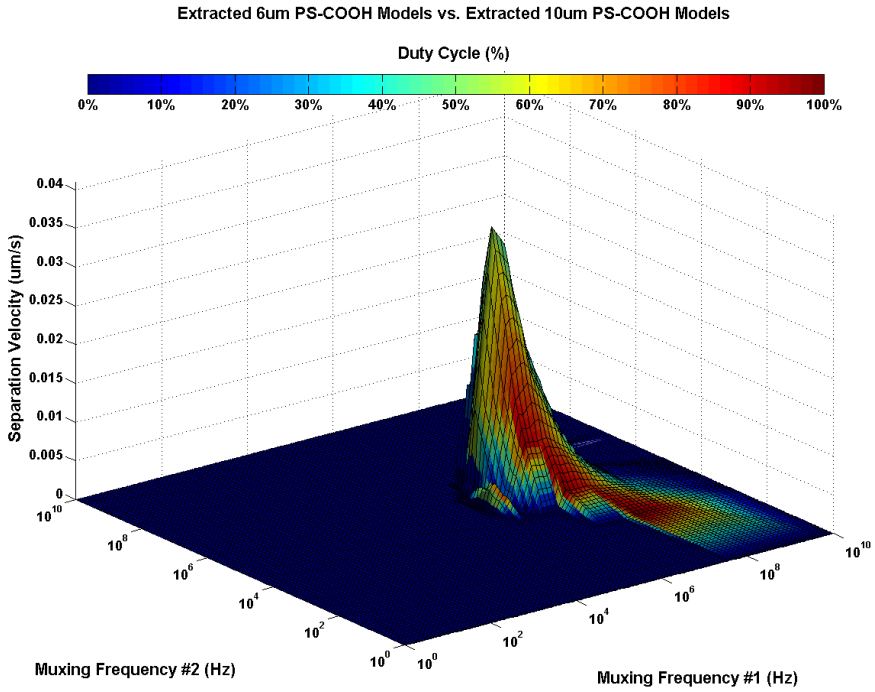

Figure 7.27 Separation velocity of extracted 6µm PS-COOH and 10µm PS models when field configurations are phase and frequency multiplexed. $max(v_{diff}) = 0.03\mu m/s$ when $\omega_1 = 500\ kHz$, $\omega_2 = 2.5\ MHz$, and $D = 0.56$

7.1.10 Polystyrene-COOH (6um) and Polystyrene (10um)

The tenth and final separation case is 6μm polystyrene-COOH microspheres (6μm PS-COOH) versus 10μm polystyrene microspheres (10μm PS). The plots of figure 7.28 show their DEP and TWDEP velocity spectra based on the extracted models. This combination of particles presents case where the particles are on average the same size but vary only in their surface chemistry.

The surface plot of figure 7.29 shows the separation velocity between 6μm PS-COOH and 10μm PS microspheres based on the experimental data. The peak differential velocity is 1.57 μm/s and occurs when $\omega_1 = 2.5MHz$ and $\omega_2 = 2.5MHz$ and the frequencies are multiplexed at a duty cycle of 50%.

Figure 7.30 shows the separation velocity between 6μm PS-COOH and 10μm PS microspheres based on the extracted models. The peak differential velocity is 1.00 μm/s and occurs when $\omega_1 = 1MHz$ and $\omega_2 = 1MHz$ and the frequencies are multiplexed at a duty cycle of 50%.

For this combination of 6μm PS-COOH and 10μm PS microspheres the maximum separation velocities resulting from both the data and models occur when the two multiplexed frequencies are the same and have a duty cycle of %50, which makes the configuration identical to just applying a constant frequency. Therefore, time-multiplexing dielectrophoresis would not be a more efficient separation method in this case.

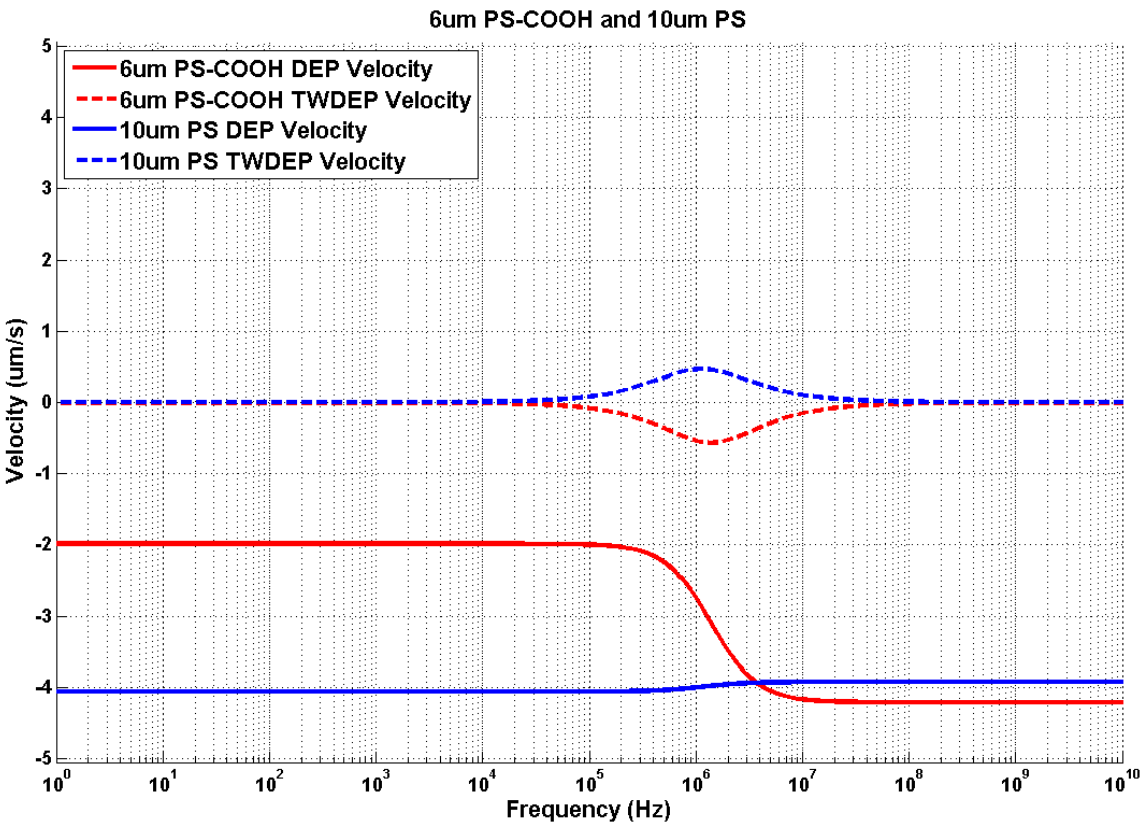

Figure 7.28 DEP and TWDEP velocity spectra for 6µm PS-COOH and 10µm PS microspheres

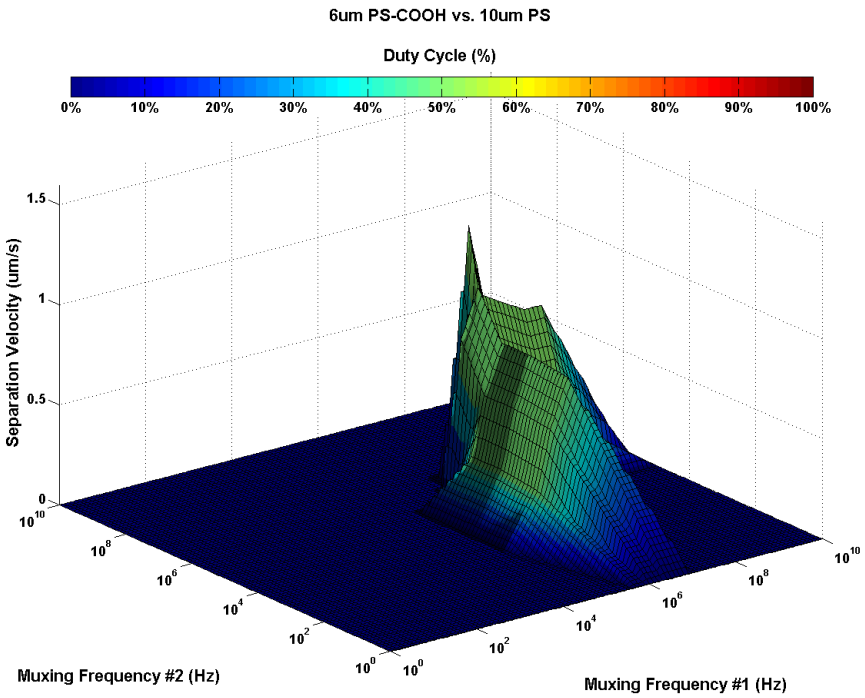

Figure 7.29 Separation velocity between 6µm PS-COOH and 10µm PS microspheres when field configurations are frequency multiplexed. $max(v_{diff}) = 1.57\ \mu m/s$ when $\omega_1 = 2.5\ MHz$, $\omega_2 = 2.5\ MHz$, and $D = 0.5$

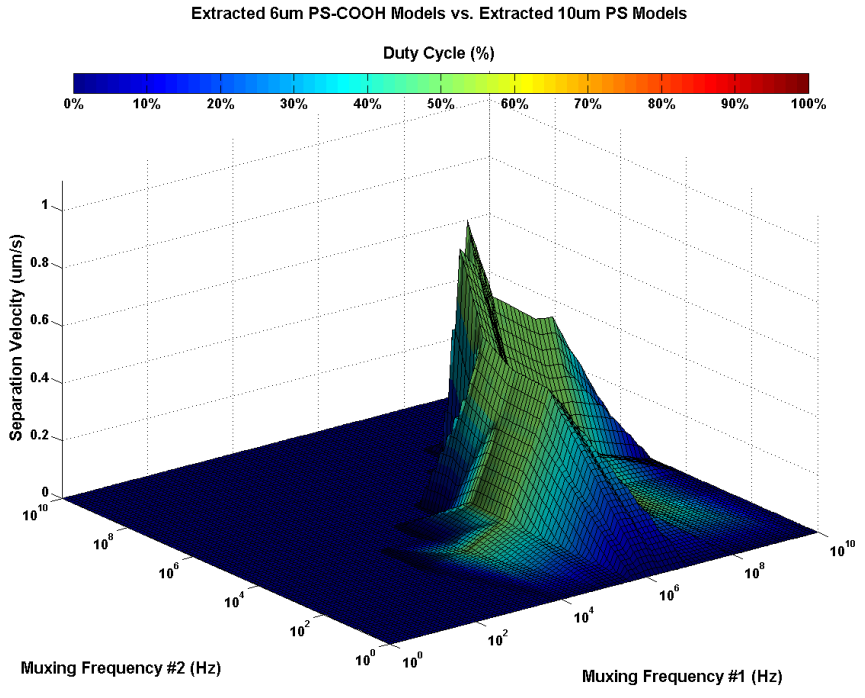

Figure 7.30 Separation velocity between extracted 6µm PS-COOH and 10µm PS models when field configurations are frequency multiplexed. $max(v_{diff}) = 1.00\mu m/s$ when $\omega_1 = 1\ MHz$, $\omega_2 = 1\ MHz$, and $D = 0.5$

7.2 DISCUSSION OF RESULTS

The result of the analysis carried out in this chapter shows that that time-multiplexing dielectrophoresis has the ability to separate particles when other dielectrophoresis based methods are not able to and also in some cases, improve the efficiency via a relative increase in separation velocity. The results of these analyses also provide a set of time-multiplexing dielectrophoresis configuration parameters that can be used to maximize the separation velocity between a given pair of particles from our characterized library.

Table 7.1 presents a summary of the results from this chapter. The blue shaded boxes show the calculated multiplexing configurations and separation velocities that were based on characterization measurements. The red shaded boxes also show the separation velocities between a given pair of particles, but as predicted by the extracted models of chapter 6 when evaluated using the same configurations. Generally for all cases, the separation velocities are in reasonable agreement. More importantly, for no cases did the models predict that the particle pairs would be inseparable if the set of frequency, phase gradient and duty cycle parameters that were calculated to result in the maximum separation velocity were used, providing further confidence that these configurations can be successfully used in experimentation. FIX

Comparing the separation velocities based on the models and data provides another important result to look at. When conducting actual time-multiplexing dielectrophoresis experiments on mixtures containing large populations of particles, there will be variation among the particles, just as there is slight variation between the experimental characterization data from chapter 6 and the predictions based on their best-fit models. However as the comparisons between calculations based on data and models show, these variations can be compensated for at a given configuration by adjusting the duty cycle, thereby maintaining separable conditions.

Looking at the results in table 7.1, it can be seen that there were two cases presented where there would be no benefit to using time-multiplexing dielectrophoresis, 10μm PS-COOH vs. 10μm PS microspheres and 10μm PS-COOH vs. 6μm PS-COOH microspheres. Their peak TWDEP velocities are opposite in sign and occur at relatively close frequencies, thus they can be separated using an affinity method and at a greater velocity than time-multiplexing would permit.

In addition to displaying an increase in separation velocity, the 10μm PS-COOH vs. 6μm PS-COOH microspheres case highlights a couple other key points of note for this dissertation. From equation 2.11 it can be seen that the dielectrophoretic force is proportional to the cube of the particle radius. However, the difference in TWDEP velocities derived from the extracted models for 10μm PS-COOH and 6μm PS-COOH microspheres do not fully reflect this relationship to radius. The reason behind this perceived discrepancy is that there is a dynamic relationship between the DEP and TWDEP forces and they cannot be consider independently. The difference in DEP velocities of the two particle types cause them to levitate at different heights, 6μm microspheres levitate at lower depths close to the electrodes and 10μm microspheres at higher depths. The lateral speed of the particles varies greatly with changes in depth, since the TWDEP force is proportional to the magnitude of the field intensity and this intensity drops off quickly as vertical distance from the electrodes increases. As a result, situations can arise where even though one of the particles has a much smaller radius than the other, as occurs in this case, the smaller particle can have a similar TWDEP velocity magnitude as the larger particle since the negative DEP forces on the smaller particle are relatively weaker. Therefore, separability analyses, such as the one presented in this chapter, can only be considered to be accurate when this dynamic interaction between the DEP and TWDEP velocity

components are taken into consideration, as we have done by basing calculations on actual measurements.

The analysis of the separability between 10μm PS-COOH and 6μm PS-COOH microspheres also demonstrates the claim we made that time-multiplexing dielectrophoresis is more efficient than field flow fractionation methods in terms of being able to separate smaller differences with fewer electrodes. According to the measurements, the two particle types move at their maximum velocities of 0.55 μm/s and 0.81 μm/s at 2.5 MHz, resulting in a maximum differential velocity of 0.26 μm/s using a single frequency field flow fractionation method to separate them. If one attempted to separate them field-flow fractionation with the 16, 15μm electrodes of our design, the maximum possible separation distance that could occur is much less than could occur using time-multiplexing dielectrophoresis. In the best case, if all the particles started from the same position and at the first electrode of the array, using field flow fractionation it would take approximately 10 minutes for the 10μm PS-COOH to traverse the length of the 480μm array. In that span of 10 minutes, the theoretical maximum separation distance that could occur via field flow fractionation is 156μm, approximately 5 electrodes and 5 electrode gaps. However, since our method always causes particles to migrate in opposite directions, we can achieve a separation distance that spans the entire length of the 480μm array using those same 16 electrodes.

Looking at the remaining cases for the separability analyses, there were three cases were an affinity method could have been used to separate particles but the application to time-multiplexing dielectrophoresis was found to be able to increase the separation velocity, 6μm PS-COOH vs. live yeast , 6μm PS-COOH vs. dead yeast and 10μm PS-COOH vs. dead yeast.

The remaining five cases, 10μm PS vs. live yeast, 10μm PS vs. dead yeast, 10μm PS-COOH vs 6μm PS-COOH, 10μm PS-COOH vs live yeast and live yeast vs. dead yeast are all inseparable using an affinity method. It was shown that time-multiplexing dielectrophoresis could be used to exert differential forces on the particles and cause them to separate by multiplexing either frequency or phase gradient and frequency, except for the 10μm PS vs. live yeast case which can only be separated if both the phase gradients and frequencies are multiplexed.

Now that the effectiveness of time-multiplexing dielectrophoresis to separate particles has been shown, based on our models in the next chapter we will present our experimental results based on the multiplexing configurations presented in this chapter.

Table 7.1 Summary of calculated multiplexing parameters for separating particles and separation velocities

Parameters based on Measurements / Parameters based on Extracted Models	10 µm PS	10 µm PS-COOH	6 µm PS-COOH	Live Yeast	Dead Yeast
10 µm PS		ω_1 = 2.5 MHz v_{diff} = 1.04 µm/s	ω_1 = 2.5 MHz v_{diff} = 0.834 µm/s	ω_1 = 100 kHz ω_2 = 2.5 MHz *D = 0.75* $\nabla\phi_{x1} > 0$ $\nabla\phi_{x2} < 0$ 5.40 µm/s	ω_1 = 2.5 MHz ω_2 = 100 MHz *D = 0.32* v_{diff} = 2.15 µm/s
10 µm PS-COOH	ω_1 = 2.5 MHz v_{diff} = 1.83 µm/s		ω_1 = 750 kHz ω_2 = 2.5 MHz *D = 0.49* $\nabla\phi_{x1} > 0$ $\nabla\phi_{x2} < 0$ v_{diff} = 0.03 µm/s	ω_1 = 100 kHz ω_2 = 500 kHz *D = 0.72* v_{diff} = 12.50 µm/s	ω_1 = 2.5 MHz ω_2 = *250* MHz *D = 0.62* $\nabla\phi_{x1} > 0$ $\nabla\phi_{x2} < 0$ v_{diff} = 4.01 µm/s
6 µm PS-COOH	ω_1 = 2.5 MHz v_{diff} = 1.57 µm/s	ω_1 = 750 kHz ω_2 = 2.5 MHz *D = 0.56* $\nabla\phi_{x1} > 0$ $\nabla\phi_{x2} < 0$ v_{diff} = 0.12 µm/s		ω_1 = 100 kHz ω_2 = 250 kHz *D = 0.50* v_{diff} = 13.87 µm/s	ω_1 = 2.5 MHz ω_2 = 250 MHz *D = 0.62* $\nabla\phi_{x1} > 0$ $\nabla\phi_{x2} < 0$ v_{diff} = 3.88 µm/s
Live Yeast	ω_1 = 100 kHz ω_2 = 2.5 MHz *D = 0.81* $\nabla\phi_{x1} > 0$ $\nabla\phi_{x2} < 0$ v_{diff} = 7.91 µm/s	ω_1 = 100 kHz ω_2 = 500 kHz *D = 0.70* v_{diff} = 11.16 µm/s	ω_1 = 100 kHz ω_2 = 250 kHz *D = 0.64* v_{diff} = 11.60 µm/s		ω_1 = 100 kHz ω_2 = 25 MHz *D = 0.80* v_{diff} = 6.57 µm/s
Dead Yeast	ω_1 = 2.5 MHz ω_2 = 100 MHz *D = 0.23* v_{diff} = 1.32 µm/s	ω_1 = 2.5 MHz ω_2 = *250* MHz *D = 0.66* $\nabla\phi_{x1} > 0$ $\nabla\phi_{x2} < 0$ v_{diff} = 4.12 µm/s	ω_1 = 2.5 MHz ω_2 = 250 MHz *D = 0.64* $\nabla\phi_{x1} > 0$ $\nabla\phi_{x2} < 0$ v_{diff} = 4.04 µm/s	ω_1 = 100 kHz ω_2 = 25 MHz *D = 0.81* v_{diff} = 6.55 µm/s	

8.0 TIME-MULTIPLEXED DIELECTROPHORESIS EXPERIMENTAL TRIALS

In this section we present time-multiplexing dielectrophoresis experiments that were conducted. The test cases presented in this chapter are ones that observably demonstrate the ability of time-multiplexing dielectrophoresis to exert differential velocities on different particle types. Results of the application of time-multiplexing dielectrophoresis fields to samples containing live and dead yeast cells are presented as, well as samples containing live yeast and 10μm PS-COOH microspheres.

8.1 EXPERIMENTAL RESULTS

In our experiments we focus on cases that involve live yeast cells because they best show the ability of time-multiplexing dielectrophoresis to exert differential forces on particles in an observable way. The models predicted, and the characterization data validated, that live yeast cells will have strong positive dielectrophoresis forces exerted on them over a wide band of frequencies. In the experimental cases to follow, the only range of frequencies for which the opposing particle, either dead yeast or 10μm PS-COOH microspheres, can be made to move laterally coincide with that same frequency band under which live yeast undergo positive dielectrophoresis and are rendered immobile. The experiments show that by time-multiplexing

between a frequency for which live yeast undergo negative dielectrophoresis and a frequency at which the other type exhibits lateral movement, particle types can be made to simultaneously move in opposite lateral directions.

8.1.1 Time-Multiplexed Dielectrophoresis of Live and Dead Yeast Cells

Based on the analysis from chapter 7, it was determined that live and dead yeast cells could be separated using multiplexing frequencies of 25 MHz and 100 kHz. First we will look at the behaviors of these two particle types individually while in the presence of TWDEP fields at these frequencies, and then make observations based on time-multiplexing between them.

Figure 8.1 shows a sample containing only dead yeast cells. The device used for these experiments is a 15μm separation electrode array, driven by 2 V_{pp} voltage signals. The medium used is a 5 mS/m KCL standard buffer solution. In this first experiment a constant, a non-multiplexing set of 25 MHz traveling-wave voltages with a negative phase gradient are applied to the electrodes, causing the cells to move from left to right. The bottom of figure 8.1 shows the displacement of the cells due to TWDEP 30 seconds later. In this case, nDEP forces keep the cells levitated above the electrode array, while TWDEP forces cause the dead cells to be laterally displaced by approximately 45μm, resulting in an average velocity of 1.5 μm/s.

The cells shown in figure 8.2 are the same sample from figure 8.1 a short time later. In this second experiment the frequency is held constant and the phase gradient is reversed, causing the particles to move in the opposite direction at a speed of approximately -1.8 μm/s. The responsiveness of the particles to the phase gradient verifies that TWDEP is force controlling its motion.

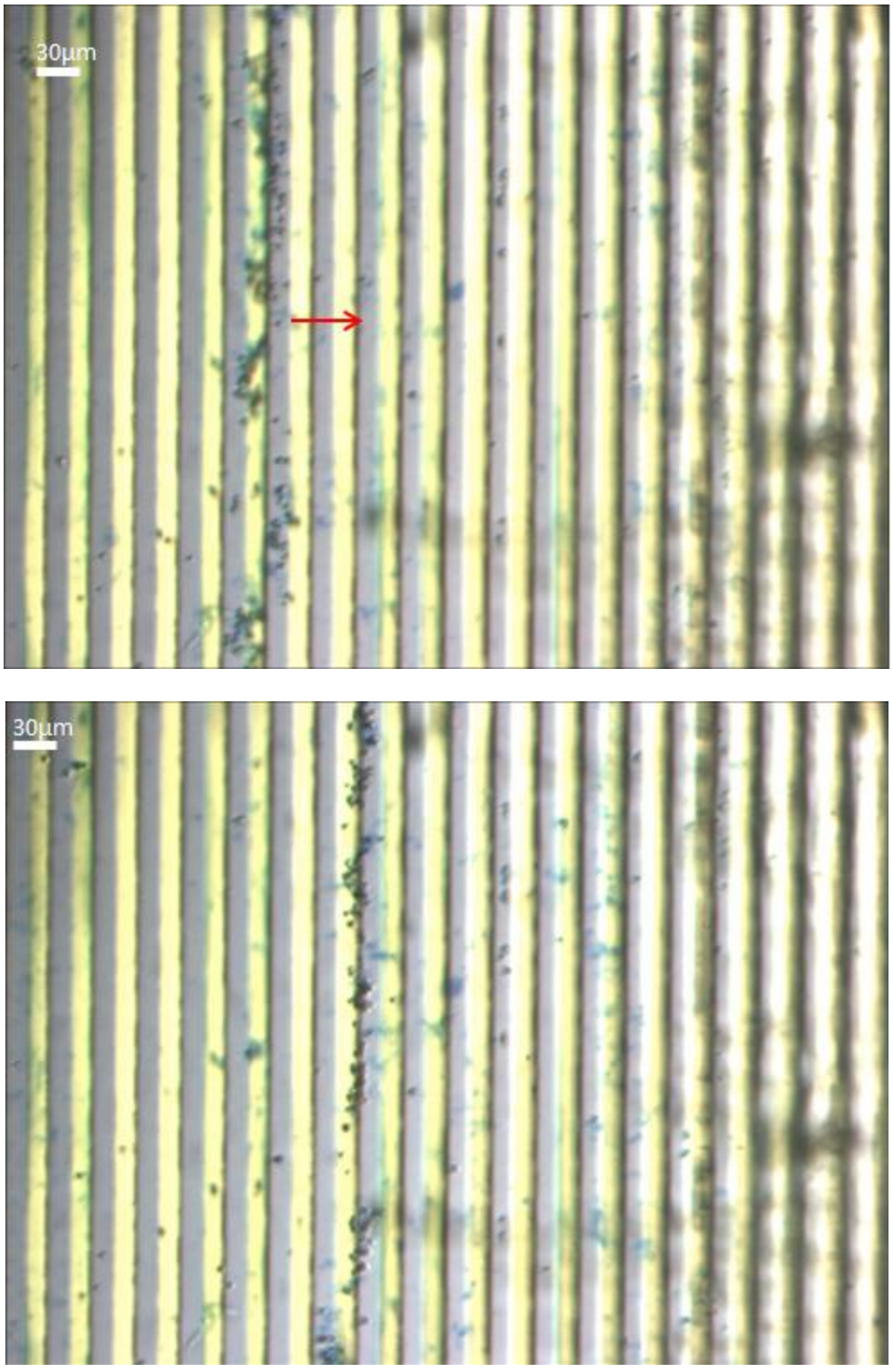

Figure 8.1 Top of figure shows initial position of a sample containing only dead yeast cells. Bottom of figure shows position of cells after a 2Vpp, 25MHz TWDEP field with a negative phase gradient is applied for 30s, resulting in an average lateral velocity of 1.5 µm/s.

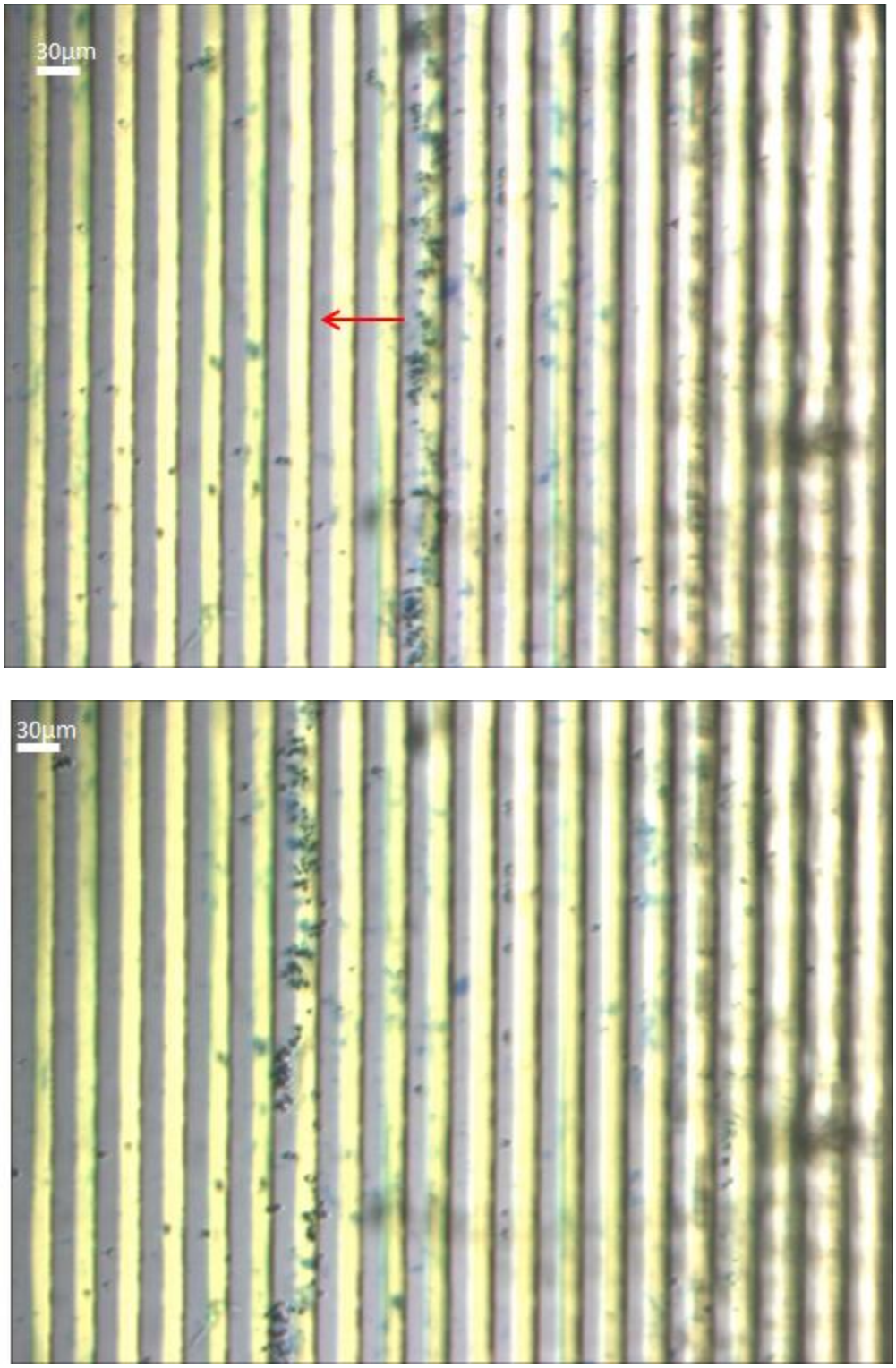

Figure 8.2 Top of figure shows initial position of a sample containing only dead yeast cells. Bottom of figure shows position of cells after a 2Vpp, 25MHz TWDEP field with a positive phase gradient is applied for 35s, nDEP forces levitate the cells while TWDEP forces result in an average lateral velocity of -1.8 µm/s.

The top of figure 8.3 shows the dead yeast sample after re-mixing. The electrodes are kept in a non-multiplexing TWDEP configuration, and the frequency is switched to 100 kHz. The bottom of figure 8.3 shows the distribution of cells after the field was applied for 30 seconds. At 100 kHz, the dead yeast cells are kept levitated above the array by strong nDEP forces, however little to no lateral movement of the cells can be observed. One of the dead cells is highlighted in red in order to provide a reference point. No deterministic lateral movement can be observed within this time period because at 100 kHz the TWDEP forces on dead cells are significantly weaker than there were at 25MHz.

The behaviors observed for dead yeast cells at these two frequencies are what are desired for the multiplexing frequencies: A pair of frequencies for which the TWDEP velocity at one frequency is significantly greater than the TWDEP velocity at the other. The fact that the dead cells moved slightly faster when being made to move from right to left versus left to right using 25 MHz is not significant. What is most important is that the velocities at either of those phase gradients configurations are consistently greater than at its 100 kHz counterpart, so that multiplexing will result in an average displacement in the direction associated with the phase gradient we choose.

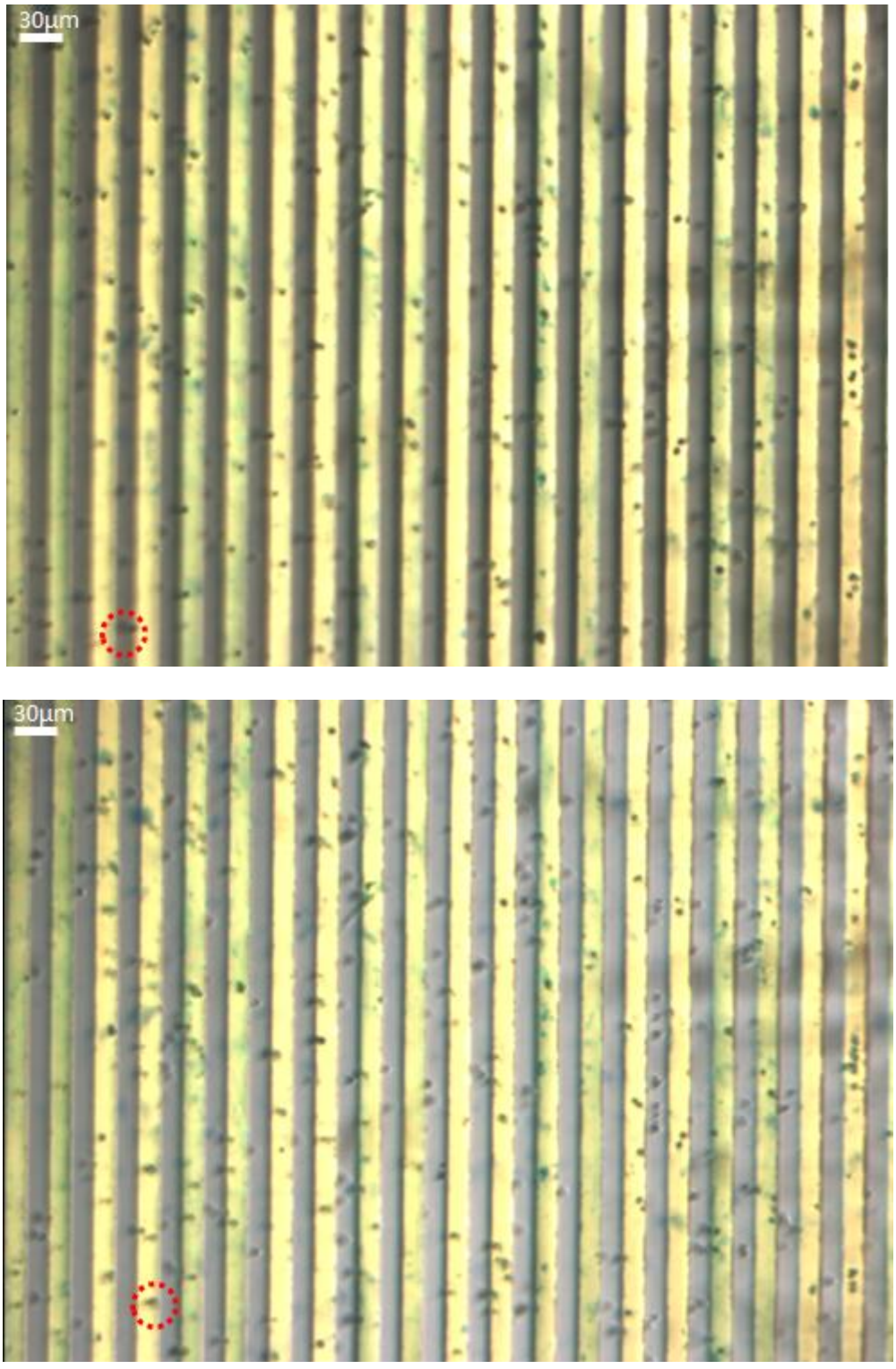

Figure 8.3 Top of figure shows dead yeast cell sample before application of fields. Bottom of figure shows distribution of dead yeast cells after the application of a $2V_{pp}$, 100 kHz TWDEP field for 30 seconds. The cells levitate due to nDEP forces and there is little to no lateral displacement due to TWDEP forces

Figure 8.4 shows a sample containing only live yeast cells, using the same device and buffer as was used for the dead cells. The top of figure 8.4 shows the distribution of cells shortly after a 100 kHz TWDEP field is applied with a positive phase gradient and the bottom of figure 8.4 shows their position 15 seconds later. The majority of the cells do not all start from the same starting location as in the previous case, so one of the cells is highlighted in red as a reference. This configuration causes the live cells to levitate and move from left to right at approximately 6μm/s. Since at 100 kHz dead cells hardly exhibit any movement, this result satisfies the requirement of having a frequency for which the TWDEP velocity of one particle will be greater than the other in a particular direction.

The top of figure 8.5 shows the same sample of live yeast cells and the bottom of figure 8.5 shows the distribution of the cells 18 seconds after a 100 kHz TWDEP field is applied with a negative phase gradient applied. This configuration causes the live cells to levitate and move in the opposite direction as the previous case , right to left, at a velocity of approximately -6.7μm/s.

Since at a field frequency of 100 kHz live cells are responsive to TWDEP forces and dead cells exhibit hardly any movement, the requirement of having a frequency for which the TWDEP velocity for one of the particle types will be greater than the other in a direction of our choosing can be satisfied.

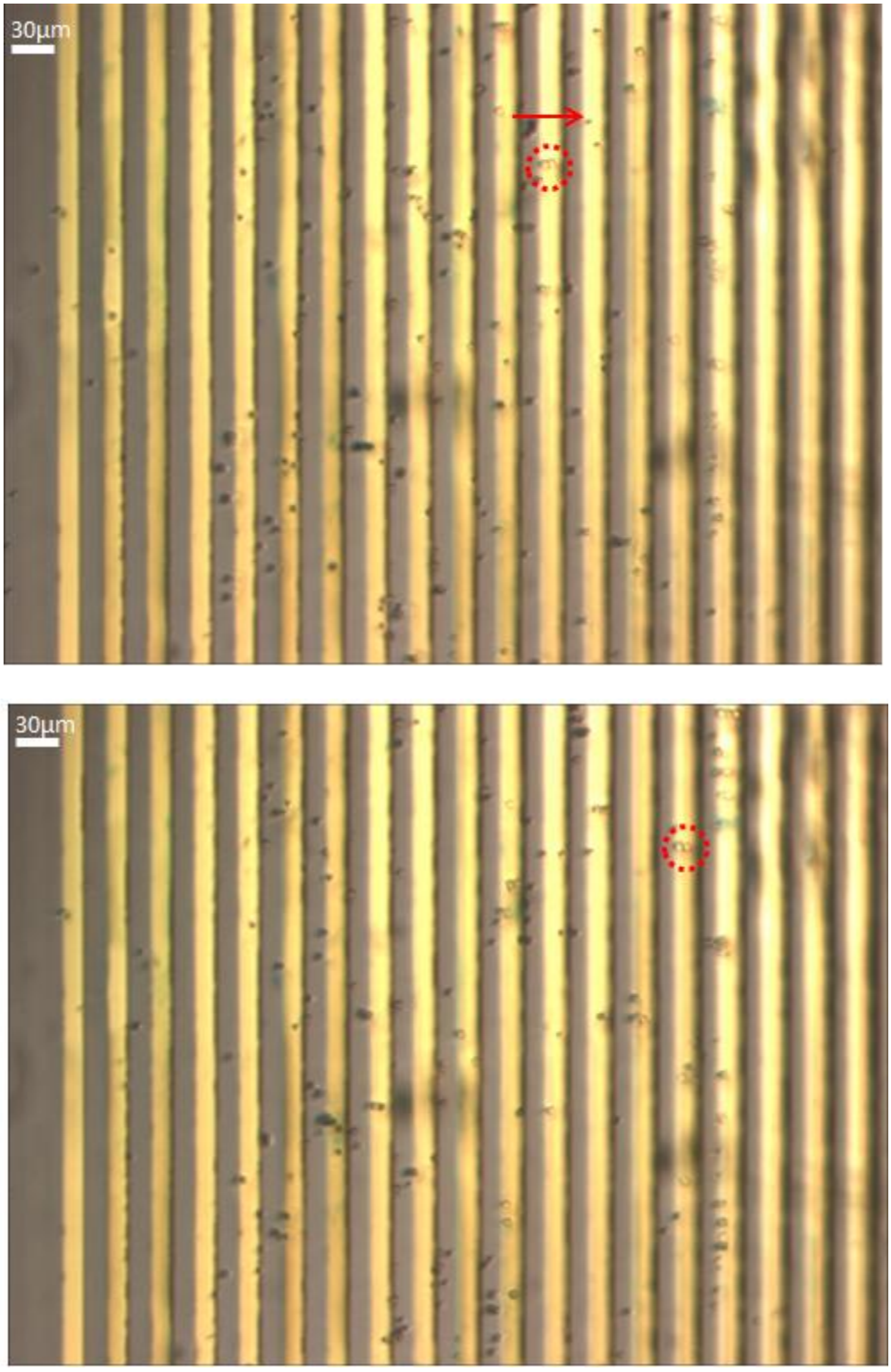

Figure 8.4 Top of figure shows initial position of a sample containing only live yeast cells. Bottom of figure shows position of cells after a 2Vpp, 100 kHz TWDEP field with a positive phase gradient is applied for 15s, resulting in an average lateral velocity of 6 µm/s.

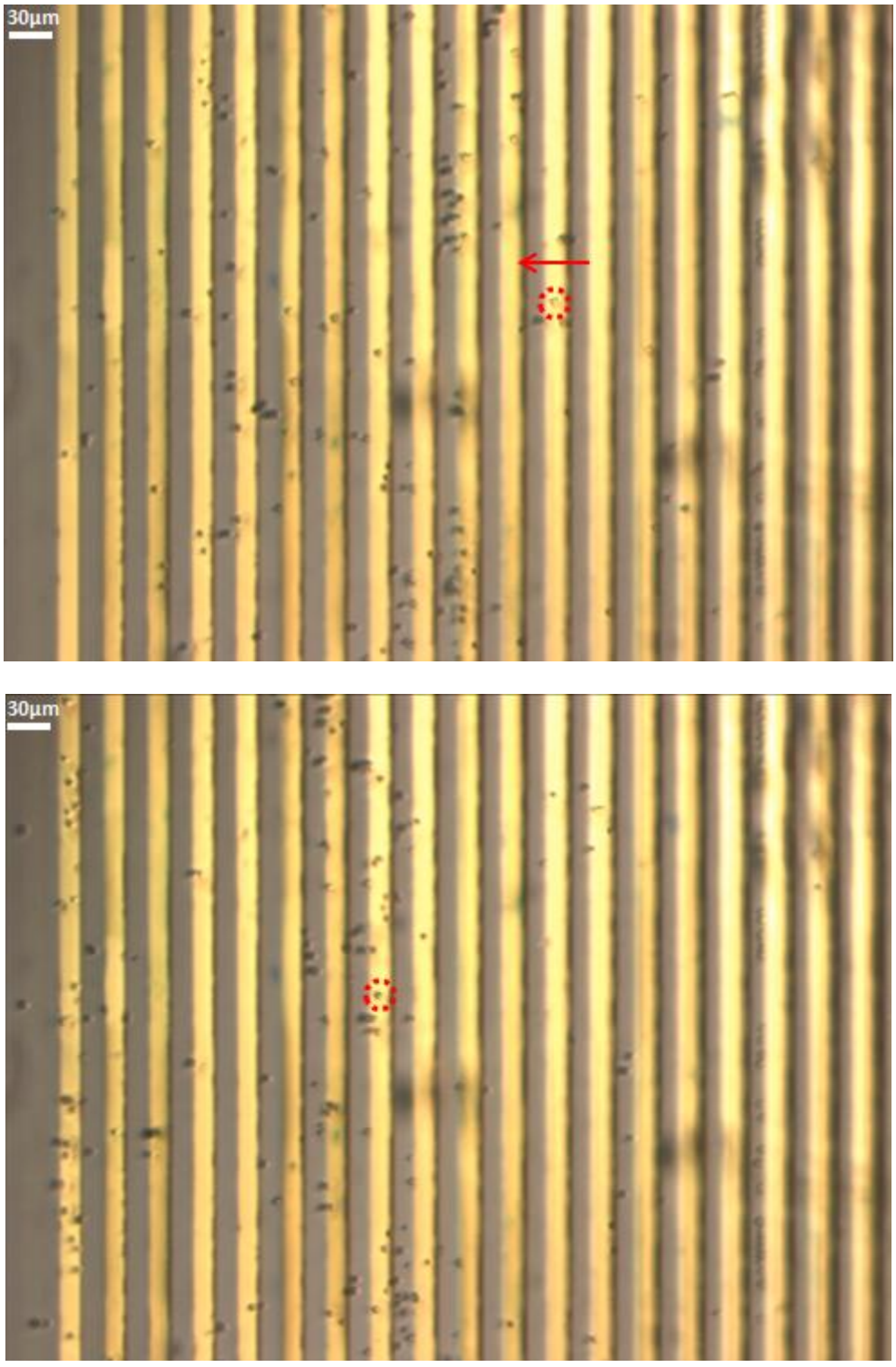

Figure 8.5 Top of figure shows initial position of a sample containing only live yeast cells. Bottom of figure shows position of cells after a 2Vpp, 100 kHz TWDEP field with a negative phase gradient is applied for 18s, resulting in an average lateral velocity of -6.7 µm/s.

The last step in the verification process before attempting to separate mixtures is to observe the behavior of live yeast cells at the second multiplexing frequency, 25 MHz. The top of figure 8.6 shows the distribution of live yeast cells above the electrode array before the application of the field. The bottom of figure 8.6 shows the cells immediately after applying a 25 MHz TWDEP field. Upon application of the field, all of the particles rigidly adhere to the electrode edges as a result of the strong positive dielectrophoresis forces and are rendered immobile. The simulation of figure 8.7 shows why this happens. The simulation shows the electric field magnitude in the region above the electrode array when a TWDEP voltage configuration is applied. The field is strongest in the region between electrodes the field magnitude gradient is at its peak at the electrode edges. Therefore, since at 25 MHz live yeast undergoes pDEP, they get drawn to the closest electrode edge.

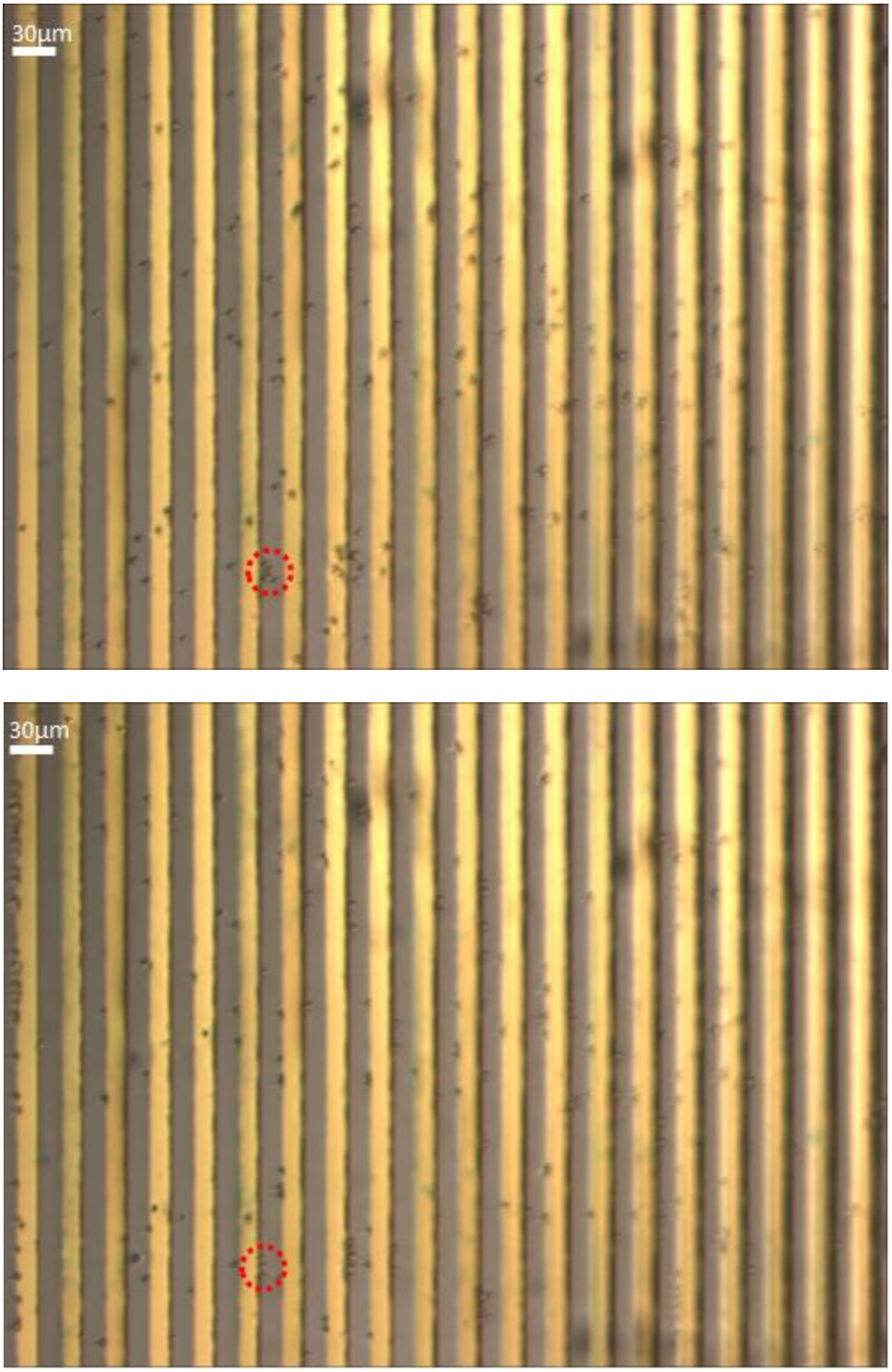

Figure 8.6 Top of figure shows initial position of a sample containing only live yeast cells. Bottom of figure shows position of cells after a 2Vpp, 25 MHz TWDEP field is applied. The cells immediately are rendered immobile by pDEP forces and cannot move

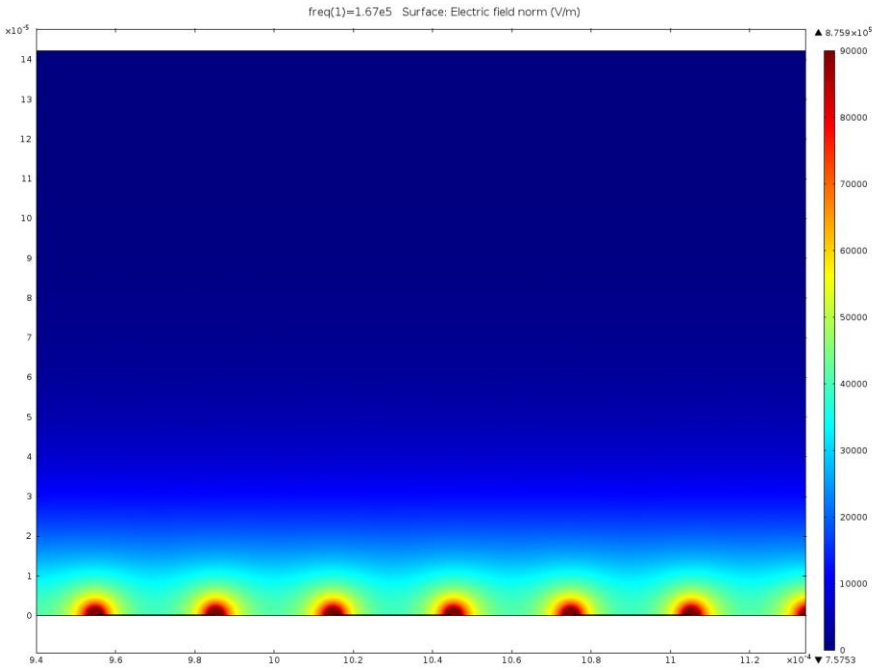

Figure 8.7 Simulation of electric field magnitude generated in region above electrode array. The field magnitude gradient is largest at the electrode corners, causing cells that undergo pDEP to be attracted to there.

Figure 8.8 shows a multiplexing experiment on a mixture containing live and dead yeast cells. Samples were prepared by diluting 100μL of 10^7 cells/ml suspensions containing each cell type into 1.5 ml of KCL solution. The field was configured to multiplex between 100 kHz for duration of 4 seconds and 25 MHz and for 6 seconds, a 67% duty cycle. TWDEP traps were configured at the ends of each array. The top of figure 8.8 shows the initial position of cells and the bottom of figure 8.8 shows the distribution of cells after the application of the multiplexing fields for 10 minutes. It is not until about ten minutes later that it appears that the cells have bifurcated into two populations. Due to the presence of a fluid flow in the direction parallel to the electrodes, the final position shown below is at the same horizontal point as the original frame but vertically below it. Verification of the purity of the separated sample presented here and the other results of this chapter will be discussed later. However, it can be seen that the population of blue dyed cells is greater in the left-hand side trap as opposed to the right hand side trap, which is what would be expected given the field configurations.

In this particular case, ten minutes is a relatively long time in comparison to the time it would take for these cells to traverse the distance shown. The reason why this was the case is shown in figure 8.9. Not only is duty cycle ratio between the two configurations critical, but the actual length of time each is applied turns out to play an important role. Figure 8.9a is a close-up view of one of the live yeast cells during an interval when the 100 kHz field is applied and figure 8.9b shows the cell towards the end of that 6 second cycle, after TWDEP forces have moved it laterally. At the time corresponding to figure 8.9c, a 25 MHz TWDEP field is applied. The combination of the particles height and trajectory at the time of the switch causes the particle to be pulled backwards by the pDEP forces and remain trapped at an electrode edge for the remainder of the 4 second 25 MHz cycle (figure 8.9d). Therefore, it is only after long periods of time that the particles happen to have enough TWDEP displacement to overcome those effects when multiplexing with field configurations of this length. While on average this type of time-multiplexing may cause particles types to separate in a stop-go manner, it is not truly averaging out the pDEP and nDEP forces and it does not permit the particles to travel simultaneously in opposite directions, thereby making the separation inefficient with respect to time. This problem is remedied by shortening the durations of each field configuration such that the transient effects that occur due to the DEP fields are too small to make an instantaneous affect on the particle motion and only the average DEP forces will play a role.

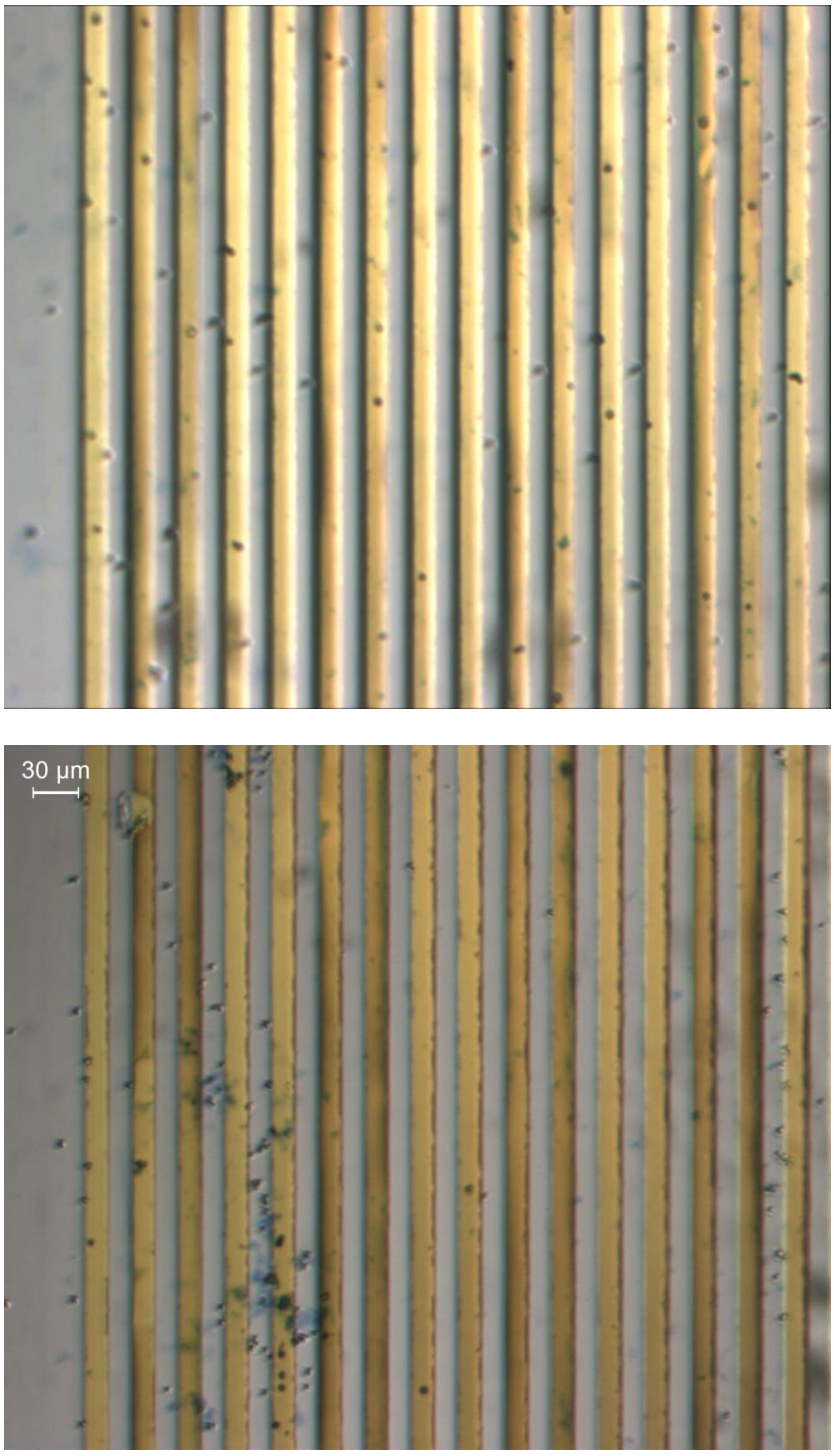

Figure 8.8 Top of figure shows frame from TWDEP electrodes before application of multiplexing fields. Bottom of figure shows distribution of cells after 10 minutes of multiplexing between 100 kHz and 25 MHz with a 67% duty cycle. Dead cells are stained in blue and gathered on the left, while live cells have collected in the TWDEP trap on the right.

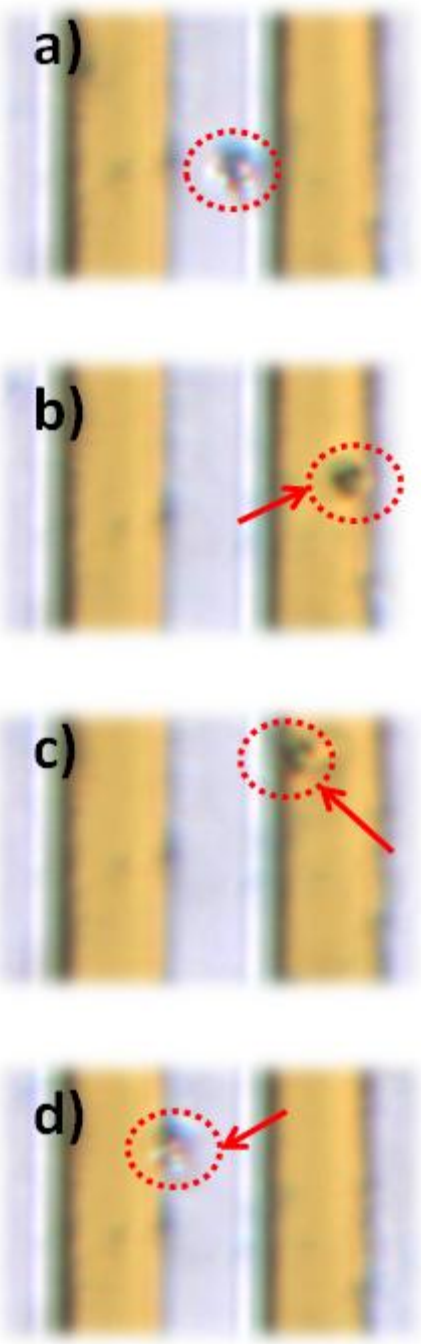

Figure 8.9 a) Initial position of live yeast cell b) TWDEP forces propel a live cell from left to right. c) As soon as 25 MHz field is applied, the cell moves down and backwards due to pDEP forces. d) Final position of cell, showing how pDEP forces disrupted the advancement made by TWDEP forces during the first phase of the multiplexing cycle

Figure 8.10 shows a time-multiplexing trial using live and dead yeast cells where the field durations where shortened to approximately 200μs and 50μs a piece, well shorter than the cells transient response to DEP forces. The fields are configured to multiplex between 100 kHz and 25 MHz and the duty cycle is set the 80% value calculated in chapter 7. The top of figure 8.10 shows the initial distribution of cells, and the bottom of the figure shows the cells positions after 40 seconds.

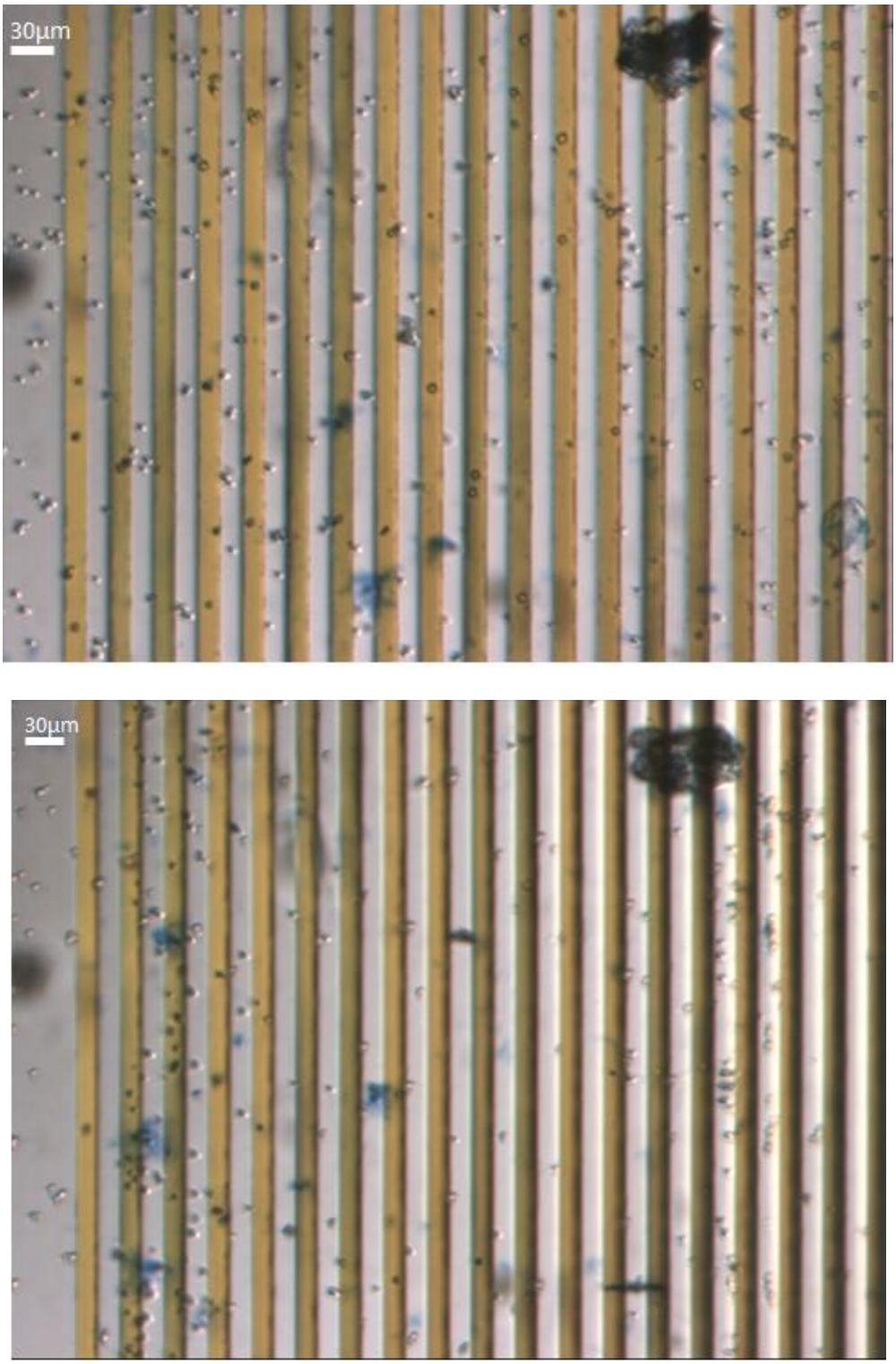

Figure 8.10 Top of figure shows initial distribution of cells in mixture containing live and dead yeast cells. Bottom of figure shows particles after 40 seconds of multiplexing between 100 kHz and 25 MHz. In this trial, the duration of each muxing cycle was shortened to 50us, short enough to average out the effects of the pDEP phase of the cycle

In this case the population within the cell mixture again bifurcates and two groups move towards the opposing trapping locations. There appears to be significantly more dead yeast cells on the left trap as opposed to the right, however it appears that some cells that are not dyed moved into the trap on the left. There are a couple of additional significant features to the result shown here. Time-multiplexing in this case manages to keep all the cells levitated for the duration of the experiment, which is in stark contrast to the previous case where live cells became immobile during the application of the 25 MHz field cycle. This shows that the motion the cells exhibited in this case were a function of the time-averaged force. In addition, as a result of shortening the duration of the fields, this bifurcation became visible much sooner, in less than 40 seconds versus 10 minutes.

Figure 8.11 shows the results of a third trial using yeast cells. In this experiment the cells being tested all come from the same 2 week old cell culture sample. A sample of this age will have cells that are at various stages in their life cycle and also vary in size. After the application of the 80% duty cycle field, the cell population once again bifurcates. The challenges behind verification of this result will be discussed further in chapter 9. However, it is significant to note, that once again because of the modification of the duty cycle, the cells remain elevated even when in their trapping locations, due to the averaging out of pDEP effects.

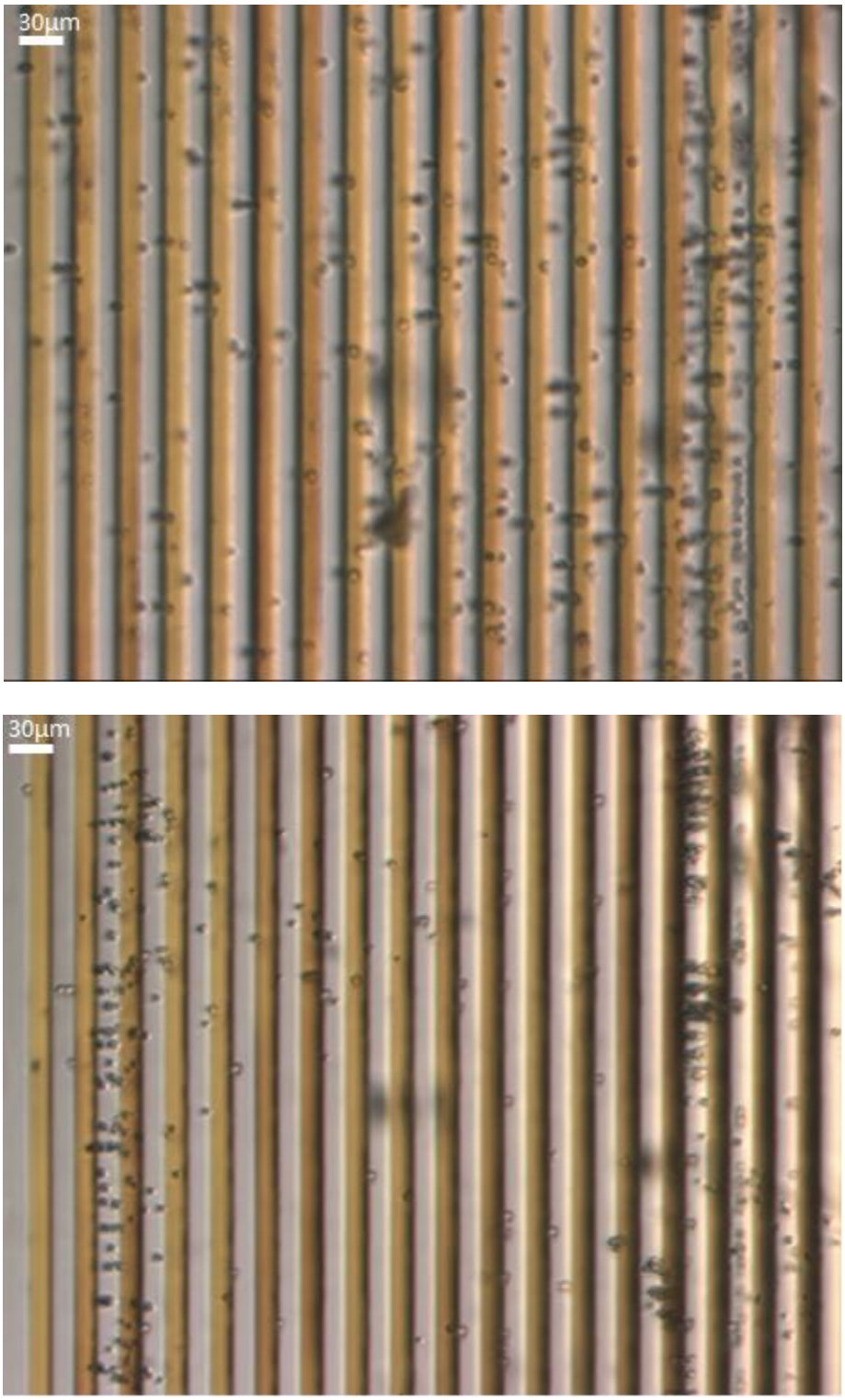

Figure 8.11 Time multiplexing dielectrophoresis trial on a 2 week old cell culture containing cells at various stages in their life cycle. The multiplexing configuration is between frequencies of 100 kHz and 25 MHz at a duty cycle of 80%. The cells bifurcate into the trapping regions after 40 seconds of multiplexing.

8.1.2 Time-Multiplexed Dielectrophoresis of Live Yeast Cells and 10μm PS-COOH

In this section, we present experimental time-multiplexing dielectrophoresis trials using live yeast cells and 10μm PS-COOH polystyrene microspheres. The top of figure 8.12 shows a mixture containing the two particle types in a 5mS/m KCL medium. If one were to attempt to separate these particles using an affinity method and based solely on their TWDEP profiles, the comparison of the velocity spectra for them (shown in figure 7.4) would suggest that the separation could be done with the application of a single frequency in the range of 1 MHz to 2 MHz, where the TWDEP velocities of the two particle types are opposite in sign. The bottom of figure 8.12 shows what happens if that approach is taken and a positive phase gradient TWDEP field is applied at a constant frequency of 1.25 MHz. The microspheres undergo nDEP at this frequency and are levitated out of the focal plane of the microscope. The microspheres then begin to travel from right to left as they are propelled by TWDEP forces. As can be seen for the live yeast cells, they have strong pDEP forces exerted on them at 1.25 MHz, adhering them to the electrodes, thereby making their TWDEP velocity components at that frequency irrelevant. The live yeast cells vigorously rotate due to TWDEP forces while stuck to the electrode edges but do not have any lateral displacement as pDEP forces prevent them from being manipulated.

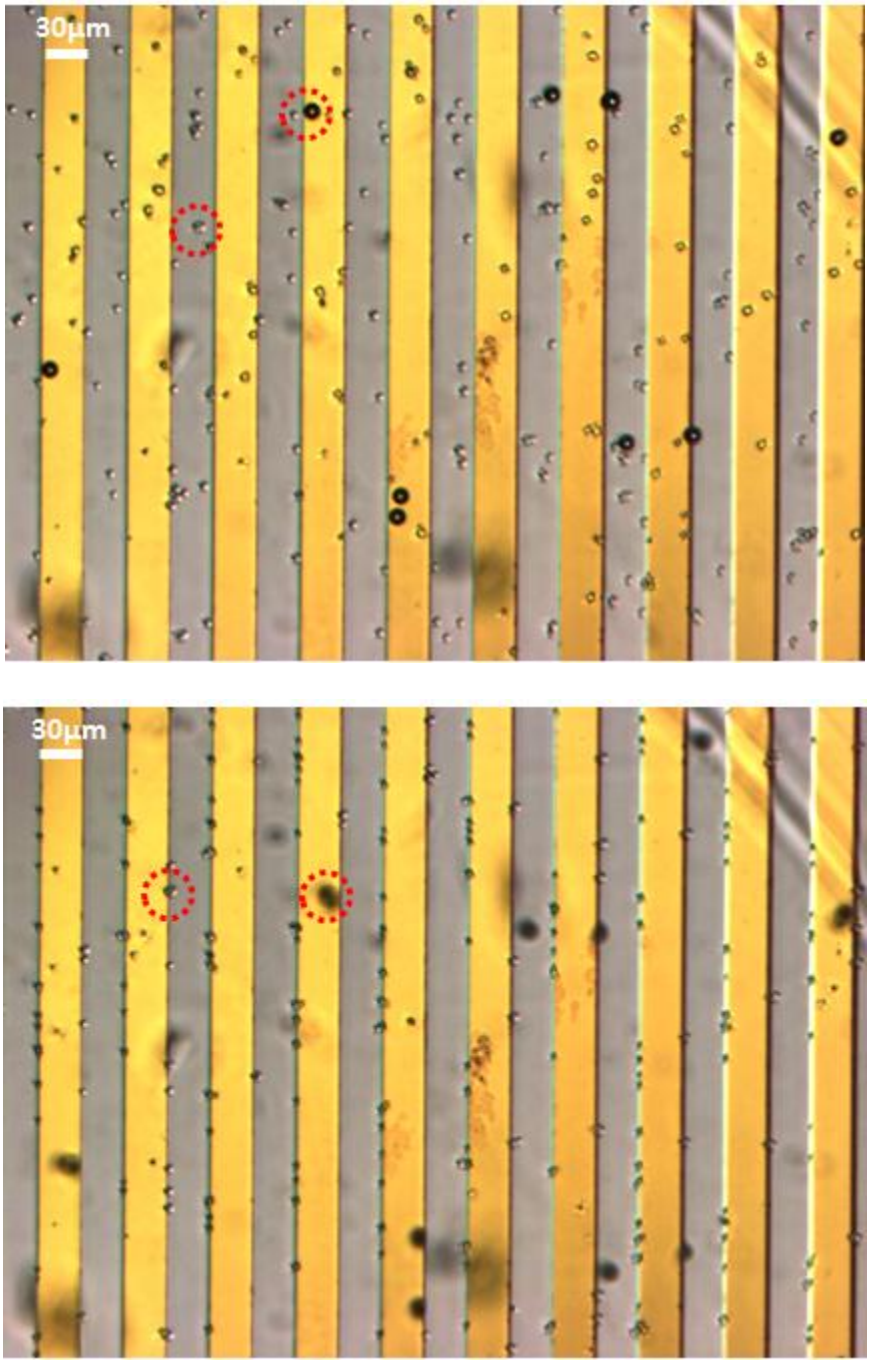

Figure 8.12 Top of figure shows initial distribution of sample containing 10um PS-COOH and live yeast cells. Bottom of figure shows sample after application of a 1.25 MHz TWDEP field. Negative DEP forces cause the microspheres to levitate and TWDEP forces propel the microspheres from right to left, while positive DEP forces render the cells immobile.

Figure 8.13 shows the results of a time-multiplexing dielectrophoresis trial involving these same two particle types. In this trial, the separation parameters calculated in chapter seven were used; a field multiplexed between 100 kHz and 500 kHz with a duty cycle of 70%. The top of figure 8.13 shows the distribution of particles shortly after the application of the field, and the middle of figure 8.13 shows the arrangement of particles 20 seconds later and then 40 seconds later at the bottom of the figure. After 40 seconds, the microspheres and cells have migrated completely apart. It should be noted that in this trial there was a significant vertical flow during the experiment that disrupted the trap for the live yeast cells and caused all the particles to be displaced along the axis parallel to the electrodes.

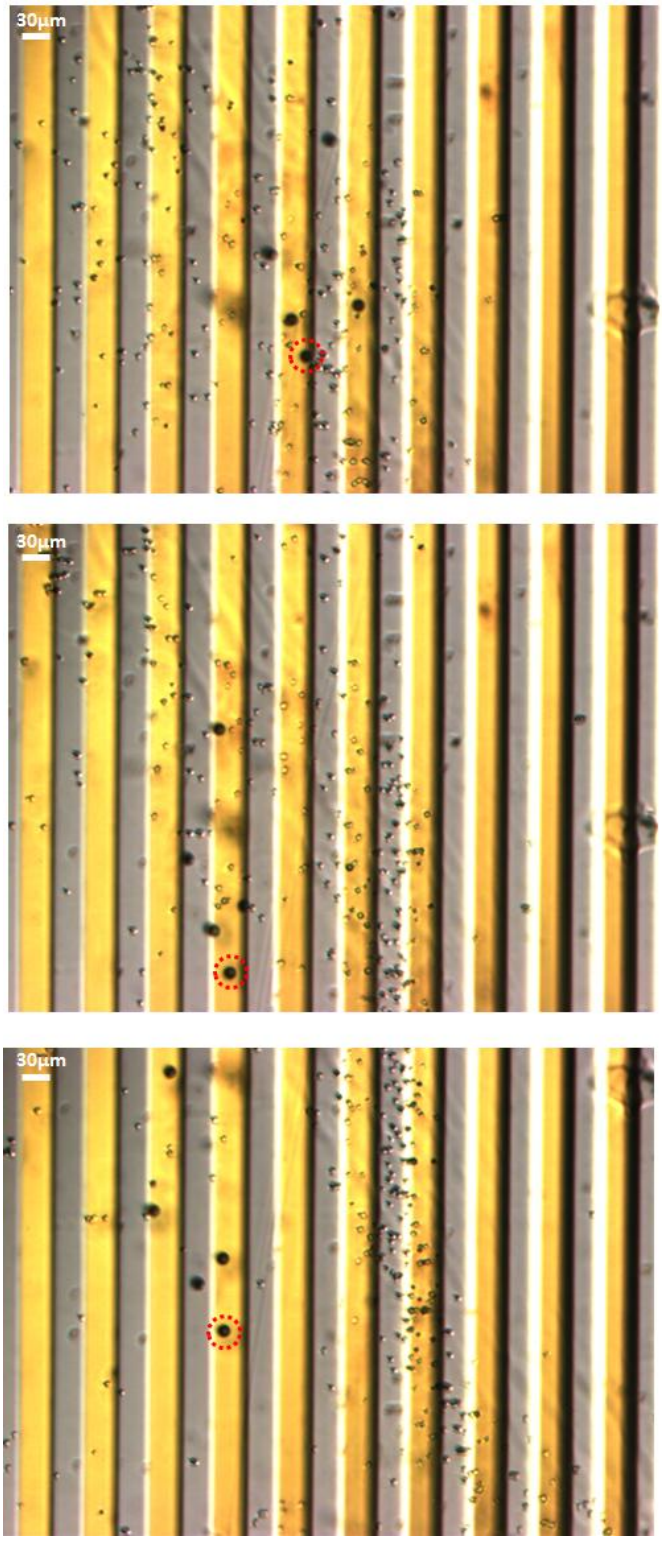

Figure 8.13 Time multiplexing of 10um PS-COOH and live yeast cells with frequencies of 100 kHz and 500 kHz at a duty cycle of 70%. Top of figure shows particle distribution shortly after application of fields, the middle shows their positions after 20 seconds and the bottom shows that the particles have migrated apart after 40 seconds.

8.2 DISCUSSION OF RESULTS

In this section experimental results showing the application of time-multiplexing dielectrophoresis on mixtures containing combinations of live cells, dead cells and polystyrene microspheres were presented. In the case of polystyrene versus live cells, a clear separation could be observed. Bifurcations among samples containing yeast cells mixtures were observed, but it is much more difficult to discern the degree and purity to which live and dead yeast cells were separated from each other. Looking at the visual data for the first two trials with live and dead yeast cells, one can empirically observe that there are more blue-dyed dead cells in one location versus the other, but a true quantitative measure is difficult to report without having access to the cells after being separated. For example, it could be that dead cells that didn't properly absorb the blue dye ended up in the proper location (false negative) and vice versa, which would have to be verified using other biological laboratory methods. However, a significant result that was observed, was the ability of the method to exert differential forces on a particle, and the use time multiplexing dielectrophoresis to create motion patterns for particles that were a result of time-averaged force values.

In the next chapter we present a summary of this dissertation and conclusions that we draw from this work.

9.0 SUMMARY AND CONCLUSIONS

In this chapter, we first present a brief summary of the results and findings from this research and then present our final conclusions.

9.1 SUMMARY

In this dissertation, we present a novel methodology and accompanying hardware lab-on-chip platform for separating microscale particles in solution. Our approach is centered on the use of a technique that we devised, time-multiplexing dielectrophoresis.

In chapter 2, we explained the theory behind the basis for our technique. Included in this chapter is a discussion of the relevant forces exerted on particles in dielectrophoresis-based microsystems, and also how dielectrophoresis has been used in the past by other researchers to separate particles.

In chapter 3, we give a detailed description of the various electrical models used to describe the relevant electrical characteristics of particles within the context of dielectrophoresis. In this chapter, we also identify a library of 5 different particle types that had varying differences in makeup and electrical properties. This library of particles is the center of the analysis, designs and results in the later chapters.

In chapter 4 we present a detailed explanation of our time-multiplexing dielectrophoresis method. Chapter 4 begins with a derivation of the average net velocity of a particle that results from being in the presence of a dielectrophoresis field with rapidly changing frequencies and phase gradients. Chapter 4 concludes by showing the benefit of the method by way of specific examples.

Chapter 5 provides the implementation details of the hardware platform designed to demonstrate our technique. Included in this chapter are the designs for dielectrophoresis electrodes for characterizing and separating particles, microfluidic interfaces for delivering and containing samples and the necessary supporting electronics.

In chapter 6, we experimentally characterize the particles from our library, and use those results to verify our original models from chapter 3. We also carry out a best-fit analysis in chapter 6 in order to extract refined model parameters. The results of this chapter are summarized in table 6.6.

In chapter 7, we use the refined models from chapter 6, to show analytically the benefits of our method. In this chapter, we carried out an analysis on every combination of particles from our library, and identified the multiplexing parameters needed to separate them. The results of the chapter are summarized in table 7.1

In chapter 8, we presented the results of experimental time-multiplexing dielectrophoresis trials on mixtures containing combinations of live yeast cells, dead yeast cells and polystyrene microspheres. The results of the trials presented in this chapter showed that time-multiplexing dielectrophoresis can be used to cause the time-averaged particle motion to be the result of the time-multiplexing fields.

In the next chapter we present our conclusions from this dissertation and in chapter 10 we present our ideas for future research.

9.2 CONCLUSIONS

In this chapter we present our conclusions based on the work carried out in this dissertation. This dissertation was centered on the premise that particles varying in type and composition have different electrical characteristics; therefore they will have unique responses to changes in the electric field they reside in. This premise was established theoretically in chapters 2 and 3 of this dissertation and experimentally verified via the characterization results of chapter 6. For demonstration purposes, in this dissertation we selected a small library of particle types that had differences in size, composition and surface chemistry in comparison to one another, two types of biological organisms and three types of manufactured microspheres and selected appropriate electrical models for each of them. A summary of the results from experimentally verifying these models and their refinement via best-fit analyses are presented in table 6.6. The results show that the differences according to type can indeed be mapped back to differences in electrical characteristics, and in turn predict that each particle type wil have a unique response when in the presence of a dielectrophoresis field.

Based on this premise, we hypothesized that separations between particle types could be achieved by employing the use of microelectrode arrays to apply specific combinations electric field phase, frequency and duty cycle repeatedly over time. These configurations can be selected such that particles contained in a fluid that are of dissimilar type can be made to travel in opposite directions and eventually separate from one another. The technique we developed to

prove this hypothesis is time-multiplexing dielectrophoresis. We claimed that time-multiplexing dielectrophoresis has the advantage of allowing for separations between particle types to take place in conditions that would otherwise make them inseparable using conventional dielectrophoresis, significantly lessen the requirements on selection of a buffer medium and reduce the number of electrodes required to carry out separations lab-on-chip separation devices that required. We revisit each of those claims in the following subsections.

Creating Separable Conditions via Time-Multiplexed Dielectrophoresis

The claim of creating separable conditions when other methods would not be able to do so effectively was demonstrated by the results of chapter 7. In real world applications, the medium conductivity is a variable that does not have free range to be varied in order to accommodate separations. Traditional dielectrophoresis separation methods require that the buffer conductivity be adjusted within a very precise range so that the velocity spectra of the particles of differing type are opposite in sign at a particular frequency. In order to demonstrate the conflicting requirements this presents when using dielectrophoresis to separate particles, the buffer medium used throughout our analyses and experiments were kept consistent throughout the dissertation and not varied in order to accommodate separations between types.

The results of the separability analyses of chapter 7 showed that for certain combinations of particles in the chosen medium, there was not a single frequency that could be applied and cause the particles to migrate apart. Therefore, dielectrophoresis affinity methods could not be used to separate the particles. This analysis was carried out based on actual characterization data. The cases for which the use of an affinity method would not permit separation were: 10μm PS vs. live yeast, 10μm PS vs. dead yeast, 10μm PS-COOH vs 6μm PS-COOH, 10μm PS-COOH vs

live yeast and live yeast vs. dead yeast. The table 7.1 summary of results show that all of these particle combinations could be made to have lateral velocities that are opposite sign if time-multiplexing dielectrophoresis is applied and appropriate multiplexing configuration parameters are selected. These results are a key research contribution as they show that differential velocities can be created by the time-multiplexing dielectrophoresis method, and not be determined by the buffer the particles are place in.

We experimentally demonstrated this claim with the experimental results of chapter 8. The live yeast cells in our particle library had the unique feature of exhibiting strong positive dielectrophoresis forces in the selected medium that rendered them immobile. In the experimental cases examined, live yeast versus 10 μm PS-COOH microspheres and dead yeast, it was shown that single frequency could not be applied that would allow them to effectively separate. The application of time-multiplexing dielectrophoresis permitted the effects of positive dielectrophoresis forces to be averaged out and for both cases. After applying time-multiplexing dielectrophoresis, a bifurcation between particle populations was observed, and particle types were made to move laterally in opposite directions.

Using Time-Multiplexed Dielectrophoresis To Increase the Efficiency of Particle Separations

The additional claim that time multiplexing can increase of the efficiency of particle separations, was demonstrated by the results of chapter 7. In three of the cases, 10μm PS-COOH vs. 10μm PS microspheres and 10μm PS-COOH vs. 6μm PS-COOH microspheres, a band of frequencies for which an affinity method could be applied and separate the particles did exist. However, it was shown, that by careful selection of multiplexing parameters, the application of time-multiplexing dielectrophoresis results in increased separation velocities over

affinity methods. This is a significant research contribution because in the context of dielectrophoresis-based particle separations, an increase in separation velocity has more implications than just faster separation times. When the separation velocity can be increased, as we have shown, then it becomes possible to separate particles that were previously considered too similar in electrical characteristics to be separated using conventional dielectrophoresis. In addition, this increase in separation velocity has a direct bearing on the hardware implementation of the device, as fewer electrodes can be used to separate smaller differences as was explained in chapter 7 of the case of 10μm PS-COOH vs. 6μm PS-COOH microspheres.

Efficient Lab-on-Chip Hardware Implementations

Another noteworthy contribution from this dissertation was demonstrated by the hardware implementation of our method. Field flow fractionation separation methods operate by mapping particle differences to electrode array lengths and as the particles being separated become increasingly similar more electrodes are required. As mentioned in the previous paragraph, our method has the advantage of increasing separation velocity and requiring fewer electrodes. However, that is not the only reason our method leads to more efficient lab-on-chip designs that require far fewer electrodes. The hardware design and our results revealed that separations between particle types can take place with as few as 16 electrodes, as our method separates by causing particles to always travel in opposite directions and is not bounded by the differences in particles themselves. In addition our designs demonstrated how a complex function such as particle separations can be achieved using relatively simple fabrication and prototyping procedures.

In conclusion, we have shown that time-multiplexing dielectrophoresis is a powerful separation methodology, with many benefits. The research contributions made by this dissertation are the type in general that are needed for dielectrophoresis-based lab-on-chip separation devices to grow out of its current status of being a subject matter for research, and into a realistic, viable option for clinicians, researchers to use in real-world scenarios.

10.0 FUTURE WORK

There are many ideas and new areas of research that could stem from the work presented in this dissertation, some directly related to the original proposed technique and method and some totally new.

The first area of future work would be the inclusion of more than just two field configurations when multiplexing. In our analysis and demonstrations, we multiplexed two field configurations together to exert differential forces on a particular particle type. It is very likely that should a 3^{rd}, 4^{th} or n^{th} profile be entered into the scheme, then more complex force-averaging patterns can be devised, creating separable conditions for cases that even our method would not be able to handle.

The analysis of chapter 7, the determination of the multiplexing parameters needed to separate a given combination of particles, revealed that time-multiplexing dielectrophoresis is a powerful method, but could be even further enhanced if the truly optimum multiplexing frequency, phase and duty cycle configurations are found. The work presented in chapter 7 lays the foundation for casting this problem in the context of a linear programming or other type of optimization problem. This would be particularly necessary should the effects of more than two multiplexing profiles be considered or even the effect of the current two profiles on samples with 3 or 4 types of particles, as the brute force approach we took would become very computationally intensive.

Another area for future research would be in the improvement of particle models, as dielectrophoresis separation methods rely heavily on accurate knowledge of particle behavior. The models used in this work, and other work like it, lean more heavily towards fitting data into existing models rather than devising new ones that may be more accurate. For example, the yeast cells used in this dissertation were modeled using a mutli-shell spherical model. In reality, yeast cells are not spheres, they are ellipsoids and the current model is just an abstraction that provides fairly accurate results. In addition, the governing dielectrophoresis equations currently used by most research groups are based on the assumption that the particles will act as infinitesimal dipoles. It very well could be possible that equations assuming the particles are hexapoles or octopoles could yield more accurate results. These types of model refinements and adjustments are what will ultimately lead dielectrophoresis based separation methods to being able to precisely target specific particle types.

There are also future areas of research in the field of hardware design that could come out of the designs we presented in this dissertation. Mentioned earlier and shown in appendix A were our attempts to create electrodes using technologies with well-established fabrication methods, PCBs and integrated circuits. The general hope in the field of lab-on-chip technology is that these types of devices will one day become pervasive and eventually be incorporated into mobile devices, or maybe even become implantable. If these devices can be easily incorporated into existing design and manufacturing flows, their chances of proliferating will be greatly increased.

Finally, looking at the big picture, the purpose of time-multiplexing dielectrophoresis is not to just separate particles, but to separate particles with a purpose of carrying out some sort of specific function, assay or diagnostic. This means that this method will have to be combined

with other types of sensing technologies, so that the results of separations can be quantitatively analyzed. One such possible idea is presented in figure 10.1. Once the particles have been separated or arranged, it could be possible that laser optics and photo detectors could be used to detect diffraction patterns created by the unique arrangement of separated fractions [60].

The ideas presented in this chapter are certainly not the only ones possible, and many more prospects for future research exits as a result of the work from this dissertation.

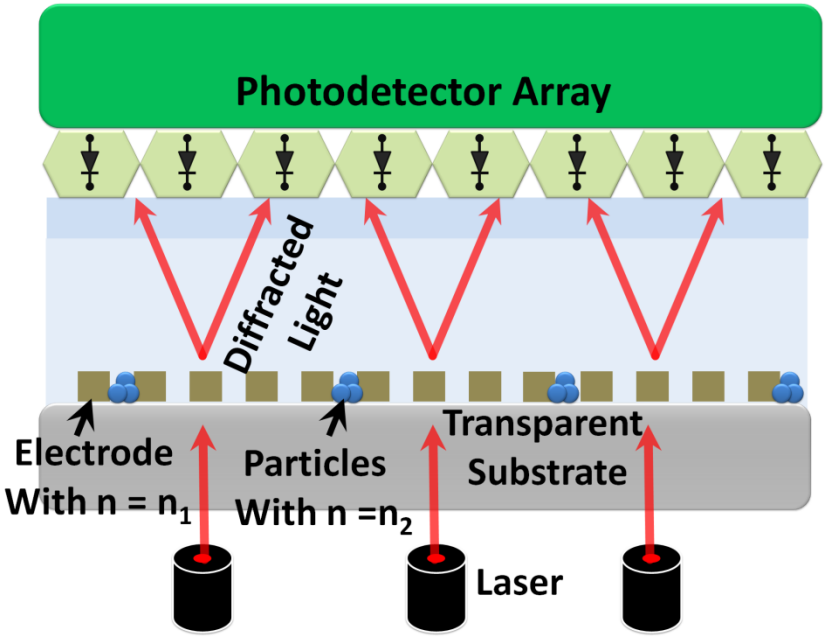

Figure 10.1 Possible implementation for lab-on-chip assay/diagnostic by using laser optics and photodetectors to sense the presence of separated particle fractions

APPENDIX A

ALTERNATIVE HARDWARE IMPLEMENTATIONS

In the course of this dissertation, we explored two other approaches to designing the lab-on-chip hardware platform: the use of printed circuit board traces for electrodes, and the use of 3D integrated circuit technology. In the sections below, we briefly describe our attempts and why they were not used.

The first approach was the use of printed circuit board traces as electrodes and was used in our preliminary investigations and the results are shown in figure A.1. Copper wire traces on the top layer of the PCB were used to create a linear array of 52 dielectrophoresis electrodes. The width of each electrode and the gap spacing between electrodes is 3 mils (76.2 μm), which corresponds to the minimum feature size available in the PCB technology we used. In order to make the electrodes accessible to the fluid, the solder-mask layer was excluded from the region above the array. Each electrode is connected to an I/O pad that allows it to be driven by an external voltage source. A close-up view of the PCB trace electrodes is shown at the bottom of figure A.1.

The lack of a solder-mask layer above the electrodes and the inclusion of it everywhere else on the board also had the effect of causing the electrode array to be recessed from the top

surface of the board. By placing a custom glass cover slip over this region, we create a channel that is used to contain the aqueous samples under test. Holes are drilled at both ends of the cover slip and can be connected to flexible tubing to allow the device to be used in configurations where a pressure-driven flow continuously transports samples on and off of the board.

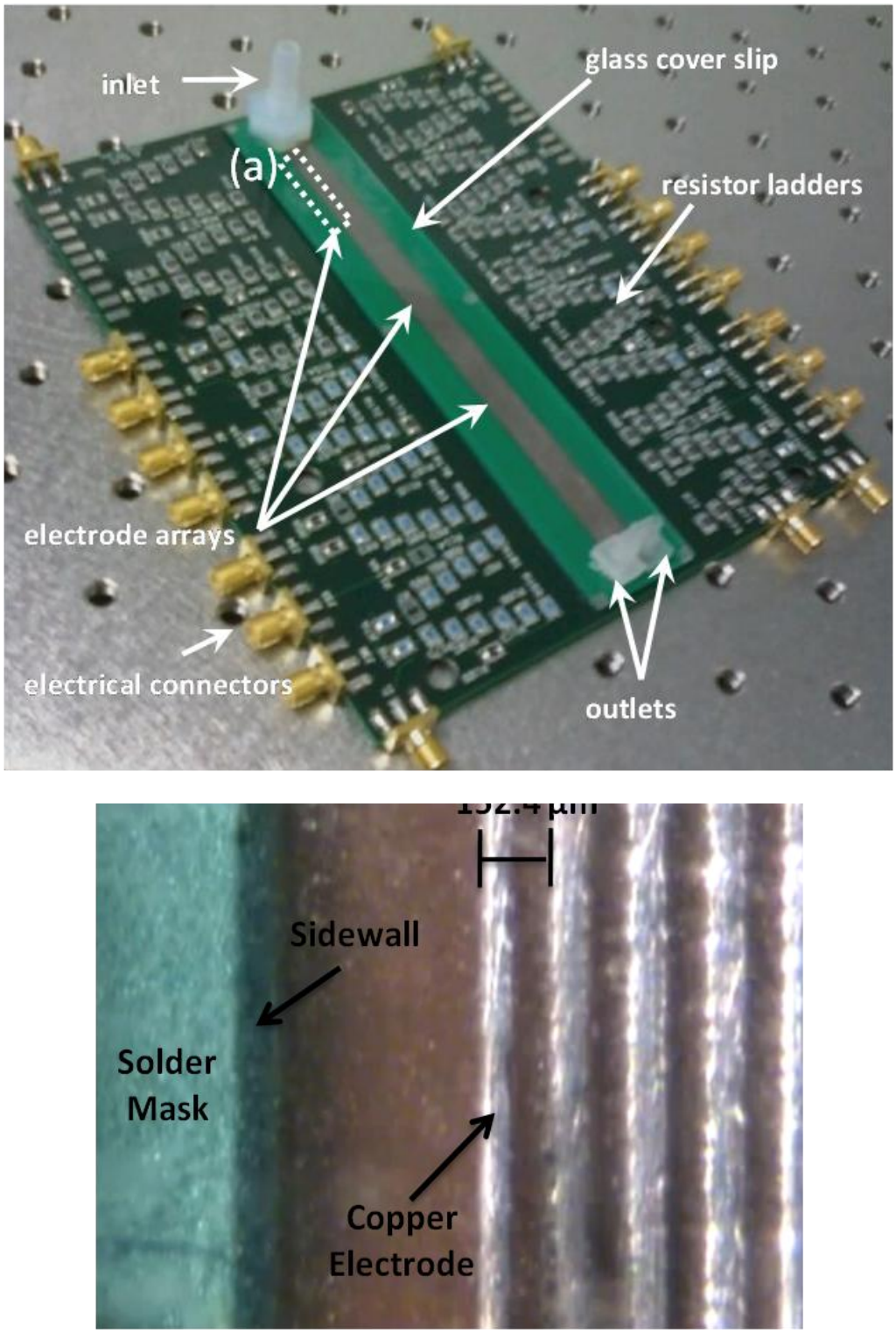

Figure A.1 Top shows custom PCB implementation of lab-on-chip. Bottom shows close-up view of electrodes formed from PCB traces and containment trench created by etching away the solder mask layer.

The advantage of this design approach was that it was very rapid and inexpensive, but it also had numerous drawback. Figure A.2 shows the PCB being used to successfully dielectrophoretically manipulate polystyrene beads that are 6μm and 43μm in diameter. The primary disadvantage was the minium attainable feature size for electrodes using this technology, 76.2 μm. At that large gap spacing, it is necessary to use to greatly increase the voltage (10V +) in order to manipulate particles in the size range we are interested in. The increase in voltage in turn also reduces the maximum bandwidth and restricts the multiplexing method. The other drawback is that since the electrodes heights are much larger than the particles, once particles fall below the electrode surface, they become permanently stuck as enough force cannot be generated to levitate them back out.

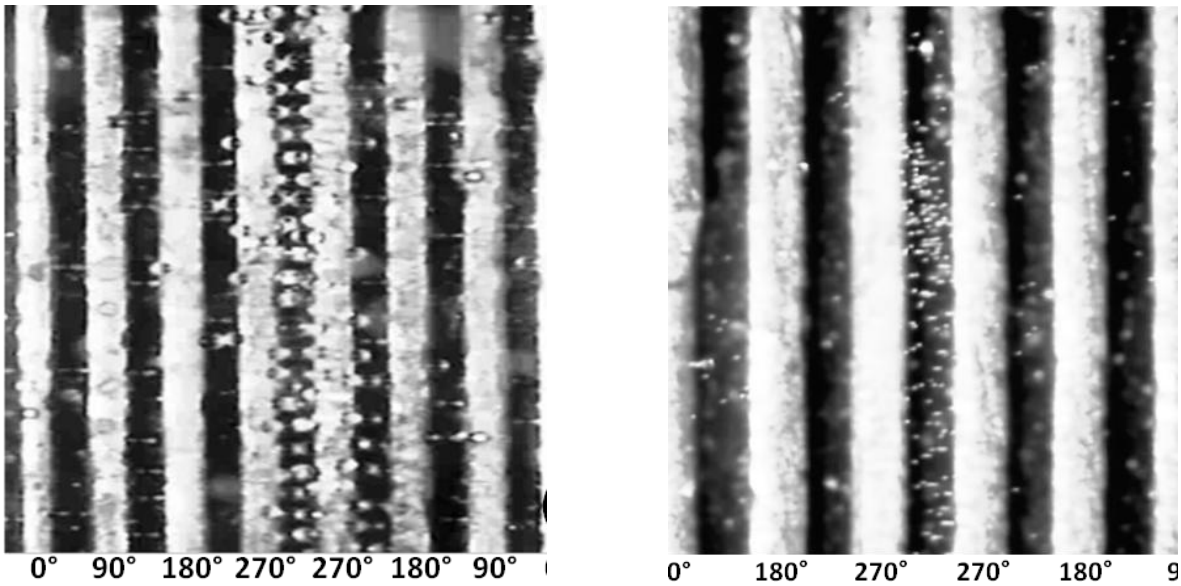

Figure A.2 Left side shows PCB implementation being used to manipulate 43μm polystyrene microspheres and right side shows device being used to manipulate 6μm polystyrene-COOH microspheres.

The other design attempt was with the use of 3D integrated circuit technology. 3D integrated circuits are fabricated by stacking multiple chips in order to increase the circuit density of the overall device. The 3D chips were fabricated using MIT Lincoln labs 0.13µm 3D process [1]. Figure A.3 shows the organization of the chip: the bottom tier contained digital control circuitry, the middle tier had analog circuitry to generate voltage waveforms and the top tier contained polysilicon nanoscale dielectrophoresis electrodes using a technique we published earlier [1].

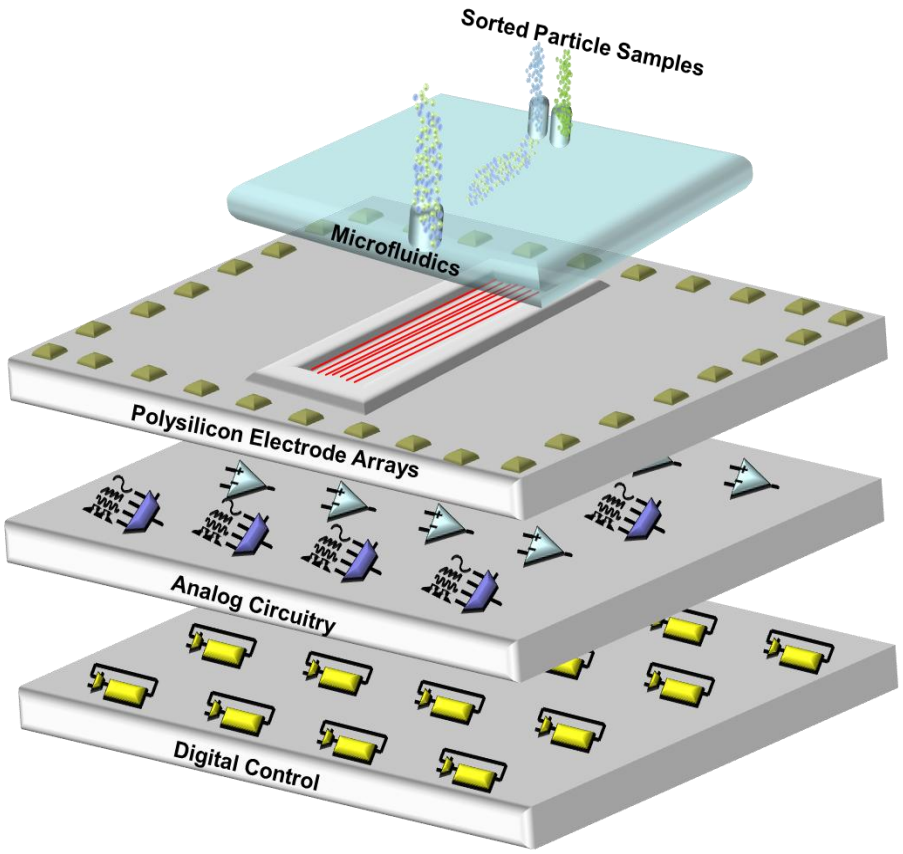

Figure A.3 Organization of nanoscale 3D integrated circuit implementation. The device contained three integrated circuit tiers: digital control circuitry, analogy waveform generation circuits and nanoscale electrodes.

The top of figure A.4 shows the 3D integrated circuit after it was fabricated and post processed. Due to manufacturing issues with the foundry's process, the chip was not able to be

tested. The fabricated chips were more fragile than the foundry expected and therefore could not be wire-bonded without destroying the chip. However, at the bottom of figure A.4 a close up of the nanoscale polysilicon electrodes we designed, after we carried out a secondary post-processing step. The vertical lines in the figure are the dielectrophoresis electrodes and are 130 nm wide, spaced 130nm apart. While the electrodes were not tested, using our design and post-processing methods, they have the distinction of being the smallest on-chip electrodes incorporated into a CMOS chip without having to modify the original fabrication process [1].

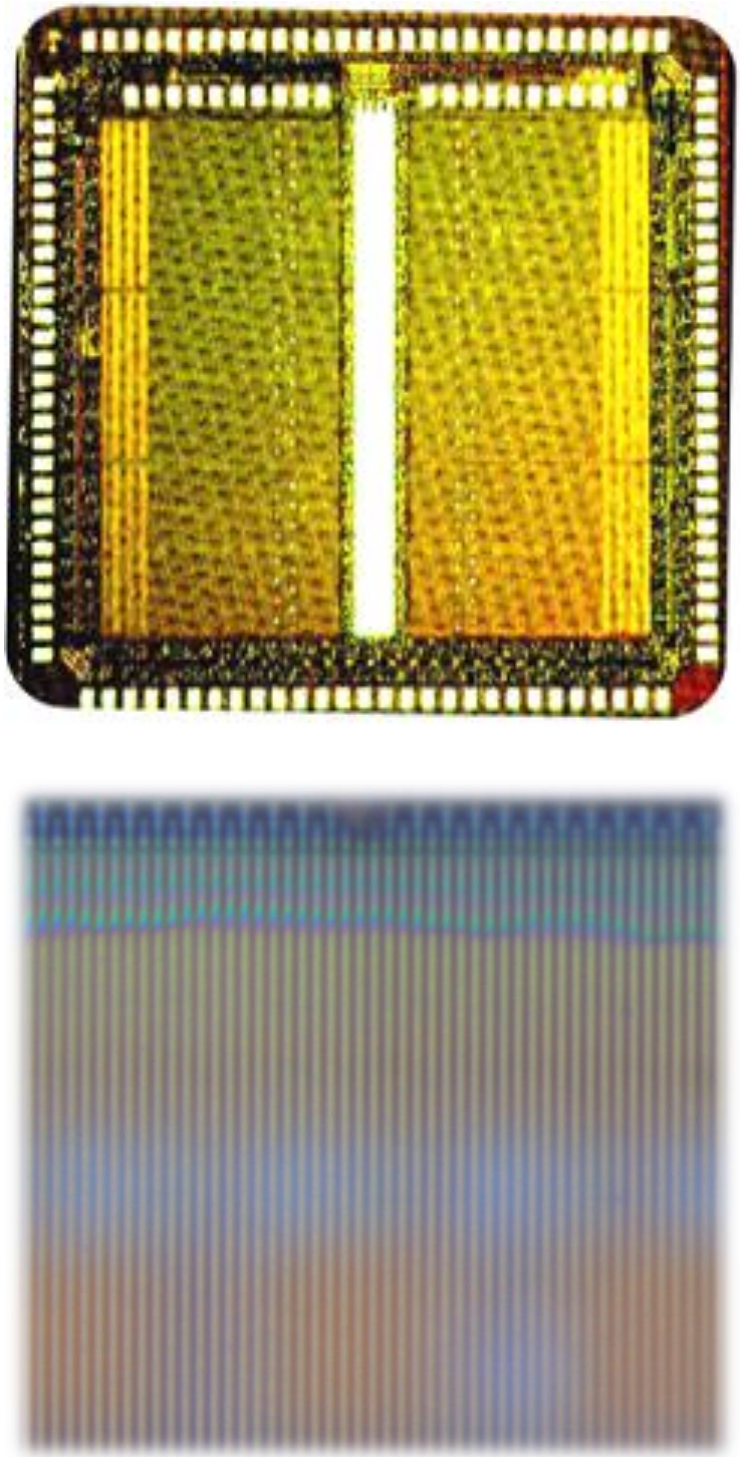

Figure A.4 Top shows 3D integrated circuit implementation after fabrication. Bottom shows close up of nanoscale polysilicon electrodes.

BIBLIOGRAPHY

1. Wikipedia, The Free Encyclopedia. Wikimedia Foundation, Inc. "**Laboratory**" Web. Retrieved November 2012. <http://en.wikipedia.org/wiki/Laboratory>

2. Pohl, Herbert A. "**The Motion and Precipitation of Suspensoids in Divergent Electric Fields**", J. Appl. Phys. 22, 869, 1951

3. World Health Orgainization. "**Enumeration of CD4 TLymphocytes**", Workshop Report SEA-HLM-390", Bangkok, Thailand, June 2006

4. Pethig, R. "**Review Article---Dielectrophoresis: Status of the theory, technology, and applications**",Biomicrofluidics 4, 2010

5. Y Huang, X B Wang, F F Becker, and P R Gascoyne "**Introducing dielectrophoresis as a new force field for field-flow fractionation**". Biophys J. 1997 August; 73(2): 1118–1129

6. Xiaoyuan Hu et al. "**Marker-specific sorting of rare cells using dielectrophoresis**" Proceedings of the National Academy of Sciences 102: 15757-15761;

7. Chin V. et al., "**Microfabricated platform for studying stem cell fates**". Biotechnology and Bioengineering vol 88, no 3, 2004

8. N. G. Green and H Morgan, "**Dielectrophoretic separation of nano-particles**". J. Phys. D: Appl. Phys. 30 (1997)

9. G. Fuhr, et al "**Dieletrophoretic field cages: Technique for cell, virus, and macromolecule handling**," Cell. Eng. Vol 1 pp. 47-57 1995.

10. Michael P. Hughes. "**Strategies for dielectrophoretic separation in laboratory-on-a-chip systems**". Electrophoresis, vol 23, no 16, 2002

11. Morgan, H. and Hughes, M.P. and Green, N.G., "**Separation of Submicron Bioparticles by Dielectrophoresis**", Biophysical Journal, vol. 77, no. 1, 1999

12. Hughes, M. P., H. Morgan, F. J. Rixon, J. P. H. Burt, and R. Pethig. "**Manipulation of herpes simplex virus type 1 by dielectrophoresis**". Biochim. Biophys. Acta. 1425:119-126, 1998

13. Michael P. Hughes, Hywel Morgan and Frazer J. Rixon, "**Measuring the dielectric properties of herpes simplex virus type 1 virions with dielectrophoresis**", Biochimica et Biophysica Acta, Volume 1571, Issue 1, 10 May 2002, Pages 1-8.

14. Hughes, M.P.; Morgan, H.; Rixon, F.J., "**Characterisation of Herpes Simplex Virus particles by dielectrophoreic crossover methods**," Engineering in Medicine and Biology Society, 1998. Proceedings of the 20th Annual International Conference of the IEEE , vol.6, no., pp.2816-2819 vol.6, 29 Oct-1 Nov 1998

15. Washizu, M. et al., "**Applications of electrostatic stretch-and-positioning of DNA**," Industry Applications, IEEE Transactions on , vol.31, no.3, pp.447-456, May/Jun 1995 Morgan separate by small changes in surface chem.

16. Z. Xiao et al. "**Dielectrophoresis-assisted deposition and alignment of single-walled carbon nanotubes for electronic-device fabrication**", J. Vac. Sci. Technol. A 28, 750 2010

17. Krupke,R. et al.. "**Separation of Metallic from Semiconducting Single-Walled Carbon Nanotubes**". Science 18 July 2003

18. Duchamp, M. et al. "**Controlled Positioning of Carbon Nanotubes by Dielectrophoresis: Insights into the Solvent and Substrate**" RoleACS Nano 2010 4 (1), 279-284

19. Agilent Technologies. "**Application Compendium for DNA, RNA, Protein and Cell Analysis with the Agilent 2100 Bioanalyzer**". Publication Number 5990-3315EN, March 2009.

20. Frost and Sullivan Research Service. "**U.S. Microfluidics/Lab-on-a-chip Markets**." May 2006.

21. Frost and Sullivan Research Service. "**U.S. Flow Cytometry Markets**." March 2008.

22. Davidson College Department of Biology. "**FACS Methodology**." Web. Retrieved July 2010. <http://www.bio.davidson.edu/courses/genomics/method/FACS.html>

23. Wikipedia, The Free Encyclopedia. Wikimedia Foundation, Inc. "**Flow Cytometery**" Web. Retrieved November 2012. < http://en.wikipedia.org/wiki/Flow_cytometry>

24. Dukhin, S.S. and Derjaguin, B.V. **Electrokinetic Phenomena**, J.Willey and Sons, 1974

25. T.B. Jones. **Electromechanics of Particles**, Cambridge Univ. Press, 1995

26. X -B Wang et al. **"A unified theory of dielectrophoresis and travelling wave dielectrophoresis"** 1994 J. Phys. D: Appl. Phys. 27 157.

27. Gascoyne, P. and Vykoukal, J. "**Particle separation by dielectrophoresis**", Electrophoresis, vol. 23, no. 13, pg 1973-1983, 2002

28. Becker F. et al. "**Separation of human breast cancer cells from blood by differential dielectric affinity**". Proc Natl Acad Sci U S A. 1995 January 31; 92(3): 860–864

29. Gascoyne, P. et al., Mahidol. "**Microsample preparation by dielectrophoresis: isolation of malaria"**. Lab on a Chip 2002

30. Stephens M. et al. "**The dielectrophoresis enrichment of CD34$^+$ cells from peripheral blood stem cells harvests**" Bone Marrow Trans. 1996; 18:777–782.

31. Gerard H. Markx, Mark S. Talary, Ronald Pethig, "**Separation of viable and non-viable yeast using dielectrophoresis**", Journal of Biotechnology, Volume 32, Issue 1, 15 January 1994, Pages 29-37

32. Cui L, Holmes D, Morgan H. "**The dielectrophoretic levitation and separation of latex beads in microchips**". Electrophoresis. 2001 Oct;22(18):3893-901.

33. Wang XB et al. "**Separation of polystyrene microbeads using dielectrophoretic gravitational field-flow-fractionation"** Biophys J. 1998 May;74(5):2689-701.

34. Yang J et al. "**Differential analysis of human leukocytes by dielectrophoretic field-flow-fractionation**" Biophysical Journal, Volume 78, Issue 5, 2680-2689, 1 May 2000

35. Huang Y et al. "**The removal of human breast cancer cells from hematopoietic CD34+ stem cells by dielectrophoretic field-flow-fractionation**" J Hematother Stem Cell Res. 1999 Oct;8(5):481-90.

36. Castellanos, A. et al. **"Electrohydrodynamics and dielectrophoresis in microsystems: scaling laws",** Journal of Physics D: Applied Physics, vol 36, no. 20, 2003

37. Green, NG , Ramos, A. and Morgan, H, **"AC electrokinetics: a survey of sub-micrometre particle dynamics",** J. Phys. D: Appl. Phys, vol. 33, 2000

38. Ramos, A. et al. "**Letter to the Editor: AC Electric-Field-Induced Fluid Flow in Microelectrodes**". J. Colloid and Interface Science 217, 1999.

39. Pethig, R. et al. "**Positive and negative dielectrophoretic collection of colloidal particles using interdigitated castellated microelectrodes**." Journal of Physics D: Applied Physics, V. 25, 5, 1992

40. Encyclopedia Britannica Online **"Electrical double layer**." Web. Retrieved July 2010. <http://www.britannica.com/EBchecked/topic/182857/electrical-double-layer>

41. Bazant, M. Z., "**AC Electro-osmotic flow**" Encyclopedia of Microfluidics and Nanofluidics, Part I, pp. 8-14,Springer, 2008

42. Ramos, A. et al. "**Pumping of liquids with traveling-wave electroosmosis**." J. Appl. Phys. 97, 2005

43. Cahill, B. "**Electro-osmotic streaming on application of traveling-wave electric fields**." Phys. Rev. E 70, 2004

44. Hughes M.P., Morgan,H. Flynn,M. "**The Dielectrophoretic Behavior of Submicron Latex Spheres: Influence of Surface Conductance**", Journal of Colloid and Interface Science, Volume 220, Issue 2, 15 December 1999,

45. Arnold , W. M., Schwan , H. P., Zimmermann ,U. "**Surface Conductance and Other Properties of Latex Particles Measured by Electrorotation**." J. Phys. Chem., 1987, 91 (19), pp 5093–5098

46. Cui L, Holmes D, Morgan H. "**The dielectrophoretic levitation and separation of latex beads in microchips**." Electrophoresis. 2001 Oct; 22(18):3893-901. PubMed

47. Simon Ostergaard, Lisbeth Olsson, Jens Nielsen. "**Metabolic Engineering of Saccharomyces cerevisiae**", Microbiol Mol Biol Rev. 2000 March; 64(1): 34–50

48. Wikipedia, The Free Encyclopedia. Wikimedia Foundation, Inc. "**Saccharomyces cerevisiae**" Web. Retrieved November 2012. <http://en.wikipedia.org/wiki/Saccharomyces_cerevisiae>

49. I Turcu and C M Lucaciu, "**Dielectrophoresis: a spherical shell model**" 1989 *J. Phys. A: Math. Gen.* 22 985-993

50. R Hölzel, "**Electrorotation of single yeast cells at frequencies between 100 Hz and 1.6 GHz**" Biophys J. 1997 August; 73(2): 1103–1109.

51. Y Huang et al. "**Differences in the AC electrodynamics of viable and non-viable yeast cells determined through combined dielectrophoresis and electrorotation studies**." Phys. Med. Biol. Vol 37, No 7 1992

52. E. M. Purcell, **"Life at low Reynolds number"**, American Journal of Physics Jan. 1977 Vol. 45 Issue 1, pp.3-11

53. Panton, Ronald, L. **Incompressible Flow,** third edition, Wiley, 2005.

54. Samir A. Haddad, Carl C. Lindegren, "**A Method for Determining the Weight of an Individual Yeast Cell**" Appl Microbiol. 1953 May; 1(3): 153–156.

55. ANSYS Inc. "**Ansys Maxwell: Electromagnetic Field Simulation**" Web. Retrieved November 2012. < http://www.ansys.com//>

56. Lifeng Zheng; Shengdong Li; Burke, P.J.; Brody, J.P.; , "**Towards single molecule manipulation with dielectrophoresis using nanoelectrodes**," *Nanotechnology, 2003. IEEE-NANO 2003.*, vol.1, no., pp. 437- 440 vol.2, 12-14 Aug. 2003

57. COMSOL Inc. "**COMSOL Multiphysics Simulation Software**". Web. Retrieved November 2012 < http://www.comsol.com/products/multiphysics/>

58. P Abgrall and A-M Gué. "**Lab-on-chip technologies: making a microfluidic network and coupling it into a complete microsystem—a review**". 2007 J. Micromech. Microeng. 17 R15

59. Yuen, Po Ki and Goral, Vasiliy "**N. Low-cost rapid prototyping of flexible microfluidic devices using a desktop digital craft cutter"**. *Lab Chip*, 2010, **10**, 384-387

60. Samuel J. Dickerson, Donald M. Chiarulli and Steven P. Levitan, "**Nondestructive Optical Assay Method for Nanoscale Biological Particles in Solution**, " IEEE Photonics Society Winter Topical Meetings 2011,Session on Optofluidics, Keystone, CO, January 10-12, 2011